Application of Transpiration Cooling on Hypersonic Vehicles to Mitigate Material Oxidation

Marc Ewenz Rocher

St Edmund Hall

University of Oxford

A thesis submitted for the degree of

Doctor of Philosophy

Michaelmas 2021

This thesis is dedicated to my grandparents,
Enriqueta, Paco, Helga and Peter.

Acknowledgements

I am deeply grateful to a large number of people who have helped and supported me on this journey.

First of all, I owe a huge debt of gratitude to my supervisor Prof. Matthew McGilvray. Your supervision balanced guidance and direction with the freedom to champion the project, enabling me to grow as a researcher. Thank you for the stimulating discussions on the analytical paper, late night and weekend shifts to operate HDT during the pandemic and most importantly, the Hamblin bread. Your tireless efforts enable us to do the exciting research we do.

Thanks must also go to my co-supervisor Dr. Tobias Hermann, whose feedback was simply brilliant. Your ability to understand the most complex problems and suggest clever and practical solutions amazes me. And your excitement about lasers is contagious.

I would like to extend my gratitude to everyone in the Hypersonics Group, especially to Luke Doherty and Chris Hambidge for being so generous with their time. Thank you Maïlys Buquet for the operation of the High Density Tunnel and the good vibes; Andrew Hyslop for your Teams praise and showing me the beauty of northwestern Wales; Imran Naved for the advice on PIRATE and your truly inspirational never-ending optimism; Philipp Kerth for joining me in abusing the Dealer app at Benito's Hat; Ikhyun Kim for helping with the nozzle change and the good company; Jack Hillyer and Eric Hembling for measuring the core flow diameter and Pitot pressure profiles. To the rest of the group, thanks for the good time and the many helpful chats throughout the years.

To Peter Jacobs and Rowan Gollan, University of Queensland, for their assistance with Eilmer 4; Jim Merrifield, Fluid Gravity Engineering, and Stefan Löhle, University of Stuttgart, for their helpful comments. I am grateful to the EPSRC (EP/P000878/1) for funding my research.

This work would not have been possible without all of the staff at the Oxford Thermofluids Institute. Special thanks must go to Greg King for his design advice and impeccable craftsmanship that was life-saving on multiple occasions. Thanks to Duncan Blake, Duncan Constable and the rest of the workshop for their dedicated attention to detail and assistance in building the experimental rigs. To Alex Weaving and Anna Erillo, for always going the extra mile.

To Hassan for being the best flatmate I could have asked for. And for introducing me to Currydor.

St Edmund Hall was my second home - thank you Kusal for creating such a vibrant and welcoming community; The biggest privilege of being at Oxford was meeting so many amazing people. In no particular order, thank you so much Julià, Núria, Martin, Lilli, Maciek, Wendy, Caro, Agata, Yasemin, Tom, Fahraz, Andrea, Freddie, Robin, Andrew, Liam, Ollie, Annika, Jess, India, Faidra, Yusuf, Mark, Aleksei and Raggy.

A separate thanks goes out to the St Edmund Hall Boat Club. Thank you Doug for motivating me to join and encouraging me to become captain. The early morning sessions, boat club dinners and winning double blades have become the fondest memories of my time in Oxford. In a particular order, thank you Dhaval, George, Josh, Joe, Marc, Ed, Ben, Doug, Will and Geordie - I had the best time.

Thank you Caroline, for your love and support throughout the years.

Finally, to my family for creating such a loving and supportive environment. Their care and guidance allowed me to pursue my dreams.

List of Publications

Journal Papers

- M. Ewenz Rocher, T. Hermann, M. McGilvray, C. Hambidge, H.S. Ifti, J. Vieira, M.K. Quinn, M. Grossman, L. Vandeperre, Pressure sensitive paint diagnostic to measure species concentration on transpiration cooled walls, *Experiments in Fluids*.

- M. Ewenz Rocher, T. Hermann, M. McGilvray, R. Gollan, Correlation for species surface concentration on a hypersonic stagnation point with mass injection, *AIAA Journal*.

- M. Ewenz Rocher, T. Hermann, M. McGilvray, M. Grossman, L. Vandeperre, Measuring the concentration of freestream species on a hypersonic transpiration-cooled stagnation point, *AIAA Journal of Spacecraft and Rockets*.

- M. Ewenz Rocher, T. Hermann, M. McGilvray, Oxidation response of transpiration cooled ZrB_2 on a hypersonic stagnation point, under review at *AIAA Journal of Spacecraft and Rockets*.

- H.S. Ifti, T. Hermann, M. Ewenz Rocher, L. Doherty, C. Hambidge, M. McGilvray, L. Vandeperre, Laminar Transpiration Cooling Experiments in Hypersonic Flow, under review at *Experiments in Fluids*

- I. Naved, T. Hermann, M. McGilvray, M. Ewenz Rocher, C. Hambidge, L. Doherty, L. Le Page, Heat transfer measurements of a transpiration cooled stagnation point in transient hypersonic flow, submitted to *AIAA Journal of Thermophysics and Heat Transfer*

Conference Papers

- M. Ewenz Rocher, T. Hermann, M. McGilvray, H.S. Ifti, F. Hufgard, M. F. Eberhart, A. Meindl, S. Loehle, T. Giovannini, L. Vandeperre, Testing a transpiration cooled zirconium-di-boride sample in the plasma tunnel at IRS, *AIAA SciTech Forum*, San Diego, US, 2019.

- M. Ewenz Rocher, T. Hermann, M. McGilvray, H.S. Ifti, M.K. Quinn, Studying the film effectiveness of transpiration cooled walls using pressure sensitive paint, *International Conference on Flight Vehicles, Aerothermodynamics and Re-entry Missions and Engineering*, Monopoli, Italy, 2019.

Abstract

This thesis investigates the application of transpiration cooling to mitigate material oxidation of hypersonic vehicles. This was motivated by the early onset of surface oxidation of many high-temperature aerospace materials and the resulting limitation of the flight envelope. For example, Ultra-High-Temperature Ceramics have melting points exceeding 3500 K, thus could balance the incoming heat flux through re-radiation alone, but start oxidising at 1000 K, which limits the passive cooling capability severely. The aim of this thesis is to increase this oxidation limit by shielding the surface from freestream oxygen through boundary layer mass injection.

A novel pressure sensitive paint diagnostic is developed in this work to measure the concentration of molecular oxygen on a transpiration cooled surface. This is a fundamental tool to quantify the ability of the coolant film to act as a barrier against freestream species that would lead to oxidation. The paint consists of $[Ru(dpp)_3]^{2+}$ luminophores, which are dissolved in a dichloromethane solution and then sprayed onto porous alumina. This method is validated experimentally on a transpiration cooled flat plate in a hypersonic cross-flow in the Oxford High Density Tunnel. Tests were conducted with no coolant injection, nitrogen injection and air injection at increasing blowing ratios. Oxygen partial pressure maps on the transpiration cooled surface were obtained for several conditions at unit Reynolds numbers between $2.58 - 5.0 \times 10^7/\mathrm{m}$ and blowing ratios between $0.016\% - 0.078\%$. It is found that the oxygen pressure decreases as the unit Reynolds number decreases and the blowing ratio increases. The direct measurements provided by this technique will aid the development of empirical correlations for the oxygen concentration on a porous surface with mass injection.

Before applying this diagnostic to a transpiration cooled stagnation point, a theoretical prediction of the species concentration at the wall is derived. This is achieved by combining the self-similar boundary layer equations with thin film theory. The resulting semi-analytical correlation explicitly expresses the concentration of freestream species on a hypersonic stagnation point as a function of freestream conditions, surface geometry and coolant properties. The concentration depends on the boundary layer edge pressure, temperature and velocity gradient, as well as the

wall temperature and injected mass flux. The molar mass and diffusion coefficient are further needed for scaling if the injected gas differs from the freestream gas. The method is compared against the numerically obtained self-similar solutions of a wide range of flow conditions and showed an accuracy of ±4%.

The correlation was compared to experiments on a transpiration cooled stagnation probe model tested in the Oxford High Density Tunnel. A porous Al_2O_3 material, developed in collaboration with Imperial College London, features a similar pore size and outflow homogeneity as ZrB_2, with the additional capability of bonding PSP. Experiments were conducted at Mach 6.9 at three different Pitot pressures: 10 kPa, 20 kPa and 30 kPa. Nitrogen, Argon and Krypton are used as injection gases at mass flow rates ranging from 0.01 - 0.55 kg/m^{2}s, in order to displace up to 99% of the freestream gas at the surface. The experimental data shows that transpiration cooling is more effective in displacing freestream gas than predicted by analytical models and numerical solutions. The microheterogeneous surface with recessed pores means there is an additional pressure gradient within the first layer of pores, which increases the displacement effectiveness.

A test campaign in the plasma wind tunnel at the Institute of Space Systems in Stuttgart provided the first qualitative data of the oxidation behaviour of transpiration cooled ZrB_2 in a continuous, steady state high-enthalpy environment. A 42% porous ZrB_2 sample is exposed to a cold-wall, fully catalytic stagnation point heat flux of 3.95 MW/m^2 at 3.22 kPa Pitot pressure. While the uncooled sample fully oxidised at a surface temperature of 2150 K, 20.25 g/m^{2}s of helium and 620.11 g/m^{2}s of nitrogen injection mitigated oxidation of the transpiration cooled samples.

Combining theoretical, numerical and experimental findings, the oxidation response of the stagnation point in a representative hypersonic flight scenario is predicted. An existing oxidation model for ZrB_2 is combined with low order correlations for the heat transfer and oxygen concentration at the surface, to yield the surface recession and oxide scale thickness. A 500 s steady state trajectory at 44 km altitude and 3.6 km/s velocity is found to lead to a 2.2 mm recession of the 3 mm nose radius. A constant mass injection at a blowing parameter of 0.6 reduces the recession to just 0.21 mm. The displacement of freestream oxygen by transpiration cooling has a significant effect on oxidation. Not accounting for the displacement of oxygen at the surface would increase the recession by up to 197%. The recession along the transient trajectory of an envisioned hypersonic vehicle with a 3 mm nose radius is found to exceed 0.94 mm with no mass injection. It is shown that nitrogen and helium injection at a blowing parameter of 0.6 can reduce the recession to 0.13 mm and 0.075 mm, respectively.

Contents

List of Figures

List of Tables

List of Abbreviations

B_h . . . . $\frac{F}{St_{h0}}$, blowing parameter for heat transfer

B_m . . . $\frac{F}{St_{m0}}$, blowing parameter for mass transfer

$B_{m,i}$ . . . $\lambda_i B_m$

$B*$ . . . . boundary layer blowoff parameter

C . . . . concentration, mol/m^3

C_2 . . . . empirical constant, m^2/s

c . . . . . mass fraction

c_p . . . . specific heat capacity, Jkg^{-1}K^{-1}

c_f . . . . skin friction coefficient

D . . . . mass diffusivity, m^{2}s^{-1}

$d_{i,j}$ . . . . Lennard-Jones parameter, Å

F . . . . $\frac{\rho_w v_w}{\rho_e v_e}$, blowing ratio

Fn . . . function of

f . . . . porosity of oxide scale

f' . . . . $\frac{u}{u_e}$, normalised velocity

h . . . . specific enthalpy, Jkg^{-1}

h_D . . . . average dissociation enthalpy, J/kg

h_{ext} . . . thickness of external boria layer, m

h_{int} . . . thickness of internal boria layer, m

h_v . . . . volumetric heat transfer coefficient, W/m^3 K

I . . . . . PSP intensity, counts

J . . . . bulk mole flux, mol/m^{2}s

J_i . . . . mole flux of species i, mol/m^{2}s

$|J|$ . . . . diffusive flux, mol/m^{2}s

j . . . . . mass flux, kgm^{-2}s^{-1}

K_D . . . Darcy coefficient, m^2

K_F . . . Forchheimer coefficient, m

K_h . . . . heat transfer coefficient, $\mathrm{Wm}^{-2}\mathrm{K}^{-1}$

K_M . . . enthalpy correlation constant for air, $\mathrm{N}^{1/2} \cdot \mathrm{m}^{1/2} \cdot \mathrm{s/kg}$

K_m . . . mass transfer coefficient, ms^{-1}

k . . . . . thermal conductivity, $\mathrm{Wm}^{-1}\mathrm{K}^{-1}$

L . . . . characteristic length or oxide scale thickness, m

L_1 . . . . sample thickness, m

Le . . . . Lewis number

l . . . . . $\frac{\rho\mu}{\rho_e\mu_e}$, Chapman-Rubesin factor

M . . . . molar mass or Mach number

$\dot{m}$ . . . . mass generation per unit area or mass flux, $\mathrm{kgm}^{-2}\mathrm{s}^{-1}$

m . . . . $\frac{\eta}{\Delta}$, dimensionless y-coordinate

N_f . . . . atomic correction factor

n . . . . mole density

$\dot{n}$ . . . . formation rate, $\mathrm{mol/m}^2\mathrm{s}$

Pr . . . . $\frac{c_p\mu}{k}$, Prandtl number

p . . . . . pressure, Pa

p_0 . . . . freestream total pressure, Pa

p_{O_2} . . . oxygen partial pressure, Pa

$\dot{q}$ . . . . . heat flux, Wm^{-2}

R . . . . effective nose radius or surface recession, m

$\mathcal{R}$ . . . . universal gas constant, J/mol K

Re . . . . $\frac{\rho u L}{\mu}$, Reynolds number

r . . . . . nose radius, m

r_1 . . . . cylindrical radius of body, m

Sc . . . . $\frac{\mu}{\rho D}$, Schmidt number

Sh . . . . $\frac{j_w}{-\rho_w D_w \frac{c_e - c_w}{L}}$, Sherwood number

St_h . . . $\frac{\dot{q}}{\rho u(h_e - h_w)}$, heat transfer Stanton number

St_m . . . $\frac{K_m}{u_e}$, mass transfer Stanton number

T . . . . temperature, K

T_0 . . . . total temperature, K

t . . . . . time, s

u . . . . x component of velocity, ms^{-1}

$\frac{du_e}{dx}$ . . . . velocity gradient, 1/s

v . . . . . y component of velocity, ms^{-1}

W . . . . molecular weight, g/mol

$\dot{w}$ . . . . mass generation per unit volume, $\mathrm{kgm}^{-3}\mathrm{s}^{-1}$

x . . . . distance along surface, m, or mass fraction

y . . . . . distance normal to surface, m, or mole fraction

z . . . . . material depth, m

α . . . . $\frac{l}{Sc}$

β . . . . generalised profile factor

β_1 . . . . molecular slip factor

Γ_{c_p} . . . . $\frac{c_p}{c_{p,e}}$, ratio of heat capacities

γ . . . . ratio of specific heats

Δ . . . . effective film thickness

Δ^* . . . . shock stand-off distance, m

δ . . . . . $\frac{\rho_e}{\rho}$, density ratio

$\delta*$ . . . . boundary layer thickness

ε . . . . . emissivity

η . . . . . defined by Eq. (4.8)

θ . . . . . $\frac{T}{T_e}$, normalized temperature

λ . . . . scaling factor or wavelength, m

λ_1 . . . . scaling factor presented in Eq. (4.3)

λ_2 . . . . scaling factor for cases in Fig. 4.6 only

λ_3 . . . . scaling factor accounting for Sc

λ_4 . . . . scaling factor accounting for Sc and $\frac{T_w}{T_e}$

λ_5 . . . . scaling factor for all cases

μ . . . . viscosity, Pa·s

ξ . . . . . defined by Eq. (4.8)

$\Pi_{O_2-B_2O_3}$ oxygen permeability in liquid boria, m^2/s

ρ . . . . . density, kgm^{-3}

σ . . . . Stefan-Boltzmann constant

τ . . . . . empirical correction factor

ϕ . . . . porosity

$\Omega_{i,j}$ . . . collision integral

Subscripts

0 . . . . . no mass injection

$0, nom$ . . nominal value provided by heat flux probe

adj . . . adjacent inner cell

aero . . . aerodynamic

aw . . . . adiabatic wall

c . . . . . coolant

cold . . . cold wall

cond . . . conductive

conv . . . internal convective

e . . . . . boundary layer edge

eq . . . . equilibrium state

ext . . . external gas

fginj . . . foreign gas injection

film . . . coolant film

fluid . . . fluid

i . . . . . ith component of mixture

in . . . . inflow

inj . . . . injected gas

int, adv . internal advective

noinj . . no injection

out . . . outflow

pl . . . . plenum

r . . . . . recovery

rad . . . radiative

reduced . reduced

ref . . . . reference condition

s . . . . . solid

stag . . . stagnation

tcx . . . tunnel condition x

w . . . . wall

∞ . . . . freestream

Superscripts

$'$ . . . . . derivative with respect to η

a . . . . . ambient

i . . . . . liquid vapor interface

s . . . . . substrate

zb . . . . zirconia boria interface

Acronyms

LEO . . . Low-earth-orbit

PSP . . . Pressure-sensitive paint

UHTC . Ultra-high-temperature ceramic

1 Introduction

Contents

Hypersonic flight is experiencing a global renaissance, with growth in commercial, military and scientific interest [1]. The primary benefit of hypersonic flight is extreme speed, greater than 1.5 km/s. This can result in shorter intercontinental travel times and a strategic advantage for defence applications. For spacecraft, hypersonic flight is inevitable when leaving Earth's atmosphere or returning. The resurgence of hypersonic vehicle development is benefited by recent technological advancements, such as inexpensive computational power for numerical modelling and next-generation high temperature materials.

The global hypersonics market has reached an annual revenue of $5.7 billion [2], which is forecast to double by the end of the decade. This encompasses funding from the private sector, industry and government for civil transportation, Low-Earth-Orbit (LEO) delivery, defence and space exploration. The venture capital

markets have invested $318 million since 2015 into promising startups for high speed civil transport aircraft. For example, Hermeus is developing a Mach 5 passenger aircraft and was awarded $16 million to flight test its new engine in late 2022, with an additional $60 million of US Air Force funding. NASA awarded SpaceX a $2.9 billion contract to develop a lunar lander by 2024 [3]. Defence funding is by far the largest contributor to hypersonic spending, with the Pentagon's hypersonic budget seeing a compound annual growth rate of 26% since 2014 [1] with a FY2021 hypersonics R&D budget of a staggering $3.2 billion.

Whatever the application, a key challenge in designing a hypersonic vehicle is handling the extreme aerodynamic heating [4]. For example, the stagnation point heating for LEO return can exceed 2 MW/m^2. To protect the crew and payload from this extreme environment, thermal protection systems (TPSs) are needed. The peak heat flux determines the type of TPS required and the integrated heat flux over the flight trajectory (*i.e.* the heat load) determines the size required. For low heat fluxes, passive systems such as high emissivity tiles or heat sinks can be used. As the heat flux increases, the operating temperature of the underlying materials are exceeded requiring active cooling. These active cooling methods can also reduce the incoming heat flux through either convective and radiative blocking mechanisms.

To date, most spacecraft use ablative heat shields which burn off during reentry and thus can not be reused. They are simple to implement, reliable and can withstand extremely high heat fluxes. Their single-use nature is appropriate for a single-use vehicle. The current push towards vehicles for high speed passenger transport and affordable LEO access, creates a requirement for the re-usability of the thermal protection system. What is more, vehicles for atmospheric flight benefit from sharp leading edges, to minimise drag and ensure sufficient propulsion. To retain control, these critical aerodynamic elements must be shape-stable, ruling out the use of ablatives. Re-usability and shape-stability are therefore the main drivers to explore better protection systems.

1.1 Hypersonic stagnation point

The stagnation point is typically the point of highest heat flux seen on the vehicle. This could be the nose of the Apollo capsule, the leading edge of a hypersonic glide vehicle or the inlet of an air-breathing engine such as a scramjet. Figure 1.1 shows the flow field and relevant flow phenomena for a hypersonic stagnation point in the body's frame of reference. The gas speed is first decreased to subsonic speeds through a normal shock. This deceleration of the gas results in an increase of the static enthalpy, leading to elevated gas temperatures of above 2000 K where real gas effects occur, such as dissociation and even ionisation. As an approximation, the post normal shock temperature in Kelvin is roughly the same as the flight speed in m/s (*i.e.* a vehicle flying at 4 km/s will have a post shock temperature of 4000 K). A thermal and velocity boundary layer will exist near the wall as the gas is accelerated around the body of the vehicle. This ultimately leads to high heat fluxes to the vehicle through convection, radiation from the gas and surface recombination.

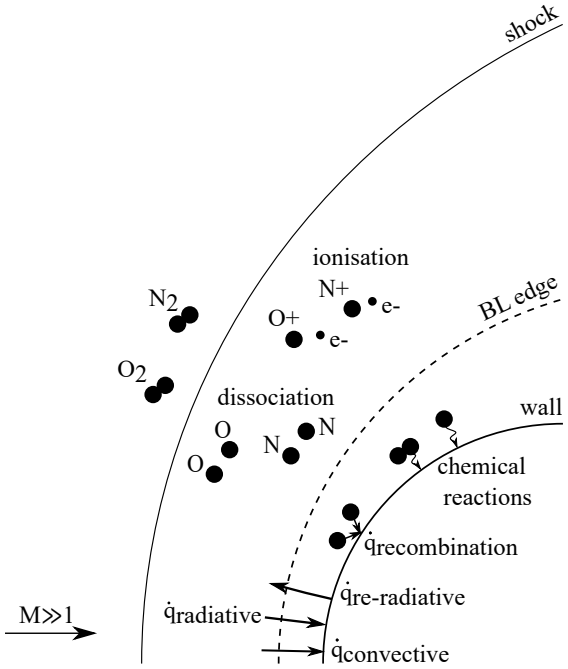

Figure 1.1: Flow field around a hypersonic blunt body in the body's frame of reference.

A thermochemical equilibrium assumption can be taken when the timescales of reaction are insignificant in comparison to the flow residence times. This holds for

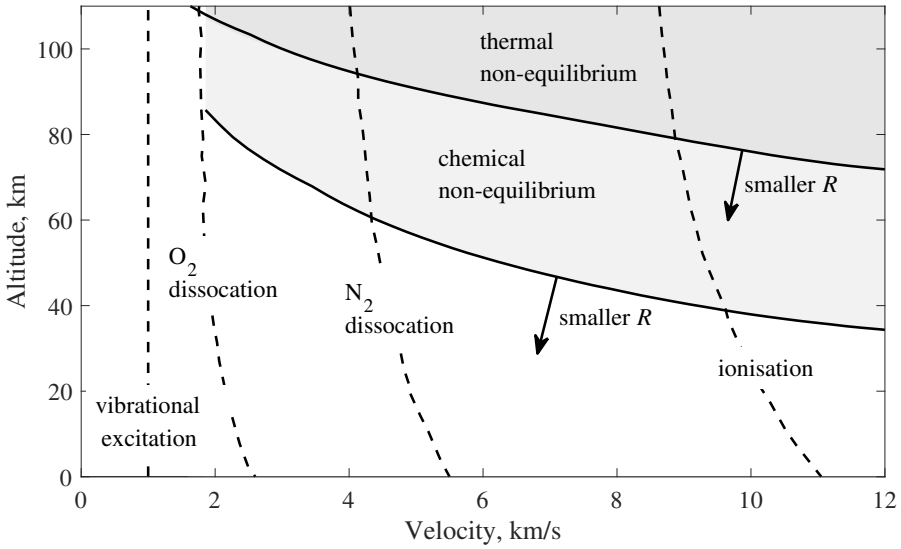

Figure 1.2: Post-shock air chemistry adapted from Ref. [5]. The non-equilibrium regions were computed for a 0.3 m axisymmetric nose radius.

large radius vehicles at lower altitude and speeds as shown in Figure 1.2. However, at high altitudes the density decreases, resulting in a longer mean free path between the particles. This reduces the number of collisions between gas particles, thus, reducing reaction rates. Additionally, the flow residency time will decrease for smaller radii due to a reduction in the shock-standoff distance and with faster vehicle speeds. If the chemical reaction time exceeds the flow residency time, the gas will will be in a state of chemical non-equilibrium. Further reducing the flow residency time also leads to thermal non-equilibrium where the energy states of the gas particles (translational, vibrational, rotational and electronic) are not equal.

1.1.1 Heat transfer

The incoming heat flux is a combination of heating from convection, gas radiation and surface recombination. They will occur in different proportions depending on the trajectory point and radius. The balance of this heat flux is discussed in Section 1.1.3.

Convection

Convective heat flux on a stagnation point denotes the energy transfer at the surface due to a temperature gradient. The convective heat flux on an axisymmetric

Table 1.1: Representative flight scenario of a hypersonic vehicle.

Nose radius [mm]	Velocity [m/s]	Altitude [km]	Emissivity [-]
3	3600	44	0.7

hypersonic stagnation point in an air freestream in thermo-chemical equilibrium is commonly predicted using the Fay and Riddell correlation[6]

$$\dot{q}_0 = 0.76 Pr_w^{-0.6} \left(\rho_w \mu_w\right)^{0.1} \left(\rho_e \mu_e\right)^{0.4} \left(1 + \left(Le^{0.52} - 1\right) \frac{h_D}{h_e}\right) \left(h_e - h_w\right) \sqrt{\frac{du_e}{dx}}, \quad (1.1)$$

where the Prandtl and Lewis number are assumed to be $Pr = 0.71$ and $Le = 1.4$, respectively. This expression was partly derived from the self-similar boundary layer equations for a laminar stagnation point. An empirical correlation is used to express the heat transfer parameter $\frac{Nu}{\sqrt{Re}}$ in terms of known quantities. It can be noted that the heat flux increases with the $1/\sqrt{\text{radius}}$ due to the velocity gradient. Thus, sharpening leading edges results in increased convective heat fluxes.

The incoming convective heat flux is reduced by having a higher wall temperature and thus wall enthalpy. Using the trajectory point and radius relevant to a hypersonic spaceplane (variables shown in Table 1.1), Figure 1.3 depicts the incoming stagnation point heat flux applying the Fay and Riddell correlation. The cold wall heat flux is nearly 8 MW/m^2 but reduces to zero at 3730 K which is the boundary layer edge temperature. Note the kink in the curve at 3000 K is due to the dissociation of the gas which converts some of its thermal energy to chemical energy.

Gas radiation

The particles in the post-shock region are continuously excited through collisions. This is balanced by a relaxation to a lower energy state, which can happen through a further collision or through the emission of electromagnetic radiation. As the energy of collisions increases with temperature, radiation starts to become significant at entry velocities of 9 km/s. Radiative heating in the shock-layer region can be modelled numerically [7], but is computationally expensive. An analytical correlation

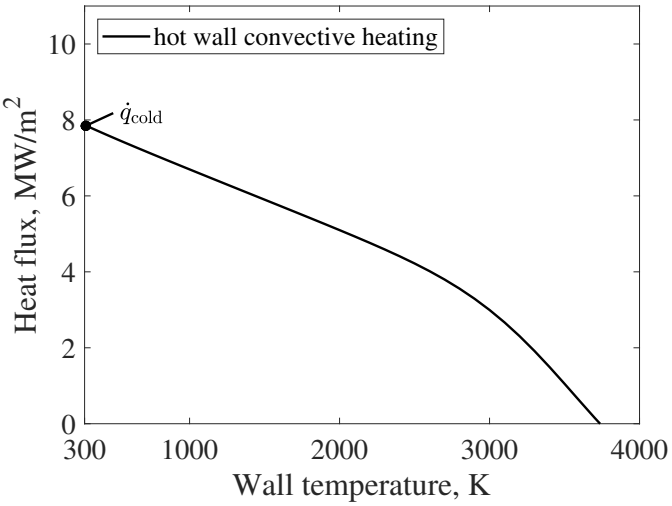

Figure 1.3: Effect of wall temperature on the convective heat flux for the flight scenario summarised in Table 1.1.

for the radiative heat flux encountered by a re-entry vehicle was presented by Tauber and Sutton [8]. In Earth's atmosphere radiative heat flux begins to be significant at velocities exceeding 9 km/s. In this thesis, radiative heating is neglected due to the lower speeds considered.

Surface recombination

If dissociated species reach the surface and the material is catalytic, an increasing fraction of the heat transfer will occur through recombination. When two atoms recombine to form a molecule, their dissociation energy is released as heat. This is also commonly referred to as catalytic heating. There are two mechanisms by which molecules can transfer from the freestream to the surface: convection and diffusion. Based on Fick's law, the molar flux of diffusion is always proportional to the concentration gradient [9]. A highly catalytic surface will deplete the atoms, thereby acting as a sink. This will increase the concentration gradient and thus the molar flux of atoms towards it. A barrier against the diffusion of atoms through the boundary layer towards the surface is therefore highly desirable.

For wall temperatures below the dissociation temperature (approximately 2000 K), a boundary layer that is in chemical equilibrium will inherently have no atoms existing near the wall. However, if the boundary layer is in chemical non-equilibrium,

atoms can significantly exist at wall temperatures at 2000 K and below. Thus, catalytic heating is more prominent in non-equilibrium boundary layers.

1.1.2 Surface oxidation

While section 1.1.1 highlighted the heat flux penalty of freestream species reacting at the surface, there is another detrimental effect. Freestream atomic oxygen must not necessarily react with another atom. It can also react with the surface material directly. The same is true for molecular oxygen. This results in material degradation and recession, which jeopardizes the structural and aerodynamic integrity of the vehicle. The depletion of oxygen through oxidation reactions at the surface further increases the diffusive flux of oxygen towards the surface, as described in section 1.1.1. For an equilibrium boundary layer and wall temperatures below 3000 K, molecular oxygen will dominate the reaction (Figure 1.4).

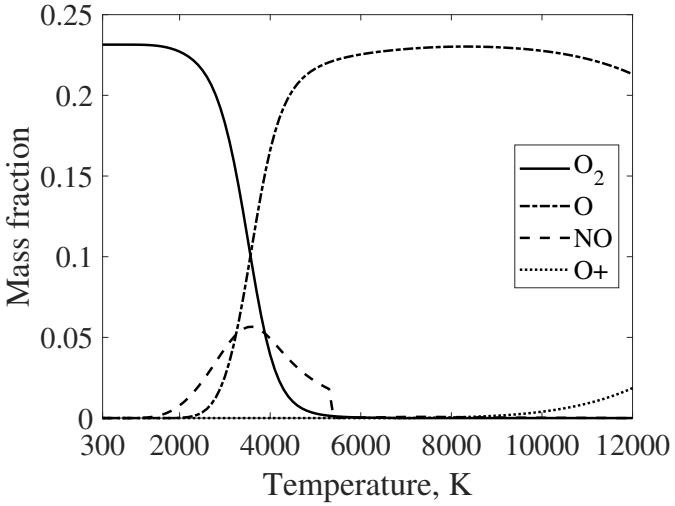

Figure 1.4: Equilibrium mass fraction of oxygen species in atmospheric air as a function of temperature.

1.1.3 Thermal protection systems

The high incoming heat fluxes are balanced within the thermal protection system (TPS) to manage the heating to the structure and payload within the vehicle. TPSs are typically categorised as passive, active and ablative systems.

Passive

Passive mechanisms are typically the lowest performing TPS. They include re-radiation and thermal diffusion and storage. The application of thermal diffusion of the peak heating to colder parts of the vehicle for storage is limited to moderate heat fluxes and short exposure times due to heating of the internal substructure. Re-radiation is used in a wide range of hypersonic vehicles (including active systems) and increases dramatically with elevated surface temperatures according to the Stefan-Boltzmann law:

$$\dot{q}_{\text{rad}} = \varepsilon \sigma T_w^4 \tag{1.2}$$

Using the example from Section 1.1.1, by balancing the convective and re-radiative heat fluxes, the equilibrium surface temperature can be determined (Figure 1.5). For this example, this temperature is well beyond the melting points of most high temperature materials. Ultra-High Temperature Ceramics (UHTCs) can survive these extreme temperatures, however, suffer from surface oxidation above 1000 K [10], making them unsuitable.

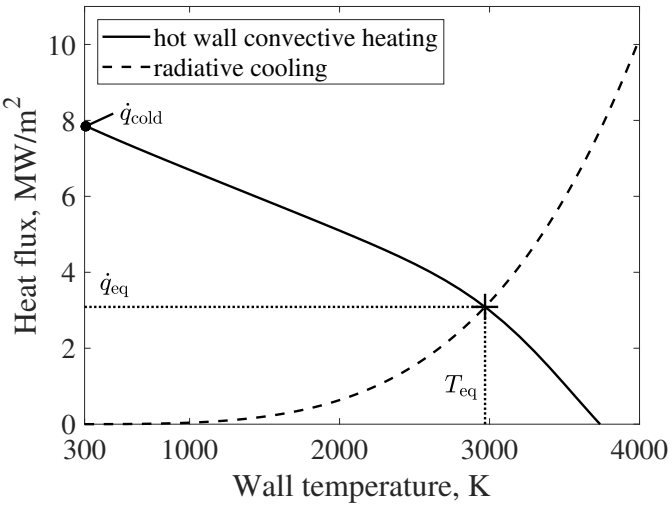

Figure 1.5: Equilibrium temperature for an uncooled stagnation point.

Active

Active systems can typically handle higher heat fluxes at the expense of increased complexity. On the Space Shuttle, liquid internal cooling of the wing leading edges was used to reduce the peak temperatures whilst not heating the internal structure of the vehicle [11]. These are ineffective at higher heat fluxes due to limited thermal diffusivity of the materials. Another potential active cooling candidate for hypersonic vehicles is transpiration cooling. It additionally blocks the incoming heat flux through blowing of a coolant gas and will be described further in Section 1.1.4. Electron transpiration cooling uses the thermionic emission of electrons to reject heat [12]. In response to being heated, the surface emits electrons, which carry the heat away. However, this technique is still in the early stages of research and therefore very immature.

Ablative

Ablatives further reduce the incoming heat flux through absorbing further energy through ablation of the solid whilst blowing pyrolysis gases (similar to transpiration cooling). Ablatives are by far the highest performing TPS. Due to their reliability and robustness, they have been employed in many vehicles in the past and present. However, their lack of re-usability and shape stability make them undesirable for certain vehicles.

1.1.4 Transpiration Cooling

Transpiration cooling feeds an inert fluid through a porous wall, thereby cooling it down through a combination of internal convection, external heat flux blockage, passive re-radiation and thermal storage. Additionally, it can decrease the recombination heating by reducing the concentration of boundary layer edge atoms through an inert coolant film. To date, this has been explored as a technology for shape stable and reusable thermal protection. The most prominent application was by DLR as part of the SHEFEX II flight demonstrator [13]. It was also briefly considered by SpaceX to protect the windward side of Starship.

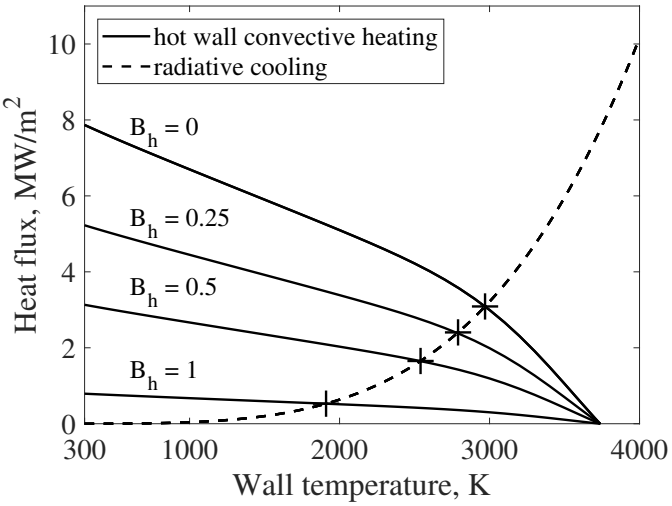

Figure 1.6: Equilibrium temperature for various amounts of blowing

By using the example from Section 1.1.1, the incoming convective heat flux is reduced as a function of the non-dimensional blowing parameter

$$B_h = \frac{F}{St_{h0}} \tag{1.3}$$

where F denotes the ratio of injected mass flux to freestream mass flux and St_h is the ratio of wall heat flux to the thermal energy flux of the passing fluid. Using the correlation provided by Yoshikawa [14] and helium as the coolant, the effect of blowing is illustrated in Figure 1.6 (Note: This ignores internal cooling and changes in recombination heating). As the blowing parameter increases, the incoming heat flux is seen to reduce by 69.3% at a B_h of 1. This has a knock-on effect of reducing the equilibrium temperature when balanced with the re-radiative cooling.

Figure 1.7 shows the equilibrium temperature over a wide range of blowing parameters for the example above. Overlaying the melting points for carbon/carbon (C/C) composites and nickel superalloys (Ni SA), one can see that high blowing parameters are required to keep these cool. This is quite large and will have a system level downside of requiring to carry more coolant. Additionally for sharp leading edges, exceeding a blowing parameter of 0.59 will blow off the boundary layer thereby aerodynamically blunting the stagnation point. As the motivation for sharp leading edges is to reduce drag at the expense of increased incoming

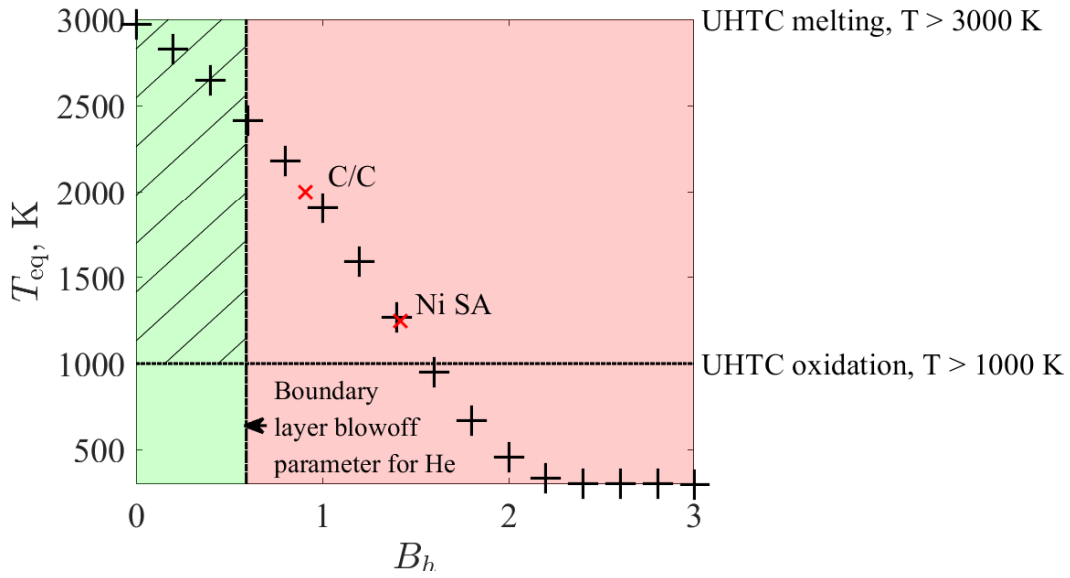

Figure 1.7: Blowing parameter required for the operation of various aerospace materials.

convective heat flux, this defeats the purpose of using transpiration cooling to enabling sharp leading edges. A material with an operating temperature exceeding 2450 K is required to avoid blowoff.

One class of refractory materials capable of sustaining these temperatures are Ultra-High-Temperature Ceramics (UHTCs). These ceramics offer excellent stability at high temperatures and feature melting points exceeding 3500 K, not even requiring cooling (Fig. 1.7). However, their drawback is the early onset of oxidation at temperatures as low as 1000 K [10].

If the oxidation limit was lifted for UHTCs, these high performing materials could be employed on hypersonic stagnation points, paving the way for global hypersonic transportation. This could be achieved by applying transpiration cooling of an inert fluid shielding the stagnation point from freestream oxygen. Additionally, it would limit any recombination heating. Recent work by the University of Oxford and Imperial College London has shown that UHTCs can be manufactured to have suitable permeability and strength [15].

1.2 Research contributions

The aim of this thesis is to:

investigate the application of transpiration cooling on hypersonic vehicles to mitigate material oxidation.

The original contributions of this research are:

Development of methods to analyse the mass transport of oxygen from the boundary layer edge to the surface with transpiration cooling

One of the major inputs to predict the level of oxidation is the concentration of oxygen at the wall. As seen in Section 1.1.2, molecular oxygen is of most interest. No methods existed in the open literature, thus, new techniques were developed to predict and measure the oxygen concentration at a stagnation point with blowing:

- A direct, non-intrusive experimental diagnostic using Pressure Sensitive Paint (PSP) for the concentration of freestream molecular oxygen on a transpiration cooled surface is developed. This uses a surrogate porous material (Alumina) to enable bonding of the PSP to the surface.
- An analytical correlation for the concentration of freestream species on a hypersonic stagnation point with mass injection is developed. This is based on film theory.

Experimental investigation of the transport of oxygen to the surface for a transpiration cooled flat plate and stagnation point

There is no existing experimental data in the literature of mass transport to a transpiration cooled surface. This work provides new data to the literature and provides a comparison to any numerical model including the correlation developed above. The following experiments were undertaken using the PSP technique developed in this thesis:

- A stagnation point experiment at Mach 7 was undertaken over a range of blowing parameters and coolant gases. It is shown that the oxidation protection is better than predicted by numerical models, due to the irregular surface of the porous material.

- A hypersonic flat plate experiment was undertaken with both laminar and turbulent boundary layers over a range of blowing parameters with nitrogen and air coolant gases.

Assessing the performance of transpiration cooling to mitigate oxidation of UHTCs

Both an experimental and numerical study were performed to explore if transpiration cooling can be used to mitigate oxidation of UHTCs on a hypersonic stagnation point:

- A proof-of-concept experiment is conducted in the plasma wind tunnel at IRS, showing that transpiration-cooling can prevent surface oxidation of ZrB_2 in temperature regimes in which oxidation is expected.

- A numerical model combining models of the heating, oxygen concentration and material oxidation response under transpiration cooling was developed. This showed transpiration cooling could significantly limit oxidation for ZrB_2 hypersonic stagnation points.

1.3 Thesis structure

This thesis consists of seven chapters, including the Introduction. The remaining chapters are

Chapter 2: Background

A review of the literature relating to this research project is provided. The main themes are transpiration cooling, material oxidation and oxidation diagnostics, in particular pressure sensitive paint.

Chapter 3: Pressure sensitive paint diagnostic to measure species concentration on transpiration cooled walls

This chapter is based on the journal paper published in *Experiments in Fluids* [16] with a small amount of additional analysis on the heat to mass transfer analogy under turbulent conditions. Different methods of employing pressure sensitive paint (PSP) on porous media are explored. This involves finding a suitable porous material. It should bond PSP, while mimicking the microstructure of common aerospace materials. Calibration procedures are established and a post-processing method is developed. The technique is validated on a well characterised transpiration cooled flat plate model in the Oxford High Density tunnel. This involves two experimental campaigns, where the first one serves as proof-of-concept and the second to further optimise the method.

Chapter 4: Correlation for species surface concentration on a hypersonic stagnation point with mass injection

This chapter is based on the journal paper published in *AIAA Journal* [17]. The self-similar governing equations of a laminar hypersonic stagnation point with mass injection are combined with thin film theory to obtain a correlation for the species concentration and mass Stanton number at the surface. The correlation is a function of the freestream parameters, coolant properties and stagnation point geometry. The approach is compared to the high-fidelity CFD solver Eilmer 4. To achieve this, a user-defined boundary condition for a porous wall with mass injection is developed and implemented.

Chapter 5: Experimental investigations of the hypersonic transpiration-cooled stagnation point

This chapter is based on the journal paper submitted to the *AIAA Journal of Spacecraft and Rockets* [18] with a small section from the AIAA Scitech conference paper [19]. A hemispherical stagnation probe with a transpiration cooled Al_2O_3 sample is designed and developed. Pressure sensitive paint is employed on the porous surface to measure the reduction of freestream oxygen at different mass

injection rates. The model is tested in the Oxford High Density tunnel and the results are compared to the analytical model and CFD simulations. A diffusion model is presented to explain porous interface phenomena not captured by numerical solvers. Proof-of-concept experiments were undertaken in the plasma wind tunnel at the Institute of Space Systems at the University of Stuttgart. A stagnation probe with a transpiration cooled ZrB_2 sample is designed and exposed to various high-enthalpy conditions. This showed qualitatively that transpiration cooling could be used to prevent oxidation of UHTCs.

Chapter 6: Oxidation response of transpiration cooled zirconium-diboride on a hypersonic stagnation point

This chapter is based on the journal paper submitted to the *AIAA Journal of Spacecraft and Rockets* [20]. An analytical model for the oxidation behaviour of ZrB_2 is taken from the literature. It is fed with the temperature and oxygen partial pressure from low-order numerical models for the heat transfer and oxygen concentration at the surface. It is applied to a representative steady state hypersonic flight scenario to show that the surface recession is significant and that oxidation protection is needed to avoid aerodynamic control problems. It is shown that low to moderate amounts of blowing can significantly reduce the oxidation rate and thus the surface recession. The oxidation behaviour for a transient trajectory of an envisaged hypersonic vehicle is calculated.

Chapter 7: Conclusions and Future Work

This chapter concludes the thesis by summarising the key results, suggesting improvements and recommending future work.

2

Background

Contents

In this chapter, literature pertinent to transpiration cooling of hypersonic stagnation points and relevant numerical and experimental techniques for measuring oxidation is reviewed. Further literature is also reviewed in each of the proceeding four chapters which are based on submitted or published journal papers that make up this thesis.

2.1 Transpiration cooling

Originally dubbed "sweat-cooling", the concept of forcing a fluid through a porous wall to reduce the incident heat flux was born in the mid-1940s in the Jet Propulsion Lab. It was motivated by the desire to increase operating temperatures and thus the efficiency of jet engines. Therefore the focus was on cylindrical ducts with a turbulent core flow, typically a fuel-air mixture. Initial experiments were limited to water injection through porous metals [21] and showed that a small mass flow rate of 0.16 kg/m^2 could lead to a large reduction in heat flux of 1.7 MW/m^2. The experimental infrastructure was built and new porous metals, including stainless steel and copper, were developed [22]. It was further postulated that the system performance will be driven by the pore size, porosity, freestream gas temperature and velocity, as well as various coolant properties including the injection rate, temperature, viscosity, thermal capacity and heat of evaporation. First empirical correlations were proposed to express the reduction in wall temperature to these parameters. For this purpose, a performance parameter called adiabatic film effectiveness was defined, which takes the following form:

$$\eta = \frac{T_\mathrm{r} - T_\mathrm{aw}}{T_\mathrm{r} - T_c} \tag{2.1}$$

where T_r is the recovery temperature of the freestream gas, T_aw is the adiabatic wall temperature with cooling and T_c denotes the temperature of the coolant in the plenum [23]. The film is 100% effective if the coolant has blocked so much heat that $T_c = T_\mathrm{aw}$.

The first analytical treatment of the problem is presented in Ref. [24]. Noting that the coolant mass flux is much smaller than the freestream mass flux, it was inferred that the wall could not be cooled through turbulent mixing alone. Instead, it was postulated that there must exist a thin laminar coolant layer, insulating the wall from the turbulent freestream. Starting with the governing equations of a laminar flat plate with mass injection, the temperature profile was shown

to be a function of $PrReF$, which can be rewritten as $\frac{F}{St_h}Nu$. The parameter F is the blowing ratio, denoted as:

$$F = \frac{\rho_c u_c}{\rho_\infty u_\infty} \tag{2.2}$$

where the subscripts c and ∞ denote the coolant and freestream properties. It is the ratio of the coolant mass flux to the freestream mass flux. The Stanton number, St_h, denotes the ratio of the heat transferred into a wall to the thermal capacity of the passing fluid

$$St_h = \frac{\dot{q}}{\rho_\infty u_\infty \left(h_e - h_w\right)} \tag{2.3}$$

Experiments in the 1950s confirmed that transpiration cooling is more effective than film cooling, due to its closer packed, smaller pores which lead to a more homogeneous outflow. Transpiration cooling is further at least three times more efficient than convective cooling whereby the fluid is passed through a duct on the backside of the material [25]. As transpiration cooling was envisaged as a thermal protection system for the outer skin of high-speed vehicles, the first studies on flat plates were conducted experimentally and theoretically [26]. A simplified model of the coolant film is presented. This so called thin film theory relates the reduction in heat, mass and momentum transfer coefficient to a dimensionless measure of mass transfer rate, which is directly proportional to an effective film thickness. However, this film thickness is not provided analytically and must be obtained from correlations. A similar method is presented in [27]. Experimental work by Moffat and Kays [28] provided the first accurate measurements of the Stanton number with blowing and established the following relationship:

$$\frac{St_h}{St_{h0}} = \frac{\ln\left(1+B\right)}{B} \tag{2.4}$$

where the blowing parameter B is defined as $B = \frac{F}{St_h} = \frac{\dot{m}(h_e - h_w)}{\dot{q}}$ and denotes the ratio of the transpired thermal energy flux, $\dot{m}\left(h_e - h_w\right)$ to the conducted heat flux, $\dot{q}$. A more convenient blowing parameter is introduced in Ref. [29], which

is instead normalised by the uncooled Stanton number, $B_h = \frac{F}{St_{h0}}$ and related to the Stanton number ratio as follows:

$$\frac{St_h}{St_{h0}} = \frac{B_h}{e^{B_h} - 1} \tag{2.5}$$

Swann and Pittman [30] did extensive research on the numerical modelling of ablatives, in particular the recession of the char layer. This shifted the geometrical focus from the flat plate to the stagnation point. As the injection of ablation products into the boundary layer was found to cause significant blockage of aerodynamic heating, it had to be included in the model. The blocking effectiveness for three mass transfer rate parameters, $\frac{\dot{m}h_e}{\dot{q}}$, of 0, 1 and 2.5, was obtained from the boundary layer equations for air-to-air injection [31]. A second-degree polynomial fit was then performed through these three data points (Eq. (1) in Ref. [30]), yielding the following equation:

$$\frac{St_h}{St_{h0}} = 1 - 0.724B_h + 0.13B_h^2, \qquad B_h < 2.5 \tag{2.6}$$

$$\frac{St_h}{St_{h0}} = 0, \qquad B_h > 2.5 \tag{2.7}$$

noting that $B_h = \frac{\dot{m}h_e}{\dot{q}}$ if $h_w << h_e$. If the wall enthalpy is of the same order as the freestream enthalpy, this correlation may become inaccurate. Note that Eq. (2.5) and Eq. (2.7) apply to a flat plate and stagnation point geometry, respectively. They are not interchangeable, as is evident from Fig. 2.1.

Both correlations describe air-to-air injection only. Kays [32] introduced a scaling factor for foreign gas injection on a flat plate. The blowing parameter is scaled by the heat capacity ratio of the injectant and the boundary layer edge gas as follows

$$\left(\frac{c_{p,\mathrm{inj}}}{c_{p,e}}\right)^n, \tag{2.8}$$

where $n = 1/3$ is used for laminar and $n = 0.6$ for turbulent cross-flow.

On the stagnation point, the following scaling parameter is suggested by Marvin and Pope [33]

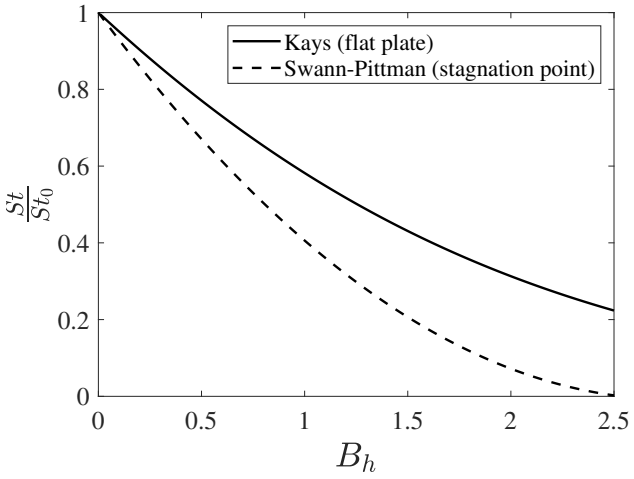

Figure 2.1: Comparison of Kays [29] and Swann-Pittman [30] correlation to predict the heat flux reduction due to mass injection.

$$\left(\frac{M_e}{M_{\text{inj}}}\right)^n, \tag{2.9}$$

where n ranges between 0.25 and 0.4 depending on the reference consulted. Meinert [34] obtained the best fit using two correction factors, for temperature and molar mass

$$\left(\frac{M_e}{M_{\text{inj}}}\right)^{0.6} \left(\frac{T_{\text{aw}}}{T_w}\right)^n, \tag{2.10}$$

where n ranges between 0.2 and 0.4. All three correlations (Eqs. (2.8), (2.9) and (2.10)) predict the same effect with different scaling parameters. It is worth noting that the heat capacity and the molar mass are directly related through kinetic theory as follows [9]:

$$c_p = \frac{\mathcal{R}}{M}\left(n'' + \frac{3}{2}\right) \tag{2.11}$$

where n'' denotes the number of atoms per molecule, and it is therefore not surprising that Eq. (2.8) and Eq. (2.9) compare well. Further, as the heat blowing parameter, B_h, is scaled by the heat capacity ratio (Eq. (2.8)), it would be intuitive that the mass blowing parameter, B_m, which is presented later in this thesis, is scaled with the molar mass.

An alternative scaling approach, using shock-layer-theory was developed by Yoshikawa [14]. The shock-layer energy equation was decoupled and linearised to yield the following expression:

$$\frac{St_h}{St_{h0}} = \frac{\dot{q}_{\text{reduced}}}{\dot{q}_0} = \frac{1}{\sqrt{K}} \frac{e^{\frac{-1}{\pi} K B_h^2}}{1 + \text{erf}\left(\sqrt{\frac{1}{\pi}K}\right) B_h} \tag{2.12}$$

$$K = \frac{\Delta}{\Delta_0} \tau^{\frac{B_h}{B*}} \tag{2.13}$$

where the blowoff parameter $B*$ is defined as

$$B* = 1.59\sqrt{\frac{M_{\text{inj}}}{M_\infty}}. \tag{2.14}$$

The blowoff parameter refers to the amount of blowing at which the injected gas is dominant over the freestream gas. It is an extremely useful indicator for secondary effects, such as aerodynamic blunting due to injection. When designing transpiration cooled stagnation points, it is therefore desirable to not exceed the blowoff parameter. For Helium into air, it is approximately 0.6, whereas for Nitrogen it increases to 1.56. The shock stand-off ratio is given as

$$\frac{\Delta}{\Delta_0} = 1 + \sqrt{\frac{\rho_s}{\rho_\infty} \frac{M_\infty}{M_{\text{inj}}}} St_{h,0} B_h, \tag{2.15}$$

while the empirical correction factor τ is defined as

$$\tau = \sqrt{\frac{M_\infty}{M_{\text{inj}}}} N_f \tag{2.16}$$

with $N_f = 5/9$ for monatomic and $N_f = 1$ for polyatomic gases.

Note that all of the above correlations describe the reduction in heat transfer on the actual porous injector. The cooling effectiveness downstream of a discrete slot injector in turbulent flow was investigated by Goldstein [35]. A transpiration cooled surface can be considered a superposition of discrete slot injectors and the resulting superimposed film effectiveness can be obtained from Sellers' method [36]. Only very few studies on the downstream film effectiveness in laminar flows have been published. Heufer and Olivier studied the downstream effectiveness

on angled plates and stagnation points [37]. A model was provided by curve-fitting their experimental data.

Based on the preceding literature review, the working principle of transpiration cooling is schematically depicted in Fig. 2.2. It combines two main cooling mechanisms. The first one is cooling through internal convection. As the pressurised coolant transpires the porous medium, heat is transferred from the hot porous structure to the relatively cool fluid. The second cooling effect stems from the formation of a thin protective layer adjacent to the surface. The injected gas mixes with the hot external flow forming a relatively cool film, which reduces the aerodynamic heating significantly on the sample [38], as well as in the downstream region [15, 39, 40]. Additionally, this barrier plays a critical role in reducing the recombination of active species on the material surface, otherwise known as catalytic effects by reducing the concentration of atoms or free radicals near the wall [41].

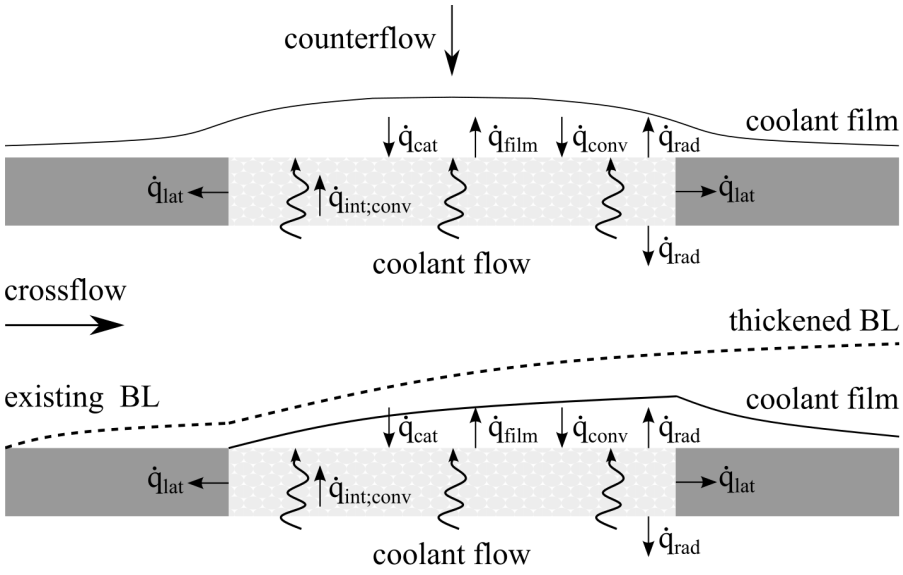

Figure 2.2: Heat flux balance of transpiration cooled medium in counterflow (top) and crossflow (bottom)

2.1.1 Darcy-Forchheimer equation

The pressure drop across an infinitesimally thin porous medium is governed by the Darcy-Forchheimer equation given as

$$-\frac{dp}{dz} = \frac{\mu}{K_D}v + \frac{\rho}{K_F}v^2 \tag{2.17}$$

where K_D and K_F are material intrinsic permeability coefficients known as the Darcy coefficient and the Forchheimer coefficient, respectively. Here, $\frac{dp}{dz}$ is the pressure gradient across the thickness of the material, and v denotes the superficial or bulk velocity of the through-flow. The first term on the right-hand-side of Equation 2.17 stands for viscous losses, whereas the second denotes the kinetic losses, which become dominant only at higher velocities. An integrated version of Equation 2.17 [42],

$$\frac{p_{\text{in}}^2 - p_{\text{out}}^2}{2p_{\text{in}}L} = \frac{\mu(T_{\text{in}})}{K_D}v_{\text{in}} + \frac{\rho(p_{\text{in}}, T_{\text{in}})}{K_F}v_{\text{in}}^2 \tag{2.18}$$

is employed here, which is valid for a constant fluid temperature over the thickness of the sample, L. The subscripts in and out stand for the inflow and outflow quantities, respectively.

2.1.2 Temperature gradient across sample

It is possible to obtain an analytical solution of the Darcy-Forchheimer equation assuming a linear temperature gradient [42]. Assuming, $b = T_{\text{out}} - T_{\text{in}}$ and $\mu = \mu_{\text{ref}}\left(\frac{T_{\text{in}}+b(z/L)}{T_{\text{ref}}}\right)^n$ the Darcy-Forchheimer equation becomes:

$$\frac{p_{\text{in}}^2 - p_{\text{out}}^2}{2p_{\text{in}}L} = \frac{\mu(T_{\text{in}})}{K_D}v_{\text{in}}\frac{1}{\frac{b}{T_{\text{in}}}(n+2)}\left[\left(1+\frac{b}{T_{\text{in}}}\right)^{n+2} - 1\right] + \frac{\rho(p_{\text{in}}, T_{\text{in}})}{K_F}v_{\text{in}}^2\left(1+\frac{b}{2T_{\text{in}}}\right) \tag{2.19}$$

More details on this method, as well as the reference dynamic viscosity quantities μ_{ref} and n, can be found in Ref. [42]. Note that the above analysis is for a one-dimensional porous medium. Ref. [43] presents a closed analytical solution for the pressure and velocity field of a two-dimensional porous medium with an arbitrary pressure distribution on its surface. However, it neglects the Forchheimer term and is thus only valid for small kinetic losses. Furthermore, it assumes an isothermal material. If the temperature distribution is unknown, the Darcy-Forchheimer differential equation in Eq. (2.17) must be solved numerically.

2.1.3 Fluids for transpiration cooling

The fluids used in transpiration cooling are mostly gaseous, but some liquids were explored as well [44, 45]. The idea is that capillary pressure would automatically distribute the liquid evenly, thus eliminating the need for a pressurised backside. This would also reduce the stresses on the wall and thereby reduce the system mass. The downside is that the mass flux cannot be throttled down below a certain threshold. Water was investigated due to its high cooling capacity per unit mass. A transpiration cooled stagnation probe was heated to 2000 K in an arc heated wind tunnel. Water injection reduced the surface temperature to 300 K and was found to be much more efficient, per unit mass, than nitrogen. However, the formation of an ice beard was observed, which partially blocked the pores. It was theorised that the water mass flux was too high and the freestream heat flux did not suffice to evaporate it completely. Instead, part of the water evaporated, extracting energy from its surroundings, thereby forming ice. Less freezing was observed when decreasing the mass flow rate, but it could not be eliminated completely. The ice beard would not only block the pores, but also disturb the flow field, leading to early transition. For the purpose of this thesis, water is not suitable as it contains oxygen. SpaceX briefly considered using liquid methane to keep the leading edge temperatures of the Starship and Super Heavy rockets below 1500 °C [46]. It is oxygen-free and has an even higher heat capacity than water.

The non-toxic noble gases, Helium, Neon, Argon, Krypton are inert and thus most suited to protect the surface from chemical attack. Note that Xenon was excluded from this list as it is extremely expensive and thus not viable. Helium and Argon were used to transpiration cool a porous flat plate in a hypersonic cross-flow [42] and a nose cone in subsonic flow [47]. Generally speaking, Helium provided the best cooling performance for a given mass flux due to its high heat capacity and low molecular weight, as reflected in Eqs. (2.8) and (2.9). However, the low molar mass also led to high outflow velocities, which were more disturbing to the boundary layer. Neon and Krypton have been neglected in the literature, possibly because they are

not as readily available. Dichlorodifluoromethane (Freon-12) was commonly used in the literature [48], but was banned due to its damaging effect on the ozone layer.

Another commonly used gas is nitrogen. While there is a risk of nitration at high temperatures, it is generally stable and inert. Nitrogen is inexpensive and readily available, thus making it a good gas for initial experiments.

2.1.4 Materials for transpiration cooling in high-enthalpy environments

The first porous media to be used in transpiration cooling were metals. Sintered porous stainless steel and bronze were investigated in Ref. [49]. Materials with smaller particle sizes performed better due to enhanced internal convective cooling. High thermal conductivities are further beneficial to remove the heat from the surface. Nickel superalloys are also commonly used for transpiration cooling applications in gas turbines. Compared to ceramics, metals have a relatively low operating temperature. Arai and Suidzu [50] investigated a ceramic coating with low thermal conductivity to insulate the Ni SA substrate from the hot flow. The porous yttria-stabilised zirconia was cooled through internal conduction of the coolant flow and increased the operating temperature of the turbine blade. Metals are well characterised and strong and thus one of the safest material classes. However, many ceramics were explored as potential alternatives due to their lighter weight and higher operating temperatures.

Procelit 170 (P170) is a composite ceramic consisting of 91% Al_2O_3 and 9% SiO_2. The ceramic can be operated at up to 2000 K and is easy to manufacture [44]. It is also much lighter than stainless steel, copper and nickel. Its downside is a low emissivity of just 0.266, thereby limiting the passive cooling through re-radiation. It is also extremely brittle and would require a protective layer to be used in a hypersonic vehicle.

Ceramic Matrix Composites, such as carbon/carbon-silicon carbide (C/C-SiC) have been investigated due to their high temperature resistance and low structural weight [51]. C/C-SiC can withstand temperatures of up to 1750 °C before oxidising,

which is significantly higher than pure C/C (450 °C). It further exhibits a high specific strength modulus [52]. However, the fibre orientation causes an anisotropic permeability, leading to significant outflow non-uniformities that can trigger early transition or separation [53].

Ultra-High-Temperature Ceramics (UHTCs) are borides, carbides and nitrites of early transition metals, such as Zr and Hf [54]. They are commonly defined as ceramic compounds which have a melting temperature exceeding 3000 °C. These compounds further exhibit high thermal conductivities, allowing them to spread concentrated heat fluxes, such as at the stagnation point. In addition, UHTCs have particle sizes smaller than 10 μm, and therefore eject the coolant in bulk as opposed to as individual jets [15]. This is desirable as it minimises the disturbance of the boundary layer and maximises the protection provided by the coolant film. Porous UHTC injectors have successfully been employed on flat plates in a hypersonic crossflow [39, 55]. Due to their superior operating temperature and outflow homogeneity, UHTCs were selected as the porous medium for the transpiration cooling experiments in this work.

2.2 Material oxidation and mitigation techniques

Ultra-High-Temperature Ceramics (UHTCs) suffer from strong oxidation effects which degrade the surface at high temperatures. The diborides (ZrB_2 and HfB_2) have the best oxidation resistance and strength at elevated temperatures [56]. ZrB_2 has the additional benefit of lower density and lower cost compared to HfB_2 [57]. It was thus deemed the ideal candidate material for this work.

Brown [58] observed that ZrB_2 starts oxidising at 1000 °C. These results were confirmed by Opeka [59] who measured the oxide layer thickness as a function of temperature after 5 hours of isothermal heating and could not detect any oxide scales below 1000 °C.

The exact oxidation behaviour of ZrB_2 depends on the surface temperature and pressure. When ZrB_2 reacts with oxygen, it produces a brittle ZrO_2 skeleton and B_2O_3 [10]. The latter is purely liquid at low temperatures (below 1000 °C) and

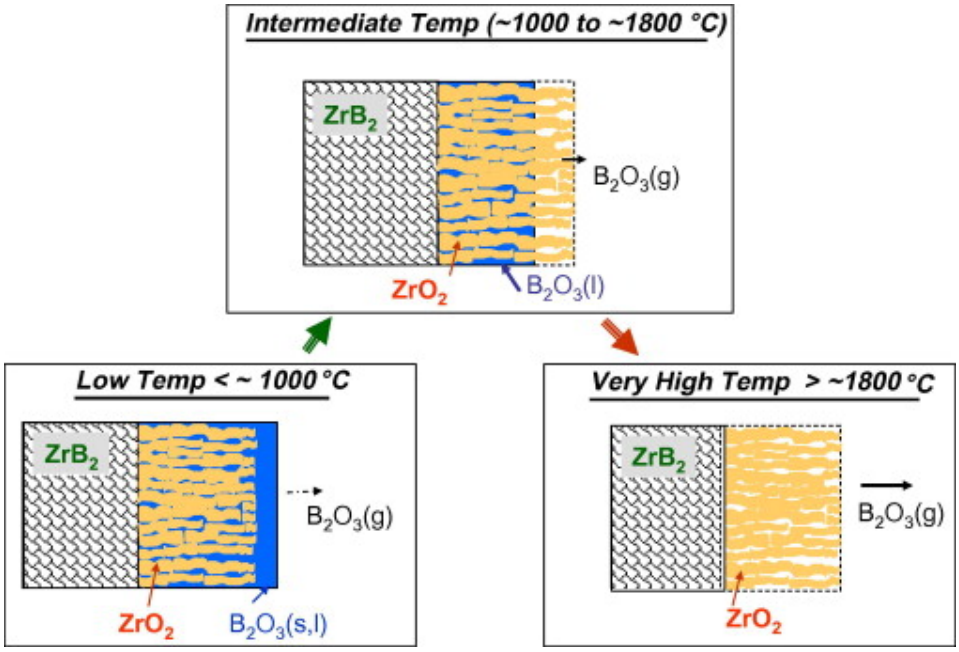

Figure 2.3: Oxidation behaviour of ZrB_2 at different temperatures [10]

purely gaseous at high temperatures (exceeding 1800 °C), with an intermediate phase in between, as depicted in Figure 2.3. More details on the kinetic model, including its governing equations are provided in Ref. [60] and section 6.3.3.

One method to improve the oxidation resistance of ZrB_2 is through the addition of SiC, which was first explored by Tripp et al. [61]. The addition of SiC slows down the oxidation kinetics through a protective SiO_2 layer [62], but oxidation rates are still significant, allowing only short-term exposure to oxygen environments [63]. The heat transport and shape stability suffer due to the low thermal conductivity and slow but steady recess of the virgin material. Lastly, the melting point is lowered by almost 1000 K. Note that the early onset of oxidation and the inefficacy of coatings is also observed in carbon-carbon composites [52].

This work explores whether oxidation can alternatively be mitigated through transpiration cooling. In this context, coatings and the formation of a viscous SiO_2 are not desirable, as they would block the pores and thus inhibit the outflow. Hence, the ZrB_2 used in this study is pure and free of any additions or coatings. As depicted in Fig. 2.2, a protective film forms as the coolant is ejected. The performance of this film in shielding the surface from freestream oxygen has not

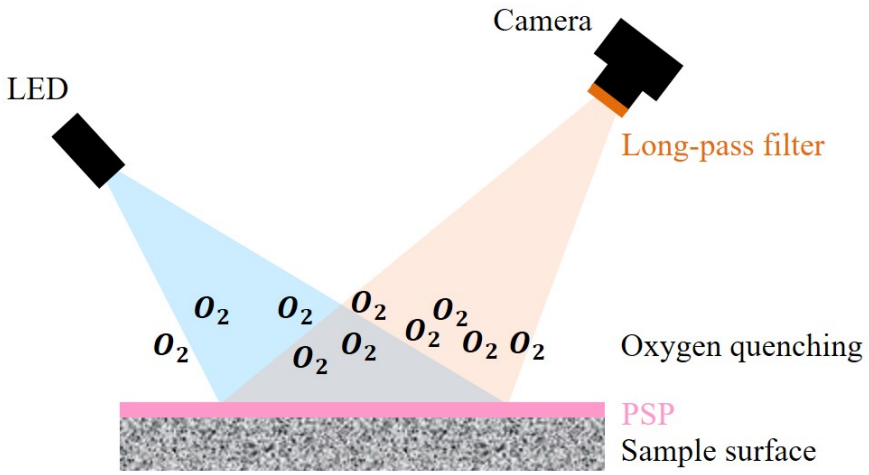

Figure 2.4: Working principle of pressure sensitive paint

been studied in the existing literature. The next section provides an overview of diagnostics that could be employed to quantify and measure oxidation, thereby enabling the experimental investigation of this problem.

2.3 Oxygen and oxidation diagnostics

This section provides an overview of measurement methods for oxidation and oxygen concentration.

2.3.1 Pressure sensitive paint

Pressure sensitive paint can be used as a non-intrusive method to investigate the fluid properties or flow patterns on a surface [64]. This measurement technique consists of a paint-like coating, which contains little luminescent molecules, called luminophores, suspended in an oxygen-permeable binder. When stimulated under a specific wavelength, the luminophores respond by fluorescing at a wavelength larger than that of the excitation. Figure 2.4 illustrates the underlying working principle of PSP.

The coating is airbrushed on the sample of interest and then cured in a high temperature furnace. An LED lamp emits light at a specific frequency, which excites the pressure sensitive luminophore inside the paint into a higher energy state. If no oxygen is present in the surrounding environment, the oxygen sensitive probe will

return to a lower energy state, emitting a photon that is subsequently detected by the CCD camera. A long-pass filter ensures that only the emissions stemming from the PSP are detected. However, this fluorescence intensity is decreased by the presence of oxygen, a process named oxygen-quenching. As opposed to the oxygen-free case, the relaxation from a higher energy state does not take place through radiation, but in a non-radiative way, hence dimming the luminescence of the PSP. Since the oxygen concentration is proportional to the oxygen partial pressure and hence to the local static pressure, the intensity of the luminescence can be related to the pressure.

In theory this relationship is described by the Stern-Volmer relation [65]:

$$\frac{I_{\text{ref}}}{I} = A(T) + B(T)\frac{p}{p_{\text{ref}}} \tag{2.20}$$

where A and B are the Stern-Volmer coefficients. However, in practice PSP behaves highly non-linearly and a more general power series form is commonly used [66]:

$$\frac{I_{\text{ref}}}{I} = \sum_{n=0}^{N} A_n(T) \left(\frac{p}{p_{\text{ref}}}\right)^n . \tag{2.21}$$

For the pressure sensitive paint and substrate used in this work, the best empirical fit to for the calibration curve was provided by an equation of the form

$$\frac{I_{\text{ref}}}{I} = \left(a\frac{p}{p_{\text{ref}}} + 1\right)^b \tag{2.22}$$

where a and b are the fitting parameters, while I denotes signal intensity and the subscript ref stands for a reference intensity at a known pressure.

There are many types of pressure sensitive paint, most of them must be suspended in an oxygen permeable binder. One type of PSP, called anodised-aluminium PSP, allows the direct application of molecules onto the surface. As the purpose of this project is to measure the oxygen concentration on a transpiration cooled material, it is desirable to select a PSP that is least likely to block the pores. A PSP that fulfils this requirement will be developed in Chapter 3.

2.3.2 Optical emission spectroscopy

At high enthalpies, PSP can not be employed and alternative optical diagnostics are required instead. The production of oxidation products can be recorded by tracking the emission signatures, i.e. the intensity of the characteristic spectral lines of the oxidation products [67]. Recalling Figure 2.3, the oxidation end product is ZrO_2 and B_2O_3. However, an intermediate step is the production of BO_2, BO and B, all of which continue to form ZrB_2 and B_2O_3 after a short time period. The advantage in tracking the interim species is simply that their emission signatures are easier to detect. Figure 2.5 compares the emission signatures of the characteristic oxidation species for two samples: one that has been oxidised before and a virgin one.

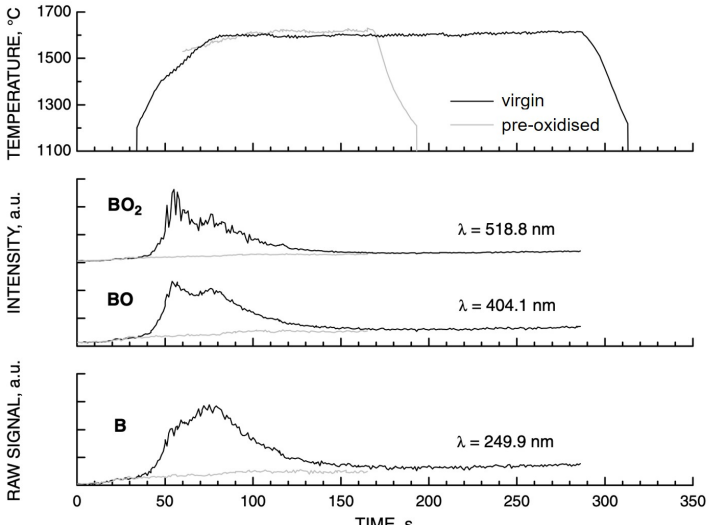

Figure 2.5: Transient profiles of the surface temperature and the emission signatures of BO_2, BO and B at 518.8, 404.1 and 249.9 nm, respectively [67]

It clearly shows how the intensity of the oxides peaks for a short period of time on the virgin material (black line), while there is no noticeable increase in the pre-oxidised material (grey). Furthermore, the intensity decreases on the previously virgin material, once it is fully oxidised and all the interim oxidation products have reacted.

The spectral lines can be measured with Echelle spectroscopy. An Echelle spectrometer separates the light by wavelength and records the signal using a camera. Light enters through a viewing slit and is collimated. The next station

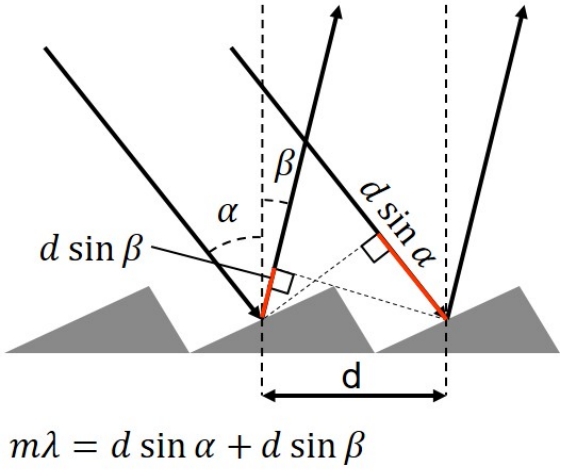

Figure 2.6: Schematic of Echelle grating

is the Echelle grating, an array of parallel grooves with a highly reflective surface coating. If the path difference $d \sin \alpha + d \sin \beta$ equals to a multiple of the wavelength, the light is diffracted to the central zeroth order or higher orders at specific angles, as schematically illustrated in Figure 2.6. Sometimes, it happens that longer wavelengths of a higher order overlap with the next order of shorter wavelengths. To correct for this undesired side-effect, a second, orthogonally placed cross disperser is inserted, which separates the orders before the light is projected on the camera sensor. Note that the higher the groove frequency (grooves per mm), the higher the optical resolution. However, this happens at the cost of wavelength coverage [68].

2.3.3 Post-test sample diagnostics

Another method of assessing oxidation is SEM imaging [69]. This qualitative method is useful to compare the surface pre- and post-experiment. The sample is soaked with epoxy to keep it shape stable while it is sectioned. The images of the cross-section can be analysed qualitatively, for instance by measuring the oxide layer and recession thickness, as well as qualitatively, by assessing changes in the microstructure of the substrate. These insights can be fed back into the oxidation model.

Oxidation products can also be detected using mass spectroscopy. In this method the sample is exposed to a beam of electrons, which occasionally collide with a molecule, causing it to break up into a positively charged ion. These ions are

accelerated by an electric field at first, then separated by a magnetic field according to their mass-to-charge ratio and finally directed to the sensor through another electric field. As the charge of most ions is unity, the molar mass of the ions is known and they therefore can be identified [70].

3

Pressure sensitive paint diagnostic to measure species concentration on transpiration cooled walls

3.1 Foreword

This chapter deals with the development of a new diagnostic to measure the molecular oxygen concentration on transpiration cooled surfaces. The aim is to obtain a direct, non-intrusive, spatially resolved surface measurement of freestream oxygen. This diagnostic is fundamental to conduct the experiments in Chapter 5. The following work has been published in *Experiments in Fluids* [16]. It is presented in this chapter with small layout changes, but unaltered content. The author contributions are summarised below:

- Marc Ewenz Rocher: Conceptualisation, Methodology, Investigation, Data analysis, Writing
- Tobias Hermann, Matthew McGilvray, Chris Hambidge: Supervision
- Hassan Saad Ifti: Development of flat plate model
- Joao Vieira: Development of calibration chamber

- Mark Kenneth Quinn: Advice on suitable luminophores
- Madeleine Grossman and Luc Vandeperre: Manufacturing of porous alumina

In addition to the above published work, the end of this chapter (section 3.10) probes whether there is a correlation between the heat and mass transfer reduction due to blowing on a turbulent flat plate. Further, a step-by-step manual detailing the application of pressure-sensitive paint on porous surfaces is included in Appendix B.

3.2 Introduction

Transpiration cooling is an active thermal protection system with the potential to be useful for aerospace applications in high speed vehicles, rocket nozzles and future turbine components. A coolant is fed through a porous wall and forms a protective film upon exiting. This coolant film acts as a barrier against the hot freestream, thereby reducing the aerothermal heating [15]. In high-enthalpy environments, the film mitigates catalytic heating and surface oxidation by inhibiting the diffusion of activated species, such as atomic oxygen, through to the surface [19].

When investigating the mass transfer on transpiration cooled surfaces, there are two measurements of interest: the surface pressure, and the coolant concentration. The surface pressure distribution directly influences the pressure differential across the porous medium and therefore the coolant mass flux distribution on its surface. The coolant concentration provides a deeper insight into the coolant path after exiting the porous wall and how it mixes with the hot external gas.

Despite their significance, there are currently no methods to measure the surface pressure, nor the coolant distribution, on transpiration cooled surfaces. Thus, most studies have focused on the downstream effects of injection [39, 40] or film cooling, whereby the PSP was applied on the solid surface in between the discrete holes [71, 72]. This work investigates a novel pressure sensitive paint diagnostic to measure the coolant distribution on a transpiration cooled surface. This method can be used to measure the mass transport from the freestream to the surface and thus to assess the effectiveness of protective coolant films in mitigating oxidation and catalytic heating.

Pressure sensitive paint (PSP) is sprayed onto the sample without affecting its permeability. The porous alumina substrate bonds the PSP by intermolecular and electrostatic forces. This work builds upon a previous successful application of PSP to anodized aluminium with no cooling feed [64, 73] and preliminary tests with transpiration cooled anodised aluminium, which provided qualitative data [74]. Tests were conducted in the Oxford High Density Tunnel (HDT) [75], using a flat plate model with a porous alumina insert. The results include pressure maps of the sample with air, nitrogen, and no injection, as well as the oxygen partial pressure ratio at a blowing ratio of $F = 0.016 - 0.078\%$. Laminar and turbulent freestream conditions were explored and compared against each other.

3.3 Pressure sensitive paint on porous alumina

Pressure sensitive paint is an optical method to measure the partial pressure of oxygen. It consists of light-emitting molecules dispersed in an oxygen permeable binder. These molecules are called luminophores and are excited into a higher energy state when illuminated by a light source at a certain wavelength. As they relax into a lower energy state, they will emit light in a different wavelength. In the presence of oxygen, part of this relaxation happens in a non-radiative way, in a process called quenching. More details on the working principle of PSP can be found in [64]. This change in brightness can be recorded by a camera, with corresponding optical filters. If the gas composition is known, for instance when injecting air into an air freestream, then the PSP signal scales directly with the local static pressure on the surface. Alternatively, if the pressure field is known, then the O_2 partial pressure measured by the PSP can be used to obtain the local concentration of a foreign gas injected into an air freestream.

The specific type of PSP used in this experiment, is known as anodised aluminium PSP. Its distinguishing feature is that it does not require a binder. Instead the luminophores can be sprayed directly onto a surface of porous alumina. This surface is typically created by anodising dense aluminium to create a thin oxidation layer, which has the right pore structure to bond PSP. In the present

case, the substrate already consisted of porous alumina, thus the anodisation procedure was not necessary. Instead, 0.1 mmol of Ruthenium-tris(4,7-diphenyl-1,10-phenanthroline) dichloride, also known as $\left[\mathrm{Ru}\left(\mathrm{dpp_3}\right)\right]^{2+}$, were diluted in 200 ml of dichloromethane and spray painted directly onto the surface, after it had been degreased in an ethanol bath. The $\left[\mathrm{Ru}\left(\mathrm{dpp_3}\right)\right]^{2+}$ luminophore was chosen for its stable luminescence and fast response time [73]. It furthermore exhibited good signal quality in previous studies [64, 76].

The porous alumina substrate was custom made by Imperial College London. Alumina powder with a particle diameter of 6.45 μm was sintered at 1700 °C for 3 hours, yielding a 39% porous substrate. Its front and back surfaces were polished to open up the pores. The resulting sample combines the ability to bond PSP with the pore size and therefore outflow homogeneity of candidate materials for transpiration cooling, such as ZrB_2 [15]. This includes the pore size, particle size, and open porosity. As depicted in Fig. 3.1, the pores of this sample feature a diameter of approximately 2 μm. More importantly, Fig. 3.2 shows that the particles do not agglomerate or otherwise block the pores, leaving the permeability unchanged. This was confirmed by permeability measurements before and after spraying the PSP on the sample.

3.4 Experimental model

A flat plate geometry was chosen to validate the PSP diagnostic method, as it provides a well characterised flow field. It is a modified version of the flat plate used in [39]. Figure 3.3 presents the main features of the 580 mm long and 125 mm wide plate. 3D printed trips can be inserted into a trip pocket 25.7 mm downstream of the leading edge to aid transition. A flush insert was used for the laminar experiments. The porous sample is located 160 mm downstream of the sharp leading edge. Thin film arrays were mounted upstream and downstream of the sample to determine whether the flow is laminar or turbulent. Two pressure gauges, one upstream, one downstream of the sample, provided static pressure measurements.

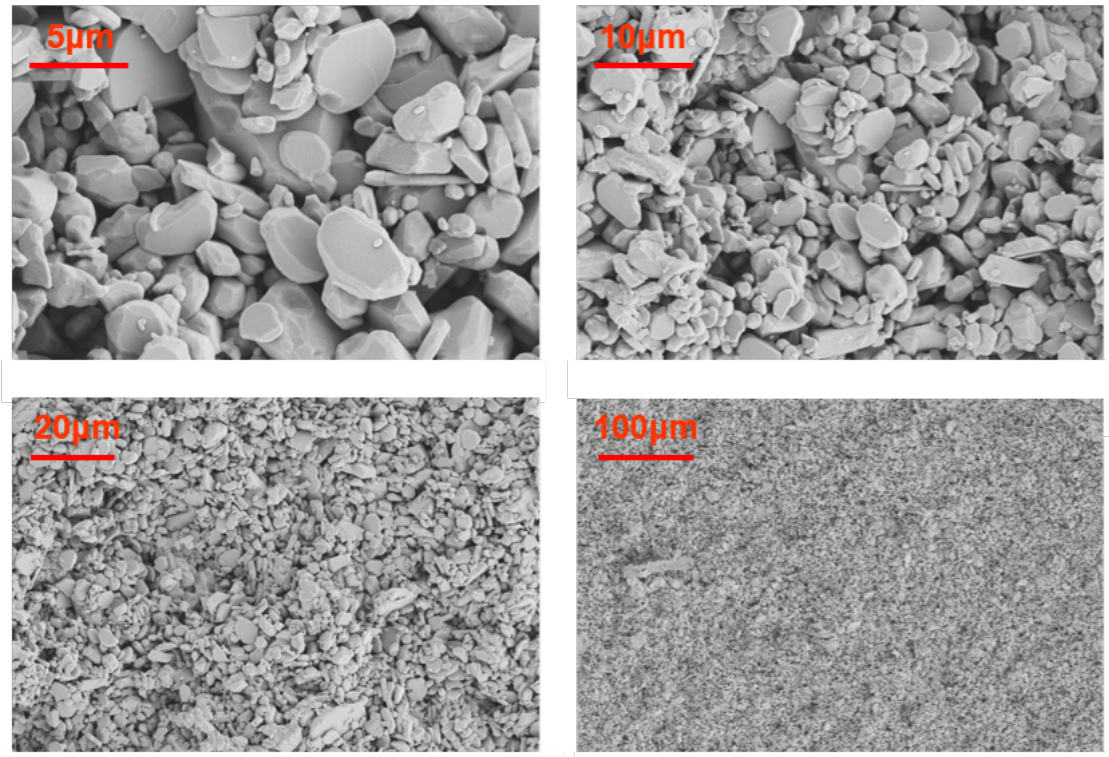

Figure 3.1: Microscopic images of porous alumina surface at different magnification factors.

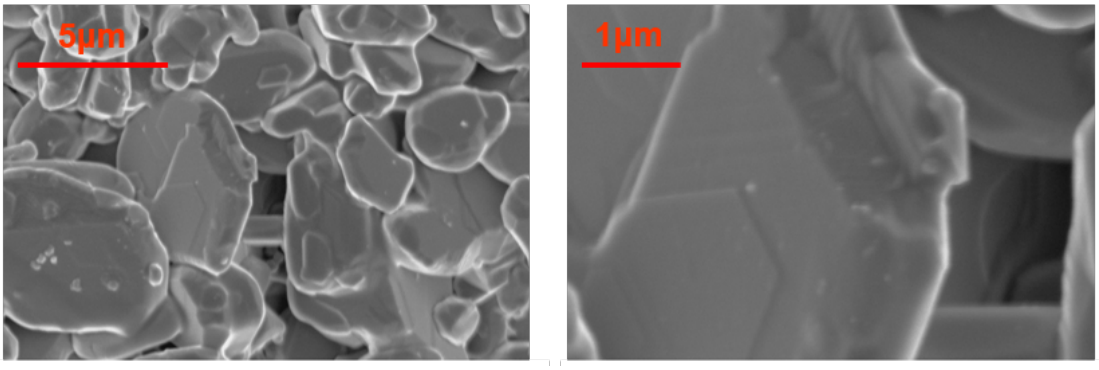

Figure 3.2: Microscopic images of porous alumina surface with pressure sensitive paint. Neither PSP particles nor agglomerates can be seen.

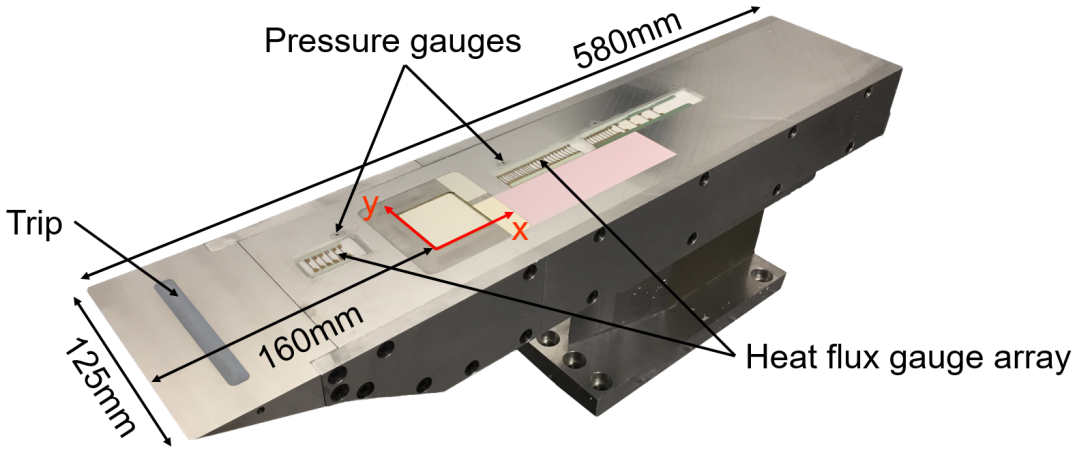

Figure 3.3: Photograph of the flat plate model, showing x and y axes in red on the sample.

The sample geometry consisted of a 2 mm thick 39.5 × 39.5 mm^2 square on top of a 3 mm thick 60 mm diameter disk, as shown in Fig. 3.4 (a). It was silicon sealed into a cover plate with QSil-216, as illustrated in Fig. 3.4. A layer of quick drying epoxy was applied around the edges beforehand to prevent the silicon from seeping into the pores. Underneath the cover plate is a plenum with a volume of 62 × 62 × 35 mm^3. The coolant properties in the plenum were measured by an Omega 5TC-TT-KI-40-1M fast response thermocouple and a Kulite HEL 375-35BarA pressure transducer. The data acquisition system consisted of a a National Instruments PXIe-8135 controller with several PXIe-6368 and PXIe-6363 cards operating at a 200 kHz sample rate. The thermocouple had an uncertainty of ± 2.2 K or ± .75% and the Kulite of ± 3.5 kPa. Two Kulite XCS-093-5A pressure transducers were mounted 55 mm upstream and 65 mm downstream of the sample. They were surface mounted and positioned on the centreline. The transducers have an accuracy of ±6.3% of the reading or ±172 Pa, whichever is smaller. A 50 Hz notch filter coupled with a 300 data points wide moving average filter was employed to remove mains noise.

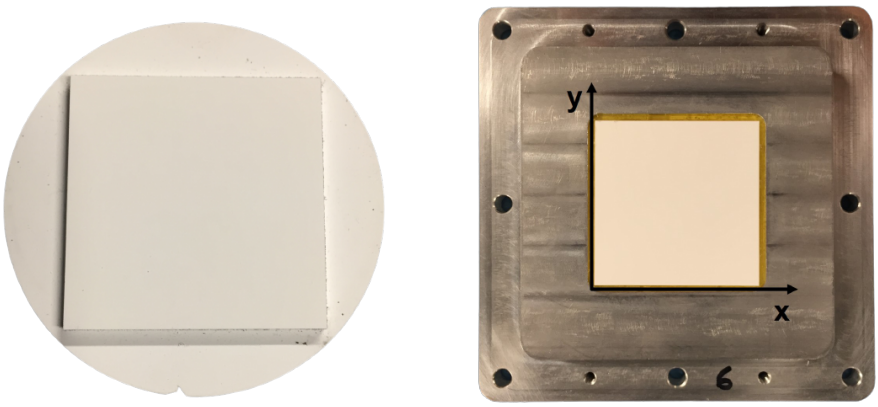

(a) Without PSP (b) With PSP in cover plate

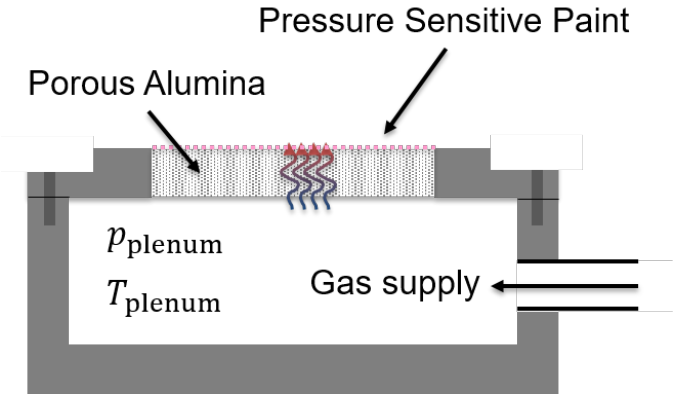

(c) Schematic of plenum

Figure 3.4: Illustrations of the porous alumina sample.

Further instrumentation includes platinum thin film gauges (TFGs) on Macor bodies, which were hand painted in-house. They were positioned upstream and downstream of the sample, and allowed for the measurement of the local heat flux. The electrical resistance of each gauge is temperature dependent and thus the change in temperature can be measured through the change in voltage if a constant current is applied. A low current of 10 mA was chosen to prevent Joule heating and the signal was recorded by an amplifier. The gain profile of the amplifier increases with frequency, which mitigates digitisation errors and reduces the signal to noise ratio for high frequency heat flux fluctuations [77]. The recorded signals are then post-processed to remove this frequency dependent gain, using a method called de-boosting [78]. The gauges were previously calibrated in a water bath at 20 - 50 °C in steps of 5 °C, which allows the conversion from voltage to temperature by

interpolation. An impulse response convolution method [78] is subsequently applied to convert the temperature data into heat flux, using the thermal product of Macor: 1705 $\mathrm{Jm^{-2}K^{-1}s^{-0.5}}$. This method assumes 1D heat conduction into a semi-infinite block of material. This condition is fulfilled in the short-duration experiments conducted in the Oxford High Density Tunnel, as the thermal penetration depth is 2.65 mm into the 7 mm thick material. The resulting heat transfer data is smoothed by a moving average filter with a length of 1 ms.

ISSI fast response PSP was applied next to the thin film gauges as part of another study that looked at the film effectiveness in the downstream region of a transpiration cooled surface. It has a characteristic pink hue that is shown in Fig. 3.3.

A schematic of the optical setup is shown in Fig. 3.5. A Luminus PT-120-B-L11-EPG LED with a 460 nm dominant wavelength excited the PSP. It was operated at 20 A electric current and featured an in-built thermistor that measured its junction temperature. The absorption and emission spectrum of the $\left[\mathrm{Ru}\left(\mathrm{dpp}\right)_3\right]^{2+}$ luminophores used in this PSP is 400-550 nm and 600 - 750 nm, respectively [64]. The PSP luminescence is reflected by a mirror before it exits the test section and is captured by a Photron Fastcam Mini AX 200 900K high speed camera, which performs an auto shading calibration before every shot. A 550 nm long-pass filter manufactured by VHBW removes any reflected radiation from the LED, ensuring that only the light emitted by the PSP is captured. The transmission spectrum of the optical filter was characterised using an integrating sphere and a spectrometer. Figure 3.6 depicts how the filter effectively blocks the LED light, but transmits the PSP signal. The images are recorded at 1000 Hz, with a 1 ms shutter speed, 12 bit depth and a 1024 x 1024 pixel resolution. Using a Tamron SP AF 70-200mm F/2.8 Di LD (IF) macro telephoto zoom lens and a Sigma Apo Tele Converter 2 X Dg for Nikon AF, it was possible to get 758x758 pixels on the cover plate and 398x398 pixels on the sample.

The outflow of the sample was characterised pre- and post-experiment. A hot wire was traversed 1.5 mm above the surface with a coolant pressure drop of 4 bar with no cross-flow using the experimental setup developed in [15]. The hot wire was

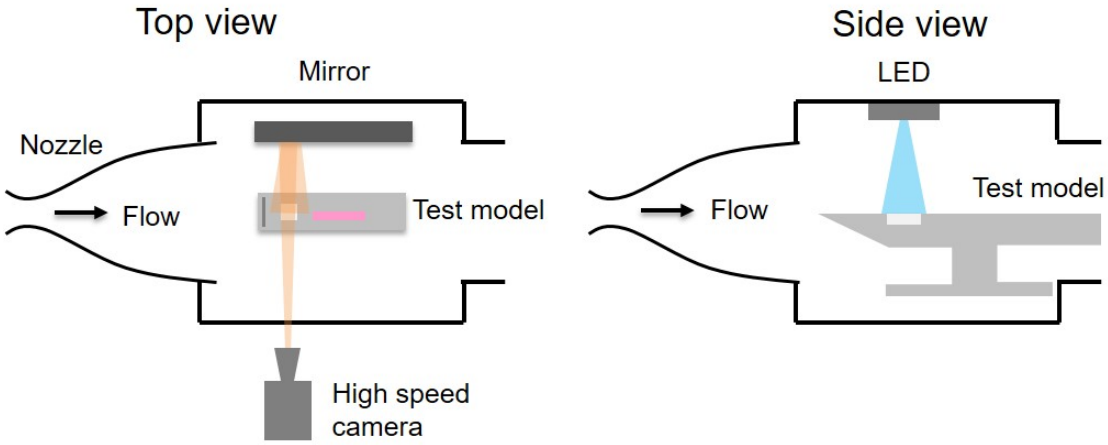

Figure 3.5: Schematic of the optical setup.

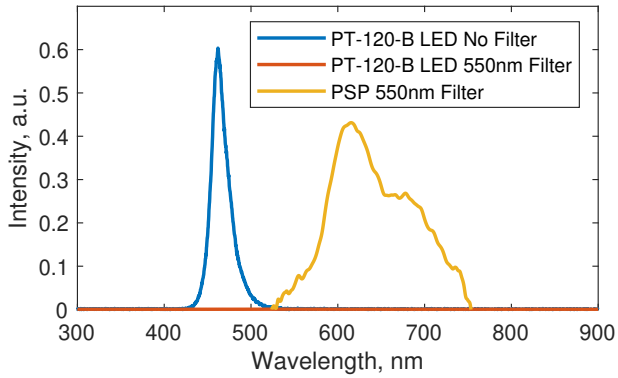

Figure 3.6: Comparison of LED and PSP spectra with and without a 550 nm long-pass filter. Note that the LED intensity with 550nm filter is zero.

calibrated for 0.02-0.5 m/s using the StreamLine Pro Automatic Calibrator. The outflow velocity for 4 bar differential pressure is shown in Fig. 3.7. The velocity field is extremely uniform at 0.045 - 0.055 m/s, indicating that the pores are small and evenly distributed. The mass flow rate was measured pre-experiment with an Alicat M-250SLPM-D/5M mass flow meter with an accuracy of ±0.25 slpm. Data points were collected in steps of 0.5 bar for pressure drops between 0 - 7 bar and normalised by the cross-sectional area to provide the mass flux. The fluid temperature is assumed to be constant across the sample. The resulting graph is interpolated to obtain the average mass flux for a given plenum pressure during testing. The Darcy and Forchheimer coefficients are $K_D = 3.9 \times 10^{-15}\text{m}^2$ and $K_F = 2.8 \times 10^{-10}\text{m}$, respectively.

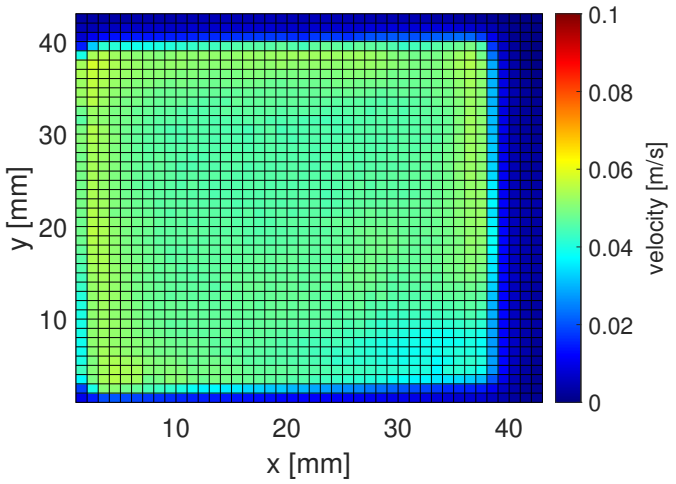

Figure 3.7: Outflow characterisation of porous alumina.

Due to the small size and uniform distribution of the pores, no jets or eddies were present and therefore the hot wire measurement is very close to the bulk flow velocity predicted by the mass flow measurement.

3.5 Experimental facility and flow conditions

The experiments in this paper were conducted in the Oxford High Density Tunnel, operated in Ludwieg Tunnel mode. A more extensive description of the facility can be found in [75]. Six conditions were investigated at a range of unit Reynolds numbers, from laminar to turbulent. The boundary layer edge conditions can be found in Table 3.1.

The blowing ratio, F, is the ratio of coolant mass flux to mass flux at the boundary layer edge:

$$F = \frac{\rho_c v_c}{\rho_e v_e}, \tag{3.1}$$

with ρ and v being the density and velocity, respectively, while the subscripts c and e denote the coolant and the boundary layer edge. The coolant mass flux is the ratio of coolant mass flow rate, $\dot{m}$, and through-flow area, $A = 39.5 \times 39.5$ mm^2:

$$\rho_c v_c = \frac{\dot{m}}{A}. \tag{3.2}$$

Table 3.1: Overview of test conditions.

Description	Mach	T_0, K	p_e, kPa	$Re_u, 10^6$/m
L1 (laminar)	6.7	435	0.95	25.8
L2 (laminar)	6.7	437	1.02	27
L3 (laminar)	6.7	440	1.08	28
T1 (turbulent)	5.7	342	2.14	46
T2 (turbulent)	5.7	350	2.30	48
T3 (turbulent)	5.7	360	2.53	50

Table 3.2: Blowing parameters and surface heating.

Description	F, %	ΔT_{PSP}, K
L1 (laminar)	0, 0.053, 0.078	0.93, 0.19, 0.11
L2 (laminar)	0, 0.051, 0.074	0.945, 0.203, 0.12
L3 (laminar)	0, 0.049, 0.070	0.96, 0.22, 0.127
T1 (turbulent)	0, 0.018, 0.037, 0.060	2.77, 2.20, 1.76, 1.36
T2 (turbulent)	0, 0.017, 0.035, 0.057	3.12, 2.49, 1.99, 1.49
T3 (turbulent)	0, 0.016, 0.032, 0.053	3.23, 2.58, 2.06, 1.59

The relationship between mass flow rate and plenum pressure is characterised pre- and post-experiment as described in section 3.4. The boundary layer edge mass flux is obtained as follows:

$$\rho_e v_e = \frac{p_e}{RT_e} M_e \sqrt{\gamma R T_e}, \tag{3.3}$$

where p_e is the static pressure recorded by the surface mounted Kulite in the no injection case and γ, R and M denote the heat capacity ratio, the specific gas constant for air and the Mach number.

A summary of the outflow conditions is provided in Table 3.2.

3.6 PSP signal post-processing

The signal emitted by the PSP is reflected by a mirror inside the test section before being captured by the camera, as illustrated in Fig. 3.5. As the running of the facility induces a vibration on the mirror, the raw image must be stabilised. This is achieved with a single-point stabilisation that corrects for horizontal and vertical

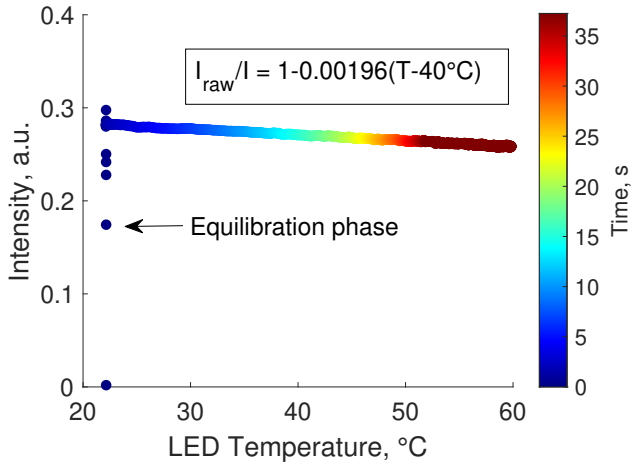

Figure 3.8: Intensity vs junction temperature for the PT-120B LED at 20 A electric current.

translation with respect to a reference frame. A two-point stabilisation can correct for rotation and stretching too, but was found to induce too much noise. The stabilised, raw intensity image is then trimmed to the region of interest: the surface of the transpiration cooled material. Frames are averaged over the 40 ms long steady test period and normalised by the pre-flow values on a pixel-by-pixel basis. Note that the intensity value is also dependent on the LED temperature, as illustrated in Figure 3.8. This effect was corrected using the following empirical relationship:

$$I = \frac{I_{\text{raw}}}{1 - 0.00196(T_{LED} - 40°C)}. \tag{3.4}$$

where T_{LED} is the LED temperature as recorded by an in-built thermistor and raw denotes the raw intensity prior to the LED temperature adjustment. The LED needs about 0.5 s to stabilise thus causing the scattered data points.
The normalised, LED adjusted intensity frames are then converted to pressure using a calibration curve.

3.6.1 Calibration

The raw intensity image can be converted to pressure using a single, global calibration curve that is applied to every pixel, or a pixel by pixel calibration whereby each

pixel has its own calibration curve. If the image is stable enough, meaning that the position of an individual pixel does not move with time, the pixel by pixel calibration is much more accurate as it accounts for variations in local PSP sensitivity. Due to satisfactory image stabilisation, the pixel-by-pixel calibration was chosen to post-process all normalised intensity images in this work.

The calibration is performed before the experiment, at room temperature without any cross-flow. The intensity of every pixel is recorded while increasing the static pressure in the test section, yielding its individual calibration curve:

$$\frac{I_{\mathrm{ref}}}{I} = \left(a \frac{p}{p_{\mathrm{ref}}} + 1 \right)^{b} \tag{3.5}$$

where a and b are the fitting parameters, while I denotes signal intensity and the subscript ref stands for a reference intensity at a known pressure. The surface temperature remains constant at all times and all changes in PSP intensity are due to pressure only. Therefore, any PSP intensity signal processed with this calibration curve, must be free of temperature effects, too. However, the PSP luminophores are heated during the wind tunnel operation. Their intensity will therefore change due to pressure and temperature. This thermal effect can be accounted for if the temperature of the PSP, T_{PSP}, is known during the test time.

3.6.2 PSP temperature

No blowing

When there is no mass injection ($F = 0$), then the pressure across the sample is relatively constant and can be determined using pressure gauges. While the Kulites are not directly on the sample, one is mounted 55 mm upstream and the other 65 mm downstream of it, as shown in Fig. 3.3. Despite their different locations they record the same pressure within 1% discrepancy. This pressure profile can be converted into an intensity profile using the calibration curve:

$$\frac{I(p_{\mathrm{ref}}, T_{\mathrm{ref}})}{I(p_{\mathrm{gauge}}, T_{\mathrm{ref}})} = \left(a \frac{p_{\mathrm{gauge}}}{p_{\mathrm{ref}}} + 1 \right)^{b}. \tag{3.6}$$

The difference between $I(p_{\text{gauge}}, T_{\text{ref}})$ and the actual intensity measured during the experiment, $I(p_{\text{gauge}}, T_{\text{PSP},F=0})$, is the PSP temperature, $T_{\text{PSP},F=0}$, which deviates from T_{ref}. Therefore

$$\frac{I(p_{\text{ref}}, T_{\text{ref}})}{I(p_{\text{gauge}}, T_{\text{PSP},F=0})} = \frac{I(p_{\text{ref}}, T_{\text{ref}})}{I(p_{\text{gauge}}, T_{\text{ref}})} \frac{I(p_{\text{gauge}}, T_{\text{ref}})}{I(p_{\text{gauge}}, T_{\text{PSP},F=0})}. \tag{3.7}$$

where the second term on the right hand side denotes the temperature effect on the PSP. The temperature sensitivity of the present PSP was experimentally obtained in a calibration chamber and found to be 1.17%/K for pressures between 1-3 kPa. This yields

$$\frac{I(p_{\text{gauge}}, T_{\text{ref}})}{I(p_{\text{gauge}}, T_{\text{PSP},F=0})} = 1 + 0.0117\,(T_{\text{PSP},F=0} - T_{\text{ref}}) \tag{3.8}$$

which can be inserted into Eq. (3.7) to solve for $T_{\text{PSP},F=0}$.

Blowing

For the blowing cases, the temperature rise $\Delta T_{\text{PSP}} = T_{\text{PSP}} - T_{\text{ref}}$ was predicted using the Porous Impulse Response Analysis for Transpiration cooling Evaluation (PIRATE) code [79]. This tool calculated the reduction in heat flux with blowing, $\frac{\dot{q}}{\dot{q}_0}$, shown in Fig. 3.9, which was used to obtain the PSP temperature for a given blowing ratio as follows:

$$\Delta T_{\text{PSP}} = \Delta T_{\text{PSP},F=0} \frac{\dot{q}}{\dot{q}_0} \tag{3.9}$$

where $\dot{q}$ and $\dot{q}_0$ are the heat fluxes with and without blowing, respectively. Combining Eqs. (3.6)-(3.8) one obtains for a given temperature rise ΔT_{PSP}:

$$\frac{I(p_{\text{ref}}, T_{\text{ref}})}{I(p, T_{\text{PSP}})} = \left(a \frac{p}{p_{\text{ref}}} + 1\right)^b \left(1 + 0.0117 \Delta T_{\text{PSP}}\right) \tag{3.10}$$

and for the pressure p:

$$p = \left(\left(\frac{I(p_{\text{ref}}, T_{\text{ref}})}{I(p, T_{\text{PSP}})} \frac{1}{1 + 0.0117 \Delta T_{\text{PSP}}} \right)^{\frac{1}{b}} - 1 \right) \frac{p_{\text{ref}}}{a}. \tag{3.11}$$

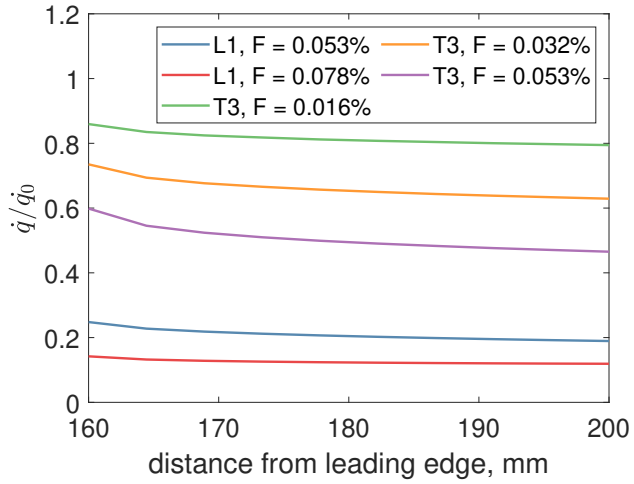

Figure 3.9: Heat flux reduction for conditions L1 and T3 at various blowing ratios.

3.7 Results and discussion

3.7.1 Porous interface

Figure 3.10 shows the oxygen partial pressure recovered from the PSP signal for condition T3. The signal was spatially averaged over the whole sample. There are 3 blowing rates for air and nitrogen, respectively. The injection always starts before the flow arrival to allow the coolant gas to equilibrate in the plenum. While there is no noticeable signal change for the nitrogen injection during this time, the oxygen pressure rises drastically for air, reaching the steady-state value shown in Fig. 3.10 (a). The fact that there is no change in PSP signal for the nitrogen injection, which has very similar thermal properties to air, rules out temperature effects. Thus, the increase has to be due to oxygen pressure. However, the static pressure in the test section does not change until the flow arrival. The increase in oxygen pressure must be local to the porous interface. As the flow exits the pores, it expands to adjust to the static pressure of the test section. This apparent pressure discontinuity on a macroscopic scale is actually a gradual expansion on a microscopic level, which was also investigated numerically in [80]. The PSP molecules that are located in the pores will be surrounded by air with slightly higher pressure than on the surface. Thus, the air, which enters the backside of the sample will not have expanded to the near vacuum static pressure in the test section yet. This pressure differential

is directly related to the depth of the material and can be approximated by the isothermal Darcy-Forchheimer equation. The results are shown in Fig. 3.11. The effective pore depth calculated with this method is of the same order of magnitude as the 2 μm pore diameter observed in Fig. 3.1. An implication of the porous interface effect is that some PSP particles, deep inside the pores, could become unreachable for the freestream air when blowing is switched on. The bulk velocity of the injected gas would quickly exceed the diffusion velocity of the freestream air. The magnitude of this effect depends on the distribution of PSP molecules and the microstructure of the porous surface and is difficult to quantify. Qualitatively speaking, the surface will be better protected from freestream oxygen than predicted by theoretical models which assume a flat, homogenous surface.

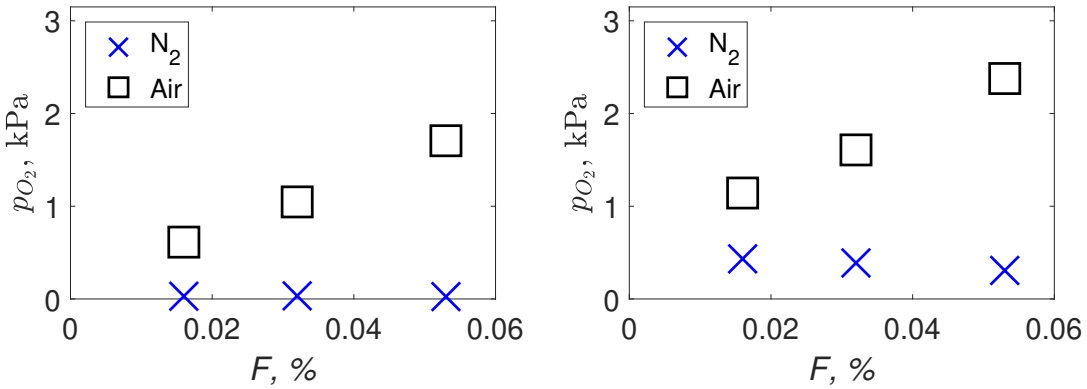

(a) No freestream (b) T3 condition

Figure 3.10: Oxygen pressure measured by PSP with and without hypersonic cross-flow.

3.7.2 Oxygen pressure maps

Figure 3.12 shows oxygen pressure maps for the turbulent cases at a range of blowing ratios. The first row of Fig. 3.12 depicts the no-blowing data ($F = 0$). The signal is spatially uniform and one can clearly see the contours of the rectangular sample. Note that the bottom right corner was contaminated with epoxy when applying the ISSI porous underlayer in the neighbouring cover plate, causing a small artefact. As expected, the partial O_2 pressure increases with the unit Reynolds number due to increasing edge pressure. This trend continues for the blowing cases.

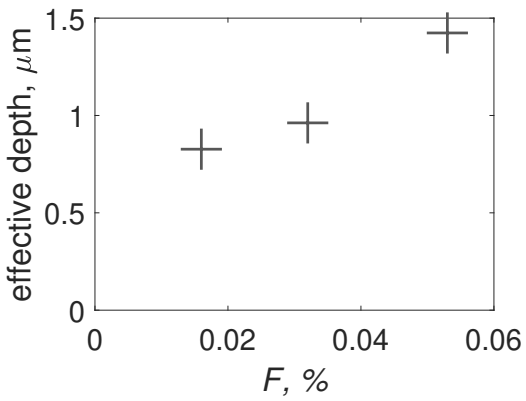

Figure 3.11: Effective depth of PSP molecules.

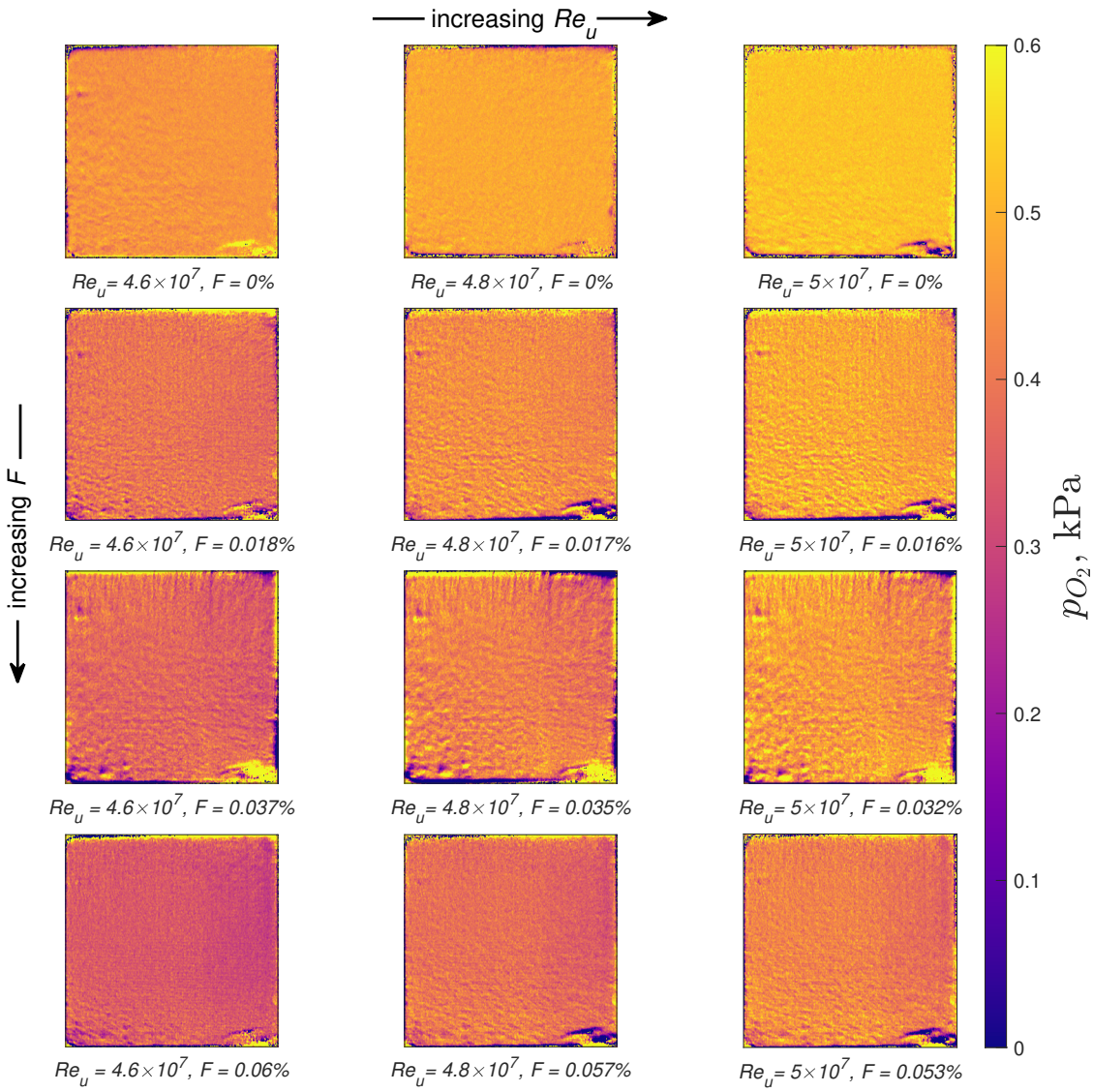

Figure 3.12: Oxygen pressure maps for N_2 injection at various Re_u and F for turbulent conditions. The freestream is flowing left to right.

The oxygen pressure decreases with increasing nitrogen injection and decreasing free-stream mass flux. Furthermore, the reduction seems to be slightly larger on the downstream side, which makes sense as the film thickness grows and mitigates oxygen convection and diffusion. It is further noted that the results are much more dependent on the blowing ratio, than the unit Reynolds number.

An uncertainty analysis for the presented data can be found in the appendix.

3.7.3 Oxygen pressure ratio

Due to different freestream conditions, in particular the static pressure, a direct comparison between laminar and turbulent cases is difficult. It is desirable to obtain a non-dimensional parameter, which quantifies how much freestream air and therefore oxygen is displaced by mass injection, as compared to the no injection case. For this purpose the oxygen pressure with injection is normalized by the oxygen pressure without injection, $\frac{p_{O_2;\mathrm{inj}}}{p_{O_2;\mathrm{noinj}}}$. Note that injection affects the pressure field. It is therefore theoretically possible that $\frac{p_{O_2;\mathrm{inj}}}{p_{O_2;\mathrm{noinj}}} > 1$ and hence that injection increases the oxygen concentration at the surface compared to no injection.

Figure 3.13 shows the oxygen pressure ratio for all blowing ratios of conditions L1 and T3. The oxygen pressure ratio decreases with increasing blowing ratio. Note that the flow was confirmed to be turbulent using the heat flux recorded by the thin film gauges. The bottom row of Fig. 3.13 (b) and top row of Fig. 3.13 (a) show the same blowing ratio in a turbulent ($Re_u = 5 \times 10^7$) and laminar ($Re_u = 2.58 \times 10^7$) flow regime, respectively. The reduction in oxygen pressure ratio along the sample is much stronger for the laminar case, where mass transport happens through diffusion alone and the diffusion velocity is directly proportional to the film thickness. As turbulent mixing comes into play at higher unit Reynolds numbers, the coolant film is much less effective at mitigating mass transport from the freestream to the surface. The eddies seem to inhibit the growth of the film, as the oxygen pressure only decreases slightly across the sample.

3.7.4 Spatially averaged oxygen pressure ratio

Figure 3.14 depicts the average oxygen pressure ratio for increasing nitrogen blowing ratios. A 100 pixel wide strip in the center was used for this average to avoid 3D effects at the edges. The oxygen pressure ratio for condition T3 at the upstream edge is 92%, 88% and 81% for blowing ratios of 0.016%, 0.032% and 0.053%, respectively. It falls to 85%, 77% and 68% at the downstream edge. The laminar case with $F = 0.053\%$ has a 7% lower oxygen ratio at the upstream edge than its turbulent counterpart with the same blowing ratio. A much larger discrepancy of 30% between the two conditions is observed at the downstream edge. The drop in oxygen pressure ratio from upstream to downstream edge for condition L1 is 36% for both blowing ratios.

The oxygen pressure ratio at the downstream edge for all cases summarised in Table 3.1, is presented in Fig. 3.15. An average value along the last 4 mm in streamwise direction was taken, to reduce noise. The oxygen pressure ratio appears to be linearly dependent on the blowing ratio in the turbulent regime, while following a curved trend for the laminar data. The presented experimental data provides a foundation to explore empirical correlations and semi-analytical models for the mass transfer reduction on transpiration cooled models with blowing.

3.8 Conclusion

This work presents a pressure sensitive paint diagnostic for the species concentration of transpiration cooled walls. It produced the first spatially resolved oxygen partial pressure map on a porous medium with foreign gas injection. The O_2 partial pressure can be converted into O_2 concentration at the wall if the static pressure is known. The concentration is critical to investigate how well the porous surface can be protected from oxidation and chemical attack.

By combining the O_2 partial pressure maps from the nitrogen injection case, with the O_2 pressure recorded in the corresponding no-injection shot, it was possible to compute the oxygen pressure ratio between blowing and non-blowing. Higher

blowing ratios and lower Reynolds numbers decrease the oxygen pressure, which is consistent with the literature. The oxygen pressure decreases across the sample, in direction of the flow, due to the growth of the coolant film. This growth is much more pronounced in the laminar condition, in which mass transfer takes place via diffusion only. Turbulent mixing inhibits the growth of the coolant layer.

The 39% porous alumina used for this experiment featured a good bond with PSP, while imitating the pore size of Ultra-High-Temperature Ceramics and exhibiting an extremely uniform outflow map. Inexpensive and quick to manufacture, it is a suitable porous substrate to experimentally study transpiration cooled systems. When the PSP molecules are sprayed onto the porous surface, some fly into pores which are deeper inside the material. If the material is transpiration cooled, they will experience a higher local pressure than at the surface. Modeling or mitigating this porous interface effect could enable static pressure measurements on transpiration cooled surfaces in the future.

The following improvements are suggested, to further increase the accuracy of the method. Firstly, filter out temperature effects by coupling every experiment with a nitrogen-freestream case. The obtained thermal response can be deducted from the air-freestream PSP signal. Secondly, improving the image stability by avoiding mirrors in the test section and instead having a direct optical path between the camera and the sample.

3.9 Uncertainty analysis

The three independent quantities of interest that are measured in this paper are the PSP pressure, the blowing ratio, and the unit Reynolds number. The PSP pressure signal will be affected by PSP degradation and absolute surface temperature, both effects however have been minimised by daily calibrations. The LED intensity correlates with its junction temperature, which is measured by a thermistor. The thermistor is extremely stable and no drift was observed between calibration runs. Given that all quantities are time averaged over at least 30 frames, the shot noise for the darkest reading with 600 counts is $\pm$ 1.49% per pixel and $\pm$ 0.15% for the

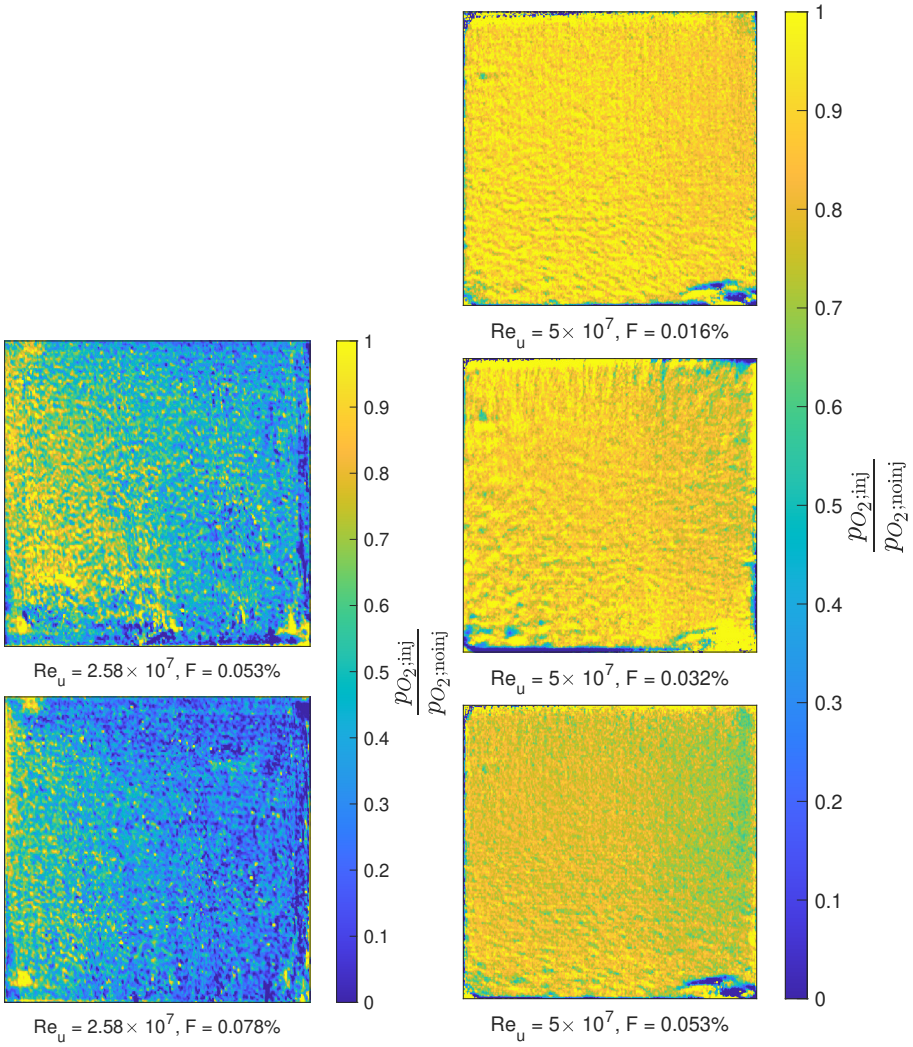

(a) laminar condition L1 (b) turbulent condition T3

Figure 3.13: Spatially resolved oxygen pressure ratio as measured by the PSP.

streamwise spatial averages. The readout noise amounted to ± 0.002% and dark current was negligible due to frequent auto-shading by the camera. Thus, the PSP temperature, T_{PSP}, remains the main error source.

The unit Reynolds number depends on the static pressure and temperature at the boundary layer edge. The pressure is recorded by a surface mounted Kulite with an accuracy of ± 6.3% of the reading. This error was found by calibrating the Kulite against an Inficon CDG025D pressure gauge, which itself has an error of 0.2% of the reading. The static temperature is derived from the total temperature trace, which was established using aspirated thermocouples with an accuracy of ±10K.

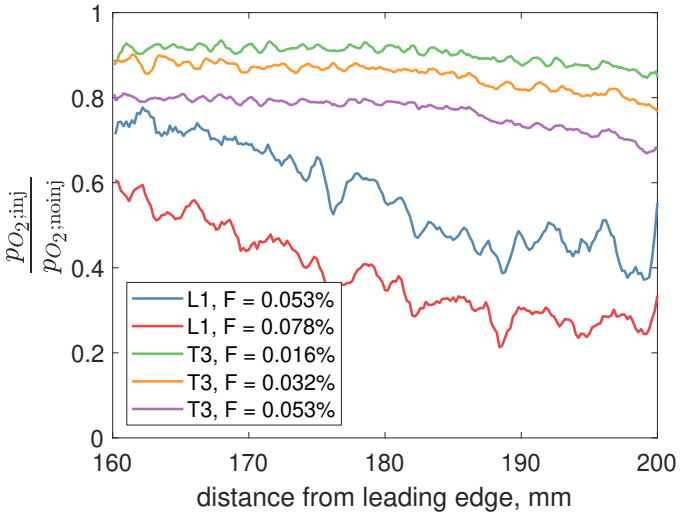

Figure 3.14: Comparison of oxygen pressure ratio reduction along the x axis for increasing blowing ratios.

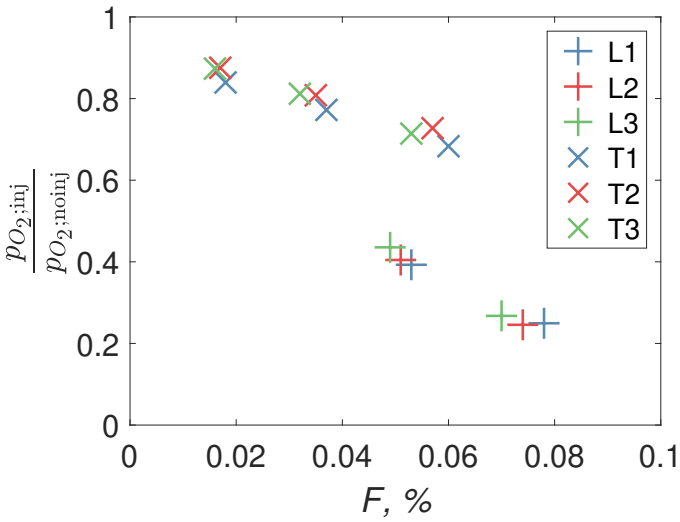

Figure 3.15: Average oxygen pressure ratio in the last 4 mm near the downstream edge plotted against the blowing ratio.

The resulting error of the Reynolds number amounts to ±8.7% for the laminar condition and ±9.3% for the turbulent condition.

The blowing ratio is calculated using Eqs. (3.1)-(3.2), thus again depending on the static temperature and pressure, as well as the mass flow rate. The mass flow meter has a fixed uncertainty of 0.25 slpm, thus the error will be smaller for increasing mass flow rates. For the laminar conditions, the resulting error for the blowing ratio amounts to ±24.3% for the smallest injection pressure, ±18.16% for medium injection and ±14.8% for the high injection pressure (Table 3.2).

Equivalently, the blowing ratios in the turbulent condition have an error of ±24.5%, ±15.5% and ±14.4% in ascending order of injection pressure, respectively. By far the largest contributor to this error is the ± 6.3% uncertainty of the surface mounted pressure gauges. In future experiments, it should be replaced by a more accurate pressure sensor.

3.10 Similarities between heat and mass transfer

The experimentally obtained ratio of oxygen partial pressure is plotted against the blowing parameter with respect to heat, B_h, as depicted in Fig. 3.16. This is achieved by taking the data from Fig. 3.15 and normalising the blowing ratio, F, by the uncooled Stanton number for heat transfer. The Stanton number was calculated using Eckert's reference enthalpy [81]. The experimental data is compared against the three most common engineering correlations in the literature, relating the blowing parameter to the reduction in heat transfer.

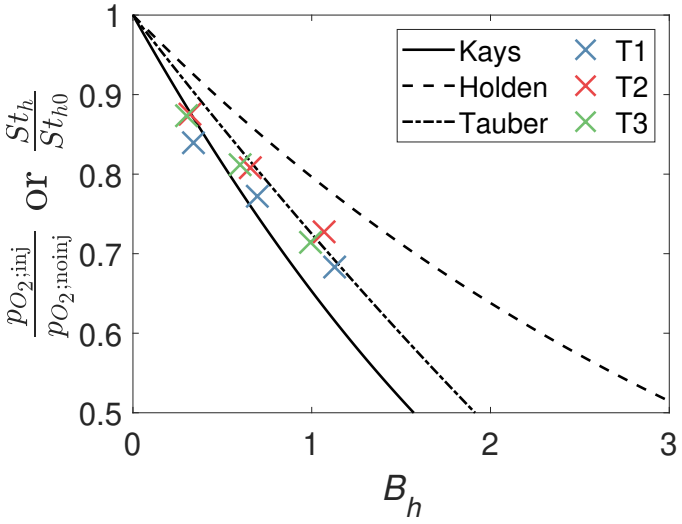

Figure 3.16: Comparison of the experimentally obtained reduction in oxygen pressure ratio to heat transfer correlations.

As derived in Section 2.1, the reduction in heat transfer between the freestream and the wall, expressed as the ratio of cooled to uncooled Stanton numbers, is given by Kays [29] as:

$$\frac{St_h}{St_{h0}} = \frac{B_h}{e^{B_h} - 1}. \tag{3.12}$$

Moyer and Rindal [82] suggested a slight correction for turbulent flows, whereby the blowing parameter is multiplied by a factor of 0.8. Further correlations for the Stanton number reduction due to blowing on a turbulent flat plate have been presented by Holden [83]:

$$\frac{St_h}{St_{h0}} = 1 - 0.92\left(1 - e^{-\frac{B_h}{4}}\right) \tag{3.13}$$

and Tauber [84]:

$$\frac{St_h}{St_{h0}} = 1 - 0.29B_h + 0.015B_h^2. \tag{3.14}$$

A similarity between the reduction in partial pressure ratio and heat Stanton number can be observed for a given blowing parameter. This is reminiscent of the heat and mass transfer analogy. The best fit is is provided by Kays' correlation, with the Moyer - Rindal correction, and Tauber's empirical relationship. Note that this result is purely an empirical observation and was not derived analytically. However, the following analytical observations are made. The oxygen partial pressure ratio can be expressed as the product of the oxygen mole fraction and the static pressure

$$p_{O_2} = y_{O_2} p \tag{3.15}$$

and thus the ratio becomes

$$\frac{p_{O_2;\mathrm{inj}}}{p_{O_2;\mathrm{noinj}}} = \frac{y_{O_2;\mathrm{inj}}}{y_{O_2;\mathrm{noinj}}} \frac{p_{\mathrm{inj}}}{p_{\mathrm{noinj}}} \tag{3.16}$$

For the purpose of this approximate, simplified analysis, the effect of blowing on the pressure field can be neglected, yielding $\frac{p_{\mathrm{inj}}}{p_{\mathrm{noinj}}} = 1$. Secondly, it is observed that the fraction of oxygen in air is constant and thus the ratio of oxygen mole fractions is equivalent to the ratio of air mole fractions, resulting in

$$\frac{y_{O_2;\mathrm{inj}}}{y_{O_2;\mathrm{noinj}}} = \frac{y_{\mathrm{air;inj}}}{y_{\mathrm{air;noinj}}} = y_{\mathrm{air;inj}} \tag{3.17}$$

noting that with no injection and an air freestream, the mole fraction of air in the flowfield is unity, $y_{\text{air;noinj}} = 1$. As the molar masses of the injected nitrogen and the freestream air are very similar, the mass fraction of air is approximately equivalent to its mole fraction an thus

$$\frac{p_{O_2;\text{inj}}}{p_{O_2;\text{noinj}}} \approx x_{\text{air;inj}}. \tag{3.18}$$

In Chapter 4 it will be shown that the mass fraction of air at the surface of a transpiration cooled stagnation point is equivalent to the mass Stanton number ratio

$$\frac{p_{O_2;\text{inj}}}{p_{O_2;\text{noinj}}} \approx x_{\text{air;inj}} = \frac{St_m}{St_{m0}}. \tag{3.19}$$

The relationship between the oxygen partial pressure and the Stanton number in Eq. (3.19) has so far only been derived for a stagnation point. However, the observed similarity in Fig. 3.16 suggests that the same relationship holds for a turbulent flat plate. This would result in $\frac{St_m}{St_{m0}} = \frac{St_h}{St_{h0}}$ for a turbulent flat plate. Further research is encouraged to explore this observation.

4

Correlation for species surface concentration on a hypersonic stagnation point with mass injection

4.1 Foreword

The diagnostic technique established in the previous chapter is a crucial experimental tool to investigate the mass transfer reduction due to transpiration cooling. In this chapter, a theoretical approach is taken to predict the reduction of freestream gas at the surface due to mass injection. It is important to understand the flow physics, starting from the governing equations, before conducting experiments with the novel diagnostic tool. This is achieved in the following chapter. This work has been accepted for publication in the *AIAA Journal* [17]. It is presented in this chapter with small layout changes, but unaltered content. The contribution of each author is summarised in the following:

- Marc Ewenz Rocher: Conceptualisation, Methodology, Analysis, Investigation, Validation, Writing
- Tobias Hermann, Matthew McGilvray: Supervision
- Rowan Gollan: Advice on Eilmer 4

More in-depth detailing of the hypersonic stagnation point boundary layer modelling is presented in Appendix A.

4.2 Introduction

Hypersonic flight is experiencing a global renaissance due to growing scientific, economic and military interest. This has catalysed the research activity in the field in recent years. NASA's X-plane revival, the surge of suborbital passenger high-speed vehicle concepts and the SR-72 development manifest this trend. The stagnation points of these vehicles generate hot, often dissociated gas as they fly through the atmosphere. This results in high heat fluxes due to radiation, convection and surface recombination of atomic species. Surface reactions in the form of oxidation or nitration further endanger the aerodynamic and structural integrity of the vehicle. To ensure the safety of crew and payload, the vehicle must be protected from thermal and chemical attack [4]. For this purpose it is necessary to model the heat flux and mass transfer of freestream species at the wall and design suitable protection systems.

Heat flux has been studied extensively for stagnation points without mass injection [6, 85] and with mass injection (analytically [32], numerically [86] and experimentally [41]). Mass injection occurs passively during ablation or actively in transpiration cooling. Mass flux in contrast, has received less attention in the literature. The two detrimental effects associated with mass flux of freestream species to the wall are catalytic recombination and surface degradation through oxidation and nitration. The blowing of gaseous reaction products in ablatives, of an inert gas in transpiration cooling or any other form of mass injection at the stagnation point, will counteract this mass flux and reduce the amount of freestream gas at the wall.

To date, engineers have focused on the cooling effect of mass injection, but the operating temperature of most aerospace materials is constrained more stringently by oxidation than melting. Common and envisioned aerospace materials such as UHTCs [87–89] or C/C composites [52, 90] corrode at up to 2500 K below their melting temperature, restraining them from tapping their full refractory potential.

Chemical attack also recesses the outer layer of ablatives. To model these processes, it is necessary to understand the freestream gas mass transfer at a stagnation point with mass injection. Beyond corrosion and chemical attack, knowledge of freestream activated species at a wall is required to predict catalytic heat flux. While the catalytic efficiency of surface materials remains an important subject of investigation [91, 92], little is known about the concentration of activated species at a given flight condition with stagnation point blowing. Fay and Riddell [6] predicted the recombination heat flux on a stagnation point in the absence of mass injection, but it is precisely this mechanism which shows a sharp decline in heat flux experimentally [41].

In order to predict the reduction in surface recombination and corrosion it is necessary to model the freestream mass transfer at a stagnation point with mass injection. This is commonly done numerically, by solving the self-similar boundary layer equations [93]. In heat transfer it is found that numerical and experimental results correlate well with the following equation, derived from film theory [26, 32]:

$$\frac{St_h}{St_{h0}} = \frac{\lambda B_h}{e^{\lambda B_h} - 1}, \tag{4.1}$$

where λ accounts for geometric effects and differences in coolant and boundary layer edge transport properties. The blowing parameter $B_h = \frac{F}{St_{h0}}$ is composed of the blowing ratio F and the heat Stanton number for no mass injection St_{h0}. Unfortunately a simple heat-mass transfer analogy, replacing B_h with $B_m = \frac{F}{St_{m0}}$ and St_h with St_m, does not lead to the desired result. The mass equivalent correlation simply does not correlate with numerically or experimentally obtained data. Ref. [94] introduced the following weighting factor

$$\frac{St_m}{St_{m0}} = \frac{\lambda_1 B_m}{e^{\lambda_1 B_m} - 1}, \tag{4.2}$$

$$\lambda_1 = 1.65 \left(\frac{M_{\text{air}}}{M_{\text{inj}}} \right)^{\frac{5}{6}}. \tag{4.3}$$

This is an empirical fit for air as the freestream gas. It explicitly shows the effect of two injectant parameters: the mass flow rate and the molecular mass. All other parameters, such as the wall to boundary layer edge temperature ratio, absolute wall temperature, diffusion coefficients, velocity gradient, are either neglected or their effect is lumped together in a numerical constant, which needs to be computed for each individual case. It is desirable to replace the numerical constants by an explicit function of said parameters. This would reduce time and complexity of the calculations and most importantly help engineers understand the underlying principles of stagnation point mass transfer when designing ablatives or transpiration cooled leading edges. It should also be noted that the above work assumed a constant heat capacity and derived the transport properties from kinetic theory, which leads to errors at the high temperatures encountered by ablatives and hypersonic stagnation points.

This paper presents a semi-analytical approach to obtain the mass transfer of freestream species at a stagnation point with mass injection. Starting with the conservation of mass, momentum, energy and species, the self-similar boundary layer equations are derived and validated against a full CFD solver. These analytical equations are then combined with thin film theory to obtain an explicit correlation for the species concentration and mass Stanton number at the surface.

4.3 Analysis

4.3.1 Governing equations

The flowfield around a hypersonic, axisymmetric stagnation point with mass injection is governed by the laminar boundary layer equations [95]

$$\frac{\partial(\rho r_1 u)}{\partial x} + \frac{\partial(\rho r_1 v)}{\partial y} = 0 \tag{4.4}$$

$$\rho u \frac{\partial u}{\partial x} + \rho v \frac{\partial u}{\partial y} = -\frac{dp}{dx} + \frac{\partial(\mu \frac{\partial u}{\partial y}))}{\partial y} \tag{4.5}$$

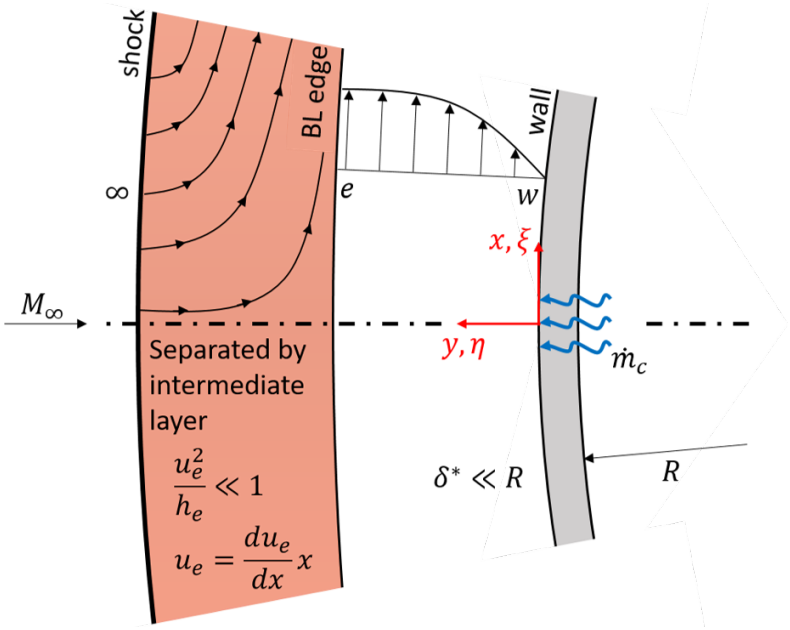

Figure 4.1: Sketch of a self-similar stagnation point, illustrating the assumptions made.

$$\rho u \frac{\partial h}{\partial x} + \rho v \frac{\partial h}{\partial y} = \frac{\partial}{\partial y}\left(k \frac{\partial T}{\partial y}\right) + u \frac{\partial p}{\partial x} + \mu \left(\frac{\partial u}{\partial y}\right)^2 \tag{4.6}$$

$$\rho u \frac{\partial c_i}{\partial x} + \rho v \frac{\partial c_i}{\partial y} = \frac{\partial (D_i \rho \frac{\partial c_i}{\partial y})}{\partial y} + \dot{w}_i \tag{4.7}$$

where Eqs. (4.4-4.7) describe the conservation of mass, momentum, energy and species, respectively. It is possible to transform these partial differential equations to a set of ordinary differential equations, in a procedure pioneered by Blasius in 1908 for incompressible flow across a flat plate and further developed for the hypersonic stagnation point by Dorodnitsyn [96] and Lees [97]. This transformation into non-dimensional space is desirable because it makes the solution self-similar. Self-similar theory makes the following assumptions, which are visualized in Figure 4.1:

1. the boundary layer edge and the shock are separated by an intermediate layer. This may be violated if the Reynolds number is too low, considering that the boundary layer thickness grows $\propto \frac{1}{\sqrt{Re}}$. For the cases considered in this work, the Reynolds number is large enough.

2. the boundary layer thickness is much smaller than the radius of curvature, such that most derivatives in ξ direction, along the surface, are negligible. The velocity gradient, $\frac{du_e}{d\xi}$ is the exception.

3. the post shock kinetic energy is small compared to the total enthalpy $\frac{u_e^2}{h_e} \ll 1$, where e denotes the boundary layer edge conditions.

4. the flow outside the boundary layer edge is inviscid and incompressible. With this in mind, one can use the Falkner-Skan wedge flow solutions to obtain the boundary layer edge velocity, $u_e = \frac{du_e}{dx}x$ [98].

Self-similar theory has been employed in the literature before, for instance to derive the stagnation point heat flux with no mass injection [6] and to numerically evaluate the velocity, temperature and concentration profiles of a transpiration cooled stagnation point in a perfect gas [93]. In the following, the self-similar equations for a stagnation point with blowing in an ideal gas are developed. The gas is assumed to be in thermochemical equilibrium.

4.3.2 Boundary layer transformation and boundary conditions

The transformed coordinates are defined as follows:

$$\xi = \int_0^x \rho_e \mu_e u_e r_1^2 dx, \quad \eta = \frac{u_e r_1}{\sqrt{2\xi}} \int_0^y \rho dy, \tag{4.8}$$

with the corresponding derivatives

$$\frac{\partial}{\partial x} = \frac{\partial}{\partial \xi} \rho_e u_e \mu_e r_1^2 + \frac{\partial}{\partial \eta} \frac{\partial \eta}{\partial x}, \tag{4.9}$$

$$\frac{\partial}{\partial y} = \frac{\partial}{\partial \xi}(0) + \frac{\partial}{\partial \eta} \frac{u_e \rho r_1}{\sqrt{2\xi}}. \tag{4.10}$$

The resulting self-similar equations for a binary coolant-freestream mixture with no chemical reactions are

$$\left(lf''\right)' + ff'' + \frac{1}{2}\left(\delta - f'^2\right) = 0 \tag{4.11}$$

$$\left(\frac{\Gamma_{c_p} l}{Pr}\theta'\right)' + \Gamma_{c_p} f\theta' + \frac{l}{Sc}\left(\frac{c_{p;\mathrm{inj}}}{c_{p;e}} - \frac{c_{p;\mathrm{ext}}}{c_{p;e}}\right)c'\theta' = 0 \tag{4.12}$$

$$\left(\frac{l}{Sc}c'\right)' + fc' + \frac{\dot{w}_i}{2\frac{du_e}{dx}\rho} = 0 \tag{4.13}$$

where $f' = \frac{u}{u_e}$ denotes the velocity ratio, $\theta = \frac{T}{T_e}$ the temperature ratio and c the coolant mass fraction. Please refer to Chapter 6.5 in Ref. [95] for a more extensive derivation of Eqs. (4.11-4.13). Note that $\dot{w}_i$ accounts for the mass injection at the wall, for instance due to transpiration cooling.

The boundary conditions are defined next. A no-slip, fixed temperature condition is applied at the wall. The coolant concentration at the boundary layer edge is set to zero, yielding

$$f'_w = 0 \tag{4.14a}$$
$$\theta_w = \frac{T_w}{T_e} \tag{4.14b}$$
$$f'_e = 1 \tag{4.14c}$$
$$\theta_e = 1 \tag{4.14d}$$
$$c_e = 0 \tag{4.14e}$$

Furthermore, the integrated velocity function at the wall, f_w, is derived from the continuity equation using the stream functions, which are expressed in transformed coordinates using Eq. (4.10):

$$\frac{\partial\psi}{\partial y} = \rho u r_1 = \rho f' u_e r_1 = \frac{\partial\psi}{\partial\eta}\frac{u_e\rho r_1}{\sqrt{2\xi}}. \tag{4.15}$$

By inspection of Eq. (4.15)

$$\frac{\partial\psi}{\partial\eta} = \sqrt{2\xi}f' \tag{4.16}$$

and thus

$$\psi = \sqrt{2\xi} f \quad \frac{\partial \psi}{\partial \xi} = \sqrt{2\xi}\frac{\partial f}{\partial \xi} + \frac{1}{\sqrt{2\xi}} f. \tag{4.17}$$

The stream function is differentiated with respect to the streamwise distance x using Eq. (4.9):

$$\begin{aligned} \frac{\partial \psi}{\partial x} =& -\rho v r_1 = \frac{\partial \psi}{\partial \xi}\rho_e u_e \mu_e r_1^2 + \frac{\partial \psi}{\partial \eta}\frac{\partial \eta}{\partial x} \\ =& \left(\sqrt{2\xi}\frac{\partial f}{\partial \xi} + \frac{1}{\sqrt{2\xi}} f\right)\rho_e u_e \mu_e r_1^2 \\ &+ \sqrt{2\xi} f' \frac{\partial \eta}{\partial x}. \end{aligned} \tag{4.18}$$

The derivatives in wall tangential (ξ) direction can be neglected, as stated in section 4.3.1. At the wall, Eq. (4.18) can be rearranged as follows, yielding the sixth boundary condition at the wall:

$$f_w = \frac{\rho_w v_w r_1 \sqrt{2\xi}}{\rho_e u_e \mu_e r_1^2} = -\frac{\rho_w v_w}{\sqrt{2\rho_e \mu_e \frac{du_e}{dx}}}. \tag{4.19}$$

The concentration boundary condition is found by applying Eq. (4.7) at the wall:

$$(\rho v)_w \frac{\partial c_{i,w}}{\partial y} = \frac{\partial (D_i \rho \frac{\partial c_i}{\partial y})_w}{\partial y} + \dot{w}_i. \tag{4.20}$$

Equation (4.21) is found by integrating Eq. (4.20) with respect to y:

$$(\rho v c_i)_w = \left(D_i \rho \frac{\partial c_i}{\partial y}\right)_w + \dot{m}_i. \tag{4.21}$$

Note that $\dot{w}_i = \frac{\partial \dot{m}_i}{\partial y}$ and $\frac{\partial (\rho v c_i)_w}{\partial y} = (\rho v)_w \frac{\partial c_{i;w}}{\partial y}$, as

$$\begin{aligned} \frac{\partial (\rho v)_w}{\partial y} &= -\sqrt{2\rho_e \mu_e \frac{du_e}{dx}}\frac{\partial f_w}{\partial y} \\ &= -\sqrt{2\rho_e \mu_e \frac{du_e}{dx}}\frac{\partial \eta}{\partial y}\frac{\partial f_w}{\partial \eta} \\ &= -\sqrt{2\rho_e \mu_e \frac{du_e}{dx}}\sqrt{\frac{2\frac{du_e}{dx}}{\rho_e \mu_e}}\frac{\partial f_w}{\partial \eta} \\ &= -4\frac{du_e}{dx} f'_w = -4\frac{du_e}{dx}\left(\frac{u}{u_e}\right)_w = 0, \end{aligned} \tag{4.22}$$

applying the no-slip condition $\left(\frac{u}{u_e}\right)_w = 0$. Defining $c_{\text{inj}} = c$ and $c_{\text{ext}} = 1 - c$ and using Eq. (4.21), the species continuity equations at the wall for the injected and the external flow in a binary mixture become

$$(\rho v c)_w = D_{12}\rho_w \left(\frac{\partial c}{\partial y}\right)_w + \dot{m}, \tag{4.23}$$

$$(\rho v)_w - (\rho v c)_w = -D_{12}\rho_w \left(\frac{\partial c}{\partial y}\right)_w, \tag{4.24}$$

respectively. The implicit assumption here is that the external flow does not enter the porous wall and that the mass flux $\dot{m}$ crossing the surface consists purely of injected gas. This should not be confused with the assumption that the coolant concentration at the wall is 100%.

Adding Eqs. (4.23) and (4.24), it is apparent that $\dot{m} = (\rho v)_w$. Eq. (4.23) uses this expression for $\dot{m}$ and is transformed into non-dimensional space to obtain a boundary condition for the concentration gradient at the wall:

$$\left(\frac{\partial c}{\partial \eta}\right)_w = \left(\frac{Sc}{l}\right)_w f_w(1 - c_w). \tag{4.25}$$

There are now 7 boundary conditions (Eqs. (4.14), (4.19) and (4.25)) for 7 unknowns $f, f', f'', \theta, \theta', c, c'$ in Eqs. (4.11-4.13). The above set of equations constitutes a boundary value problem, which can be solved numerically. The velocity gradient is obtained from Modified Newtonian Theory [95], which is only applicable to hypersonic flows:

$$\frac{du_e}{dx} = \frac{1}{R}\sqrt{\frac{2(p_e - p_\infty)}{\rho_e}}. \tag{4.26}$$

For lower Mach numbers a correlation is provided in Ref. [99], however, the Mach number needs to be high enough for the post-shock flow to be assumed incompressible and thus for the Falkner-Skan solution to hold. Note that the diffusion coefficient was modelled using the Lennard-Jones parameters, as described in Chapter 17.3 of Ref. [9], while all other thermophysical properties were obtained from CEA2 [100].

4.3.3 Validation with high-fidelity CFD solver

In this work, the validation of the self-similar method is undertaken by comparison with the high-fidelity CFD solver Eilmer 4 [101, 102]. This validation method was chosen due to the lack of experimental reference data in the literature. Figure 4.2 illustrates the setup of the CFD simulation. Since the modelled hemisphere is axisymmetric, the southern boundary has a no-slip condition. The western boundary is fitted to the shock, while the northern boundary assumes a supersonic outflow. The mass injection is modelled with a porous injection boundary condition, which works as follows:

1. At every time step, every interface along the boundary is assigned a pressure, temperature, concentration and velocity.

2. Pressure continuity is assumed and thus the pressure of the adjacent inner cell is assigned to the interface.

3. The coolant temperature is predefined and kept constant. The gas and the wall are assumed to have the same temperature.

4. The coolant concentration is solved using Eq. (4.23), noting that $(\rho v)_w = \dot{m}$. It is discretized as follows:

$$\left(\frac{\partial c}{\partial y}\right)_w = (c_w - 1)\frac{v_w}{D_{12}} \tag{4.27}$$

$$\frac{c_{\text{adj}} - c_w}{\Delta x} = (c_w - 1)\frac{v_w}{D_{12}} \tag{4.28}$$

$$c_w = \frac{c_{\text{adj}} + \frac{v_w \Delta x}{D_{12}}}{1 + \frac{v_w \Delta x}{D_{12}}} \tag{4.29}$$

   where c_{adj} is the coolant concentration of the adjacent inner cell and Δx the distance between the midpoints of the interface and the adjacent inner cell.

5. The normal velocity is calculated using the predefined injection mass flux and the density at the wall, $v_w = \frac{\dot{m}_{\text{inj}}}{\rho_w}$. The tangential velocity is set to zero to implement the no-slip condition.

Table 4.1: Parameters of the validation test cases. All cases had an air freestream, $p_e = 11.9$ kPa and $T_w = 300$ K.

Case	Inj	T_e/K	$\dot{m}/(\frac{\text{kg}}{\text{m}^2\text{s}})$
1	N_2	537	0.2
2	N_2	1800	0.2
3	Ne	537	0.2
4	Ar	537	0.2

Figure 4.4 compares the velocity, temperature and concentration profiles as computed by the self-similar solutions to the ones obtained by Eilmer 4. The test case featured a 25 mm radius hemispherical probehead in a Mach 7 air freestream, with $p_\infty = 187.7$ Pa, $u_\infty = 989$ m/s and $T_\infty = 49.7$ K. The velocity gradient was 6% higher than predicted by Eq. (4.26), due to 3D effects and the geometry change caused by the injected gas. A value of $\frac{du_e}{dx} = 23410\text{s}^{-1}$ was obtained and used in the self-similar solution as well. Table 4.1 summarises the properties of the injected coolants. The mesh was clustered near the shock and boundary layer, as illustrated in Fig. 4.3. The solution converged at a mesh size of 10 μm normal to the wall. The mesh size was decreased further and the results compared to confirm mesh independence. A blend of the low dissipation AUSMDV scheme for the regions away from shocks and a more diffusive Hanel-Schwane-Seider scheme for the interfaces near shocks was employed as flux calculator. Figures 4.2 and 4.3 depict the coolant concentration around the whole hemisphere and just in the stagnation region, respectively, for case 1. The model compares well with the CFD solver, despite its simplifying assumptions (see section 4.3.1). Cases with very dissimilar coolant and freestream gases display a larger discrepancy than a homogeneous boundary layer. The error for all three profiles is within 5% for all conditions described in Table 4.1. Thus, the self-similar solutions are deemed suitable to numerically validate the analytical solutions derived in the following section.

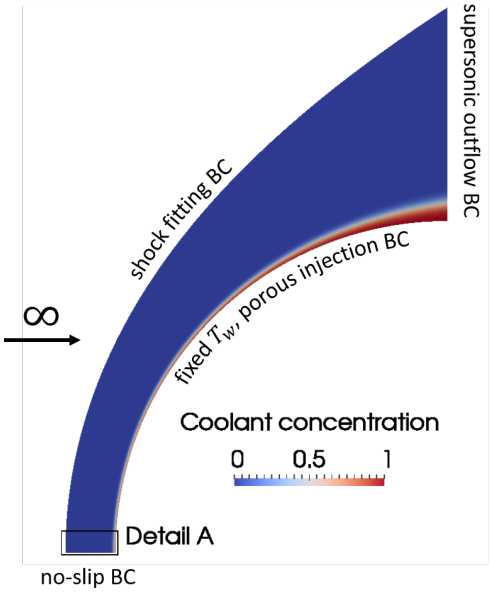

Figure 4.2: Eilmer 4 result, depicting the coolant concentration for the test case shown in Table 4.1.

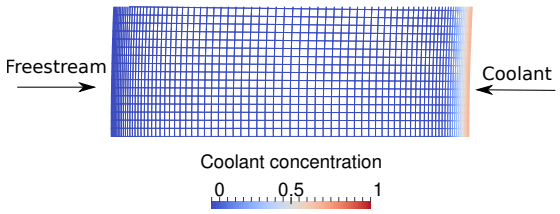

Figure 4.3: Wireframe of detail A from Fig. 4.2, illustrating the the mesh size and coolant concentration near the stagnation point.

4.3.4 Mass transfer coefficient for no mass injection and fixed wall concentration

Before considering a stagnation point with mass injection, the mass transfer of freestream species to the surface in the absence of blowing is reviewed. The same approach that Fay-Riddell used to derive the heat transfer on a stagnation [6] will be employed here to find its mass transfer equivalent. The mass flux of freestream gas at the wall is given as

$$j_w = -\rho_w D_{12} \left(\frac{\partial c}{\partial y} \right)_w , \tag{4.30}$$

which can be transformed into non-dimensional space and simplified using the definition of ξ (Eq. (4.8)):

$$j_w = -\rho_w D_{12} \sqrt{\frac{2\rho_w}{\mu_w} \frac{\partial u_e}{\partial x}} \left(\frac{\partial c}{\partial \eta} \right)_w . \tag{4.31}$$

Analogously to the heat transfer parameter $\frac{Nu}{\sqrt{Re}}$, the mass transfer parameter can be defined as [98]

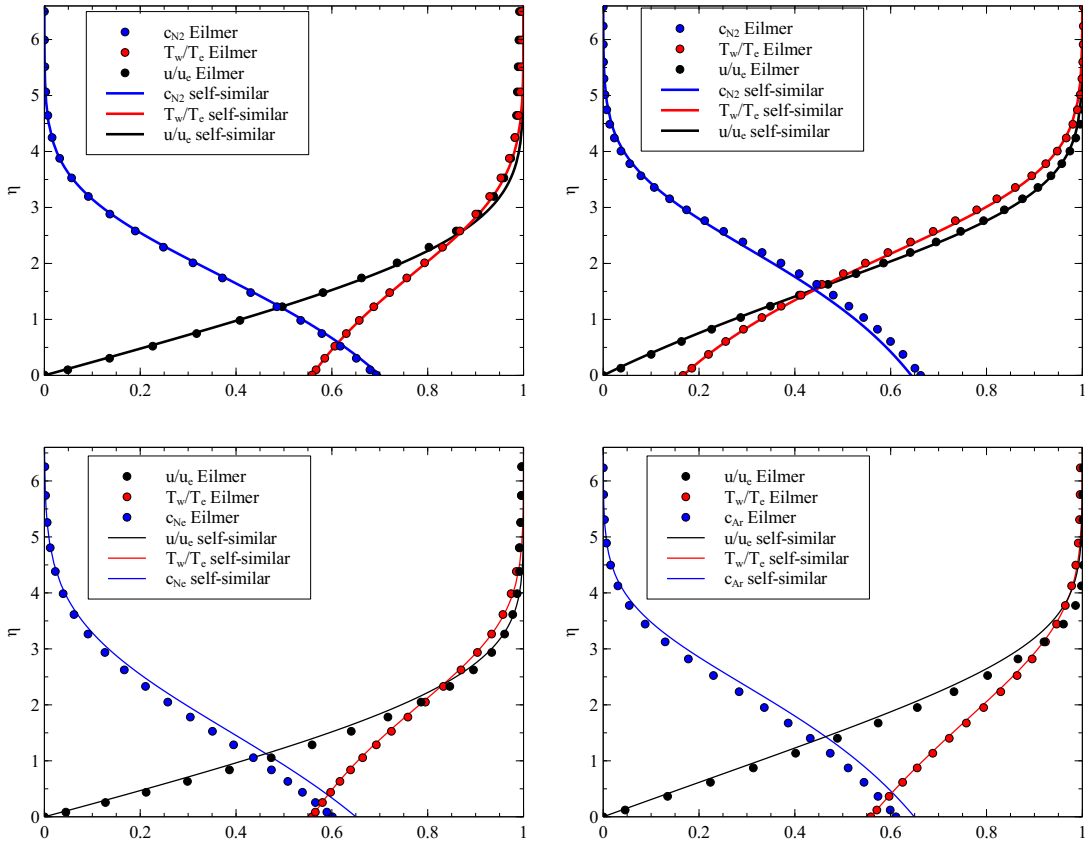

Figure 4.4: Comparison of the self-similar solution to the high fidelity CFD solver result for test cases in Table 4.1. Cases 1-4 are shown in chronological order from top left to bottom right.

$$\begin{aligned}\frac{Sh}{\sqrt{Re}} &= \frac{j_w}{-\rho_w D_{12}(c_e - c_w)/x}\sqrt{\frac{\mu_w}{\rho_w u_e x}} \\ &= \frac{Sc_w}{c_w}\frac{j_w}{\sqrt{\mu_w \rho_w \frac{\partial u_e}{\partial x}}}.\end{aligned} \tag{4.32}$$

Note that $c_e = 0$, as defined in Eq. (4.14). Equation (4.32) is rearranged as follows:

$$j_w = \frac{Sh}{\sqrt{Re}} c_w \sqrt{\mu_w \rho_w \frac{\partial u_e}{\partial x}} \frac{1}{Sc_w}. \tag{4.33}$$

By inspection with Eq. (4.31), the mass transfer parameter for a stagnation point with no injection is

$$\frac{Sh}{\sqrt{Re}} = -\frac{\sqrt{2}}{c_w}\left(\frac{\partial c}{\partial \eta}\right)_w. \tag{4.34}$$

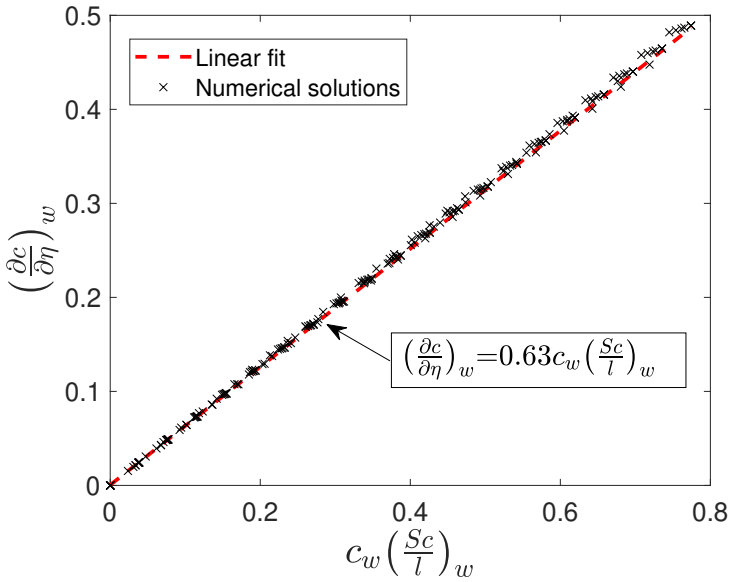

Figure 4.5: Results of the parameter study to obtain the factor K.

The concentration gradient at the wall, $\left(\frac{\partial c}{\partial \eta}\right)_w$ for no mass injection is derived starting with the self-similar species conservation equation Eq. (4.13). Since f_w and $\dot{w}$ are zero for no injection, it can be simplified as follows:

$$\left(\frac{l}{Sc} c'\right)' = 0 \tag{4.35a}$$

$$\left(\frac{\partial c}{\partial \eta}\right)_w = K \left(\frac{Sc}{l}\right)_w . \tag{4.35b}$$

The factor K is found to be $K = 0.63 c_w$ following a numerical parameter study, depicted in Fig. 4.5, including the conditions shown in Table 4.2. This correlation is only accurate if the coolant and freestream gas are identical or similar, such as N_2 and air. The concentration gradient for a stagnation point with no mass injection is found to be

$$\left(\frac{\partial c}{\partial \eta}\right)_{w;0} = 0.63 c_w \left(\frac{Sc}{l}\right)_w \tag{4.36}$$

and the mass transfer parameter becomes

$$\frac{Sh}{\sqrt{Re}} = 0.89 \left(\frac{Sc}{l}\right)_w . \tag{4.37}$$

Table 4.2: Conditions of the parameter study to find K.

#	Inj	Ext	p_e/kPa	T_w/K	T_e/K	R/mm
1	Air	Air	11.9	300	300	25
2	Air	Air	11.9	300	300	50
3	Air	Air	23.8	300	300	25
4	N_2	Air	11.9	300	515	25
5	Air	Air	11.9	300	1500	25
6	Air	Air	11.9	1000	1500	25
7	Air	Air	60	1000	2000	10
8	Ar	Ar	11.9	300	300	25
9	He	He	11.9	300	300	25
10	Ne	Ne	11.9	300	300	25
11	Xe	Xe	11.9	300	300	25

The mass transfer rate simplifies to

$$j_w = 0.89 \frac{\rho_e \mu_e}{\sqrt{\rho_w \mu_w}} c_w \sqrt{\frac{\partial u_e}{\partial x}}. \tag{4.38}$$

Finally, the mass transfer coefficient for no mass injection, but a fixed c_w, is simply the mass transfer rate divided by the driving force, noting that $c_e = 0$,

$$K_{m0} = \frac{j_w}{\rho_w c_w - \rho_e c_e} \tag{4.39a}$$

$$K_{m0} = 0.89 \frac{\rho_e}{\rho_w} \frac{\mu_e}{\sqrt{\rho_w \mu_w}} \sqrt{\frac{\partial u_e}{\partial x}}, \tag{4.39b}$$

and the corresponding Stanton number becomes

$$St_{m0} = 0.89 \frac{\rho_e}{\rho_w} \frac{\mu_e}{\sqrt{\rho_w \mu_w}} \sqrt{\frac{\partial u_e}{\partial x}} \frac{1}{u_e}. \tag{4.40}$$

4.3.5 Film theory approach

This section attempts to derive St_m analytically using film theory. Film theory, firstly described in Ref. [26], predicts the ratio of mass transfer coefficients with mass injection, K_m to the mass transfer coefficient in the absence of mass injection, K_{m0}. It is less realistic than the boundary layer concept, but greatly simplifies

the analysis of the mass transport between the freestream and the wall. It is shown that an equation of the form

$$\frac{d^2\beta}{dm^2} - B_m\left(\frac{d\beta}{dm}\right) = 0, \tag{4.41}$$

with boundary conditions $\beta = 0$ when $m = 0$ and $\beta = 1$ when $m = 1$ has the following dimensionless gradient at the wall:

$$\left(\frac{\partial\beta}{\partial m}\right)_w = \frac{B_m}{e^{B_m} - 1}. \tag{4.42}$$

β is the normalized velocity, temperature or concentration and is called generalized profile factor, while m is the normalized y coordinate. Furthermore, it is demonstrated that the ratio of non-dimensional gradients, corresponds to the ratio of mass transfer coefficients [26]

$$\frac{\left(\frac{\partial\beta}{\partial\eta}\right)_w}{\left(\frac{\partial\beta}{\partial\eta}\right)_{w;0}} = \frac{K_m}{K_{m;0}} = \frac{B_m\frac{\Delta_0}{\Delta}}{e^{B_m} - 1}, \tag{4.43}$$

where $\frac{\Delta}{\Delta_0}$ denotes the ratio of film thicknesses with and without mass injection. Film theory assumes that this ratio is unity.

This paper presents a simplification which relates the above ratio of non-dimensional gradients directly to the surface concentration of external species. Using Eqs. (4.25) and (4.36):

$$\frac{\left(\frac{\partial\beta}{\partial\eta}\right)_w}{\left(\frac{\partial\beta}{\partial\eta}\right)_{w;0}} = \frac{\left(\frac{\partial c}{\partial\eta}\right)_w}{\left(\frac{\partial c}{\partial\eta}\right)_{w;0}} = \frac{f_w(1 - c_w)}{0.63c_w} \approx 1 - c_w. \tag{4.44}$$

The approximation holds well for all blowing rates considered in this study. The ratio $\frac{f_w}{0.63c_w} \to 1$ for small blowing ratios can be inferred by setting the right hand side of Eq. (4.25) equal to that of Eq. (4.36). While Eq. (4.36) strictly speaking is only valid for no blowing, it is found that the above approximation is accurate for small to moderate mass fluxes. For large mass fluxes, which lead to $\frac{K_m}{K_{m;0}} = 1 - c_w \ll 0.01$, the approximation will not hold. However, the absolute

difference to the correct value will be small. The following correlation is obtained when combining Eq. (4.43) and (4.44):

$$1 - c_w = \frac{B_m}{e^{B_m} - 1}, \tag{4.45}$$

with B_m defined as the blowing parameter for mass transfer.

In heat transfer it is common practice to denote the ratio of heat transfer coefficients as the ratio of Stanton numbers, as shown for instance in Ref. [103]. The Stanton number is the ratio of heat transfer at the surface to the thermal capacity of the passing fluid. Analogously, the mass transfer Stanton number, St_m, is defined as the ratio of mass transfer at the surface to the velocity of the passing fluid: $St_m = \frac{K_m}{u_e}$. Thus, Eq. (4.43) can be rewritten as

$$\frac{St_m}{St_{m0}} = \frac{B_m}{e^{B_m} - 1}, \tag{4.46}$$

where St_{m0} denotes the mass Stanton number in the absence of blowing.

Figure 4.6 presents the concentration of freestream species at the surface, $1 - c_w$, plotted against the mass flux $\dot{m}$. Note that by inspection of Eqs. (4.45) and (4.46), $\frac{St}{St_{m0}} = 1 - c_w$. c_w was obtained numerically using the self-similar equations. Intuitively, smaller nose radii and higher boundary layer edge pressures increase the concentration of freestream species at the wall. It is desirable to replace $\dot{m}$ by a quantity that makes the data collapse.

The blowing parameter for mass transfer, $B_m = \frac{F}{St_{m0}}$ presents itself as an obvious candidate. However, as can be seen in Fig. 4.7, the data does not collapse satisfactorily. Despite the narrow subset of cases with constant gas and temperature, $B_m = \frac{F}{St_{m0}}$ alone does not seem to be a good predictor for the ratio of mass Stanton numbers. It corrects for the geometry, specifically the nose radius, but not for the boundary layer edge pressure. The correction factor presented in Eq. (4.3), yielding $B_{m,1} = \lambda_1 B_m$ does not provide a satisfactory fit either. All cases considered in Fig. 4.7 involve air injection into an air freestream, thus $\lambda_1 = 1$. The aim of this paper is to improve this scaling factor λ.

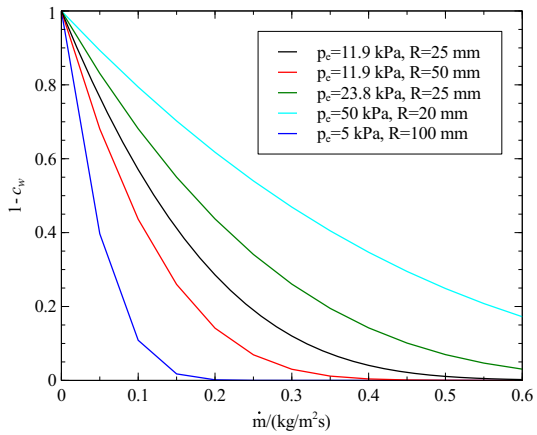

Figure 4.6: Effect of pressure and nose radius for air injection in air at $T_w = 300K$ and $T_e = 537K$.

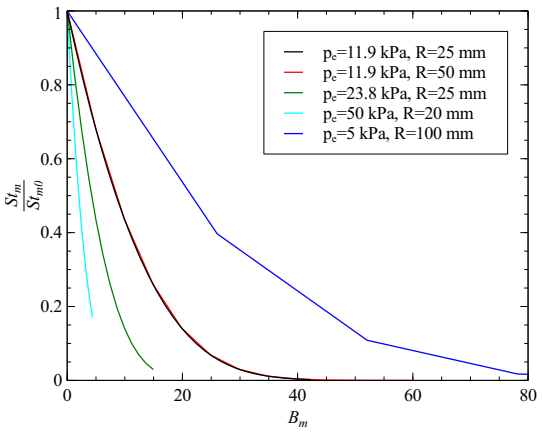

Figure 4.7: Effect of pressure and nose radius for air injection in air at $T_w = 300K$ and $T_e = 537K$.

4.4 Parameter scaling and results

The aim of this section is to derive a scaling factor λ analytically, starting with the self-similar governing equations for a laminar boundary layer in thermochemical equilibrium. Neglecting the third term (mass generation) of Eq. (4.13), which is found to be small compared to the first (advection) and the second term (diffusion), one obtains

$$\frac{d^2c}{d\eta^2} + \frac{f + \frac{\partial\alpha}{\partial\eta}}{\alpha}\left(\frac{dc}{d\eta}\right) = 0, \tag{4.47}$$

β and m are now defined such that the boundary conditions described after Eq. (4.41) are met. Note that the coolant concentration, c_e, is assumed to be zero at the boundary layer edge. Defining $m = \frac{\eta}{\Delta}$ and $\beta = \frac{c - c_w}{c_e - c_w} = 1 - \frac{c}{c_w}$ one obtains

$$\frac{d^2\beta}{dm^2} + \frac{f + \frac{\partial\alpha}{\partial\eta}}{\alpha}\Delta\left(\frac{d\beta}{dm}\right) = 0. \tag{4.48}$$

By comparison with Eq. (4.41), it is clear that the dimensionless measure of mass transfer rate in the present case is

$$B_m = -\frac{f + \frac{\partial\alpha}{\partial\eta}}{\alpha}\Delta. \tag{4.49}$$

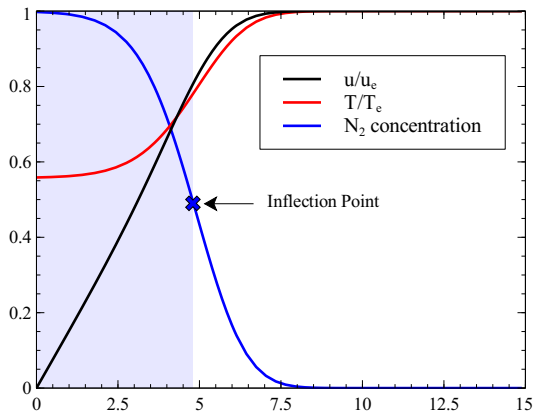

Figure 4.8: Velocity, temperature and concentration profiles for the condition shown in Table 4.3.

Table 4.3: Input parameters of the reference test case.

M	p_e/kPa	T_w/K	T_e/K	$\dot{m}/(\frac{\text{kg}}{\text{m}^2\text{s}})$	R/mm
7	11.9	300	537	0.6	25

The first observation is that B_m is directly proportional to the effective film thickness, Δ. It is defined as the thickness of a laminar fluid, which would offer the experimentally observed resistance to the transport of freestream gas to the wall. Thus far, however, there is no expression relating the effective film thickness to known quantities, such as freestream, coolant and geometrical parameters.

Figure 4.8 presents the numerically obtained self-similar profiles for a Mach 7, $T_w = 300$ K, $T_e = 537$K, $p_e = 11.9$kPa freestream condition and will be used to illustrate the steps and assumptions made in the following analytical treatment. In this work, the following assumption is made: Δ is proportional to the area under the concentration curve in Fig. 4.8. After all, this area could be redistributed into a rectangular shape, with 100% coolant gas concentration inside and 0% outside of it, thus representing the effective coolant gas film thickness. Observing Fig. 4.8, it is found that this area can be approximated by a rectangle spanning from zero to the inflection point of the concentration profile. Looking at Eq. (4.13) this observation is no coincidence. Applying the chain rule and dropping the mass

generation term, which is zero away from the wall, one obtains

$$\left(\frac{l}{Sc}\right)c'' = -\left(\frac{l}{Sc}\right)'c' - fc' = 0. \tag{4.50}$$

Clearly, c' is not zero at the inflection point, thus the condition is only satisfied if

$$f = \left(\frac{l}{Sc}\right)' \approx 0. \tag{4.51}$$

The assumption that the gradient $\left(\frac{l}{Sc}\right)' \approx 0$ at the inflection point was found to be valid through a numerical parameter study. This will change if the injected and freestream gases have significantly different molar masses - an increase in complexity that will be considered in section 4.4.3. Note that from the definition of f (Eq. (4.19)), the position of the inflection point coincides with the distance from the wall, at which the velocity, v changes from being positive (flow moving away from the wall) to negative (flow moving towards the wall). In other words, the concentration layer thickness coincides with the distance away from the wall at which the injected momentum and the freestream momentum balance each other out. In order to find that position it is necessary to derive an expression for f. In Fig. 4.8 one can see that the velocity profile between the wall and the inflection point is approximately linear. Thus, f, which is required to solve Eq. (4.51), can be approximated as

$$f(\eta) = \int_0^\eta f' d\eta = \int_0^\eta f''_w \eta d\eta = f''_w \frac{\eta^2}{2} + f_w. \tag{4.52}$$

It remains to find an expression for the velocity gradient, f''_w, at the wall. After applying the no-slip condition, Eq. (4.11) at the wall reduces to

$$f''_w = -\frac{\left(0.5\delta_w + l f'''_w\right)}{\left(f_w + l'_w\right)} \approx -\frac{\delta_w}{2f_w}, \tag{4.53}$$

noting that $l f'''_w \ll 0.5\delta_w$ and $l'_w \ll f_w$. Finally, the position of the inflection point is obtained by finding the root of f. Combining Eqs. (4.52) and (4.53) one obtains

$$f(\eta) = -\frac{\delta_w}{2f_w}\frac{\eta^2}{2} + f_w = 0 \tag{4.54}$$

and thus for the root:

$$\eta_{c''=0} = \sqrt{\frac{-2f_w}{f''_w}} = \sqrt{\frac{2}{\rho_e \mu_e \frac{du_e}{dx} \delta_w}} \dot{m}. \tag{4.55}$$

The effective film thickness then becomes

$$\Delta = \eta_{c''=0} = \sqrt{\frac{2}{\rho_e \mu_e \frac{du_e}{dx} \delta_w}} \dot{m}. \tag{4.56}$$

Following the assumption made in this work, that the blowing parameter is proportional to Δ, the results were plotted against $B_{m,2} = 1.29\Delta$ in Fig. 4.9. In fact, it is found that cases with different freestream pressures and nose radii all collapse onto the same line when plotted against $B_{m,2} = 1.29\Delta$, confirming this analytical relationship (Eq. (4.49)). Using the definition of Δ (Eq. (4.56)) and St_{m0} (Eq. (4.40)), one can also express $B_{m,2}$ as follows:

$$\lambda_2 = 1.625 \left(\frac{\mu_e}{\mu_w} \right)^{0.5} \frac{\rho_e}{\rho_w} \tag{4.57}$$

$$B_{m,2} = \lambda_2 B_m = \lambda_2 \frac{F}{St_{m0}}. \tag{4.58}$$

Using thin film theory, it was thus possible to derive the scaling factor for B_m that is required to obtain a good fit. The aim of the next part is to refine Eq. (4.57). The factor of 1.625 is unique to the cases considered in Figs. 4.6 and 4.9. Currently, it must be obtained numerically each time one of the input parameters, such as T_w, is changed. It is much more desirable to have an analytical expression of T_w and all other relevant quantities, $Fn(T_w, ...)$, which covers the full parameter space and provides the K_m ratio for every flight scenario. Equation (4.49) suggests that an analytical correlation for the mass transfer rate B_m is a function of the Schmidt number, the Chapman-Rubesin factor and the blowing parameter:

$$B_m = \Delta \times Fn(Sc, l, f). \tag{4.59}$$

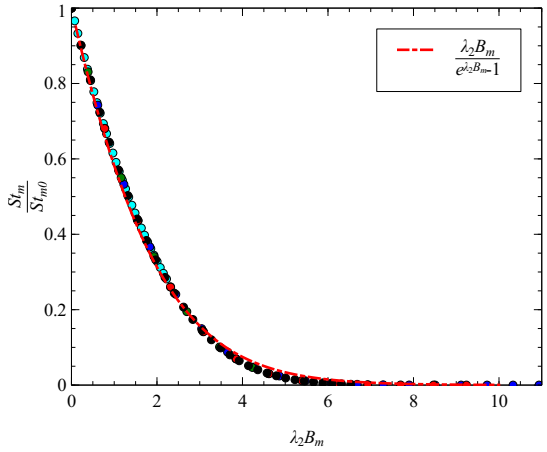

Figure 4.9: All cases from Fig. 4.6 plotted against $B_{m,2}$.

4.4.1 Schmidt number scaling

The dependence on Sc, l and f is found by gradually increasing the complexity of the considered cases. The most simple case is air injection into an air freestream with constant temperature throughout the boundary layer. Thus, $l = \frac{\rho\mu}{\rho_e\mu_e}$ is constant. By comparing cases with constant f, λ_3 is now merely a function of Schmidt number if Eq. (4.59) holds true. Figure 4.10 depicts the numerically obtained mass fraction of external gas at the wall against the previously derived $B_{m,2} = \lambda_2 B_m$. In addition, it compares it to the surface concentration computed by Eq. (4.45). It is apparent that all data points collapse if stretched by a factor $\lambda_3 = \lambda_2 \times Fn(Sc)$. More specifically, this factor is found to be $2Sc_w^{0.6}$, as illustrated in Fig. 4.11. The Schmidt number describes the ratio of momentum diffusivity, characterized by the dynamic viscosity $\frac{\mu}{\rho}$, to mass diffusivity, linked to the diffusion coefficient, D. Particles with low Sc are very volatile, having a high mass diffusivity and low viscous forces holding them back. It is intuitive that for the same effective film thickness, Δ, coolants with low Sc provide a weaker barrier against mass transfer from the external flow to the surface. Thus the factor $\lambda_3 = \lambda_2 \times 2Sc_w^{0.6}$ does not only provide an excellent fit, but can also be explained physically. It is important to point out that a slight mismatch persists, because λ_3 is not derived fully analytically anymore, but semi-empirically

Table 4.4: Legend of cases considered in Figs. 4.10 and 4.11.

#	Inj	Ext	T_w/K	T_e/K	Sc_w
1	Air	Air	300	300	0.774
2	Ar	Ar	300	300	0.765
3	CO_2	CO_2	300	300	0.432
4	He	He	300	300	0.745
5	Ne	Ne	300	300	0.761
6	Xe	Xe	300	300	0.754
7	N_2	Air	2000	2000	0.768
8	N_2	Air	4000	4000	0.776
9	N_2	Air	6000	6000	0.907
10	N_2	Air	8000	8000	1.381
11	N_2	Air	10000	10000	1.446
12	N_2	Air	12000	12000	1.348

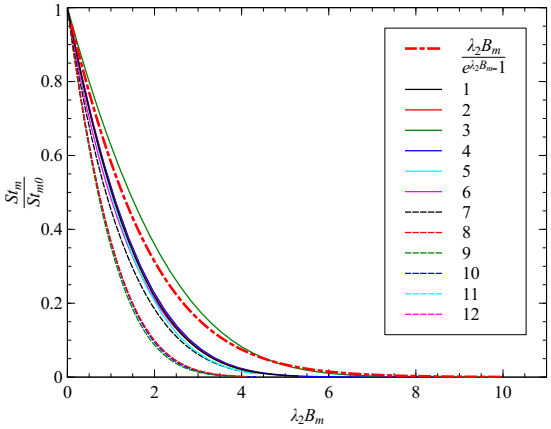

Figure 4.10: Mass fraction of external gas at the wall for cases with varying Schmidt numbers, plotted against $B_{m,2}$. A legend is provided in Table 4.4.

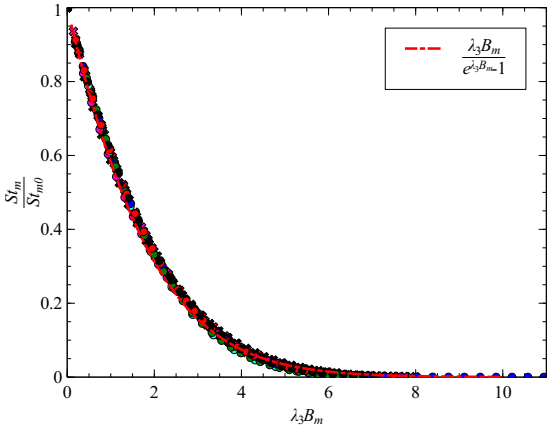

Figure 4.11: Cases shown in Fig. 4.10, plotted against $B_{m,3}$.

instead. A heat-mass transfer analogy is found in Eq. (23) of Ref. [104], where the heat transfer is found to scale with $Pr^{0.6}$.

4.4.2 Temperature scaling

The next increment in complexity consists of allowing temperature differences in the boundary layer. Figure 4.12 shows various numerical results plotted against $B_{m,3} = \lambda_3 B_m$. It is apparent that the ratio of boundary layer edge temperature to

Table 4.5: Legend of cases considered in Figs. 4.12 and 4.13.

#	Inj	Ext	T_w/K	T_e/K
1	N_2	Air	300	537
2	N_2	Air	300	2000
3	CO_2	CO_2	300	2000
4	N_2	Air	300	3000
5	N_2	Air	1428	6180

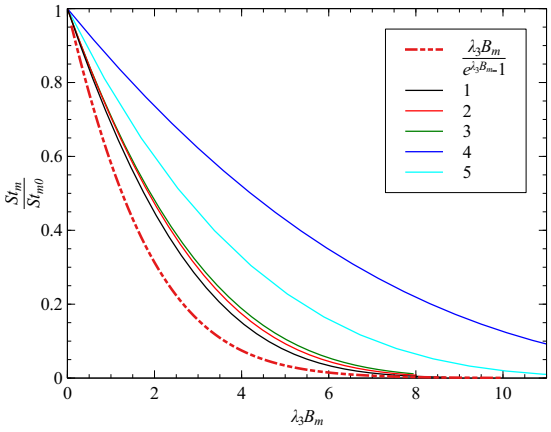

Figure 4.12: Mass fraction of external gas at the wall for cases with varying wall and boundary layer edge temperatures, plotted against $B_{m,3}$. A legend is provided in Table 4.5.

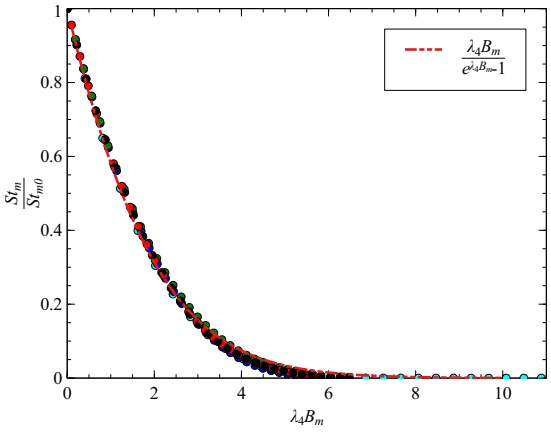

Figure 4.13: Cases shown in Fig. 4.12, plotted against $B_{m,4}$.

wall temperature has an effect on the results. More specifically, Fig. 4.13 shows that the data collapses if B_m is stretched by the scaling factor $\lambda_4 = \lambda_3 \times \sqrt{\frac{T_w}{T_e}}$, thus

$$\lambda_4 = \left(\frac{\mu_e T_w}{\mu_w T_e}\right)^{0.5} Sc_w^{0.6} 2.52 \frac{\rho_e}{\rho_w} \tag{4.60}$$

$$B_{m,4} = \lambda_4 B_m \tag{4.61}$$

4.4.3 Foreign gas injection

Note that even though nitrogen and air dissociate at slightly different temperatures, the difference is minor enough to consider them to be the same gas and thus use λ_4 (Eq. (4.60)) even beyond 2500 K. If the injected and freestream gases are very

dissimilar, for instance in a helium cooled stagnation point in a CO_2 freestream, the above theory does not hold. First of all, the assumption made in Eq. (4.51) becomes invalid, because the gas property gradients affecting l' and Sc' are too large. Secondly, the concentration profile such as the one shown in Fig. 4.8 becomes skewed. In other words, the inflection point ceases to correlate with the area under the curve. However, combining the following qualitative arguments with numerical observations, it was possible to amend the mass transfer parameter, to provide accurate results even for very dissimilar gases. Considering the hypothetical case of helium injection into a CO_2 freestream, encountered for instance during a Mars descent, the first step would be to obtain the effective film thickness assuming the coolant to equal the freestream gas, in this case CO_2. A qualitative argument can be made about the performance of other coolants relative to CO_2. A coolant with a higher mass diffusivity is more volatile and will diffuse into the freestream more quickly, thus providing less protection to the surface. However, this is not the full picture. Since gases are compared for a constant mass injection $\dot{m}$ at the wall, the quantity of interest should not be just the diffusivity, but the diffusive mass transfer, in other words how much mass per second diffuses into the freestream. A good approximation is given by multiplying the diffusivity by the density at the wall, ρD. Since the above qualitative argument is just relative to the freestream gas, in this case CO_2, the scaling factor for any other coolant must directly relate to it and is found to be in the form of a ratio:

$$\left(\frac{M_{\text{ext}} D_{\text{ext}-\text{ext}}}{M D_{\text{inj}-\text{ext}}}\right)_w, \tag{4.62}$$

noting that T_w and p_w will not be affected by the coolant gas change and thus $\left(\frac{\rho_{\text{ext}}}{\rho}\right)_w = \left(\frac{M_{\text{ext}}}{M}\right)_w$. In fact, Figs. 4.14 and 4.15 show how cases ranging from 300 - 6180K, various pressures, stagnation point radii and eight different gases all collapse if the following final scaling factor is applied:

Table 4.6: Legend of cases considered in Figs. 4.14 and 4.15.

#	Inj	Ext	T_e/K	T_w/K	p_e/kPa	R/mm
1	Kr	Air	1790	1000	5	100
2	Ar	Air	1790	1000	5	100
3	Ar	Air	6180	1428	3.2	25
4	He	Air	6180	1428	11.9	25
5	N_2	CO_2	2000	1000	11.9	25
6	Ne	Ne	300	300	11.9	25
7	Xe	Xe	300	300	11.9	25
8	N_2	Air	1800	1000	100	1000
9	N_2	Air	3000	1000	200	1000

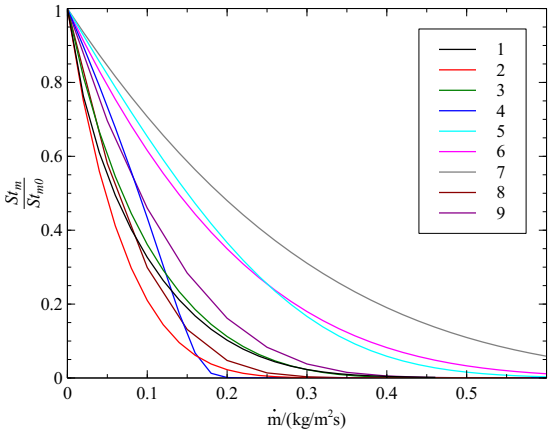

Figure 4.14: Cases described in Table 4.6 plotted against the mass flow rate at the wall.

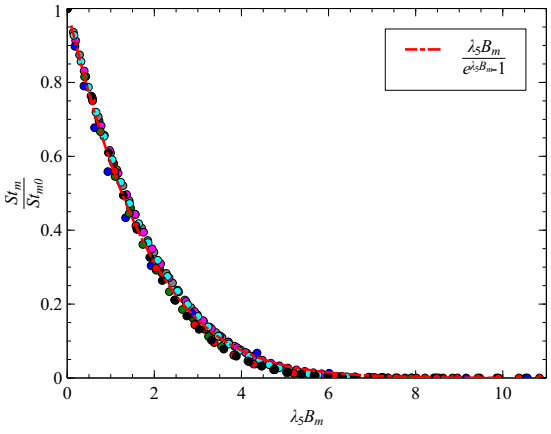

Figure 4.15: Cases described in Table 4.6 plotted against the blowing parameter presented in this paper.

$$\lambda_5 = \lambda_4 \times \left(\frac{M_{\text{ext}} D_{\text{ext-ext}}}{M D_{\text{inj-ext}}} \right)_w^{0.75} \tag{4.63}$$

$$B_{m,5} = \lambda_5 B_m \tag{4.64}$$

$$1 - c_w = \frac{B_{m,5}}{e^{B_{m,5}} - 1} \tag{4.65}$$

where inj and ext denote the injected and external gas type. Note that $M_w = Fn(c_w)$, thus making the expression implicit. However, the solution is unique and converges. Generally two or three iterations are sufficient to be within 0.5% of the fully converged result for very dissimilar gases. One starts with an initial

guess for c_w and then applies Eq. (4.63) and Eq. (4.65) in alternation to update $B_{m,5}$ and c_w, respectively. Alternatively, using the definitions of F and St_0, $B_{m,5}$ can be expressed as follows:

$$B_{m,5} = \sqrt{\frac{8}{\rho_e \mu_e \frac{du_e}{dx}}} Sc_{w;\mathrm{ext}}^{0.6} \dot{m} \left(\frac{M_{\mathrm{ext}} D_{\mathrm{ext-ext}}}{M D_{\mathrm{inj-ext}}} \right)_w^{0.75}. \tag{4.66}$$

This formulation combines the effects of boundary layer edge pressure and temperature, nose radius, wall temperature, freestream species Schmidt number, injected mass flow rate, as well as foreign gas injection.

4.5 Discussion

Analogous to the blowing parameter with respect to heat transfer B_h, B_m can now be used for flight to ground scaling. Similar to Kolesnikov's [105] Local Heat Transfer Simulation, used to replicate in-flight heat fluxes in ground facilities, this work presents the concept of Local Surface Concentration Simulation. The wall concentration of external flow or equivalently the ratio of mass Stanton numbers, will be the same as long as the B_m parameter is matched. In an air freestream which is in thermal and chemical equilibrium, B_m is only a function of p_e, T_e, $\frac{du_e}{dx}$, T_w, $\dot{m}$ as well as the two coolant properties M_{inj} and $D_{\mathrm{inj-ext}}$. Inspection of Eq. (4.66) further reveals that the best foreign gas is the one with the smallest $MD_{\mathrm{inj-ext}}$ term and not just M as suggested by Eq. (4.3). Best protection, for a given $\dot{m}$, is thus provided by a light gas with low mass diffusivity. Helium has a relatively high diffusivity and is thus sometimes outperformed by nitrogen. Note, however, that a boundary layer with large amounts of helium injection ceases to be self-similar and thus the correlation presented in this paper cannot be used. This is also true for other extremely light gases, such as hydrogen. This is because the $\frac{u_e^2}{h_e} \ll 1$ assumption becomes inaccurate. In the full self-similar solutions, $\frac{u_e^2}{h_e}$ is multiplied with $\frac{\rho_e}{\rho}$ and f''^2, both of which become so large for very light gases, that the product cannot be neglected anymore. However, if $u_e = \frac{\partial u_e}{\partial x} x$ is kept, the solution would depend on x and thus cannot be solved in a self-similar way. The discrepancies were limited to

hydrogen and moderate to large amounts of helium blowing. Boundary layers with injection of heavier gases, such as neon, into air, were all found to be self-similar.

An uncertainty analysis for the representative set of cases considered in this paper (Tables 4.4 to 4.6) showed an error of ±4% or ±1.5 percentage points, whichever is greater. The method presented in this work can be used with any freestream gas and for high-temperature cases, as long as the self-similar assumptions listed in section 4.3.1 are met. This marks a significant improvement to previous works [94]. Furthermore, it is derived semi-analytically and explicitly reveals the effect of all parameters involved. This makes it a practical tool for early design decisions, such as choosing the blowing rate for a transpiration cooled wall or the flight trajectory of an ablative heat shield. This analytical approximation is also useful for existing oxidation models, such as the one in Ref. [10] for ZrB_2 at 1273 - 2073K. The chemical rate of reaction is an essential parameter of the model and is directly dependent on the oxygen concentration at the wall. The correlation presented in this paper is also helpful to speed up convergence of high-fidelity numerical simulations by providing an estimate of the surface concentration for a given injection rate. Currently the surface concentration is computed by balancing the advective and diffusive flux (employing Eq. (4.25)), which requires many expensive iterations. The modelling used in this paper and matching CFD assumes that the flow is in thermochemical equilibrium. However, some non-equilibrium conditions were chosen deliberately in Table 4 (#8-12), Table 5 (#5) and Table 6 (#3,4). The aim of expanding the range outside of where the equilibrium assumption would hold was to ensure the data still collapsed. Non-equilibrium effects will be explored in future studies.

4.6 Conclusion

This paper presents a tool for the design of hypersonic stagnation points with mass injection. It assumes flow in thermochemical equilibrium and can be used with any freestream gas and for high-temperature cases, as long as the self-similar assumptions listed in section 4.3.1 are met. Note that boundary layers with hydrogen and helium injection were often found to not be self-similar and can thus not be modeled reliably

with this correlation. However, the discrepancy was limited to these two coolants and did not persist for heavier gases, such as Neon. The main advantage of this semi-analytically derived method over numerical solvers is that it explicitly reveals the effect of each component in the parameter space. It was validated against the numerically obtained self-similar solutions and featured an error of ± 4 percent or ± 1.5 percentage points, whichever is greater. However, similar to the Fay-Riddell heat transfer prediction, it is not intended to provide perfect accuracy, but instead to aid early design decisions, such as the choice of coolant, the nose radius or the rate of mass injection. The method is also very useful for flight to ground scaling of surface concentrations and mass Stanton numbers. In addition, it can complement existing theoretical oxidation models, by providing a concentration value and thus the oxygen partial pressure for a real flight condition, which directly affects the chemical rate of reaction. Furthermore, it can be employed to provide an initial c_w guess for numerical models to speed up convergence. Future tests are planned to validate this method experimentally in a hypersonic flow facility.

5

Experimental investigations of the hypersonic transpiration-cooled stagnation point

5.1 Foreword

In this chapter, the application of transpiration cooling on a hypersonic stagnation point is investigated experimentally. The aim was to study the performance in real life aerodynamic and thermodynamic conditions. As no available facility could replicate both simultaneously, the tests were split between the Oxford High Density tunnel and the IRS plasma wind tunnel.

In the Oxford High Density tunnel, the concentration of freestream species on a transpiration cooled stagnation probe is measured experimentally in a low enthalpy environment. This is achieved by employing the novel PSP diagnostic developed in Chapter 3. The results are compared to the semi-analytical correlation derived in Chapter 4. This work was accepted at *AIAA Journal of Spacecraft and Rockets* [18]. It is presented in this chapter with small layout changes, but unaltered content. The contributions of each author are summarised in the following:

- Marc Ewenz Rocher: Conceptualisation, methodology, investigation, analysis, writing

- Tobias Hermann, Matthew McGilvray: Supervision
- Madeleine Grossman, Luc Vandeperre: Manufacture of porous alumina samples

In the plasma wind tunnel at IRS, the oxidation behaviour of transpiration cooled ZrB_2 was experimentally investigated for the first time. The goal of these proof-of-concept experiments was to show that transpiration cooling can mitigate oxidation in a high-enthalpy environment. This work is only briefly discussed due to the qualitative nature of the results. More details on the experiment is provided in Appendix C, which is a duplicate of the AIAA Scitech conference paper [19].

5.2 Introduction

Hypersonic flight incurs high heat fluxes requiring a thermal protection system (TPS) to protect the crew and payload. Stagnation points, leading edges on slender bodies and scramjet intakes have extreme heat fluxes and heat loads due to their small radii, which are designed to minimize aerodynamic drag. This results in elevated surface temperatures over the duration of the flight path. Thermally and chemically protecting these key vehicle components is crucial to extending the flight envelope.

The most common TPS is an ablative, as used in many hypervelocity re-entry vehicles, such as the Hayabusa capsule [106]. Transpiration cooling is a potential shape-stable TPS in which a coolant is fed through a porous wall, forming a protective film upon exiting [13]. Although both technologies eject gas, pyrolisis products and a coolant, respectively, their performance is limited by oxidation and surface recombination. This is because oxygen, both molecular and atomic, diffuses to the material, degrading [19] and heating [41] the surface, respectively. Charred ablative surfaces recess due to oxidation and nitration [107], while transpiration cooling materials oxidize up to 2500 K below their melting temperature [52, 87, 88]. Predicting the oxidation behavior is vital to improve the performance of these protection systems.

Oxidation is driven by high temperatures, but also by the oxygen partial pressure at the surface [108]. Thus, the oxygen concentration at a stagnation point with mass injection needs to be predicted. This can be achieved numerically using the self-similar laminar boundary layer equations [93] or a full CFD solver. Alternatively it can be found using a semi-analytical correlation [17], which is reviewed in section 5.3.

These methods have not been validated experimentally due to the lack of data. This work aims to provide the first experimental measurements of oxygen concentration at a stagnation point with blowing. While oxidation is caused by atomic oxygen in some real-flight trajectories, the present study focuses on molecular oxygen diffusion only. This is due to the temperature limitations imposed by the experimental facilities and diagnostics. The concentration of molecular oxygen at the wall is measured directly using a novel pressure sensitive paint diagnostic [16] on a flat faced hemispherical probe in the Oxford High Density Tunnel. A range of freestream conditions, coolant gases and blowing ratios are explored and compared to the analytical solution described in the next section.

5.3 Analytical correlation

When modeling the mass transfer of freestream oxygen to the wall, it is desirable to non-dimensionalise the characteristic quantities. Ref. [17] showed analytically and numerically that the mass transfer reduction is related to the mass blowing parameter $B_m = \frac{F}{St_{m0}}$, which is the blowing ratio, normalised by the uncooled mass Stanton number. The blowing ratio denotes the ratio of coolant to freestream mass flux, $F = \frac{\rho_c u_c}{\rho_e u_e}$, while the uncooled Stanton number is defined as the uncooled mass transfer coefficient to the freestream velocity, $St_{m0} = \frac{K_{m0}}{u_e}$.

The mass Stanton number at the stagnation point in the absence of blowing was derived as [17]

$$St_{m0} = 0.89 \frac{\rho_e}{\rho_w} \frac{\mu_e}{\sqrt{\rho_w \mu_w}} \sqrt{\frac{du_e}{dx}} \frac{1}{u_e}, \tag{5.1}$$

where $\frac{du_e}{dx}$ is the velocity gradient at the boundary layer edge. The blowing parameter is related to the mass Stanton number ratio as follows:

$$\frac{St_m}{St_{m0}} = \frac{\lambda B_m}{e^{\lambda B_m} - 1}, \tag{5.2}$$

where λ is a weighting factor defined as

$$\lambda = \left(\frac{\mu_e T_w}{\mu_w T_e}\right)^{0.5} Sc_w^{0.6} 2.52 \frac{\rho_e}{\rho_w} \times \left(\frac{W_{\text{ext}} D_{\text{ext;ext}}}{W D_{\text{inj;ext}}}\right)_w^{0.75}. \tag{5.3}$$

The reduction in the ratio of mass Stanton numbers is directly related to the mass fraction of coolant at the wall, $x_{c,w}$:

$$\frac{St_m}{St_{m0}} = 1 - x_{c,w}, \tag{5.4}$$

which can be obtained experimentally by the pressure sensitive paint diagnostic used in this work.

5.4 Experimental setup

The experiments were conducted on the stagnation probe model shown in Figure 5.1, featuring a 25 mm radius hemispherical probehead. The nose of the probehead was machined off creating a 21 mm diameter flat face with a 16 mm diameter hole in its center. A flat, 5mm thick porous sample is glued in centrally from the back using Deluxe Materials AD68 Speed Epoxy II, which also acts as sealant. Kapton tape kept the front and back surface clean and was stripped off after the epoxy had cured. Then, a pressure sensitive paint solution consisting of 0.1 mmol $\left[\mathrm{Ru}\left(\mathrm{dpp_3}\right)\right]^{2+}$ luminophores suspended in 200 ml Dichloromethane, was applied with an air brush. More details on the PSP and the application method can be found in [16]. The rest of the hemisphere was also spray painted with PSP, after being primed with an ISSI fast response porous underlayer. The PSP coated probehead can be seen in Fig 5.3. Note that the layer is so thin, that the orange hue of the luminophores is barely visible.

The alumina samples with 39% porosity were produced by the Centre for Advanced Structural Ceramics at Imperial College London and used in all tests. Materials typically used in transpiration cooling, such as UHTCs [88], C/C composites [90], stainless steel and bronze [49] do not bond PSP, creating the need for a representative material. Alumina particles with a diameter of 6.45 μm were sintered for 3 hours at 1700 °C. More details and images of the surface microstructure can be found in [16], where the same material is used. The geometry consisted of a 2 mm thick, 14 mm diameter disk on top of a 3 mm thick, 20 mm diameter disk. The sample was sintered in a mold with the correct diameters, but made slightly thicker and polished down afterwards. This allowed precise control over the thickness and opened the pores at the surface. A subsequent ultrasonic bath removed any dust and lose particles clogging the pores.

The pressure and temperature in the pressurized plenum behind the sample were measured by an XT-190M-35bara Kulite and an Omega 5TC-TT-KI-40-1M fast response thermocouple, respectively. The Kulite has an accuracy of ± 3.5 kPa and the thermocouple of ± 2.2 K or ± 0.75%, whichever is greater. A National Instruments PXIe-8135 controller equipped with a PXIe-6368 (2 MHz/channel) card recorded the pressure and temperature data at 200 kHz.

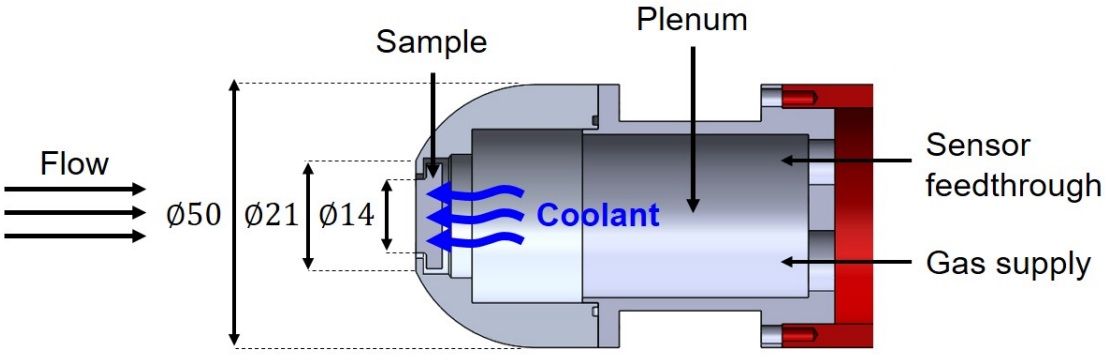

Figure 5.1: Annotated section view of the experimental model.

A schematic of the optical setup is shown in Fig. 5.2. A Luminus PT-120-B-L11-EPG with a dominant wavelength of 460 nm illuminated the PSP. The LED intensity varies with temperature, but an in-built thermistor was used to calibrate

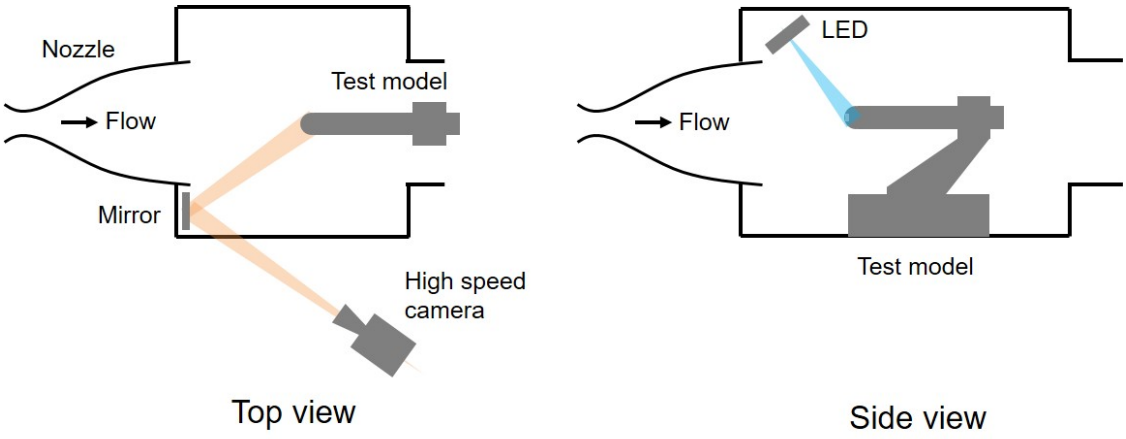

Figure 5.2: Schematic of the optical setup.

this effect and account for it in the post-processing step [16]. A mirror next to the nozzle exit reflects the luminescence of the sample into the Photron Fastcam Mini AX 200 900K high speed camera, which is equipped with a 550 nm long pass filter to block scattered blue light from the LED. The camera was operated at a 2000 Hz frame rate, 0.5 ms shutter speed, 512 x 512 pixel resolution and a bit depth of 12 bit. It was equipped with a Tamron SP AF 70-200mm F/2.8 Di LD (IF) macro telephoto zoom lens, enabling it to capture 256 x 256 pixels on the probehead and 50 x 50 pixels on the sample. For calibration of the PSP, the static pressure in the test section was measured by an Inficon Sky CDG025D 100 torr gauge with an accuracy of 0.2% of the reading.

The permeability of the sample was measured pre- and post-experiment according to the procedure detailed in [15]. As the plenum pressure increased from 0 to 20 bar, the mass flux was recorded by an Omega FMA5518A mass flow controller with an accuracy of ± 0.05 slpm. The Darcy and Forchheimer coefficients are K_D = 3.04 $\times 10^{-15}$ m^2 and K_F = 1.16 $\times 10^{-9}$ m, respectively.

The outflow distribution of the employed porous injector is characterized by hot-wire anemometry with air injection and no cross-flow. The air remained isothermal, at room temperature, throughout the sample. The measurements were taken by a Dantec Dynamics 55P11 hot wire with the following dimensions: 5 μm in diameter and 1.25 mm in length. More details on this technique can be found in [15]. The

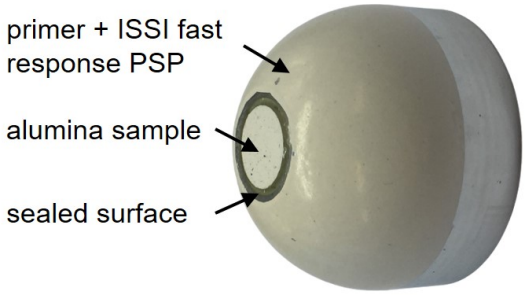

Figure 5.3: Post-campaign photograph of the porous alumina glued into the probehead.

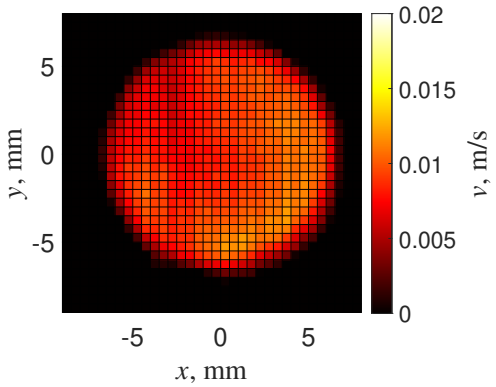

Figure 5.4: Velocity map of the sample at 4 bar differential pressure and no cross flow.

Table 5.1: Overview of test conditions.

Condition	Injectant	p_0 [kPa]	T_0 [K]	p_∞ [kPa]	T_∞ [K]	p_e [kPa]	T_e [K]	ρ_e [$\frac{kg}{m^3}$]	μ_e [Pa.s]	$St_{m0} \times 10^3$ [-]
1	N_2	612	436	0.162	41.7	10	436	0.08	2.32×10^{-5}	1.17
2	N_2	1224	436	0.324	41.7	20	436	0.16	2.32×10^{-5}	0.82
3	N_2	1836	436	0.486	41.7	30	436	0.24	2.32×10^{-5}	0.67
4	Ar	612	436	0.162	41.7	10	436	0.08	2.32×10^{-5}	1.17
5	Kr	612	436	0.162	41.7	10	436	0.08	2.32×10^{-5}	1.17

outflow is extremely uniform, between 0.008 - 0.012 m/s. Note that the outflow velocity is very similar to the bulk velocity at 4 bar differential pressure of 0.009 m/s, predicted by the Darcy-Forchheimer equation.

The experiments were conducted in the Oxford High Density Tunnel at Mach 6.9. More details on this facility can be found in [75]. A new feature developed prior to this experimental campaign is the use of pure nitrogen in the freestream. The stagnation temperature and Pitot pressures are summarised in Table 5.1. The injection parameters are shown in Table 5.2, while Tables 5.3 and 5.4 summarize the wall, freestream and diffusion parameters. Note that the velocity gradient for for a perfect hemisphere is given as $\frac{du_e}{dx} = \frac{1}{R}\sqrt{\frac{2(p_e - p_\infty)}{\rho_e}}$. The effective radius for the flat faced hemisphere used in this work is $R = 43.9$ mm and was obtained using CFD.

Table 5.2: Injection parameters.

Condition	Injected mass flux $[\frac{\text{kg}}{\text{m}^2\text{s}}]$	F [%]	λB_m [-]
1	0.017, 0.074, 0.197, 0.232, 0.310	0.143, 0.637, 1.658, 1.959, 2.623	0.281, 1.245, 3.315, 3.912, 5.229
2	0.107, 0.278, 0.445	0.443, 1.151, 1.847	1.275, 3.318, 5.310
3	0.135, 0.346, 0.546	0.374, 0.957, 1.507	1.319, 3.366, 5.313
4	0.014, 0.072, 0.226, 0.279, 0.371	0.120, 0.609, 1.914, 2.237, 3.138	0.226, 1.047, 3.061, 3.747, 4.957
5	0.009, 0.044, 0.094	0.076, 0.370, 0.801	0.123, 0.534, 1.080

Table 5.3: Wall and freestream parameters for all experiments.

T_w [K]	μ_w [Pa.s]	Sc_w [-]	M [-]	u_∞ $[\frac{\text{m}}{\text{s}}]$	$\frac{du_e}{dx}$ $[\frac{1}{\text{s}}]$
295	1.73×10^{-5}	0.7812	6.9	891	11300

5.5 PSP post-processing

The raw image recorded by the camera is depicted in Fig. 5.5. It shows the photon count per pixel, where the dark current has already been subtracted. Due to the 550 nm long pass filter only the PSP luminescence is captured. The frames are averaged over the steady-state test period. All frames are normalized by the reference intensity I_{ref} recorded just before starting the wind tunnel, with its corresponding reference pressure, p_{ref}. The normalized intensity signal $\frac{I_{\text{ref}}}{I}$ is then spatially averaged over the region of interest marked in red in Fig. 5.5. This provides further noise reduction and improves the signal quality.

5.5.1 Temperature effects

Pressure sensitive paint is also sensitive to temperature: $I = Fn\,(p, T)$. Thermal effects need to be removed from the PSP signal, before it is converted into pressure. For this purpose, every air freestream shot was coupled with a N_2 freestream shot. When an oxygen-deficient gas, such as N_2, Kr or Ar is injected into a N_2

Table 5.4: Molar mass and binary diffusion coefficients at $p_e = 10$ kPa.

W_{air} $[\frac{\text{g}}{\text{mol}}]$	W_{N_2} $[\frac{\text{g}}{\text{mol}}]$	W_{Ar} $[\frac{\text{g}}{\text{mol}}]$	W_{Kr} $[\frac{\text{g}}{\text{mol}}]$	$D_{\text{air;air}}$ $[\frac{\text{m}^2}{s}]$	$D_{\text{Ar;air}}$ $[\frac{\text{m}^2}{s}]$	$D_{\text{Kr;air}}$ $[\frac{\text{m}^2}{s}]$
28.97	28	40	83.8	2.02×10^{-4}	1.92×10^{-4}	1.51×10^{-4}

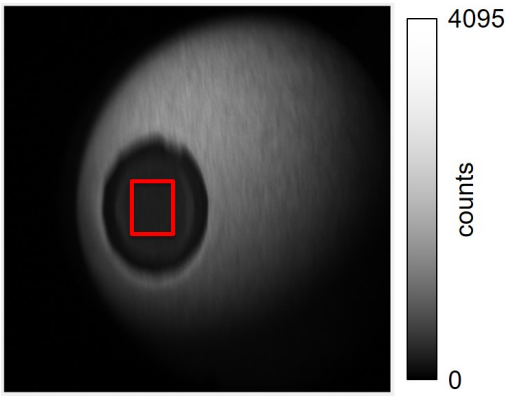

Figure 5.5: Raw image of PSP luminescence with region of interest marked in red.

crossflow, all changes in the PSP signal will be due to temperature effects only, $I = Fn\,(p_{\mathrm{ref}}, T)$. This thermal PSP trace, $\frac{I(p_{\mathrm{ref}},T)}{I(p_{\mathrm{ref}},T_{\mathrm{ref}})}$, is used to extract the pure pressure signal from the respective air freestream shots, assuming that the thermal properties of air and N_2 are similar. Even though the shots were recorded across 2 weeks, they exhibit a good repeatability. The pure pressure signal is extracted by normalizing the air-freestream data (second term on the RHS) by the respective nitrogen-freestream intensity (first term on the RHS):

$$\frac{I\,(p_{\mathrm{ref}}, T_{\mathrm{ref}})}{I\,(p, T_{\mathrm{ref}})} = \frac{I\,(p_{\mathrm{ref}}, T)}{I\,(p_{\mathrm{ref}}, T_{\mathrm{ref}})} \frac{I\,(p_{\mathrm{ref}}, T_{\mathrm{ref}})}{I\,(p, T)} \tag{5.5}$$

The pure pressure signal, $\frac{I(p_{\mathrm{ref}},T_{\mathrm{ref}})}{I(p,T_{\mathrm{ref}})}$, can be converted to pressure using a calibration curve, which is described in the following.

5.5.2 Obtaining the calibration curve

In theory PSP is described by the Stern-Volmer equation

$$\frac{I\,(p_{\mathrm{ref}}, T_{\mathrm{ref}})}{I\,(p, T_{\mathrm{ref}})} = A(T_{\mathrm{ref}}) + B(T_{\mathrm{ref}}) \left(\frac{p}{p_{\mathrm{ref}}} \right), \tag{5.6}$$

where A and B are the Stern-Volmer coefficients. However, in practice PSP behaves highly non-linearly and it is therefore more practical to express the relationship between intensity and pressure as:

$$p = C\left(\left(\frac{I\left(p_{\mathrm{ref}}, T_{\mathrm{ref}}\right)}{I\left(p, T_{\mathrm{ref}}\right)}\right)^{D} - 1\right) \tag{5.7}$$

where the fitting parameters C and D were obtained in-situ before the experiment at room temperature with no crossflow. The intensity is recorded from vacuum to atmospheric pressure. Each intensity measurement is plotted against the corresponding pressure reading. The fitting parameters are found to be $C = 7.383 \pm 0.040$ and $D = 3.728 \pm 0.011$. A new calibration curve was obtained every day to account for changes in room temperature and photodegradation. The oxygen partial pressure for every experiment was obtained by removing the temperature effects, using Eq. (5.5) and then applying Eq. (5.7).

5.6 Results and discussion

The aim of this experiment is to measure the coolant concentration on a transpiration cooled surface. The quantity measured by the PSP is the partial pressure of oxygen, p_{O_2}. Because the injected gases are oxygen-free, p_{O_2} is directly related to the partial pressure of freestream air, p_{air} via the mole fraction of O_2 in air:

$$p_{\mathrm{air}} = \frac{p_{O_2}}{y_{O_2;\mathrm{air}}}. \tag{5.8}$$

Due to the binary nature of the mixture, the coolant partial pressure is simply the difference between the boundary layer edge pressure and the air partial pressure, $p_c = p_e - p_{\mathrm{air}}$. The injection does not affect the pressure field at the stagnation point. Thus, the boundary layer edge pressure is the pressure measured by the PSP in the no-injection case, $p_e = p_{\mathrm{air;noinj}}$. The mole fraction of the coolant during injection thus becomes

$$p_c = p_{\mathrm{air;noinj}} - p_{\mathrm{air;fginj}} \tag{5.9}$$

$$y_c = 1 - \frac{p_{\mathrm{air;fginj}}}{p_{\mathrm{air;noinj}}} = 1 - \frac{p_{O_2;\mathrm{fginj}}}{p_{O_2;\mathrm{noinj}}}, \tag{5.10}$$

where the subscript fginj denotes foreign gas injection. The mass fraction of coolant is the product of its mole fraction and molar mass divided by the average molar mass:

$$x_c = \frac{y_c W_c}{y_c W_c + y_{\text{air}} W_{\text{air}}} \tag{5.11}$$

$$= \frac{y_c W_c}{y_c W_c + (1 - y_c) W_{\text{air}}}. \tag{5.12}$$

The coolant concentration is recovered by multiplying the mass fraction, by the density at the wall, $\rho_w = \frac{p_e}{RT_w}$. The pressure is known from the uncooled case and the molar mass required for the gas constant is a function of the known mass fraction. The fluid wall temperature is assumed to be equal to the solid wall temperature, which was calculated using the Porous Impulse Response Analysis for Transpiration cooling Evaluation (PIRATE) code [79]. It was found to rise by less than 5 K for the uncooled cases and less than 3K for the cooled cases. These values were used in the uncertainty analysis to quantify the error of ρ_w.

Figure 5.6 shows the mass fraction of air at the surface against the blowing ratio for all conditions. A trend can be observed, whereby increasing blowing ratios reduce the mass fraction of freestream air at the wall. As expected, the data points do not collapse, indicating that the blowing ratio alone is not sufficient to characterize the displacement of freestream gas at the surface. Furthermore there is no quantitative correlation relating the blowing ratio F to the air mass fraction.

Figure 5.7 presents the same data, but now plotted against the analytically obtained, scaled mass blowing parameter, λB_m. While the data generally follows the trend and is reasonably close to the analytical solution, a greater reduction in freestream mass transfer is seen than predicted by the theory. It is theorized that the reduced oxygen concentration compared to theory is due to the porous interface effect. When the PSP particles are spray painted onto the porous surface, they are evenly distributed across the irregular surface. This means that some fly inside the pores, as schematically depicted in Fig. 5.8. As the channels are small and the mass flux high, there still exists a pressure gradient during injection [16]. The theoretical and numerical results, which are represented by the black line in Fig. 5.7 only model

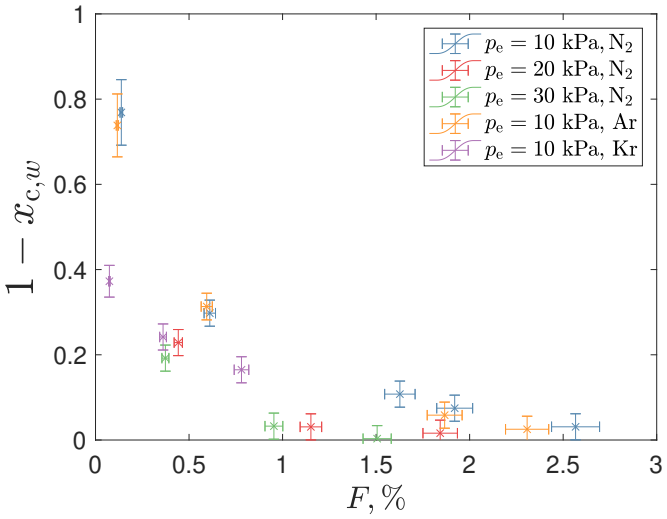

Figure 5.6: Mass fraction of air at the wall vs blowing ratio for all conditions.

the diffusion through the boundary layer up to the surface of the material, marked by the dotted line in Fig. 5.8. However, in the experiment, the oxygen molecules need to additionally overcome an adverse pressure gradient to reach the luminophores inside the pores. Numerical simulations usually assume a perfectly flat and homogeneous wall, neglecting this porous interface effect [93]. They will therefore produce a conservative estimate of the mass Stanton number reduction, which is useful for initial design work. Further investigation is required to understand whether the PSP distribution is uniform across the material surface and therefore whether their luminescence can be taken as the average luminescence of the interface. Since the calibration curve is linear up to about 10 kPa, this would yield the average O_2 partial pressure on the real, microheterogeneous boundary of the porous material.

The experimental data for conditions 2 and 3, illustrated in Fig. 5.7, shows an even larger discrepancy to the theoretical prediction than condition 1. The freestream pressure was doubled and tripled, while the mass flow rate was increased by 41% and 73%, respectively. According to the theoretical prediction and CFD simulations, this should yield the same $\frac{St_m}{St_{m0}}$ reduction as for condition 1. However, as the mass flux and therefore the pressure gradient across the material increases, the porous interface effect is accentuated and even less luminophores are reached by the freestream gas. The Argon data follows the same trend as the nitrogen

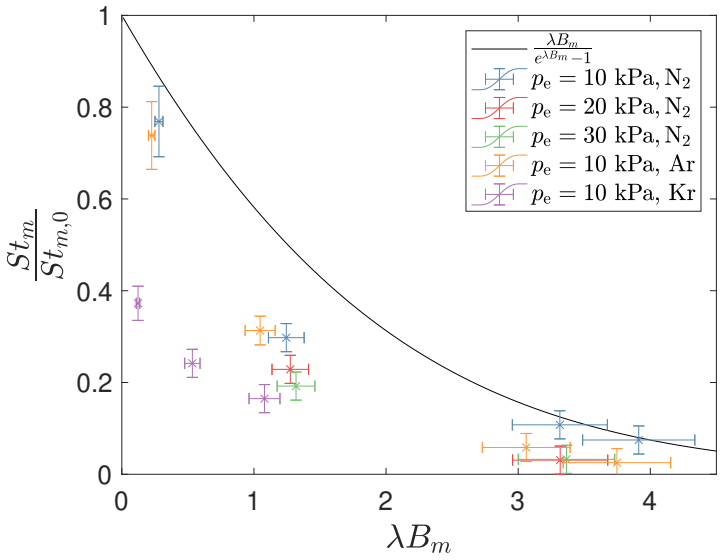

(a) Linear

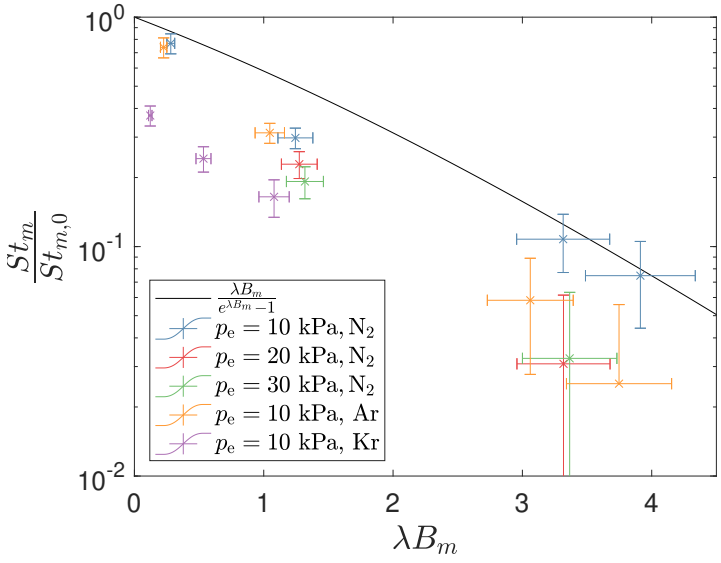

(a) Semi-logarithmic

Figure 5.7: Stanton number reduction vs blowing parameter for all conditions.

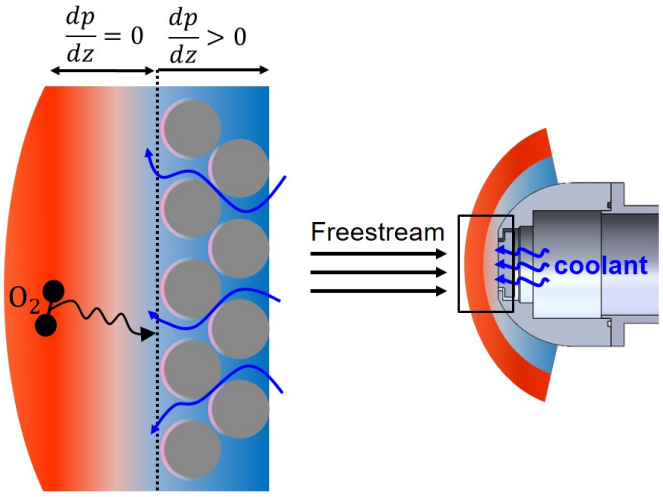

Figure 5.8: Schematic of the PSP distribution and pressure gradient on the porous interface.

results, while the Krypton results deviate from the theoretical prediction the most. Krypton appears to be much more effective in displacing oxygen than anticipated. An analytical model for the diffusion against a pressure gradient is needed to explain these observations.

5.6.1 Diffusion against a pressure gradient

The effect of a pressure gradient on the gaseous diffusion in porous media was first quantified in Ref. [109]. The analysis starts with the species continuity equation:

$$J_1 = -n\,(D_1)_{\text{eff}} \left(\frac{dy_1}{dz}\right) + y_1 J \delta_1 \tag{5.13}$$

where the first term describes diffusion and the second advection. The parameter $n = \frac{p}{\mathcal{R}T}$ is the mole density. $(D_1)_{\text{eff}}$ is an effective diffusion coefficient defined as

$$\frac{1}{(D_1)_{\text{eff}}} = \frac{1}{(D_{12})_{\text{eff}}} + \frac{1}{(D_{1\text{k}})} \tag{5.14}$$

where D_{1k} is the Knudsen diffusivity and D_{12} the binary diffusion coefficient. The subscript eff denotes the effective diffusion coefficient, which takes into account the tortuosity of the porous medium. For the small material depths studied in this work, it is assumed to be equal to the normal diffusion coefficient.

The factor δ_1 is zero for Knudsen diffusion and unity for normal diffusion and is defined as follows:

$$\frac{1}{\delta_1} = 1 + \frac{(D_{12})_{\text{eff}}}{D_{1k}} = \frac{(D_{12})_{\text{eff}}}{(D_1)_{\text{eff}}}, \tag{5.15}$$

where D_{1k} is the Knudsen diffusivity. The pores of the material used in this study were small enough for Knudsen diffusion to be significant. For $T_w = 295$ K, $p_e = 10$ kPa, a collision diameter for air of 3.617 Å and a pore diameter of 2 μm, the Knudsen number is 0.35. J denotes the bulk flow of molecules and is defined by the forced flow equation

$$J = \beta J_1 - \left(\frac{C_2}{kT}\right)\frac{dp}{dz} \tag{5.16}$$

where the first term represents the molecular slip and the second term accounts for a mole flux due to a pressure gradient across the porous material. In the absence of a pressure gradient, a bulk flow of molecules can still exist if the particles on either side of the porous medium have different molar masses. The lighter molecules diffuse quicker thereby creating a net flux towards the heavy molecules. The slip term $\beta = 1 - \sqrt{\frac{W_1}{W_2}}$ relates this molecular slip to the molar mass. The second term in Eq. (5.16) strongly resembles the Darcy term of the Darcy-Forchheimer equation [15]. In fact, it is the mole flux due to a pressure gradient which can be obtained from Table 5.2, dividing the mass flux by the average molar mass of molecules. Inserting Eq. (5.16) into Eq. (5.13) one obtains

$$J_1 = -nD_1\left(\frac{dy_1}{dz}\right) + y_1\left(\beta J_1 - \frac{\dot{m}}{\bar{W}}\right)\delta_1 \tag{5.17}$$

$$J_1\left(1 - \beta y_1 \delta_1\right) = -nD_1\left(\frac{dy_1}{dz}\right) - y_1\frac{\dot{m}}{\bar{W}}\delta_1 \tag{5.18}$$

Assuming that no air enters the plenum and thus that the diffusive and advective molar fluxes balance each other out throughout the porous medium, one can set the net molar flux J_1 to zero and obtains

$$nD_1\left(\frac{dy_1}{dz}\right) = -y_1\frac{\dot{m}}{\bar{W}}\delta_1 \tag{5.19}$$

$$nD_1\left(\frac{dy_1}{dz}\right) = -y_1\frac{\dot{m}}{\bar{W}}\frac{D_1}{D_{12}} \tag{5.20}$$

$$nD_{12}\left(\frac{dy_1}{dz}\right) = -y_1\frac{\dot{m}}{\bar{W}} \tag{5.21}$$

The term nD_{12} is constant throughout the porous material because the pressure terms in the molar density and the diffusivity cancel each other out. Thus, one can integrate the partial differential equation and use the known mole fraction of air at the surface to obtain

$$y_{\text{air}}(z) = y_{\text{air};w}e^{\frac{\mathcal{R}T_w}{p_e D_{\text{air;inj}}}\frac{\dot{m}}{\bar{W}}z} \tag{5.22}$$

In this calculation, it was assumed that the mole fraction of air at the surface, $y_{\text{air};w}$, was that predicted by the semi-analytical correlation derived in Chapter 4. It can be seen from Eq. (5.22) that for a constant wall temperature, the porous diffusion is only a function of the mass flow rate and the injectant parameters, which affect the average molar mass and the diffusion coefficient. Figure 5.9 (a) illustrates how an increase in mass flux causes a larger relative reduction in air mass fraction inside the pores. This can also be observed in Figure 5.7. The three data points with edge pressures of 10, 20 and 30 kPa at a λB_m of about 1.27 all have the same numerically predicted air mass fraction. However, due to increasing mass fluxes (Table 5.2) from the 10 kPa through to the 30 kPa case, lower mass fractions are expected (Eq. (5.22)), despite having the same λB_m.

The effect of injectant properties on the diffusion of air into the pores is less obvious. A heavier gas, such as Krypton will reduce the molar flux $\frac{\dot{m}}{\bar{W}}$ in Eq. (5.22) and this will lead to a higher mole fraction of air for a given mass flow rate. However, when taking into account the change in diffusion coefficient and the conversion from mole to mass fraction of air (Eq. (5.12)), Krypton is more effective at displacing freestream gas if the mass fraction of air at the surface is high. If the mass fraction

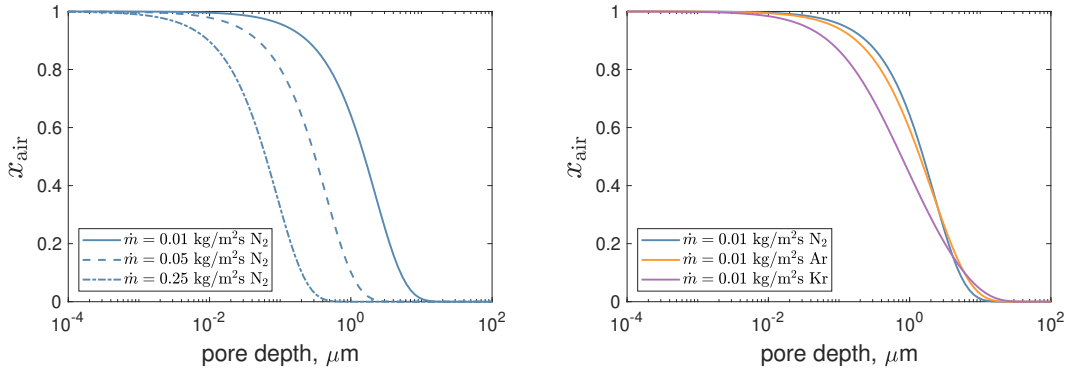

(a) Effect of mass flux (b) Effect of injectant

Figure 5.9: Diffusion of freestream gas into a pore with mass injection.

of air at the surface is low then the reduction in mole flux outweighs the conversion from mole to mass flux and Krypton becomes less effective. This effect is depicted in Fig. 5.9 (b). One can see in Fig. 5.7 that Krypton is much more effective than nitrogen at high mass fractions of air at the wall, corresponding to low λB_m values. Argon, however, has a similar effectiveness as nitrogen.

The effective depth is the distance to which the predicted oxygen which reaches the porous interface (dotted line in Fig. 8) has to diffuse into the pores to match the experiment.

The marker in Figure 5.10 (a) shows the effective depth for the low blowing case of condition 1. The relative error in the large blowing cases was too high to make a sensible calculation. Figure 5.10 (b) depicts the effective depth for all low blowing conditions. One can see that it is approximately 0.1 - 1 μm, which matches the order of the pore size of the porous medium of 2μm. It is stressed that the prediction of the effective pore depth is simply an approximation to understand whether this could be a physical effect and it should not be considered to be a quantitative model. The mass flux deeper inside the pores will be higher due to the area ratio and a detailed direct numerical simulation would be required to model this effect.

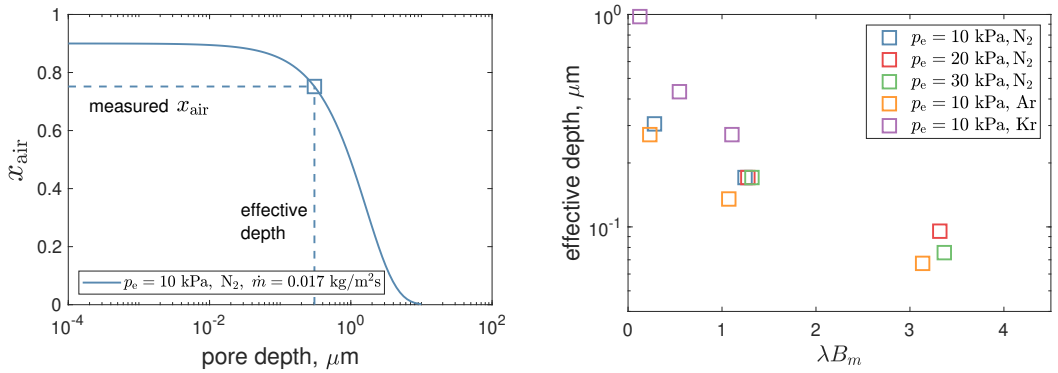

(a) Calculation of effective depth(b) Effective depth for all low blowing conditions

Figure 5.10: Effective depth of PSP molecules inside the pores.

5.7 Conclusion

The concentration of freestream species on a hypersonic stagnation point with mass injection was measured experimentally for the first time. The experimental data follows the theoretical trends well, but shows higher oxidation protection than predicted. This is because of the irregular porous surface. Numerical models assume that the porous surface is perfectly flat, but in reality it also has pores. The freestream air needs to overcome an adverse pressure gradient to reach the projected surface. This effect is not taken into account by the models, which is why they underpredict the oxygen protection provided by mass injection. The analytical models with a flat surface assumption will remain extremely useful for a conservative estimate of freestream gas at the surface. However, they could be improved in the future using the experimental data presented in this work to take into account the microheterogeneity of the porous surface.

5.8 Uncertainty analysis

The blowing parameter scales linearly with the mass flux, thus accurately measuring the mass flux is crucial. The permeability was measured twice, before and after the experimental campaign. The permeability decreased by 5% throughout the 3 week long test campaign. This could be due to a small leak in the experimental setup during the pre-campaign permeability measurement. Alternatively it may

have been caused by freestream debris blocking the pores. The black particles can clearly be seen in Fig. 5.3. A conservative error of ±5% was assumed in the results to account for these effects.

The second largest error source is the velocity gradient. The velocity gradient was assessed using CFD as the flat face did preclude the use of an analytical approximation for perfect hemispheres. The velocity gradient was found to be 11300 ± 300 1/s. The boundary layer edge pressure and temperature were given an error of ±0.4 kPa and ±5 K, respectively. This amounts to 4% for a boundary layer edge pressure of 10 kPa and 1.1% for a temperature of 436 K. The freestream mass flux is defined as:

$$\dot{m}_e = \rho_e v_e = \frac{p_e}{RT_e} M_e \sqrt{\gamma R T_e} = \frac{p_e}{\sqrt{RT_e}} M_e \sqrt{\gamma}, \tag{5.23}$$

Thus, taking into account the errors of the pressure and temperature, the combined uncertainty becomes

$$\delta \dot{m}_e = \sqrt{\left(\frac{\partial \dot{m}_e}{\partial p_e} \delta p_e\right)^2 + \left(\frac{\partial \dot{m}_e}{\partial T_e} \delta T_e\right)^2} \tag{5.24}$$

yielding a relative error $\frac{\delta \dot{m}_e}{\dot{m}_e}$ of 4.04%

The same method is applied to chain the individual uncertainties together for the blowing ratio, $F = fn\left(\dot{m}_{\text{inj}}, \dot{m}_e\right)$. This yields an error of 6.4 %.

The camera has three error sources: shot noise, dark current and readout noise. The shot noise can be quantified by adding the total number of photon counts required for each data point in Fig. 5.7. Each CCD sensor counts between 600 - 1200 photons, depending on the setting. The lower bound of 600 will be used as a conservative value. As the data is spatially averaged by 39 x 29 pixels and then time averaged across 80 frames, the total counts for one data point are 600 x 39 x 29 x 80 = 54,288,000. Thus the signal to noise ratio is $\sqrt{54,288,000} = 7368$ and the 95% confidence interval for each measurement ±0.027%. The dark current was found to introduce a standard deviation of 20 counts. This leads to a 95% confidence interval of $\frac{\pm 2 \times 20}{600} = \pm 6.7\%$ per pixel and 0.022% for 29 x 39 x 80 pixels.

A readout noise value of 41e- was provided by the manufacturer, which at a full well capacity of 16,000e- yields an error of approximately ±0.002%. Therefore, all camera error sources are deemed negligible.

The experiments were conducted in the span of two weeks. Daily calibrations were conducted as described in section 5.5.2 to account for photodegradation, ambient temperature, humidity, drifts in the optical setup and any other environmental factors that may have affected the PSP response. Eleven calibration curves were produced which for a given intensity ratio $\frac{I_{\text{ref}}}{I}$ output pressures with a spread of up to ±10%. The spread did not correlate with any of the above factors. Therefore a very conservative error of ± 10% on any PSP readings was applied in the post-processing. To further account for inaccuracies in the pressure gauge used for calibration, an error of ±300 Pa was applied for low pressure readings.

The error bars shown in Fig. 5.7 account for all errors mentioned in this section.

5.9 High enthalpy oxidation protection experiments

The first part of this chapter presented the low-enthalpy experiments conducted in the Oxford High Density tunnel. This facility replicated the aerodynamic conditions encountered by a hypersonic vehicle, but not the thermodynamic environment. It provided insights into the diffusion of freestream species against boundary layer mass injection, but the temperatures were too low to study oxidation itself. A facility that can generate the high-enthalpy environment encountered during hypersonic flight is the plasma wind tunnel at the University of Stuttgart. It is used to carry out experiments with transpiration cooled ZrB_2. The aim is to experimentally investigate its oxidation behaviour and to assess whether transpiration cooling can mitigate it. In the following, the experimental setup and key qualitative results are presented. The full report can be found in Appendix C.

5.9.1 Experimental setup

A 5 mm thick, 42% porous ZrB_2 sample forms the centrepiece of this experiment. It was housed by a hemispherical, water cooled copper head. To mitigate lateral heat conduction, the sample was surrounded by an insulation ring made out of solid ZrO_2. The stagnation probe is placed next to the exit nozzle of the plasma generator, which can produce a steady, supersonic, high-enthalpy freestream. The condition tested was a 3.95 MW/m^2 cold-wall, fully catalytic heat flux at 3.22 kPa Pitot pressure. More details about this facility can be found in Appendix C.

5.9.2 Results

Three ZrB_2 samples were tested in this facility. The first was uncooled and used to assess the oxidation behaviour without blowing. The second and third sample were cooled by 620.11 g/m^2 of nitrogen and 20.25 kg/m^2 of helium, respectively. All three samples were exposed to a 3.95 MW/m^2 cold-wall heat flux at 3.22 kPa Pitot pressure. Due to different amounts of blowing, their steady-state surface temperatures were different. The uncooled sample reached a temperature of 2150 K,

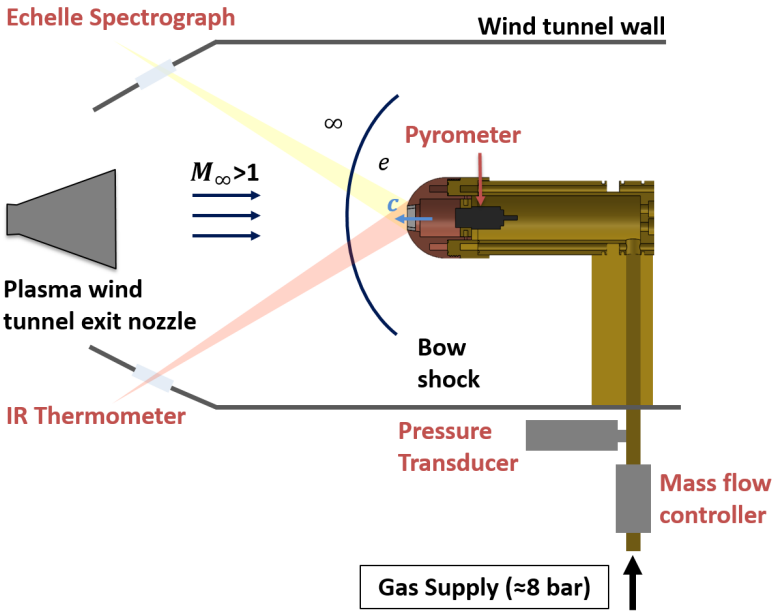

Figure 5.11: Sketch of experimental setup of the UHTC test in the plasma wind tunnel.

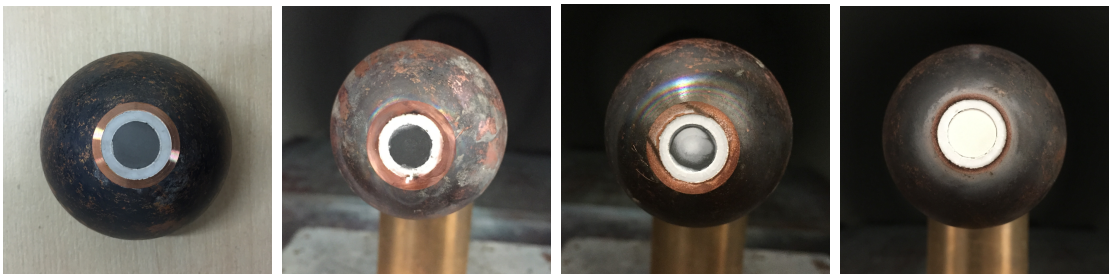

Figure 5.12: Untested virgin sample (left), post-test nitrogen cooled sample (center left), post-test helium cooled sample (center right) and post-test uncooled sample (right).

while the nitrogen and helium cooled samples experienced 1128 K and 1428 K. Figure 5.12 shows the probeheads before and after testing.

The uncooled sample can be seen on the right. As expected, it oxidised severely as is evident from the white oxide layer covering it. In contrast, the nitrogen sample shows no signs of oxidation, despite being heated to a temperature regime at which oxidation is expected. It has a dark grey colour, similar to that of the untested, virgin sample on the left. Note that the insulation ring of the helium sample cracked when the mass flux was lowered and the flow leaked through said cracks instead of transpiring the sample. With the loss of the protective coolant film, the sample surface started to oxidise. This first qualitative data shows that transpiration cooling can mitigate oxidation of ZrB_2, even though the question

remains how much of the protection was provided through cooling and how much through oxygen displacement.

Further analysis was conducted by sectioning the samples, SEM imaging and mass spectroscopy. The surface of the uncooled reference sample, which was not cooled during the exposures to the plasma, became white and as shown in Fig. 5.13 a crust has formed on top of the sample. Elemental analysis, as well as mass spectroscopy of the crust showed it consisted of oxygen and zirconium alone and hence can be identified as ZrO_2. In order to look beneath the surface and characterise the sample at different depths, the sample was cut. The cross-section confirms that an oxide layer of approximately 80 µm has formed, see Fig. 5.14, with a clear interface with the remaining ZrO_2 material. Consistent with the literature for oxidation of ZrB_2 above 1800°C [10], all boron had evaporated from the oxide scale.

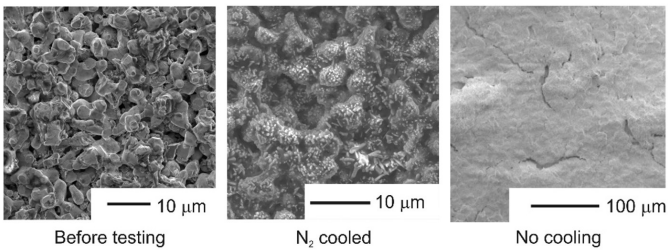

Figure 5.13: Surface microstructure before and after testing.

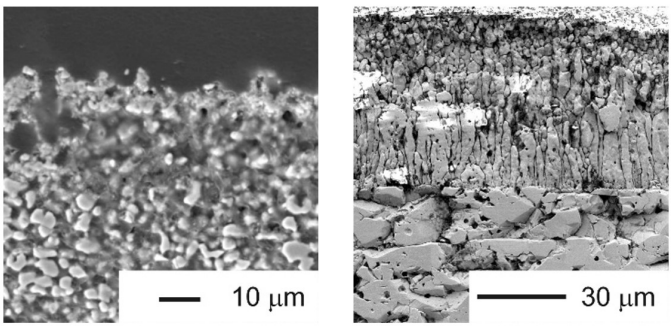

Figure 5.14: Cross-sections of cooled and uncooled sample.

The surface of the nitrogen cooled sample became darker during testing but showed no discoloration towards white. Fig. 5.13 also illustrates that this sample showed the smallest change in morphology from the untested material: the grains and pores are still clearly visible but some of the grains are now covered in small

crystals, which formed during the low blowing rates. Elemental analysis showed the presence of zirconium, oxygen, boron, carbon, magnesium and silicon. The silicon and magnesium again are attributed to re-deposition of the eroded adhesive on the sample surface. The cross section at the surface of the sample, shown in Fig. 5.14, also shows very little evidence of morphological changes apart from the epoxy infiltration of the pores, suggesting almost no oxidation has occurred in this case.

Whether oxidation was prevented solely by mitigating the diffusion of oxygen through to the surface or whether it was aided by mitigating catalytic heating in general, which reduced the surface temperature down to values at which the oxidation rate is low, remains to be investigated. The next test campaign will compare probes with different blowing parameters, but constant front surface temperatures to isolate these effects. Appendix D provides an overview of the design improvements and preparation work for this campaign.

6

Oxidation response of transpiration cooled zirconium-diboride on a hypersonic stagnation point

6.1 Foreword

The insights gained in the previous chapters, in particular the semi-analytical correlation, are combined with an existing oxidation model to study the performance of a hypersonic vehicle on a representative flight scenario. The aim is to predict the oxidation response of transpiration cooled ZrB_2 and thus the effectiveness of blowing in mitigating surface oxidation. This work has been submitted to *AIAA Journal of Spacecraft and Rockets* [20]. It is presented in this chapter with minor layout changes, but unaltered content. The author contributions are summarised in the following:

- Marc Ewenz Rocher: Conceptualisation, methodology, investigation, analysis, writing

- Tobias Hermann, Matthew McGilvray: Supervision

6.2 Introduction

Hypersonic flight is characterized by extreme aerodynamic heating. This results in elevated surface temperatures and chemical reactions, such as oxidation and nitration. The most exposed vehicle components are the stagnation points, both for blunt and slender vehicles [4]. As they generally pose the most stringent limit to the flight envelope, thermally and chemically protecting them is critical. For slender vehicles, an additional requirement for the leading edges is shape-stability, thereby excluding the use of ablatives. High melting temperature aerospace materials such as UHTCs [87–89] or C/C composites [52, 90] reduce the incident, hot wall corrected convective heat flux, while drastically increasing passive cooling through re-radiation. This passive cooling potential, however, remains untapped due to the early onset of oxidation at temperatures below 1000 K [10]. It is therefore highly desirable to mitigate the surface oxidation of hypersonic stagnation points.

Transpiration cooling is a potential means to reduce oxidation [19]. This active thermal protection system feeds a fluid through a porous wall, cooling it through internal convection. Upon exiting, the coolant forms a protective film that reduces part of the aerothermal heating [15] and catalytic heating [41]. Additionally, the film reduces the mole fraction of freestream oxygen at the surface [18].

Oxidation depends on both the temperature and oxygen partial pressure at the wall [10]. Thus, transpiration cooling has two mitigating effects on oxidation: it lowers the surface temperature and reduces the oxygen partial pressure by displacing the freestream oxygen with an oxygen-free injectant. In the existing literature, the oxidation response of a hypersonic stagnation point has only been investigated experimentally for no blowing [110]. The oxidation protection provided to any material by transpiration cooling has not been dealt with, despite its significance in enabling higher operating temperatures and thus extending the hypersonic flight envelope.

In this paper, the oxidation response of transpiration cooled ZrB_2 on a hypersonic stagnation point is modeled. This is achieved by combining three analytical models for heat transfer, oxygen concentration and the ZrB_2 oxidation response. The

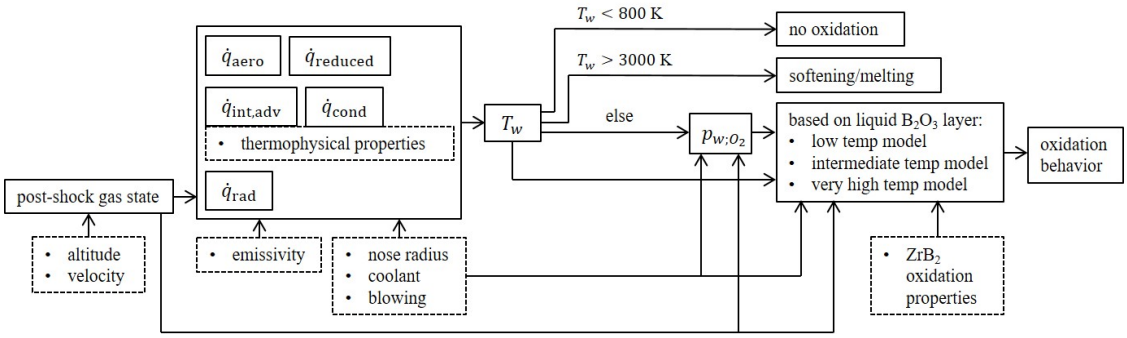

Figure 6.1: Flow chart of the numerical approach.

combined model is then applied to three increasingly complex test cases: A furnace with constant temperature and pressure and no transpiration cooling, a steady state flight path with blowing and a transient flight path with blowing.

6.3 Model overview

This section outlines the working principles and assumptions of the models used in this work. A schematic of the work flow is provided in Fig. 6.1. The analysis starts with an initial guess for the surface temperature, and by defining the trajectory of the vehicle. The resulting post-shock gas properties, together with the emissivity, nose radius, coolant type and amount of blowing, are fed into the heat transfer model.

By balancing the heat fluxes acting on the model, illustrated in Fig. 6.2, an updated surface temperature is found. This process is repeated until the temperature converges. Below 800 K, no oxidation will occur. The maximum operating temperature of ZrB_2, before it starts softening is assumed to be 3000 K, given that the melting point is at 3519 K. Within this range, the oxygen partial pressure at the surface is computed, before it is fed into the oxidation model. The oxidation kinetics of ZrB_2 depend on the thickness of the boria layer, as illustrated in Fig. 6.5. The appropriate oxidation model is chosen and outputs three oxidation parameters: the oxide scale thickness, the boria layer depth and the surface recession.

This is the first model predicting the oxidation behavior of transpiration cooled ZrB_2 on a hypersonic stagnation point. Due to the lack of existing literature, the following simplifying assumptions were made:

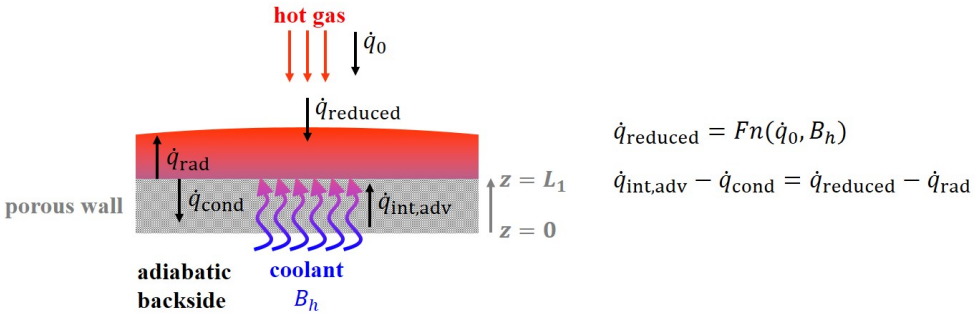

Figure 6.2: Heat balance on a 1-D stagnation point.

1. the flow is in thermochemical equilibrium.
2. atomic oxygen causes the same oxidation behavior as molecular oxygen.
3. the substrate porosity does not affect the oxidation rate.
4. mass injection does not change the aerodynamic radius.

In the following, the models are described more extensively.

6.3.1 Heat transfer model

It is possible to conduct a full CFD simulation for every condition along the flight trajectory. However, time and computational cost make this very impractical. Instead, the approach used here employs established correlations and simplified numerical models to compute the surface temperature of a transpiration cooled hypersonic stagnation point by balancing the heat fluxes on a 1-D porous wall with mass injection, as shown in Fig. 6.2. Note that due to the 1-D assumption, lateral heat fluxes were ignored. The backside of the porous material is assumed to be adiabatic, as the conductivity of the coolant is low and the radiated heat will mostly be reflected back by the sub-structure [111].

The convective aerodynamic heat transfer for a hypersonic stagnation point in the absence of mass injection is calculated by the Fay-Riddell [6] correlation:

$$\dot{q}_0 = 0.76 Pr_w^{-0.6} \left(\rho_w \mu_w\right)^{0.1} \left(\rho_e \mu_e\right)^{0.4} \left(1 + \left(Le^{0.52} - 1\right) \frac{h_D}{h_e}\right) \left(h_e - h_w\right) \sqrt{\frac{du_e}{dx}}, \quad (6.1)$$

where the Prandtl and Lewis number are assumed to be $Pr = 0.71$ and $Le = 1.4$, respectively. The heat flux reduction due to mass injection is commonly described using the non-dimensional heat blowing parameter

$$B_h = \frac{F}{St_{h0}} \tag{6.2}$$

where the blowing ratio, F, and uncooled Stanton number, St_{h0}, are defined as

$$F = \frac{\rho_{\text{inj}} u_{\text{inj}}}{\rho_\infty u_\infty} \tag{6.3}$$

$$St_{h0} = \frac{\dot{q}_0}{\rho_\infty u_\infty \left(h_e - h_w\right)}. \tag{6.4}$$

The heat flux reduction due to blowing is computed using the correlation presented in Ref. [14]

$$\frac{St_h}{St_{h0}} = \frac{\dot{q}_{\text{reduced}}}{\dot{q}_0} = \frac{1}{\sqrt{K}} \frac{e^{\frac{-1}{\pi} K B_h^2}}{1 + \text{erf}\left(\sqrt{\frac{1}{\pi}K}\right) B_h} \tag{6.5}$$

$$K = \frac{\Delta^*}{\Delta_0^*} \tau^{\frac{B_h}{B*}} \tag{6.6}$$

where $B*$ is defined as

$$B* = 1.59 \sqrt{\frac{M_{\text{inj}}}{M_\infty}} \tag{6.7}$$

Throughout this study, the chosen blowing parameters, B_h were smaller than the boundary layer blowoff parameter, $B*$. The shock stand-off ratio is calculated as follows:

$$\frac{\Delta^*}{\Delta_0^*} = 1 + \sqrt{\frac{\rho_s}{\rho_\infty} \frac{M_\infty}{M_{\text{inj}}}} St_{h,0} B_h \tag{6.8}$$

Finally, the empirical correction factor τ accounts for the molecular weight of the injected fluid as follows:

$$\tau = \sqrt{\frac{M_\infty}{M_{\text{inj}}}} N_f \tag{6.9}$$

Table 6.1: Parameters used in Fig. 6.3

M_∞	M_{inj}	St_{h0}	ρ_∞	ρ_s
[g/mol]	[g/mol]	[-]	[kg/m^3]	[kg/m^3]
28.97	28 (N_2) , 4 (He)	0.14	0.0022	0.0233

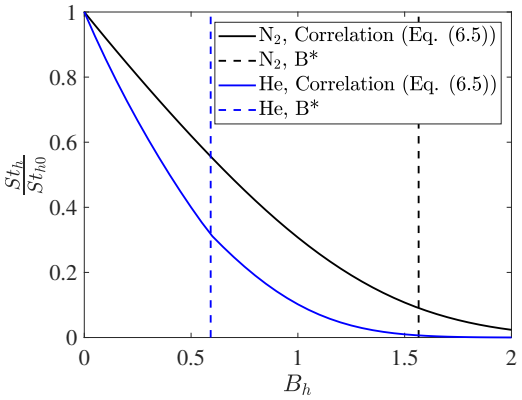

Figure 6.3: Stanton number reduction due to blowing, indicating blowoff parameter.

with $N_f = 5/9$ for monatomic and $N_f = 1$ for polyatomic gases. Figure 6.3 shows the relationship between the heat blowing parameter and the Stanton number reduction for the parameters in Table 6.1, encountered by a 3 mm nose radius at 44 km altitude and 3.6 km/s velocity, cooled by nitrogen and helium injection.

The wall temperature is obtained by balancing the reduced aerodynamic heat flux, $\dot{q}_{\text{reduced}}$, with re-radiation, $\dot{q}_{\text{rad}}$, internal advective cooling, $\dot{q}_{\text{int,adv}}$ and conduction $\dot{q}_{\text{cond}}$. This can be achieved by simultaneously solving the steady-state energy equations of the fluid and solid in the porous medium, given as

$$\underbrace{\rho_f u_f c_{p,f} \frac{dT_f}{dz}}_{\text{internal advection}} = \underbrace{h_v \left(T_s - T_f\right)}_{\text{fluid-solid heat exchange}} \tag{6.10}$$

$$\underbrace{k_s \left(1-\phi\right) \frac{dT_s^2}{dz^2}}_{\text{conduction}} = \underbrace{h_v \left(T_f - T_s\right)}_{\text{solid-fluid heat exchange}} \tag{6.11}$$

Eq. (6.10) balances the advective heat flux of the transpiring fluid with the fluid-solid heat exchange, while Eq. (6.11) equals the conductive heat flux through the solid with the solid-fluid heat exchange. These coupled ordinary differential equations

are solved analytically [112] and the following boundary conditions are applied:

$$T_f\big|_{z=0} = T_{\mathrm{pl}} \tag{6.12}$$

$$\left.\frac{dT_s}{dz}\right|_{z=0} = 0 \tag{6.13}$$

$$\tag{6.14}$$

where T_{pl} is the coolant temperature in the plenum and the second boundary condition denotes the adiabatic backside. The net incident heat flux is applied at the front surface:

$$k_s\,(1-\phi)\left.\frac{dT_s}{dz}\right|_{z=L_1} = \dot{q}_{\mathrm{reduced}} - \dot{q}_{\mathrm{rad}} \tag{6.15}$$

$$\tag{6.16}$$

where the radiative heat flux is obtained from the Stefan-Boltzmann law

$$\dot{q}_{\mathrm{rad}} = \varepsilon\sigma T_s^4\big|_{z=L_1}. \tag{6.17}$$

Note that $z = 0$ denotes the cooled side and $z = L_1$ the heated side.

6.3.2 Oxygen concentration model

The oxygen concentration on a hemispherical transpiration cooled hypersonic stagnation point can be obtained for any freestream condition, nose radius and injection parameters, using the correlation developed in Ref. [17]. It requires knowledge of the viscosity, density and velocity gradient at the boundary layer edge, as well as the Schmidt number and the mass flux at the wall, all of which are readily available. If the injected gas differs from the freestream gas, an additional correction for the molar mass and diffusion coefficient is required. The mass fraction of air at the wall is then found as follows:

$$c_{\mathrm{air},w} = \frac{St_m}{St_{m0}} = \frac{\lambda B_m}{e^{\lambda B_m} - 1} \tag{6.18}$$

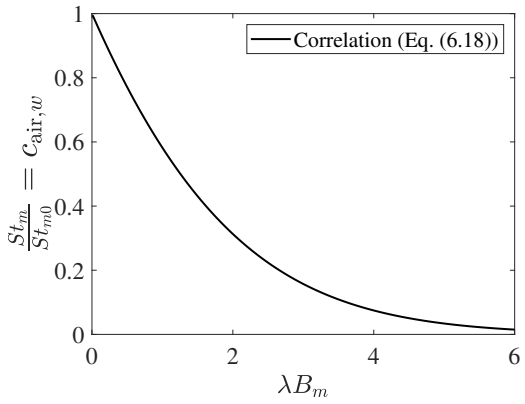

Figure 6.4: Relationship between the mass blowing parameter and the Stanton number ratio.

using the mass blowing parameter B_m with a scaling factor λ from Ref. [17], which are defined as follows:

$$B_m = \frac{F}{St_{m0}} \tag{6.19}$$

$$St_{m0} = 0.89 \frac{\rho_e}{\rho_w} \frac{\mu_e}{\sqrt{\rho_w \mu_w}} \sqrt{\frac{\partial u_e}{\partial x}} \frac{1}{u_e} \tag{6.20}$$

$$\lambda = \left(\frac{\mu_e T_w}{\mu_w T_e} \right)^{0.5} Sc_w^{0.6} 2.52 \frac{\rho_e}{\rho_w} \times \left(\frac{M_{\mathrm{ext}} D_{\mathrm{ext-ext}}}{M D_{\mathrm{inj-ext}}} \right)_w^{0.75} \tag{6.21}$$

All high temperature quantities, in particular the molar mass of dissociated air are obtained using the CEA-NASA code [100]. The diffusion coefficients are calculated using kinetic theory with the Lennard-Jones parameters [9]. Figure 6.4 visualizes the relationship between the scaled blowing parameter and the mass Stanton number ratio.

The oxygen partial pressure at the wall is found as follows:

$$y_{\mathrm{air},w} = \frac{c_{\mathrm{air},w}/M_{\mathrm{air}}}{c_{\mathrm{air},w}/M_{\mathrm{air}} + (1 - c_{\mathrm{air},w})/M_{\mathrm{inj}}} \tag{6.22}$$

$$y_{\mathrm{O}_2,w} = 0.21 y_{\mathrm{air},w} \tag{6.23}$$

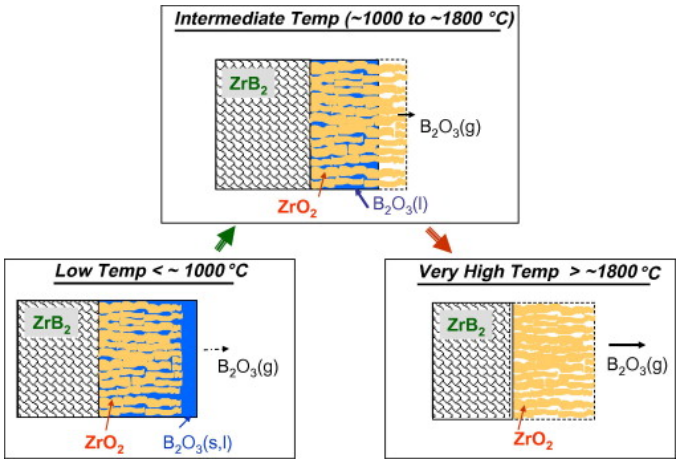

Figure 6.5: Oxidation regimes of ZrB_2. Figure taken from Ref. [10].

$$p_{O_2,w} = p_e y_{O_2,w} \tag{6.24}$$

The edge pressure, p_e is obtained from normal shock relations for a given freestream condition. Note that the pressure field around the stagnation point is not affected by injection when the blowing parameter is smaller than the boundary layer blowoff parameter, $B_h < B*$.

6.3.3 Oxidation model

The analytical oxidation model applied in this work was developed by Parthasarathy et al. [60]. When ZrB_2 oxidizes, it produces a porous ZrO_2 scale, as well as liquid or gaseous B_2O_3, depending on the temperature and oxygen pressure [10], as shown in Fig. 6.5. The analytical model quantifies the diffusion of oxygen through the oxide scale and the boria layer and assumes it to be the rate limiting step for oxidation activity at the substrate.

The model was developed for dense ZrB_2, but as no porous ZrB_2 oxidation model is available in the existing literature, it was deemed suitable for this initial study. Figure 6.6 shows the cross-section of a 42% porous ZrB_2 substrate, which was heated to 2150 K in a plasma wind tunnel [19]. The ZrO_2 scale has the same columnar microstructure as in Fig. 6.5. The 42% porosity of the substrate

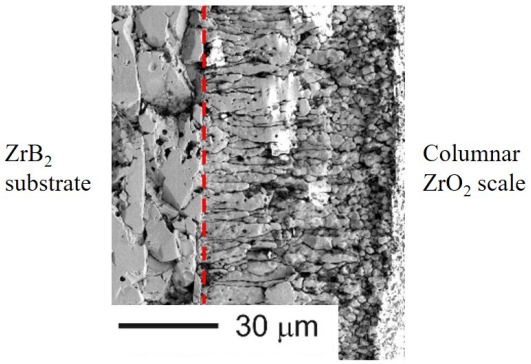

Figure 6.6: Cross-section of porous ZrB_2 after an exposure time of 60 seconds at 2150 K [19]

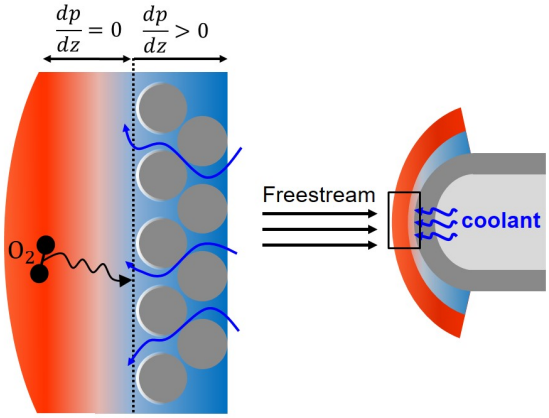

Figure 6.7: Schematic of oxidation of porous interface, adapted from Ref. [18].

therefore did not affect the oxidation microstructure, encouraging the use of the aforementioned oxidation model for porous substrates.

The model presented in this work only predicts the oxidation behavior on the surface of the porous interface, marked by the dotted line in Fig. 6.7, as the diffusion into a porous medium against a pressure gradient has not yet been modeled quantitatively in the existing literature. This diffusion is strongly dependent on the material microstructure. By not accounting for the adverse pressure gradient, the model will overpredict oxidation for the blowing cases [18]. It thus provides a conservative estimate of the oxidation protection provided by mass injection. The uncooled cases do not have a pressure gradient and are therefore not affected by this simplification.

In all temperature regimes shown in Fig. 6.5, the following reaction takes place at the ZrB_2 surface

$$ZrB_2 + \frac{5}{2}O_2 \longrightarrow ZrO_2 + B_2O_3 \tag{6.25}$$

If atomic oxygen is present, it is assumed that it recombines and behaves the same as molecular oxygen. Therefore, the rate of formation of zirconia, $\dot{n}_{ZrO_2}$, is proportional to the rate of oxygen diffusion to the substrate.

$$\dot{n}_{ZrO_2} = \frac{2}{5}|J_{O_2}| \tag{6.26}$$

Taking into account the porosity of the oxide scale, $f = 0.05$, the scale thickness growth is obtained as

$$\begin{aligned} \frac{dL}{dt} &= \left(\frac{M_{ZrO_2}}{\rho_{ZrO_2}}\right)\left(\frac{1}{1-f}\right)\dot{n}_{ZrO_2} \\ &= \left(\frac{M_{ZrO_2}}{\rho_{ZrO_2}}\right)\left(\frac{1}{1-f}\right)\frac{2}{5}|J_{O_2}| \end{aligned} \tag{6.27}$$

Following the numerical integration of Eq. (6.27), the magnitude of recession of the ZrB_2 substrate is given by

$$R = L\,(1-f)\,\frac{M_{ZrB_2}/\rho_{ZrB_2}}{M_{ZrO_2}/\rho_{ZrO_2}} \tag{6.28}$$

It remains to find the magnitude of oxygen diffusion through the ZrO_2 scale and the B_2O_3 layer to the ZrB_2 surface, $|J_{O_2}|$. The diffusion will be governed by a different mechanism for each of the three temperature regions of the oxidation model.

In the low temperature region, typically starting at around 600°C, the boria layer exceeds the thickness of the zirconia scale, as shown in Fig. 6.5. Oxygen must diffuse through the external boria layer and then through the pore channels up until the surface. In steady state, the oxygen flux through both regions must be equal, therefore

$$|J_{O_2}| = f\frac{\Pi_{O_2-B_2O_3}}{L}\left(P^{zb}_{O_2} - P^{s}_{O_2}\right) \tag{6.29}$$

$$= \frac{\Pi_{O_2-B_2O_3}}{h_{\text{ext}}}\left(P^{a}_{O_2} - P^{zb}_{O_2}\right) \tag{6.30}$$

where the temperature dependent correlations for $P^s_{O_2}$ and $\Pi_{O_2-B_2O_3}$ are provided by Eq. (10) and (12) of Ref. [10], respectively. The thickness of the external boria layer, h_{ext}, is found by balancing the rate of formation of liquid boria at the substrate, less that which resides in the porous scale and the rate of evaporation, using Eqs. (4) - (6) in Ref. [60]. Here, $P^a_{O_2}$ is the oxygen pressure at the ambient interface, which needs to be supplied by the oxidation model presented in section 6.3.2. The ambient interface is equivalent to the wall and thus $p^a_{O_2} = p_{O_2,w}$ can be obtained from Eq. (6.24). $P^{zb}_{O_2}$ is found by equating Eqs. (6.29) and (6.30). Eq. (6.29) is then inserted into Eq. (6.27) to find the scale thickness and consequently the recession using Eq. (6.28).

At temperatures exceeding about 1000°C, the external layer evaporates and only a fraction of the scale length is filled with boria. In this intermediate regime, gaseous oxygen must diffuse through the pore channels and then permeate through the liquid boria layer at the end of the channel to reach the surface and react with virgin ZrB_2. The rate of oxygen diffusion through the pores is given as

$$|J_{O_2}| = fD_{O_2}\frac{C^a_{O_2} - C^i_{O_2}}{L - h_{\text{int}}} \tag{6.31}$$

Here, $C^a_{O_2}$ is the concentration of oxygen at the scale-ambient interface, which needs to be supplied by the oxidation model presented in section 6.3.2. The concentration of molecular oxygen at the boria liquid-vapor interface, $C^i_{O_2}$ is obtained by balancing the diffusion of boria through the oxide scale, $|J_{B_2O_3}|$ with the formation of boria at the ZrB_2 interface, $\dot{n}_{B_2O_3}$. The formation of boria is linked to the diffusion of oxygen via Eq. (6.25).

$$\dot{n}_{B_2O_3} = |J_{B_2O_3}| = fD_{B_2O_3}\frac{C^i_{B_2O_3} - C^a_{B_2O_3}}{L - h_{\text{int}}} = \frac{2}{5}|J_{O_2}| \tag{6.32}$$

and thus,

$$C^i_{O_2} = C^a_{O_2} - \frac{5}{2}\frac{D_{\mathrm{B_2O_3}}}{D_{\mathrm{D_{O_2}}}}\left(C^i_{\mathrm{B_2O_3}} - C^a_{\mathrm{B_2O_3}}\right) \tag{6.33}$$

where $C^a_{\mathrm{B_2O_3}}$ is assumed to be zero and $C^i_{\mathrm{B_2O_3}}$ is found from a temperature dependent correlation [10]. The last unknown variable in Eq. (6.31) is the boria layer thickness, h. It is found by balancing the diffusion of oxygen through the liquid boria layer with its diffusion through the oxide scale.

$$|J_{\mathrm{O_2}}\,(\mathrm{B_2O_3})\,| = |J_{\mathrm{O_2}}| \tag{6.34}$$

$$f\Pi_{\mathrm{O_2-B_2O_3}}\frac{P^i_{\mathrm{O_2}} - P^s_{\mathrm{O_2}}}{h} = fD_{\mathrm{O_2}}\frac{C^a_{\mathrm{O_2}} - C^i_{\mathrm{O_2}}}{L - h_{\mathrm{int}}}. \tag{6.35}$$

where $\Pi_{\mathrm{O_2-B_2O_3}}$ and $P^s_{\mathrm{O_2}}$ are found from a correlations [10] and $P^i_{\mathrm{O_2}} = RTC^i_{\mathrm{O_2}}$. Inserting Eq. (6.31) into (6.27) yields the scale thickness.

At elevated temperatures, the boria layer will evaporate completely. The oxidation will be limited by the rate of diffusion through the porous ZrO_2 scale [60]. The flux of oxygen and boria, as well as the balance of fluxes is given by

$$|J_{O_2}| = fD_{O_2}\frac{C^a_{O_2} - C^s_{O_2}}{L} \tag{6.36}$$

$$|J_{\mathrm{B_2O_3}}| = fD_{\mathrm{B_2O_3}}\frac{C^a_{\mathrm{B_2O_3}} - C^s_{\mathrm{B_2O_3}}}{L} \tag{6.37}$$

$$|J_{O_2}| = \frac{5}{2}|J_{\mathrm{B_2O_3}}| \tag{6.38}$$

The boria concentration is assumed to be negligible at the ambient interface, $C^a_{\mathrm{B_2O_3}} = 0$, and can be related to the oxygen concentration at the substrate, $C^s_{\mathrm{B_2O_3}} = F(C^s_{O_2})$, using Eq. (9) in Ref. [60]. Combining Eqs. (6.36) - (6.38), $C^s_{O_2}$ is found and inserted into Eq. (6.36). Further increasing the temparature to about 2500°C leads to evaporation of the oxide layer, thereby accelerating oxidation and surface recession. Eq. (6.27) is amended to account for this as follows

$$\left(\frac{M_{\mathrm{ZrO_2}}}{\rho_{\mathrm{ZrO_2}}}\right)\left(\frac{1}{1-f}\right)\frac{2}{5}|J_{\mathrm{O_2}}| - J_{\mathrm{evap;ZrO_2}} \tag{6.39}$$

where $J_{\mathrm{evap;ZrO_2}}$ is found from a correlation provided in Eq. (15) of [60].

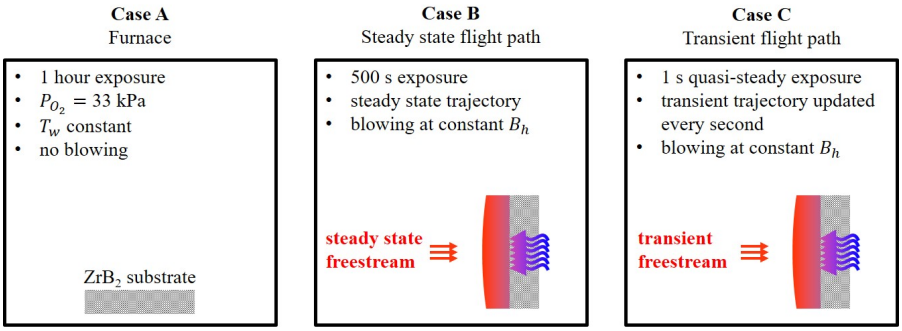

Figure 6.8: Illustration of the three cases examined in this study.

Table 6.2: Coolant temperature and material properties [87] used in this study.

T_{pl}	ε	h_v	L_1	ϕ	k_s
[K]	[-]	[W/m^3 K]	[mm]	[-]	[W/mK]
300	0.7	5.5×10^4	2.5	0.42	41.4

A more detailed derivation of the model equations used in this study can be found in Refs. [10] and [60]. With this model one can calculate the scale thickness, virgin surface recession and boria layer thickness for a given temperature and oxygen partial pressure.

6.4 Results and discussion

Three cases are examined in this study, schematically depicted in Fig. 6.8. In the first, the oxidation behavior of a ZrB_2 substrate with no mass injection is investigated. The second case studies the oxidation behavior of a transpiration cooled stagnation point on a steady state trajectory. Finally, a transient trajectory of an envisaged hypersonic vehicle is examined. Table 6.2 shows the thermophysical properties of the ZrB_2 substrate modeled in this work.

Case A: Oxidation behavior with no mass injection

In this case the ZrB_2 substrate is placed in the furnace for 1 hour at constant temperature and 33 kPa of pure oxygen. Fig. 6.9 shows the oxide scale thickness, recession and boria layer depth as a function of time for a fixed temperature of 1500 K.

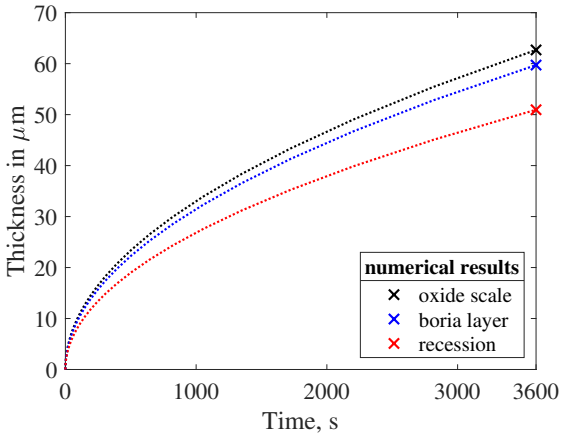

Figure 6.9: Oxide scale, recession and boria layer growth over time at 1500 K and 33 kPa of pure oxygen.

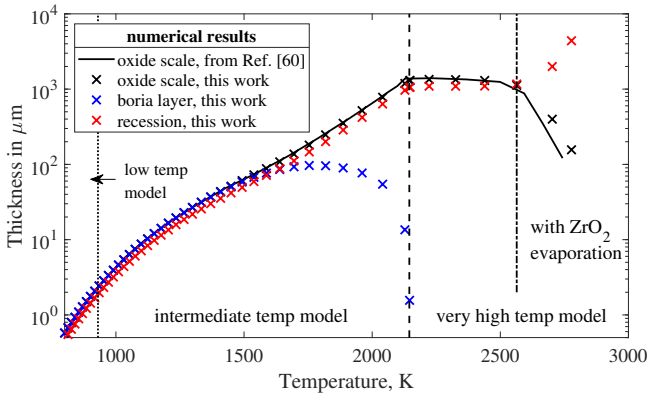

Figure 6.10: Numerical model predictions for the oxide scale, recession and boria layer thickness after 1 hr exposure at 33 kPa of pure oxygen. Validation with the numerical prediction provided in Ref. [60].

The oxidation rate decelerates as the oxide layer grows and shields the substrate with the mechanisms detailed in section 6.3.3. The markers indicate the final thickness of all three quantities after an exposure time of 1 hour. This calculation was then repeated for temperatures between 800 K and 2800 K. The final values, denoted by the markers were plotted against temperature in Fig. 6.10. All data points in this figure were obtained numerically. The numerical implementation of the code in this work was validated against Fig. 4 of Ref. [60], which also modeled the oxidation after a 1 hour exposure at 33 kPa of pure oxygen.

One can see the distinguishing features of the temperature regimes. An external boria layer exists at low temperatures and evaporates at around 930 K, marking the

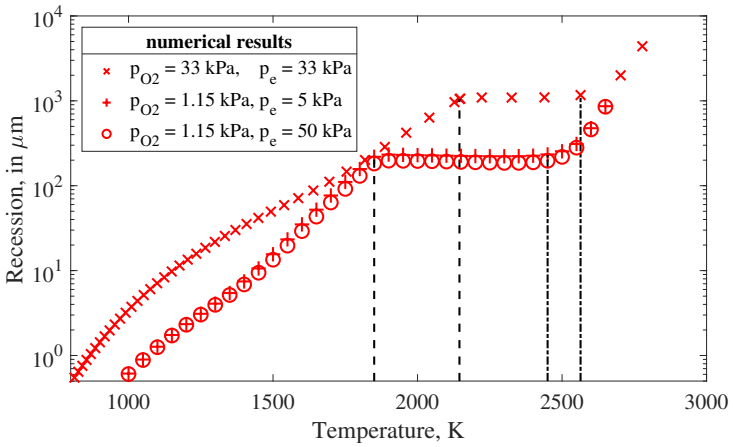

Figure 6.11: Recession after 1 hour for different oxygen pressures.

transition from the low to intermediate temperature model. At approximately 2200 K, the internal boria layer between the oxide scale evaporates as well, activating the very high temperature model. This oxidation model contains a ZrO_2 evaporation term which becomes significant at around 2600 K.

The transition temperature of the oxidation models is also oxygen pressure dependent and will therefore vary with static pressure and oxygen mole fraction at the surface. This effect is illustrated in Fig. 6.11 (a), which repeated the numerical calculations conducted for Fig. 6.10, but with different oxygen pressures.

At lower oxygen pressures, the transition temperature between the intermediate and the very high temperature model is lower. This is due to a faster evaporation of the boria layer. The ZrO_2 evaporation is also enhanced and therefore occurs at lower temperatures. It is also interesting to note that the effect of oxygen pressure is largest in the very high temperature regime. In parts of the intermediate regime, at around 1800 K, the oxidation behavior appears to be completely independent of oxygen pressure. Minor differences persist due to the influence of the static pressure, p_e on empirically obtained quantities, such as the boria vapor mole fraction. Since the influence of p_e is small (Fig. 6.11), it is possible to visualize the oxidation behavior on a temperature - oxygen pressure map, shown in Fig. 6.12 The map shows the relative recession rate with respect to a reference case at 1 kPa oxygen pressure and 1375 K surface temperature. As expected, the recession rate increases

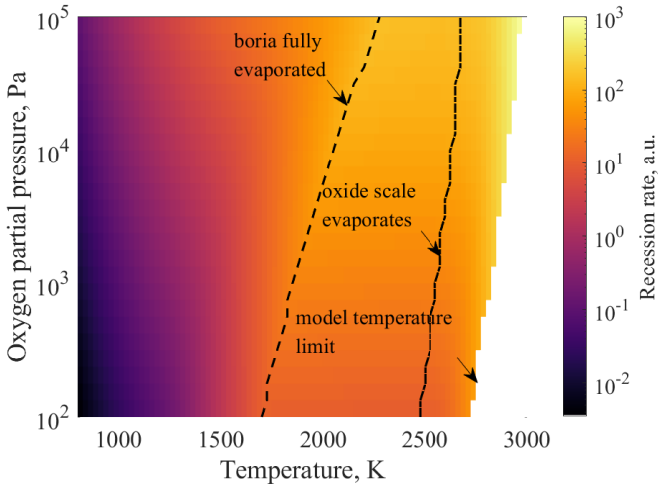

Figure 6.12: Relative recession rate as a function of wall temperature and oxygen pressure.

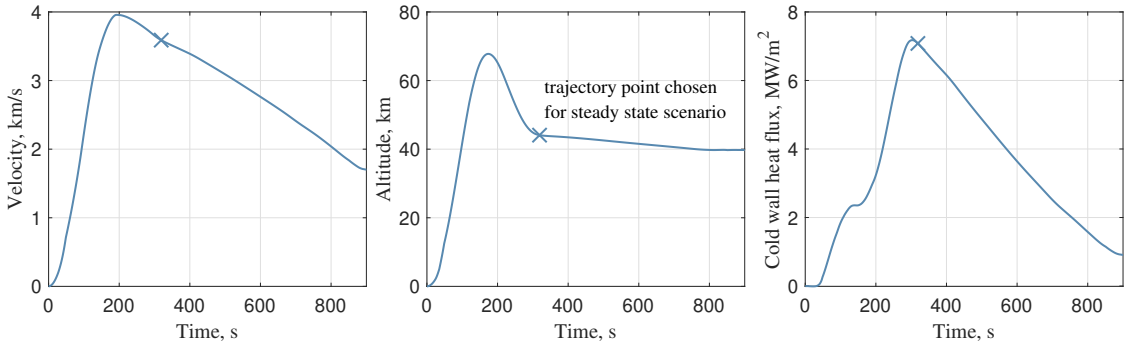

Figure 6.13: Nominal trajectory of a hypersonic vehicle.

with increasing temperature and decreasing oxygen pressure. The evaporation temperature for liquid boria and the oxide scale increases with increasing pressure.

Case B: Steady state flight case

A representative flight scenario, depicted in Fig. 6.13, is used to assess the potential of transpiration cooling on the oxidation behavior of real flight vehicles. Initially, a single trajectory point is investigated at the condition described in Table 6.3. This case has a cold wall heat flux of 7.1 MW/m^2 and includes mass injection. The thermophysical properties used to calculate the internal advective and conductive heat flux are summarized in Table 6.2.

The initial radius, r_{t_0}, is provided for the start of the trajectory. Throughout the 500 second flight, the stagnation point will recess, blunting the nose. The heat

Table 6.3: Overview of steady state flight condition.

Initial radius [mm]	Coolant [-]	B_h [-]	$B*$ [-]	$\dot{m}$ [kg/m^{2}s]	Velocity [m/s]	Altitude [km]	$\dot{q}_{0,\text{cold}}$ [MW/m^2]	Flight time [s]
3	N_2, He	0 - 1.5	1.56, 0.6	0 - 1.66	3600	44	7.1	500

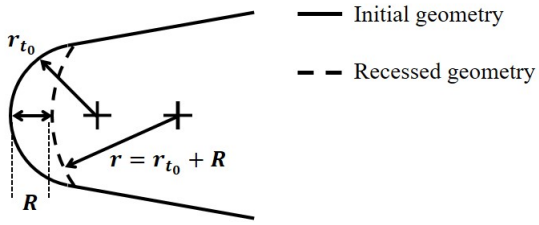

Figure 6.14: Stagnation point blunting due to surface recession.

flux and thus the surface temperature and the uncooled Stanton number, St_{h0}, were re-evaluated in time intervals of 1 second with an updated, effective radius. The 1-D model employed in this study cannot accurately model the 2-D deformation of the stagnation point. In order to obtain a first approximation of the blunting effect, the recession at every time step was added to the initial radius, to obtain the effective, blunted radius of curvature, as shown in Fig. 6.14.

Figure 6.15 illustrates how transpiration cooling at different blowing parameters impacts the oxidation behavior.

One can see that no blowing leads to 2.2 mm surface recession after 500 s flight at this condition. This amounts to 73% of the nose radius and will thus have significantly blunted the stagnation point. The dashed lines in Fig. 6.15 show what the heat flux and temperature would be if this blunting effect was ignored. The sharper radius would have increased the heat flux and thus the surface temperature. Fig. 6.16 shows the resulting increase in recession, in particular for the low blowing parameters. For no blowing, the recession would more than double. The dash-dotted line in Fig. 6.15 (d) highlights the importance of modelling the displacement of freestream oxygen by the injectant at the wall. If the oxygen displacement is ignored, and thus $y_{\text{inj,w}} = 0$, than the predicted recession is higher.

The geometry change caused by strong recession can lead to significant control problems and aerodynamic issues. It is caused by the elevated temperature of

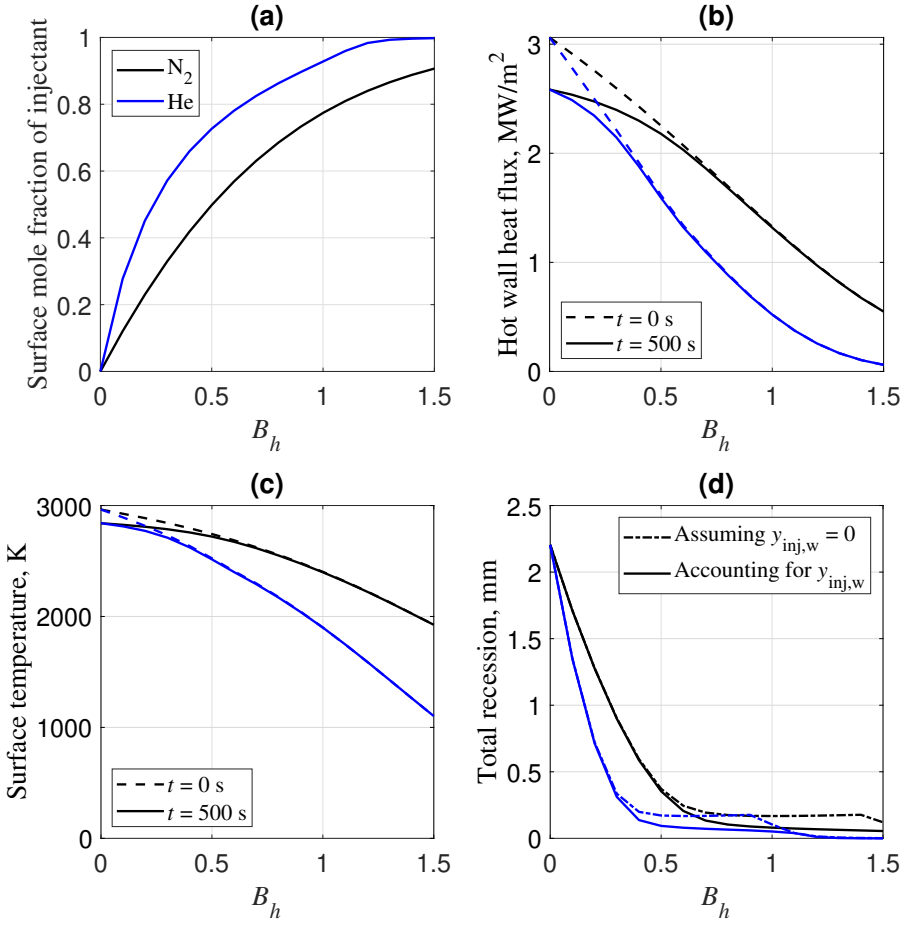

Figure 6.15: Effect of blowing parameter on the wall quantities of a hypersonic stagnation point on a steady trajectory, as described in Table 6.3

2841 K that leads to the evaporation of ZrO_2. This can be prevented by low to moderate blowing parameters.

Comparison of coolant gases

This section compares the injection of nitrogen and Helium gas. The comparison is made in two dimensions. Firstly, at a constant blowing parameter, for instance $B_h = 0.6$. Secondly, at the respective boundary layer blowoff parameter, which is $B* = 0.6$ for Helium and $B* = 1.56$ for nitrogen.

For nitrogen, a blowing parameter of $B_h = 0.6$ reduces the surface recession to 0.21 mm. This is a significant improvement compared to the no blowing case. Nitrogen blowing ratios $B_h = 0.6 - 1.5$ are all in the very high temperature regime and therefore their oxidation protection is irrespective of temperature, as can be seen

in Fig. 6.11. The improved oxidation protection provided by $B_h = 1.5$, compared to $B_h = 0.6$ is due to the higher surface mole fraction of the injected gas, reducing the partial pressure of freestream oxygen at the surface. The surface only recesses by 0.055 mm at $B_h = 1.5$. The effect of oxygen mole fraction is most pronounced at $B_h = 1.4$. The predicted surface recession, assuming that $y_{\text{inj},w} = 0$ is 197% higher than when accounting for $y_{\text{inj},w}$. This highlights the importance of modelling the concentration of oxygen on a hypersonic transpiration cooled stagnation point.

Helium generally outperforms nitrogen for the same blowing parameter. It is much more effective at displacing freestream air and reducing the surface temperature, as depicted in Fig. 6.15 (a) and (c). However, it is extremely light and thus for the same mass flux will have a much higher outflow velocity, which can disturb the external flow field. The boundary layer blowoff parameter (Eq. (6.7)) for Helium is just $B* = 0.6$ and exceeding it is likely to cause injection induced turbulence and other secondary effects. Comparing both gases at their respective blowoff parameters, $B_h = 0.6$ for Helium and $B_h = 1.5$ for nitrogen, shows that nitrogen provides a slightly better oxidation protection. The total recession is 0.055 mm for nitrogen and 0.08 mm for Helium.

One cannot categorically say that one gas is superior to the other. Instead, it is highlighted that this comparison will depend on the metric. For the same B_h, Helium performs better. For the corresponding blowoff parameter, nitrogen performs better for this flight scenario. This currently ignores the greater system, where storage, weight and robustness must also be considered.

Case C: Transient flight path

The oxidation response of a transpiration cooled stagnation point is calculated for a nominal trajectory of a hypersonic vehicle, shown in Fig. 6.13. It was calculated using a quasi-steady time stepping method whereby the freestream conditions were assumed to be in steady state for 1 s before being updated. The surface recession and oxide scale thickness at the end of a quasi-steady time step were used as initial condition for the following time step.

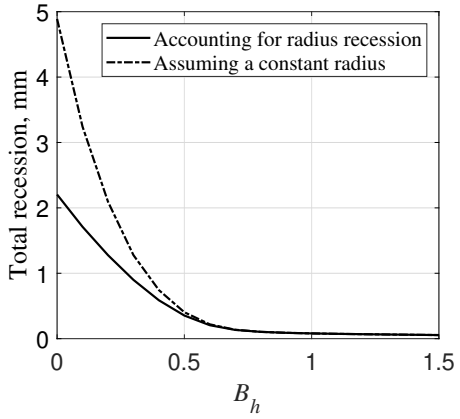

Figure 6.16: Total radius recession after the 500 s steady state flight with nitrogen injection.

The oxidation behavior is initially calculated with no mass injection, $B_h = 0$. Figure 6.17 (d) shows the surface recession over time. The oxidation starts at around 66 s, when the surface temperature exceeds 800 K and quickly enters the very high temperature regime at 112 s. At 250 s the evaporation temperature of ZrO_2 is exceeded, drastically reducing the oxide scale thickness. The oxide scale previously mitigated the diffusion of freestream oxygen to the surface. Removing it triggers a rapid acceleration in surface recession.

At approximately 300 s, the oxide scale starts growing again and thus the rate of recession decelerates. At 700 s, the surface temperatures falls below 2000 K, marking the transition into the intermediate oxidation regime. The oxide scale thickness plateaus at 0.15 mm. The total recession reaches 0.94 mm, which is equivalent to 31% of the 3 mm nose radius. The deformation of this key aerodynamic vehicle component is likely to lead to control problems and additional drag. Through mass injection at $B_h = 0.6$, the surface is kept up to 500 K cooler, as illustrated in Fig. 6.17 (c). The total surface recession in this cooled case only amounts to 0.13 mm or 4.3% of the radius. This is because the surface remains below the evaporation temperature of ZrO_2, as depicted by the monotonically increasing red line in Fig. 6.17 (d).

Further increasing the blowing parameter to $B_h = 1.5$ moves a large proportion of the trajectory from the very high temperature into the intermediate temperature

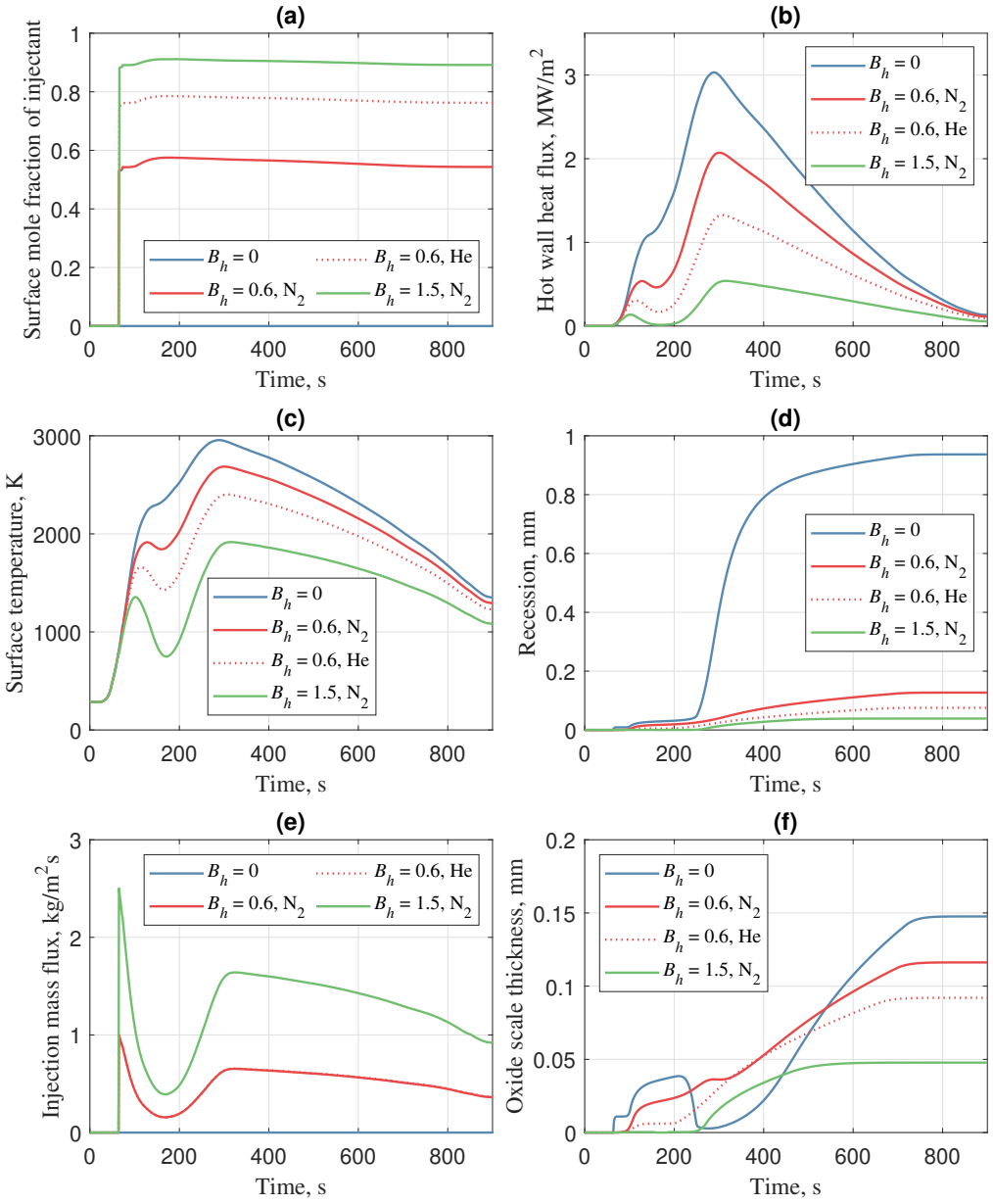

Figure 6.17: Material response injection properties of the transpiration cooled stagnation point.

oxidation regime. This further reduces the recession thickness to 0.039 mm or 1.3% of the radius, due to the additional protection provided by the liquid boria layer.

Helium performs better for the same blowing parameter, as depicted in Fig. 6.17. The mole fraction of Helium at the wall is 78% and therefore higher than that of nitrogen at the same blowing parameter. Furthermore, Helium is much more efficient at reducing the incident heat flux and thus the wall temperature. The resulting recession at $B_h = 0.6$ is 0.075 mm and therefore 58% lower than that of nitrogen for the same B_h. If both coolants are compared at their boundary layer blowoff parameter, like in Case B, nitrogen outperforms Helium.

Fig. 6.17 (e) shows that the mass flux of nitrogen is only moderate for the blowing parameters considered, peaking at 1 kg/m^{2}s and 2.5 kg/m^{2}s, respectively. The same mass fluxes are required for Helium, as the blowing parameter and the freestream conditions are kept constant. The pressure required to drive a given mass flux through a porous medium is much higher for helium than for heavier gases, such as nitrogen. This might lead to structural problems or added mass for reinforced walls. A full systems study, taking into account the vehicle mass is thus required to assess which coolant is more suited for a specific mission and vehicle type. The analysis shown in this paper will provide the coolant mass needed to achieve a certain oxidation protection and can be used to optimise the performance of this subsystem.

One can see that much mass flux is injected in the first 66 s, during which no oxidation occurs for the no injection case. To reduce system mass, it is desirable to only inject gas when it is really needed. Constant blowing parameters throughout the transient trajectory are not optimal. Instead, a real system would adjust the blowing parameter such that the ZrO_2 evaporation regime is never entered.

It is important to note that several real-flight phenomena were not accounted for in this analysis. The employed oxidation model has only been validated experimentally in the furnace. The hypersonic flow is likely to enhance the evaporation of the boria layer and the oxide scale. Vibration, shear and pressure forces may cause the oxide layer to spall. The comparison with transpiration experiments was attempted in Ref. [19], but only provided qualitative results

due to large uncertainties. A second experiment will be undertaken soon. First encouraging results were obtained in Ref. [110] for a similar material. A UHTC, specifically 20 vol%SiC-HfB_2, was exposed to simulated hypersonic flight conditions. The corresponding oxidation model predicted the recession within reasonable error, showing that the above mentioned effects were only secondary.

Further, questions on the practical implementation of this system remain. Ref. [113] has shown that porous ZrB_2 at pore sizes of less than 10 μm is manufacturable, resulting in a high flow uniformity, coupled with good structural strength. Further work is required to make a more complex cooling architecture. The practical implementation will also hinge on the weight penalty incurred by the coolant gas, pressure tanks, valves and other system components. Together with added safety layers and redundancy due to the high system complexity of transpiration cooling the disadvantages might outweigh the benefits of this cooling technology. Future work to quantify these effects is encouraged.

6.5 Conclusion

This paper presents the methodology and results of a systems study on the material response of transpiration cooled hypersonic stagnation points. A validated oxidation model for ZrB_2 was used to compute the recession and oxide scale thickness. A recently developed correlation for a hypersonic stagnation point with blowing provided the oxygen partial pressure at any flight condition, which is a critical input parameter for the oxidation model. The surface temperature was computed using validated low-order models, which take into account the heat flux reduction due to the coolant film.

A representative steady state flight scenario at 44 km altitude and 3.6 km/s velocity is chosen to assess the effect of mass injection on the oxidation behavior. No blowing causes the 3 mm radius to recess by 73%. Moderate amounts of blowing ($B_h = 0.6$) reduce this recession to just 4.3%. The displacement of freestream air at the surface through transpiration cooling has a strong effect on the oxidation behavior. If it is not accounted for, the recession increases by as much as 197%.

The total surface recession along the transient flight path of an envisaged hypersonic vehicle with a 3 mm nose radius exceeds 0.93 mm. This could lead to aerodynamic and control problems. With a moderate blowing parameter of $B_h = 0.6$, the recession can be reduced to 0.13 mm and 0.075 mm, for N_2 and He injection, respectively. The required mass flux does not exceed 1 kg/m^{2}s.

7 Conclusions and Future Work

The aim of this thesis was to investigate the application of transpiration cooling on hypersonic vehicles to mitigate material oxidation. In the following, the key results of a theoretical analysis, a numerical study and four experimental test campaigns, conducted as part of this thesis, are presented. The original research contributions are highlighted and their impact on the field is discussed.

7.1 Conclusions

A direct, non-intrusive experimental diagnostic for the concentration of freestream molecular oxygen on a transpiration cooled surface is developed. With this method the reduction in freestream species due to blowing can be measured. It produced the first spatially resolved image of the oxygen partial pressure on a porous medium with blowing. The oxygen partial pressure can be converted into oxygen mole fraction if the static pressure at the wall is known. The 39% porous alumina used for this experiment featured a good bond with PSP, while imitating the pore size of Ultra-High-Temperature Ceramics and exhibiting an extremely uniform outflow distribution. Inexpensive and quick to manufacture, it is a suitable porous substrate to experimentally study transpiration cooled systems. The experimentally obtained data provides direct insights into the performance of these systems, in particular

how well the blowing acts as a barrier against freestream diffusion to the surface. The experimental data also provides a foundation to develop low order models and empirical correlations for the mass transfer reduction on transpiration cooled models with blowing. It can further be used to validate numerical models.

An analytical correlation for the concentration of freestream species on a hypersonic stagnation point with mass injection is presented. The analytical expression can be used for any freestream condition, nose radius and coolant properties. It can also be used for high-enthalpy conditions, as long as thermal equilibrium is assumed and the self-similar assumptions are met. The main advantage of this semi-analytically derived method over numerical solvers is that it explicitly reveals the effect of each component in the parameter space. It was validated against the numerically obtained self-similar solutions and featured an error of ± 4 percent or ± 1.5 percentage points, whichever is greater. Similar to the Fay-Riddell heat transfer prediction, it is not intended to provide perfect accuracy, but instead to aid early design decisions, such as the choice of coolant, the nose radius or the rate of mass injection. The method is also very useful for flight to ground scaling of surface concentrations and mass Stanton numbers. In addition, it can complement existing theoretical oxidation models, by providing a concentration value and thus the oxygen partial pressure for a real flight condition, which directly affects the chemical rate of reaction. Furthermore, it can be employed to provide an initial guess of the surface species concentration for numerical models to speed up convergence.

Using both of the aforementioned tools, the mass transport of freestream oxygen to a transpiration cooled surface is evaluated. The PSP diagnostic is employed on a transpiration cooled stagnation probe model in the Oxford High Density Tunnel. The ability of transpiration to act as barrier against freestream species is quantified experimentally for the first time. The experimental data follows the analytically predicted trend, but reveals a slightly higher oxidation protection than expected. This is due to the irregular surface microstructure of the porous material. Common

numerical models assume a perfectly flat surface, which in reality consists of pores and troughs. The freestream air needs to overcome an additional pressure gradient to reach the wall at the bottom of these pores. As this effect is not accounted for in numerical models, they underpredict the oxidation protection and thus provide a conservative estimate. The experimental results provide a first set of data to investigate this porous interface effect. As the surface microheterogeneity is expected to be highly material dependent, further research is encouraged to identify the defining material characteristics. If these are found, materials can be optimised for oxidation protection, for instance by having a certain pore size or pore distribution.

The ability of transpiration cooling to mitigate oxidation of ZrB_2 is assessed numerically. A numerical systems study on the material response of transpiration cooled hypersonic stagnation points was conducted. A validated oxidation model for ZrB_2 was used to compute the recession and oxide scale thickness. The correlation developed in chapter 4 provided the oxygen partial pressure at any flight condition, which is a critical input parameter for the oxidation model. The surface temperature was computed using validated low-order models, which take into account the heat flux reduction due to the coolant film. A representative steady state flight scenario at 44 km altitude and 3.6 km/s velocity is chosen to assess the effect of mass injection on the oxidation behaviour. No blowing causes the 3 mm radius to recess by 73%. Moderate amounts of blowing ($B_h = 0.6$) reduce this recession to just 4.3%. The displacement of freestream air at the surface through transpiration cooling has a strong effect on the oxidation behaviour. If it is not accounted for, the recession increases by as much as 197%. The total surface recession along the transient flight path of an envisaged hypersonic vehicle with a 3 mm nose radius exceeds 0.93 mm. This could lead to aerodynamic and control problems. With a moderate blowing parameter of $B_h = 0.6$, the recession can be reduced to 0.13 mm and 0.075 mm, for N_2 and He injection, respectively. The required mass flux does not exceed 1 kg/m^{2}s. These results show that moderate amounts of transpiration cooling can lead to a significant reduction in surface oxidation.

They are important to prove that this cooling technology can have an impact on real flight vehicles. At the same time, this is the first model available in the literature that predicts the oxidation of a transpiration cooled stagnation point and it contains many simplifying assumptions. Further research is recommended to address these simplifications and refine the model.

A first experimental assessment was conducted in the plasma wind tunnel at the Institute of Space Systems in Stuttgart. This first high-enthalpy test proved that that transpiration cooling can prevent surface oxidation of transpiration cooled ZrB_2.

7.1.1 Future Work

Whether oxidation in the plasma wind tunnel experiments was prevented solely by mitigating the diffusion of oxygen through to the surface or whether it was aided by mitigating catalytic heating in general, which reduced the surface temperature down to values at which the oxidation rate is low, remains to be investigated. A second high-enthalpy test campaign at IRS was prepared to complement the existing qualitative results with quantitative measurements. It will compare probes with different blowing parameters, but constant front surface temperatures to isolate these effects. The revised model design features much lower thermal stresses and lateral heat fluxes, which improve its reliability and reduce the experimental uncertainty. The accuracy of optical temperature measurements will further be improved by characterising the sample emissivity pre-experiment in a dedicated emissivity measurement facility at IRS. The stagnation probe model is envisaged to be tested in the plasma wind tunnel at IRS in 2022.

Appendices

A

Stagnation point boundary layer modelling

The flow field around a hypersonic stagnation point is governed by three basic principles: the conservation of mass, momentum and energy. Applying these principles to an infinitesimal control volume, the general governing equations of fluid dynamics, called Navier-Stokes equations, can be derived. This is done, for instance, in chapter 15 of Ref. [114]. As there is no analytical solution to the complete set of equations, they can only be solved numerically using high-fidelity CFD solvers. This is very computationally expensive and thus there is a desire to simplify them using an appropriate set of physics-informed assumptions [95]. In this thesis, the flow is assumed to be steady and two-dimensional axisymmetric. As this section is concerned with the governing equations of the stagnation point boundary layer, three further simplifying assumptions can be made:

1. The flow is laminar.

2. The gradients are much larger normal to the wall than in tangential direction.

3. Thermal and pressure diffusion are negligible.

This yields the laminar *boundary layer equations* for an axisymmetric stagnation point [95]:

mass:

$$\frac{\partial(\rho r_1 u)}{\partial x} + \frac{\partial(\rho r_1 v)}{\partial y} = 0 \tag{A.1}$$

x-momentum:

$$\rho u \frac{\partial u}{\partial x} + \rho v \frac{\partial u}{\partial y} = -\frac{dp}{dx} + \frac{\partial(\mu \frac{\partial u}{\partial y}))}{\partial y} \tag{A.2}$$

y-momentum:

$$\frac{dp}{dy} = 0 \tag{A.3}$$

energy:

$$\rho u \frac{\partial h}{\partial x} + \rho v \frac{\partial h}{\partial y} = \frac{\partial}{\partial y}\left(k \frac{\partial T}{\partial y}\right) + u \frac{\partial p}{\partial x} + \mu \left(\frac{\partial u}{\partial y}\right)^2 \tag{A.4}$$

If the flow field contains more than one gas, for instance if a coolant is injected into the freestream, then mass continuity must not just be applied to the mixture, but also to its individual species. The so called species conservation equation has the following form:

species:

$$\underbrace{\rho u \frac{\partial c_i}{\partial x} + \rho v \frac{\partial c_i}{\partial y}}_{\text{convection}} = \underbrace{\frac{\partial(D_i \rho \frac{\partial c_i}{\partial y})}{\partial y}}_{\text{diffusion}} + \underbrace{\dot{w}_i}_{\text{mass generation}} \tag{A.5}$$

As this thesis is concerned with the mixing of an inert injectant and the freestream air, the species conservation equation will be elaborated further. The two terms on the left hand side denote convection and thus the movement of species with the bulk flow. The second term on the right hand side denotes mass generation, for instance due to mass injection or chemical reactions. As air is treated as a species in this thesis, the chemical reactions between its components were not modelled. In other words, atomic and molecular oxygen do not have their individual species conservation equations. Instead, the mass of air is conserved.

A.1 Mass diffusion

The first term on the right hand side of Eq. (A.5) denotes mass diffusion, defined as the molecular transport of one species relative to another [9]. Diffusion is driven by concentration gradients [115] and is governed by *Fick's first law of diffusion*:

$$\dot{m} = -\rho D \frac{dc}{dy} \tag{A.6}$$

Note that there is no general agreement on whether the mole or mass fraction is the better quantity for the gradient. In this thesis, the mass fraction will be used, which is consistent with Ref. [9]. This gradient is then multiplied by the local density, ρ and the mass diffusivity, D. There are two methods to obtain the mass diffusivity: experimentally and using kinetic theory. As conducting experiments is very time and labour intensive, this thesis uses kinetic theory to obtain the diffusion coefficients.

Chapman-Enskog kinetic theory assumes that a volume of gas consists of a large number of particles that are in random, constant and rapid motion. By modelling the collisions of particles, it can predict their mixing behaviour. Kinetic theory is based on the Boltzmann equation which describes the probability of particles to be within a given space and having a given velocity. A derivation of kinetic theory from the Boltzmann equation is beyond the scope of this thesis, but is provided in Appendix D of Ref. [9]. The resulting expression for the mass diffusivity of a binary mixture is given by

$$D_{i,j} = 0.0188 \sqrt{T^3 \left(\frac{1}{M_i} + \frac{1}{M_j} \right)} \frac{1}{p d_{ij}^2 \Omega_{i,j}} \tag{A.7}$$

Note that kinetic theory is only valid for gases at low density, where the distance between molecules is many times the diameter. This condition is met for air at sea level. For binary mixtures of non-polar gases it can predict the coefficients with an error of less than 5% [9].

A.2 Self-similar transformation

The velocity, temperature and coolant concentration distribution between the wall and the boundary layer edge can be obtained numerically from the system of partial differential equations (PDEs) (Eqs. (A.1) - (A.5)) for a laminar, axisymmetric stagnation point. They are much less computationally expensive than the general Navier-Stokes equations. However, an additional leap in efficiency can be achieved if the PDEs were converted into ordinary differential equations. In other words, Eqs. (A.1) - (A.5) depend on two independent variables, x and y. If they could be transformed such that the number of independent variables is reduced to one, this would significantly accelerate the computation.

This can be achieved through a self-similar transformation. The governing equations are transformed from (x, y) into the non-dimensional (η, ξ) space. The aim is to make them independent of ξ, the non-dimensional x or wall tangential coordinate.

The Lees-Dorodnitsyn transformation [97] assumes the following transformed variables, which will not be derived. The Howart and Mangler transformation adds the r_1 variable for axisymmetric bodies. x is the distance along the surface, while r_1 is the normal distance to the axis. For small $x, r_1 \approx x$.

$$\xi = \int_0^x \rho_e \mu_e u_e r_1^2 dx, \quad \eta = \frac{u_e r_1}{\sqrt{2\xi}} \int_0^y \rho dy, \tag{A.8}$$

Using these transformed variables the derivatives with respect to x and y are found as follows:

$$\begin{aligned} \frac{\partial}{\partial x} &= \left(\frac{\partial}{\partial \xi}\right)\left(\frac{\partial \xi}{\partial x}\right) + \left(\frac{\partial}{\partial \eta}\right)\left(\frac{\partial \eta}{\partial x}\right) \\ &= \frac{\partial}{\partial \xi} \rho_e u_e \mu_e r_1^2 + \frac{\partial}{\partial \eta}\frac{\partial \eta}{\partial x}, \end{aligned} \tag{A.9}$$

$$\begin{aligned} \frac{\partial}{\partial y} &= \left(\frac{\partial}{\partial \xi}\right)\left(\frac{\partial \xi}{\partial y}\right) + \left(\frac{\partial}{\partial \eta}\right)\left(\frac{\partial \eta}{\partial y}\right) \\ &= \frac{\partial}{\partial \xi}(0) + \frac{\partial}{\partial \eta}\frac{u_e \rho r_1}{\sqrt{2\xi}}. \end{aligned} \tag{A.10}$$

The resulting self-similar equations for a binary coolant-freestream mixture with no chemical reactions are

$$\Big(lf''\Big)' + ff'' + \frac{1}{2}\Big(\delta - f'^2\Big) = 0 \tag{A.11}$$

$$\left(\frac{\Gamma_{c_p} l}{Pr}\theta'\right)' + \Gamma_{c_p} f\theta' + \frac{l}{Sc}\left(\frac{c_{p;\mathrm{inj}}}{c_{p;e}} - \frac{c_{p;\mathrm{ext}}}{c_{p;e}}\right)c'\theta' = 0 \tag{A.12}$$

$$\left(\frac{l}{Sc}c'\right)' + fc' + \frac{\dot{w}_i}{2\frac{du_e}{dx}\rho} = 0 \tag{A.13}$$

where $f' = \frac{u}{u_e}$ is the velocity ratio, $\theta = \frac{T}{T_e}$ the temperature ratio and c the coolant mass fraction. Please refer to Chapter 6.5 in Ref. [95] for a more extensive derivation of Eqs. (A.11-A.13). The following assumptions have been made during the derivation:

1. the boundary layer edge and the shock are separated by an intermediate layer. This may be violated if the Reynolds number is too low, considering that the boundary layer thickness grows $\propto \frac{1}{\sqrt{Re}}$. For the cases considered in this work, the Reynolds number is large enough.

2. the boundary layer thickness is much smaller than the radius of curvature, such that most derivatives in ξ direction, along the surface, are negligible. The velocity gradient, $\frac{du_e}{d\xi}$ is the exception.

3. the post shock kinetic energy is small compared to the total enthalpy $\frac{u_e^2}{h_e} \ll 1$, where e denotes the boundary layer edge conditions.

4. the flow outside the boundary layer edge is inviscid and incompressible. With this in mind, one can use the Falkner-Skan wedge flow solutions to obtain the boundary layer edge velocity, $u_e = \frac{du_e}{dx}x$ [98].

The self-similar boundary layer equations have been used in the literature before to derive a semi-analytical correlation for the heat flux on a hypersonic stagnation point [6]. Further, a numerical investigation was conducted to assess the

concentration profile on a transpiration cooled stagnation point [93]. The aim of this thesis is to apply the methodology of the former to the problem of the latter. In other words, to obtain a semi-analytical correlation for the concentration profile on a transpiration cooled stagnation point. This will be attempted in chapter 4.

B

PSP Application Manual

This report details how pressure-sensitive paint is applied on porous surfaces. Read the relevant risk assessment and all steps of the following manual before starting.

The PSP can be bought at Fisher Scientific. The 0.5 g bottle will be plenty and costs approximately 150 GBP.

Name: Tris(4,7-diphenyl-1,10-phenanthroline)ruthenium(II) dichloride

CAS Number: 36309-88-3

B.1 Preparation

☐ Put on a lab coat, safety glasses and nitrile gloves.

☐ Optional: dim light or switch from white to orange light to protect PSP.

☐ Switch on extraction fans.

☐ Pre-heat oven to 80 °C.

☐ Open the Ethanol bottle. Use the ethanol syringe to fill 50mL of ethanol into petri dish. Cover the petri dish. Close the ethanol bottle.

☐ Place a container on the chemical grade scale. Open the PSP bottle. With a spatula, place 5.85mg of PSP powder in the container. Close PSP bottle. Using a syringe, fill 66.5g (50mL) of dichloromethane into the container. Close it and store it in a dark place. This is sufficient paint to spray approximately 100 cm^2.

☐ Store ethanol, dichloromethane and PSP safely in the cabinet.

B.2 Process

☐ Check that the sample has undergone pre-PSP permeability and outflow tests.

☐ Wash the sample in ethanol to take off any oils. Place on tray using tongs and then dry in oven at 80 °C for 10 minutes.

☐ Prepare the air brush

(a) An Anest Iwata LPH-80 air brush can be found in the drawer cabinet next to the extraction fan in the intrumentation workshop.

(b) Read its manual.

(c) Assemble the air brush, using the smaller nozzle.

(d) Connect to pressurised air supply and set it to 2 bar abs. pressure.

(e) Fill with IPA and test spray pattern. This will also remove any residues of previous paints.

☐ Place sample on white sheet of paper. This will serve as a reference colour.

☐ Optional: Note down environmental factors such as temperature and humidity in logbook.

☐ Put on a face mask

1. Half mask respirator with 3M ABE1 filter can be found in the same cabinet as the air brush.

☐ Switch on the extraction fan.

☐ Keep a distance of 15 cm between the nozzle and the sample, continuously spraying "layers" from left to right and then from right to left to achieve a homogenous coating. Rotate the sample to improve the uniformity even further. The instrumentation workshop has a rotating table which can be placed underneath the sample for this purpose.

☐ As a rule of thumb, keep spraying until you see a faint orange hue.

(a) This should typically occur after 20 layers or so, but it heavily depends on the air brush settings, humidity, sample geometry and spraying distance.

(b) It can be extremely useful to keep a logbook, where these parameters are noted with a photo of the end result and a comment on the signal quality.

(c) Spraying too little may not give enough signal intensity. However, spraying too much can quickly saturate the signal and thus make the coating pressure insensitive. It is therefore always better to err on the low side, check the signal intensity and if necessary apply extra layers.

☐ At this point the sample is fully prepared. Place it in a dark box.

☐ Clean the air brush thoroughly with IPA.

B.3 Disposal

☐ Using a funnel, dispose of all chemical in the designated bottles. Make sure they are not overfilled and well-labelled.

☐ Contact the Chemical Safety Officer (julie.scott@eng.ox.ac.uk) if you need more bottles.

☐ Drop them in the waste area on the ground floor (next to the cage). Contact the CSO to organise collection.

B.4 Calibration

The calibration chamber is located in the red area, next to the 3D printing room. It can be seen in Fig. 1. It is managed by Holt Wong (holt.wong@eng.ox.ac.uk). Please reach out to him before using it.

- ☐ Read the risk assessment. A copy of it is taped onto the chamber.
- ☐ Open the calibration chamber and place the sample in the pressure chamber.
- ☐ Point the photodetector at the sample and read out its signal on the laptop.
- ☐ Record the pressure reading from the gauge underneath the chamber via the cDAQ.
- ☐ Adjust the pressure in the chamber either by using the manual pump or by switching on the vacuum pump.
- ☐ Record both the PSP intensity and the pressure change over time to obtain the calibration curve. If the sample is too dark/signal to noise ratio is high, go back to step 2 and add extra layers of paint. If the calibration curve is flat you might have used too much PSP thereby saturating it.
- ☐ Finally, it is possible to calibrate the PSP with respect to temperature. Place the sample on a Peltier device, ideally with thermal paste in between to improve thermal contact. It's best to calibrate in intervals of 10 K or even 20 K, i.e. 5°C, 25°C, 45°C. This way, photodegration is minimised and the intensity change is dominated by the temperature change.
- ☐ A more detailed operating procedure can be found in engs-thames\hypersonics-repository\docs\HYP\manuals\optics\PSP.

B.5 Testing

The sample is ready to test. Please refer to the "Operating Manual for PSP rig" in engs-thames\hypersonics-repository\docs\HYP\manuals\optics\PSP for further information.

C

Testing a transpiration cooled zirconium-di-boride sample in the plasma tunnel at IRS

This appendix chapter provides the first qualitative results of the oxidation protection provided by transpiration cooling on a hypersonic stagnation point with mass injection.

C.1 Introduction

When hypersonic vehicles fly through an atmosphere, they need a Thermal Protection System (TPS) to shield the payload from the searing heat around the capsule [4]. In the past, they relied on thermal soaks [116] with low thermal conductivity and high re-radiation or ablative heat shields [117]. The latter additionally have a pyrolysis zone, which produces a driving gas that flows through the porous upper layers and cools them by convection while also mitigating incident heat flux through blowing.

Transpiration cooling is a promising new TPS, in which a coolant gas transpires a porous Ultra-High-Temperature-Ceramic (UHTC). It cools it down internally by convection and externally through film cooling, which creates a barrier between the searing hot shocked gas and the UHTC wall [15]. It has the potential to enable fully re-usable, light TPSs that can sustain very high peak heat loads. Transpiration

cooling is a key technology to realise sharp edge designs of hypersonic vehicles. Small radii of curvature, usually encountered at the leading edge, are very desirable from an aerodynamic viewpoint [118], but lead to high local heat fluxes of several MW/m^2. The key advantage of transpiration cooling over ablative heat shields is that it maintains the shape stability of these critical aerodynamic components. The first real flight concept validation was performed by SHEFEX II in June 2012 and showed that the surface temperature of a facet could successfully be lowered with up to 58% cooling efficiency [13].

Currently, the most popular candidates for the transpiration cooled porous medium are Ultra-High-Temperature-Ceramics (UHTCs) [15] or C/C composites [13]. These materials are chosen for their high melting points, which promise a large passive cooling potential through re-radiation. ZrB_2, a UHTC, for instance has a very high melting point of 3519 K [119]. However, significant oxidation of UHTCs occurs from 1000 K upwards [120]. Oxidation products start blocking the pores and form an impermeable layer [10], while the virgin material recesses. This significantly limits the operating temperature and prevents the ZrB_2 from achieving its full passive cooling potential. Since the radiative heat flux of a material is proportional to the fourth power of surface temperature, an increase of the operating temperature from 1000 K to 2500 K would entail an almost forty-fold increase in re-radiation.

This paper investigates whether transpiration cooling with helium and nitrogen can shield UHTCs from atmospheric oxygen, thus increasing the range of operation in terms of surface temperature and incident heat flux. A porous UHTC sample is tested in the IRS PWK4 plasma wind tunnel in an air free-stream. During testing, the front and rear surface temperatures of ZrB_2, the coolant gas injection conditions and the emission spectra at the surface are measured. Additionally, a method to determine the stagnation point heat flux from the plenum pressure impulse response was applied[121]. After plasma heating, the surfaces were observed in a SEM with the samples still in the holders. Subsequently the samples were removed, impregnated in a low viscosity epoxy and sectioned to investigate the cross-sections in the SEM using secondary electron imaging and energy dispersive x-ray spectroscopy.

C.2 Experimental setup

The experiment took place in the PWK4 plasma wind tunnel at IRS in Stuttgart[122, 123]. Figure C.2 shows the probe mount in the tunnel chamber. In the following, the operational characteristics of the plasma generator and the detailed probe design are presented.

Figure C.1: Porous UHTC sample sealed in the probe head before testing.

Figure C.2: Probe head mounted in the PWK4 plasma wind tunnel.

C.2.1 PWK4 plasma wind tunnel and conditions

PWK 4, as shown in Fig. C.3, is a continuous high-enthalpy facility that produces a steady-state plasma free jet and therewith allows the study of long duration thermochemical effects. It is equipped with the coaxial thermal arc-generator RB3 [122]. RB3 has a bi-throat geometry and injects the working gases in a two-stage process. While nitrogen is added close to the cathode, oxygen is injected further downstream to prevent the said cathode from oxidation. The gas is heated by an electric arc in the discharge chamber, before passing the second throat and accelerating through the nozzle.

A flow condition is characterised by the working gas mass flow, the generator power, the pressure in the vacuum chamber and the axial distance between the test

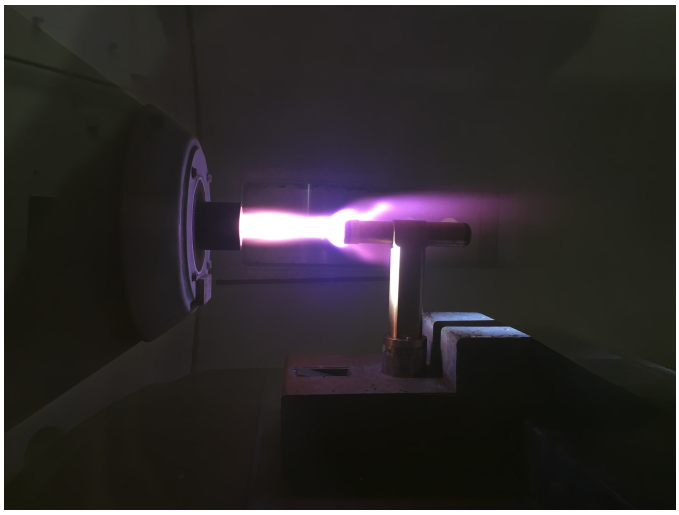

Figure C.3: Picture of the probe in an air plasma stream in PWK 4.

object and the plasma generator. A traverse can re-position the probes during testing. Operation can be conducted for hours and provides a continuous thermochemical load to probes in the flow.

The tunnel was operated at three different conditions, as summarised in Table C.1. All conditions refer to an artificial air plasma, which consisted of 76.85% nitrogen and 23.15% oxygen by mass and was modelled as air. Conditions 1 and 2 were chosen as intermediate steps to carefully ramp up the heat flux and front surface temperature to the desired value. They had been replicated from previous experiments [123]. Condition 4 was used for the NISIp calibrations [121], which identify the pressure impulse response of a system and later reconstruct the surface heat flux based on the plenum pressure history. The target front surface temperature for the uncooled sample was 2100 K – high enough to still be above the 1000 K oxidation threshold temperature in the cooled cases and low enough to account for the temperature limits of other probe components. This was achieved by using condition 2 as a starting point and slowly moving the probe closer to the nozzle. Condition 3 was reached at a distance of 178mm between nozzle exit and probe head stagnation point.

The enthalpy was found from an empirical equation provided by Zoby[124]:

Table C.1: Overview of the test conditions in the PWK4 plasma wind tunnel.

Tunnel Condition	1	2	3	4 (NISIp)	Uncertainty
Facility	PWK4 (RB3)	PWK4 (RB3)	PWK4 (RB3)	PWK4 (RB3)	
$T_{\text{front;uncooled}}$	1400 K	1600 K	2150 K	<550 K	± 2 %
h_w	1.215 MJ/kg	1.462 MJ/kg	2.216 MJ/kg	0.252 MJ/kg	
$q_{0;\text{cold}}$	2 MW/m^2	3 MW/m^2	3.95 MW/m^2	2 MW/m^2	± 20 %
h_e	19.02 MJ/kg	28.76 MJ/kg	30.42 MJ/kg	23.16 MJ/kg	
p_{stag}	2035 Pa	1970 Pa	3220 Pa	1250 Pa	± 0.5 %
p_{static}	330 Pa	275 Pa	275 Pa	30 Pa	± 0.15 %
$T_{\text{e,eq}}$	5435 K	5950 K	6180 K	5550 K	
$c_{p,e}$	16695 Jkg^{-1}K^{-1}	17787 Jkg^{-1}K^{-1}	16023 Jkg^{-1}K^{-1}	19844 Jkg^{-1}K^{-1}	
$\dot{m}_\infty$	4.99 g/s	4.99 g/s	4.99 g/s	6.52 g/s	± 0.4 %

$$h_e = K_M \dot{q}_0 \sqrt{\frac{r}{p_{\text{stag}}}} + h_w. \tag{C.1}$$

The hot gas equilibrium temperature was calculated with the Chemical Equilibrium with Applications online tool [100] in a tp problem type. For a known pressure the hot gas temperature was varied until the stagnation enthalpy was matched.

C.2.2 Probe design

The probe was designed to house the porous ZrB_2 sample while it is exposed to the desired thermal loads. It consists of a hemispherical copper head, a pyrometer mount and a brass adapter. The probe design is depicted in Fig. C.4, with an exploded CAD view. A ZrO_2 insulation ring mitigates the lateral heat flux from the hot ZrB_2 to the water cooled copper. It has a low thermal conductivity of about 2 W/mK ± 0.5 W/mK [125]. The ZrB_2 sample has a front diameter of 10.6 mm and a draft angle of 3°. It has a porosity of $(42 \pm 1)\%$, thermal conductivity of $k_s = 48 \pm 1$ Wm^{-1}K^{-1} and a surface emissivity of $\varepsilon_s = 0.75$[126]. The volumetric heat transfer coefficient is assumed to be $h_v = 5 \times 10^4$ Wm^{-3}K^{-1}. Both parts are glued into the stagnation point of the copper head with a ultra-high temperature adhesive. For the adhesive, Aremco 516 was chosen for the uncooled probe for its ultra high operating temperature, whereas Glassbond Sauereisen Zircon Potting Cement No. 13RW was chosen for its superior sealing properties in the cooled probes. During the experiment, the probe chamber is pressurised with the used coolant, which is fed in from a gas supply outside of the facility. The Optris CT 1MH1 CF pyrometer

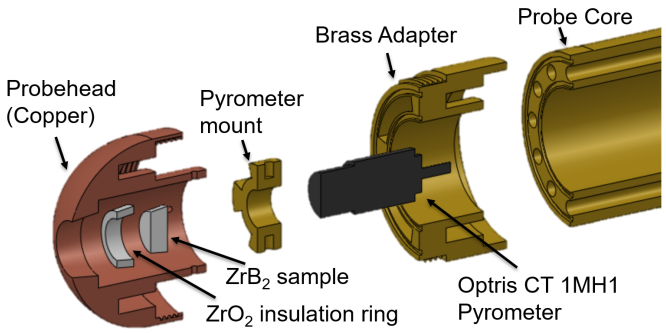

Figure C.4: Exploded CAD schematic of the probe.

measures temperatures in the range of 1073 K to 2473 K from the sample backside. It has a system accuracy of $\pm$(0.3% of reading $+ 2$ K). The distance to the surface amounted to 24.5mm, which corresponds to a spot size of 5.4 mm.

The experimental setup of the instrumentation is shown in Fig. C.5. An Omega PXM-319 absolute 0-15 bar pressure sensor records the transient pressure behind the sample with 0.25% accuracy. An Aryelle 150 UV-VIS-NIR echelle spectrometer records 20 spectra/s at an exposure time of 50 ms and a spectral resolution of 29241 in the range of 249.9333 nm to 884.5532 nm. The ZrB_2 front surface temperature in the uncooled cases was measured by a FLIR A6751sc Midwave Infrared camera at 33.33 Hz for condition 1 and 2 and at 8.33 Hz for condition 3. It operates in the 3.0 μm-5.0 μm waveband and has a pixel resolution of 640$\times$512. A LumaSense MCS640 Thermal Imager was employed to measure the front surface temperature of the cooled cases. It operates in the 978-1559 K temperature range and recorded 3 frames/s in the helium test (Probe #2) and 15 frames/s in the nitrogen test (Probe #5). The mass flow controller was a Tylan 2900 Series operated by an in-house flow regulator.

The sample is calibrated as a heat flux gauge using the non-integer system identification approach for plenum pressure [127]. The sample's surface is heated by a laser with a maximum optical power of 540 W at 980 nm (Laserline LDM500-100) and both the input power and the transient plenum pressure signal are recorded with a LeCroy 24Xs-A oscilloscope. More details can be obtained in Ref [121].

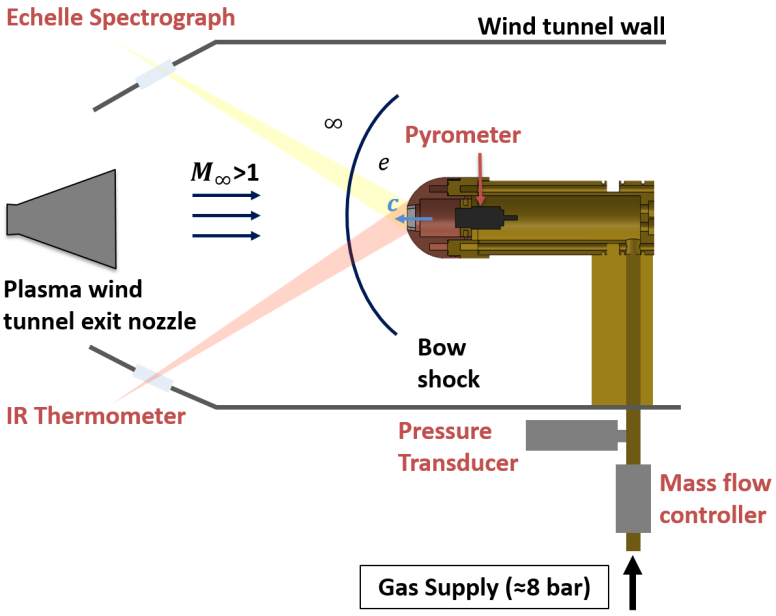

Figure C.5: Sketch of experimental setup of the UHTC test in the PWK4 plasma wind tunnel.

C.2.3 UHTC material properties and through-flow characteristics

Porous ZrB_2 was selected as UHTC material for its high melting point (3519 K) and good high temperature strength. A relatively high thermal conductivity[128] of 48 W/(mK) aids the cooling through internal conduction by distributing the heat evenly. Note that the thermal conductivity scales with porosity and is 28 W/(mK) for the 42 % porous sample. The ZrB_2 disks (Ø80 mm x 5 mm) were produced by hot pressing Grade-B ZrB_2 powder from H.C. Starck at 1750°C for 1 h under 35 MPa in a graphite hot press, whereas the solid, 100% dense ZrB_2 was produced by hot pressing a mixture of the same powder, a phenolic resin and boron carbide at 2000°C also under a pressure of 35 MPa. Various samples were cut from these disks using electro-discharge machining.

The pressure drop across a porous medium is governed by the Darcy-Forchheimer equation given as

$$-\frac{dp}{dx} = \frac{\mu}{K_D}v + \frac{\rho}{K_F}v^2. \tag{C.2}$$

Table C.2: Permeability coefficients with their corresponding uncertainties of the tested samples[15]

Coefficient	Value, X	Uncertainties, δX	$\frac{\delta X}{X}$
UHTC-2 (Probe #2)			
K_D, m^2	2.1494×10^{-14}	$\pm 0.0385 \times 10^{-14}$	1.79%
K_F, m	1.003×10^{-7}	$\pm 0.262 \times 10^{-7}$	26.08%
UHTC-5 (Probe #5)			
K_D, m^2	2.956×10^{-14}	$\pm 0.064 \times 10^{-14}$	2.17%
K_F, m	1.105×10^{-7}	$\pm 0.292 \times 10^{-7}$	26.43%

The former term on the right-hand-side of Eq. (C.2) stands for viscous losses, whereas the latter term denotes the kinetic losses, which become dominant only at higher coolant velocities.

The permeability characteristics of the tested sample were determined using a permeability test rig built according to $ISO-4022$ [129] at the Oxford Thermofluids Institute, where the pressure differential across the sample is recorded for increasing mass flow rates at room temperature [15]. An integrated version of Eq. (C.2),

$$\frac{p_{in}^2 - p_{out}^2}{2 p_{in} L} = \frac{\mu(T_{in})}{K_D} v_{in} + \frac{\rho(p_{in}, T_{in})}{K_F} v_{in}^2, \tag{C.3}$$

is employed here, which is valid for a constant fluid temperature over the thickness of the sample. Further details on the calculation can be found in Ref [15].

The permeability test results are plotted in Fig. C.6 and the obtained permeability coefficients are given in Table C.2. It can be seen that the experimental data follow the Darcy-Forchheimer equation and the curve thereof (solid line) is well within the uncertainty-bounds. Further, it can be observed that the flow enters the Forchheimer regime at higher velocities and deviates from the projected Darcy equation (dashed line), as the kinetic losses increase.

C.3 Experimental results

Three different experiments were conducted. A fully dense sample without any blowing was tested to assess the oxidation characteristics in a completely uncooled case. In addition, two samples were tested which were cooled by nitrogen and

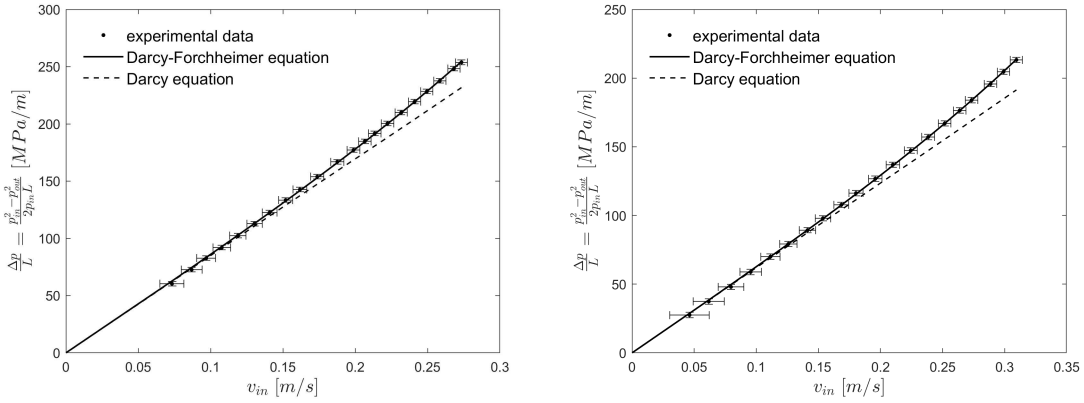

Figure C.6: Experimental results of the through flow characteristics of the porous UHTC-2 (left) and UHTC-5 (right) samples and comparison to the fitted Darcy-Forchheimer equation.

helium respectively. An overview of the tests performed is given in Table C.3. Note that the blowing ratio F is defined as the ratio of coolant mass flux to the mass flux of the post-shock gas at the boundary layer edge:

$$F = \frac{\rho_c v_c}{\rho_e v_e}, \tag{C.4}$$

while the blowing parameter is denoted as the blowing ratio normalised by the Stanton number of the uncooled case [32]:

$$B_h = \frac{F}{St_0}, \tag{C.5}$$

where

$$St_0 = \frac{\dot{q}_0}{\rho_e v_e (h_e - h_w)}. \tag{C.6}$$

A correlation factor is introduced, if the heat capacities of the coolant and the freestream are very different, which is the case for transpiration cooled probes exposed to the plasma freestream at condition 3. For laminar flow, the blowing parameter is multiplied by the following correlation factor[32]:

$$\left(\frac{c_{p,c}}{c_{p,e}}\right)^{1/3}. \tag{C.7}$$

Figure C.7 shows pictures of the probe heads post-testing. Probe # 5 was cooled by 620.11 g/m^{2}s of nitrogen and heated up to a front surface temperature of 1128

Table C.3: Summary of steady state experiments

Condition	Probe	Gas	Time in stream	T_{front}	T_{back}	F	$B_h\left(\frac{c_{p,c}}{c_{p,e}}\right)^{1/3}$
			[s]	[K]	[K]		
1	#4 (Solid)	None	305.2	1400	1313	-	-
2	#4 (Solid)	None	132.9	1600	1492	-	-
3	#4 (Solid)	None	81.4	2150	1980	-	-
3	#2 (UHTC-2)	Helium	75	1428	1233	0.0080	0.1094
3	#5 (UHTC-5)	Nitrogen	128	1128	<1073	0.2440	1.9586

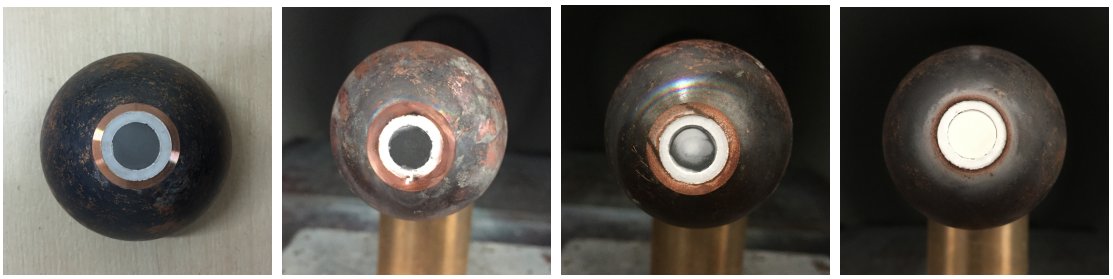

Figure C.7: Untested virgin sample (left), post-test nitrogen cooled sample (center left), post-test helium cooled sample (center right) and post-test uncooled sample (right).

K. Despite being in a temperature regime in which oxidation is expected, it did not oxidise and only a dark grey discoloration was observed. The uncooled sample did oxidise when it was exposed to the same tunnel conditions. It reached a maximum surface temperature of 2150 K and was covered in a white oxide layer post-test. When probe #2 was transpiration cooled by 20.25g/m^{2}s of helium it heated up to 1428 K and did not oxidise. However, the insulation ring cracked when the mass flux was lowered and the flow leaked through said cracks instead of transpiring the sample. With the loss of the protective coolant film, the sample surface started to oxidise.

C.3.1 Effect of blowing parameter on surface temperature.

This section presents the calculation of the transient blowing parameter for the helium cooled test. This is done to assess the effectiveness of transpiration cooling for different gases at high enthalpy conditions. The blowing parameter, as defined in Eq. (C.5), is only a function of the coolant mass flux for a quasi steady state wind tunnel condition, in which the uncooled Stanton number and the boundary layer edge mass flux are constant. Hence, only the coolant mass flux must be obtained at each time step to calculate the transient blowing parameter.

This is achieved by solving the Darcy-Forchheimer equation (Eq. (C.2)) for a given fluid temperature and plenum pressure. It is assumed that the fluid temperature varies linearly from room temperature at the backside to the solid wall temperature on the front surface. The measured plenum pressure is fed into the equation at each time step. Hence, all variables in Eq. (C.5) are known and the blowing parameter can be calculated. More details on the Darcy-Forchheimer solution that is used in this calculation can be obtained in Ref. [42]. The boundary layer edge mass flow rate is assumed to be equal to the free stream mass flow rate provided in Table C.1. The diameter of the bright plasma stream in Fig. C.3 was estimated to be similar to the diameter of the probe. The mass flow rate was hence divided by the cross-sectional area of the probe, which had a radius of $r = 25$mm, to obtain the boundary layer edge mass flux.

Figure C.8 compares the blowing parameter to the surface temperatures and plenum pressure for the helium cooled case. The coolant mass flux is driven by the pressure drop across the sample and is hence dependent on the reservoir pressure. If the plenum pressure rises, the mass flux and blowing parameter will increase. However, the pressure drop is not the only variable in the equation governing the mass flux across the sample. For a constant pressure differential, less fluid will transpire the sample if the fluid temperature and hence the fluid viscosity are higher. This can be seen in Fig. C.8, where the blowing parameter drops at $t = 17$s, despite a constant pressure differential, due to the rise in surface temperatures – and consequently fluid temperature. Less blowing entails less cooling, which in turn increases the surface temperature. It is hence critical to ensure that the coolant mass flux can be maintained at high surface temperatures. This can be achieved by either increasing the permeability of the porous medium or by increasing the maximum allowable supply pressure, such that the dangerous spiral of a blowing reduction due to a temperature increase can be counteracted.

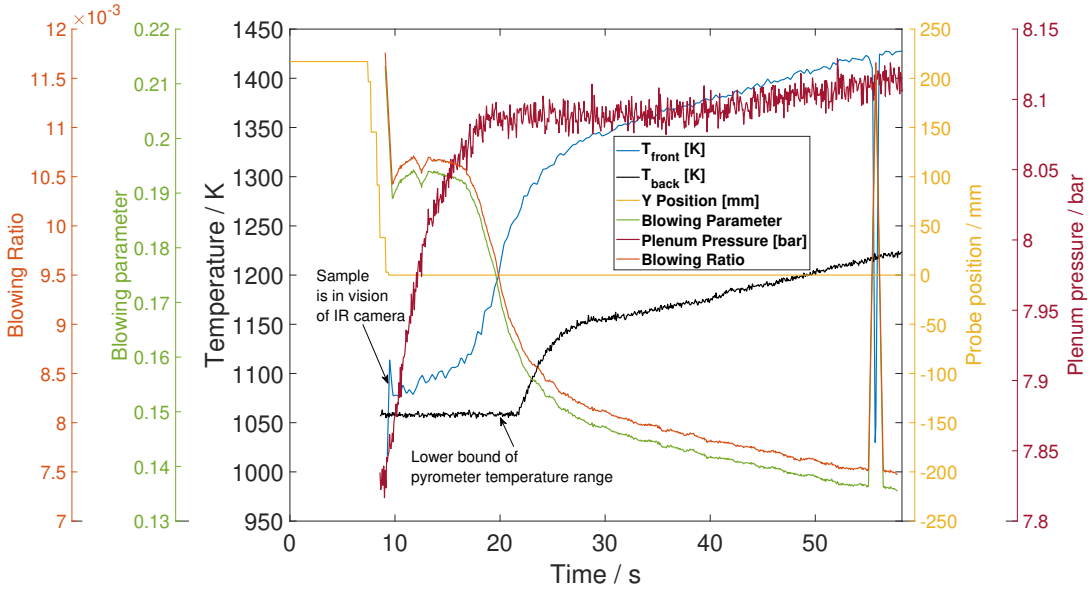

Figure C.8: Interaction of blowing parameter, blowing ratio, surface temperatures and plenum pressure in the helium cooled case.

C.3.2 Incident heat flux reduction of transpiration cooled samples

In quasi steady state conditions, the incident heat flux on the samples must equal to the heat flux out of the sample, namely, the heat flux due to the internal convective cooling and the radiative heat flux on both surfaces (Eq. (C.8)). Lateral heat loss must be added for completeness. The sample surface temperatures are taken from Table C.3 and the results for both samples are summarised in Table C.4. The internal convective heat flux is equal to the steady-state solid-fluid heat exchange term in the energy equation of a fluid transpiring a porous medium (Eq. (C.9)).

$$\dot{q}_{\text{rad}} = \sigma \varepsilon_s (T_{\text{front}}^4 + T_{\text{back}}^4) \tag{C.8}$$

$$0 = \underbrace{\rho_c c_{p,c} v_c \frac{\partial T_c}{\partial x}}_{\text{Convection}} + \underbrace{h_v (T_s - T_c)}_{\text{Solid-fluid heat exchange}} \tag{C.9}$$

$$\partial T_c = -\frac{1}{\rho_c v_c c_{p,c}} h_v (T_s - T_c) \partial x \tag{C.10}$$

The solid temperature is known on both surfaces and is assumed to vary exponentially from the back surface to the front surface of the sample. To find the steady-state values, the equation is rearranged as shown in Eq. (C.10). The coolant mass flux is still unknown, but correlates with the pressure drop across the sample. Hence, a mass flux is assumed to solve Eq. (C.10) and obtain the fluid temperature across the sample. Afterwards, the pressure drop between the back and front surface is computed based on these fluid temperature values, by rearranging and discretising the Darcy-Forchheimer differential equation (Eq. (C.2)) in Eq. (C.11).

$$p_x = p_{x-1} - \left(\frac{\mu_c(T_c)}{K_D} v + \frac{\rho_c(T_c, p_c)}{K_F} v^2\right)\Delta x, \tag{C.11}$$

In an iterative process, the mass flux is adjusted until the pressure drop across the sample matches the boundary conditions, namely the measured plenum pressure at the back surface and the stagnation pressure at the front surface. The viscosity in Eq. (C.11) is calculated based on Sutherland's law. The density of the coolant is evaluated from the ideal gas equation and the velocity is found from continuity. Finally, the Shomate equation with the coefficients provided by Chase [130] is used to find the heat capacity of the fluid at every spatial iteration. The through-flow area is known and used to convert between mass flux and mass flow rate. It was deduced from a velocity map, which was obtained before the plasma wind tunnel test. A hot wire hovered about 2 mm above the ZrB_2 sample and recorded the exit velocity of the coolant flow with a 1 mm x 1 mm pixel resolution. For both samples the through-flow area was approximately circular with a diameter of 9 mm.

Once the cooling temperature is determined, the term denoting the solid-fluid heat exchange in Eq. (C.9) is computed at every step. It represents the heat flux absorbed by the fluid phase at a spatial location x and is integrated throughout the sample depth to obtain the total internal convective heat flux of the sample. Normalisation is needed to compare the data obtained at different wind tunnel conditions. It is performed by the nominal heat flux, provided by the fully catalytic, oxidised copper heat flux probe. The latter is obtained by multiplying the cold wall heat flux from Table C.1 with a correction factor to account for the difference in

Table C.4: Heat Fluxes of Tested Sample.

Probe	$\dot{q}_{\text{rad}}$	$\dot{q}_{\text{conv}}$	$\dot{q}_{\text{reduced}}$	$\frac{\dot{Q}_{\text{lateral}}}{A_{\text{front}}}$	$\dot{q}_{0,\text{nom,tc3}}$
	$[MW/m^2]$	$[MW/m^2]$	$[MW/m^2]$	$[MW/m^2]$	$[MW/m^2]$
#2	0.2655	0.0911	0.3566	1.425	3.59
#5	0.108	0.1505	0.2585	1.100	3.59

Table C.5: Coolant Properties and Geometric Parameters of Tested Samples.

Probe	Coolant	p_{plenum}	$\dot{m}$	L_1	A	$\mathcal{R}$	$c_{p,c}$
		[bar]	[mg/s]	[mm]	[mm^2]	[Jkg^{-1}K^{-1}]	[Jkg^{-1}K^{-1}]
#2	Helium	8.10	1.288	4.63	63.617	2077.1	5193
#5	Nitrogen	7.87	39.45	5.11	63.617	296.80	1061

wall temperatures between the water cooled heat flux probe and the the uncooled ZrB_2 probe. This is done as follows:

$$\dot{q}_{0,\text{nom}} = \dot{q}_{0,\text{cold}} \frac{h_e - h_w}{h_e - h_{\text{cold}}}. \tag{C.12}$$

A summary of the heat fluxes is provided in Table C.4. Table C.5 summarises the values used in this calculation.

The transient heat flux reduction values for different mass fluxes of coolant gas are provided by Ref [121]. They formed part of the NISIp calibration method and were obtained while the probe was exposed to a free stream at condition 4. The values are already normalised by $\dot{q}_{0,\text{nom,tc4}} = 2\text{MW/m}^2$. During these transient exposures, the sample surface did not exceed 550 K. Hence h_w is negligible and there is no need for a correction (Eq. (C.12)).

$$\frac{\dot{q}}{\dot{q}_0} = \frac{B_h}{e^{B_h} - 1} \tag{C.13}$$

Now that the heat flux reduction $\frac{\dot{q}}{\dot{q}_0}$ is known, it remains to find the corresponding blowing parameters. They are calculated by multiplying Eq. (C.5) by the correction factor (Eq. (C.7)):

$$B_h \left(\frac{c_{p,c}}{c_{p,e}}\right)^{1/3} = \frac{F c_{p,e} \rho_e v_e (T_e - T_w)}{\dot{q}_0} \left(\frac{c_{p,c}}{c_{p,e}}\right)^{1/3} = \frac{\rho_c v_c (h_e - h_w)}{\dot{q}_0} \left(\frac{c_{p,c}}{c_{p,e}}\right)^{1/3} \tag{C.14}$$

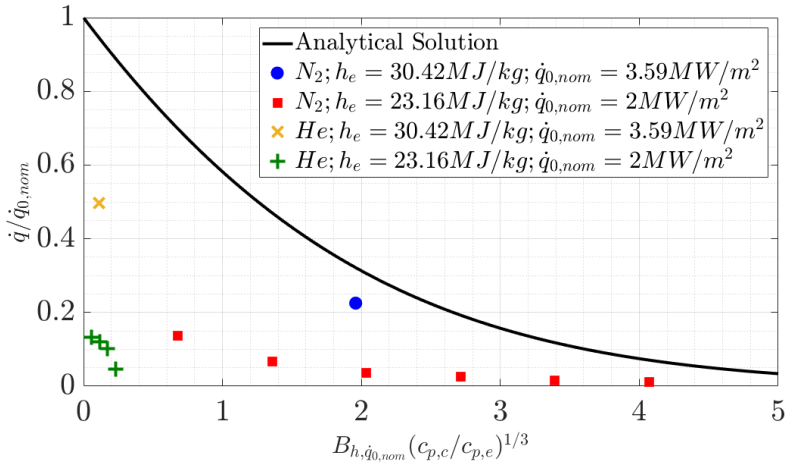

Figure C.9: Heat flux reduction due to blowing, normalised by the nominal heat flux.

The mass fluxes for the steady state and the transient tests are known, as well as the difference in enthalpies, which can be deduced from Table C.1. The heat capacities are given in Table C.1 and C.5.

As previously discussed, $\dot{q}_0$ is normalised by $\dot{q}_{0,\text{nom}}$. The heat capacity of the coolant exiting the porous medium is again computed from the Shomate equations based on the coefficients provided by Chase [130] and the fluid temperature at the wall, previously computed by solving Eq. (C.9). The equilibrium heat capacity of the post-shock gas at the boundary layer edge, $c_{p,e}$ was evaluated in a tp type problem using CEA[100], with pressure and temperature taken from Table C.1.

The results, normalised by $\dot{q}_{0,\text{nom}}$ are plotted in Fig. C.9. It is apparent that the experimental results show a much stronger cooling than predicted by theory for the nominal normalisation. At this point it should be noted that the analytical solution provided by Kays & Crawford [32] does not take into account real gas effects, of which there are many in high-enthalpy flows. Clearly, the uncooled sample experienced a strong, exothermic, surface oxidation, possibly also nitration. In addition, there are many other activated species in the post-shock plasma flow that could have recombined at the surface and lead to even more catalytic heating. It is unclear, how much of the total heat flux can be linked to these catalytic effects.

However, the steep drop in incident heat flux even at low blowing parameters, suggests that the smallest amounts of the ejected fluid create a barrier that mitigates

the diffusion of activated species through to the surface, which drastically reduces the incident heat flux. This extreme reduction in heat flux with the smallest amount of blowing has previously been observed and studied in Ref [41]. As the temperature of the post-shock gas rises, the relative amount of dissociated, ionised and activated species increases as well, which suggests that the share of catalytic heat flux of the total heat flux grows. The drop in heat flux for the helium cooled sample in condition 3 is much deeper than in condition 4, perhaps precisely because the share of catalytic heat flux is much higher and is removed with the slightest blowing.

Despite the multiplication of the correlation factor, there is a discrepancy in cooling performance between the two gases, with Helium being the better coolant by a margin. To the author's knowledge it has not been specified in literature whether the correlation factor should contain the equilibrium or the frozen heat capacity of the post-shock gas. As the flow moves through the nozzle, the electrical energy will gradually be transferred into internal energy and finally into kinetic energy when it leaves the nozzle and crosses the bow shock. The equilibrium values have been chosen for these calculations. A second unknown and possible source of discrepancy in the results is the Reynolds number of the transpiration cooled stagnation point. If the flow was turbulent, the exponent of the correlation factor would be 0.6 instead of 1/3. The low pressure and high temperature suggest that the Reynolds number is very low and the flow hence laminar. However, the high-frequency, transient oscillations of the arc-generator could break up the laminar structures. It is also unclear to which extent the Reynolds number is affected by the blowing. Since both of the latter effects would need further investigation to be confirmed, the flow was assumed to be laminar in this case.

C.3.3 Extracting front surface temperature and emissivity from the spectra

In this section, emission spectra of the Echelle spectrograph measurements are analysed. The spectra contain the plasma line emission and the black body radiation

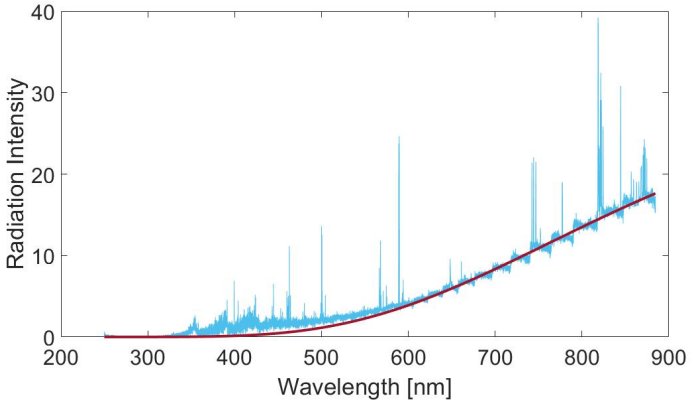

Figure C.10: The front surface temperature is obtained by fitting the Planck curve to the spectrum.

of the sample surface. The spectral distribution of electromagnetic radiation emitted by a grey body is described by Planck's law:

$$B_\lambda(\lambda, T, \varepsilon_s) = \frac{2hc^2}{\lambda^5} \frac{1}{e^{\frac{hc}{\lambda k_B T}} - 1} \varepsilon_s. \tag{C.15}$$

The front surface temperature of an object can be obtained by fitting Eq. (C.15) to the recorded spectra, as illustrated in Fig. C.10

Not all of the radiation the Echelle spectrometer records is blackbody radiation. The lines and bands, especially at small wavelengths are emitted by specific atoms or molecules. The spectral band of N_2^+ can clearly be seen at around 400 nm, which is why the curve fit is only performed in the relatively clean interval from 600-900 nm.

The result for the uncooled probe (probe #4) at condition 3 is plotted in Fig. C.11 and compared to the temperature values obtained by the infrared camera. The discrepancy in the measurements could be due the changing surface emissivity of oxidising ZrB_2. Temperature is purely a function of curvature in the Planck fit, while the IR camera necessitates an emissivity value to convert the detected irradiance to a temperature value. While ZrB_2 has an emissivity of $\varepsilon_s = 0.75$ at room temperature [126], the emissivity might have changed at elevated temperatures and after surface oxidation. Both temperature measurements match for an emissivity of $\varepsilon_s = 0.562$.

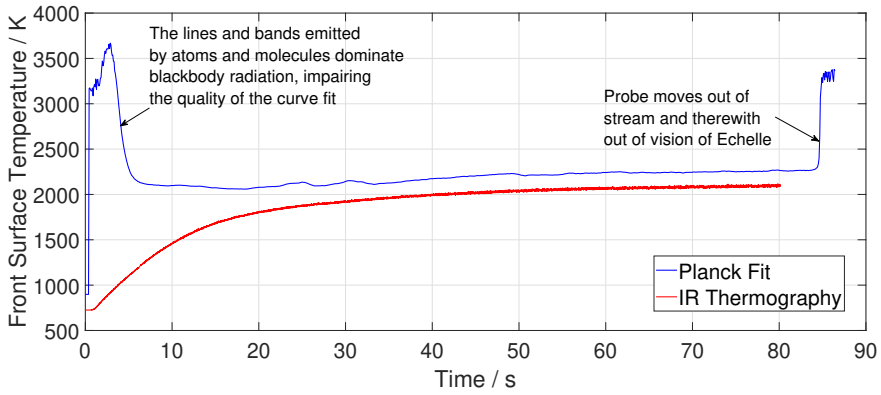

Figure C.11: Surface temperature obtained through Planck curve fit vs surface temperature measured by IR thermography camera assuming $\varepsilon_s = 0.75$.

C.3.4 Qualitative assessment of spectra

Figure C.12 shows a comparison between the emission spectra in front of the sample in the cases of the solid sample and the helium cooled sample. Figure C.13 shows the comparison between an uncooled sample and a nitrogen cooled sample. The spectra of the solid sample was taken 17 s after it was moved into the stream, while the helium and nitrogen spectra were obtained after 11 s and 4 s in the stream, respectively. The expected air plasma lines (N_2^+, N, O) and bands are observed which are naturally present at these high enthalpy conditions. In addition, many foreign species can be identified that stem from the interaction of the plasma with the sample. The oxidation and ablation of the surface leads to a diffusion of various material sample species into the hot stagnation point plasma. The inner degrees of freedom of those particles are then excited and the the characteristic radiative transitions can be observed by the Echelle spectrometer. As expected, Zr lines are visible which show that the surface is recessing over time and the material is slowly eroded. Furthermore, species originating from the insulating high temperature glue are present in the boundary layer (C, Si, Mg) as well as common impurities like Na.

Except for the massive difference in background radiation level, only very little difference in line radiation is noticed between a cooled case and an uncooled case. Additional lines of Zr, Si and C are visible as well as the Balmer alpha line of H. Only two notable differences between the two cooled cases are observed. In

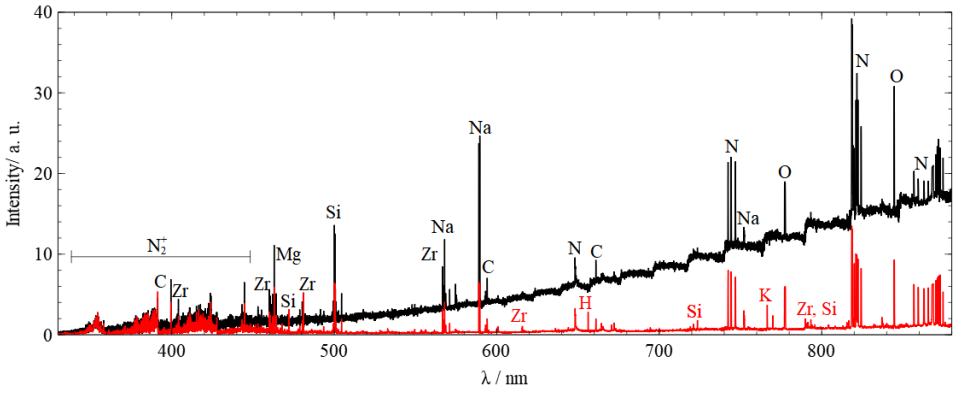

Figure C.12: Spectra of solid sample (black) and helium cooled sample (red).

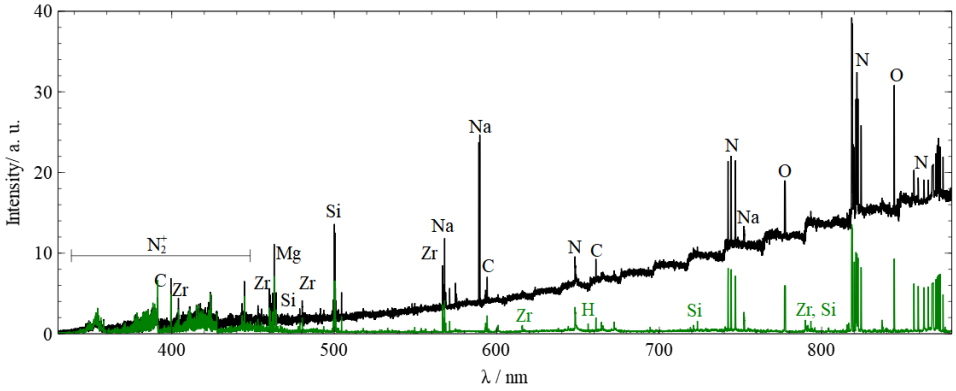

Figure C.13: Spectra of solid sample (black) and nitrogen cooled sample (green).

the case of nitrogen blowing, the Na lines at 598 nm are completely suppressed. For helium cooling two additional lines at 766.4 nm and 769.9 nm appear that are characteristic of K.

As will be shown in section C.3.5, many of these species can be retraced to different points of origin of the probe design, such as the porous sample itself, the high temperature glue or the coolant.

C.3.5 Post-test characterisation of samples

As the surface was observed in a SEM, radial cracks in the ZrO_2 ring, as well as circumferential cracks at the interface between said ring and the ZrB_2 sample were found in all three tested probes. The cracks in the insulation ring could have been caused by a thermal shock, inducing a sudden expansion. The circumferential

cracks were most likely caused at high temperatures at which the glue started to erode. By sintering the ZrB_2 directly into the insulation ring, these cracks could be avoided and better sealing achieved even at low blowing rates.

The surface of the dense reference sample, which was not cooled during the exposures to the plasma, became white and as shown in Fig. C.14 a crust has formed on top of the sample. Elemental analysis, as well as mass spectroscopy of the crust showed it consisted of oxygen and zirconium alone and hence can be identified as ZrO_2. In order to look beneath the surface and characterise the sample at different depths, the sample was cut. The cross-section confirms that an oxide layer of approximately 80 μm has formed, see Fig. C.15, with a clear interface with the remaining ZrO_2 material. Consistent with the literature for oxidation of ZrB_2 above 1800°C [10], all boron had evaporated from the oxide scale.

The surface of the helium cooled sample had partly discoloured white, but only as a result of the final exposures at lower mass flow rate. The surface morphology has changed substantially from the untested surface. Elemental analysis indicated the presence of zirconium, oxygen and some silicon. This is consistent with the species identified through spectral analysis. The silicon is believed to originate from the high temperature cement used to seal the specimens in the sample holder and which was found to be eroded substantially. The cross section together with elemental mapping indicates that the oxide layer consist essentially of a single row of grains and hence is very thin (<5 μm). Below this the material is essentially unchanged from the untested microstructure apart from the fact that the pores have now been filled with the epoxy used to stabilise the microstructure before cutting.

The surface of the nitrogen cooled sample became darker during testing but showed no discoloration towards white. Fig. C.14 also illustrates that this sample showed the smallest change in morphology from the untested material: the grains and pores are still clearly visible but some of the grains are now covered in small crystals, which formed during the low blowing rates. Elemental analysis showed the presence of zirconium, oxygen, boron, carbon, magnesium and silicon. The silicon and magnesium again are attributed to re-deposition of the eroded cement

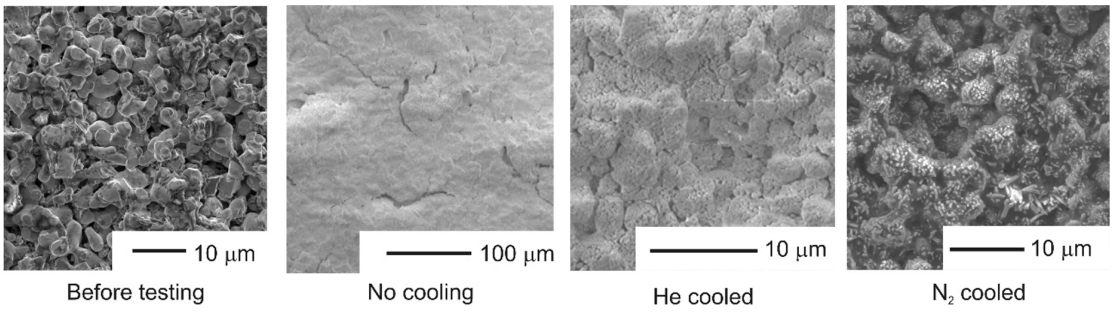

Figure C.14: Surface microstructure before and after testing.

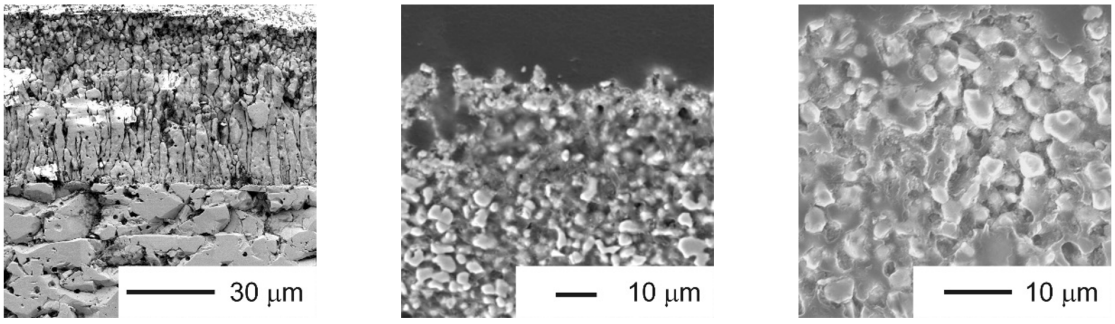

Figure C.15: Cross-sections after testing for the uncooled (left), helium cooled (center) and nitrogen cooled sample (right).

on the sample surface. The cross section at the surface of the sample, shown in Fig. C.15, also shows very little evidence of morphological changes apart from the epoxy infiltration of the pores, suggesting almost no oxidation has occurred in this case.

C.4 Conclusion

Three stagnation probes with transpiration cooled ZrB_2 samples were tested in a plasma wind tunnel. After exposure to the same flow conditions, the uncooled ZrB_2 sample was covered in an 80μm oxide layer, while the nitrogen transpiration cooled counterpart showed no signs of oxidation at a coolant mass flux of 620.11 g/m^{2}s. The helium cooled sample did not oxidise at a coolant mass flux of 20.25 g/m^{2}s. The uncooled probe reached a front surface temperature of 2150 K at a nominal heat flux of 3.59 MW/m^2. The helium and nitrogen cooled probes were cooled down to 1428 K and 1128 K respectively. Helium is the much better coolant for a given blowing parameter. The incident heat flux was reduced by 50.3 % compared to the uncooled sample for a mass flow rate of 1.288 mg/s. The incident heat flux

on the nitrogen cooled sample was reduced by 62.2 % compared to the uncooled sample for a mass flow rate of 39.45 mg/s. Catalytic heat flux makes up a large percentage of the total heat flux in high-enthalpy flows and is not accounted for by the analytical prediction for heat flux reduction suggested by Kays & Crawford. Even smallest amounts of coolant reduce the incident heat flux drastically. A Planck curve fit of the spectrum of the uncooled sample, suggests that the emissivity of the oxidised surface at 2150 K is $\varepsilon_s = 0.562$. A post-test characterisation confirmed that the crust on the uncooled ZrB_2 sample consists of ZrO_2. Whether oxidation was prevented solely by mitigating the diffusion of oxygen through to the surface or whether it was aided by mitigating catalytic heating in general, which reduced the surface temperature down to values at which the oxidation rate is low, remains to be investigated. The next test campaign will compare probes with different blowing parameters, but constant front surface temperatures to isolate these effects.

D

Design improvements for the next test campaign

This section provides an overview of the design improvements derived from the lessons learnt from the initial qualitative test campaign. In particular the probe design has been revised extensively, as shown in Fig. D.1. The new design features two critical improvements:

Lower thermal stresses The porous sample and the tube are both made from the same material and thus have the same coefficient of thermal expansion. Furthermore, an air gap around the porous sample allows it to expand freely as it is heated up. The gap is 0.5 mm wide, while the thermal expansion at 2200 K is numerically predicted to reach 0.16 mm, therefore leaving enough margin.

Less lateral heat fluxes The 1.5 mm thin, 25 mm long tube wall separates the hot sample on one end from the water cooled copper at the other. The heat flux is 50 % lower than with the previously employed ZrO_2 insulation ring. Thus, higher surface temperatures can be reached with the same freestream condition, expanding the testing envelope.

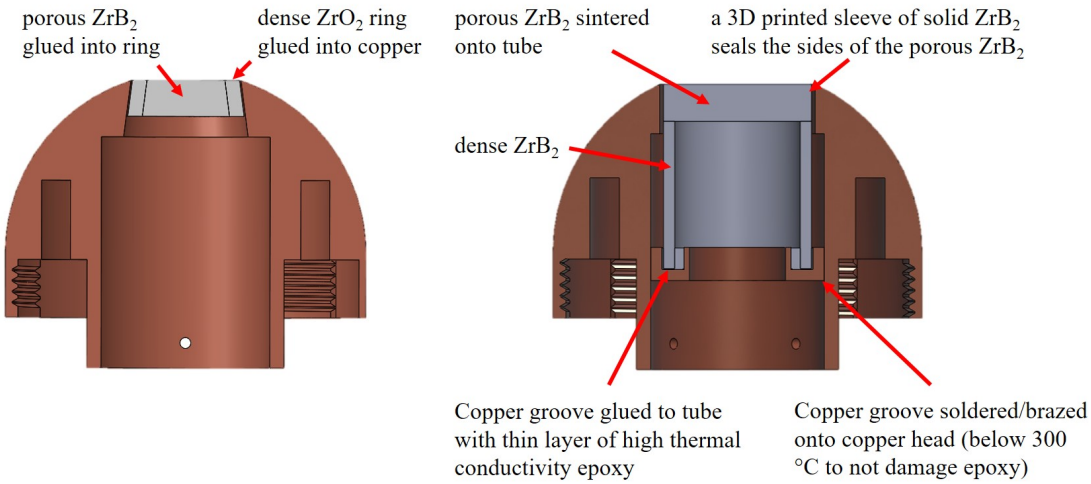

Figure D.1: Design of old (left) and new (right) transpiration cooled stagnation probe.

In order to avoid a buildup of heat at the connection between the copper groove and the ZrB_2, Epotek H77 high thermal conductivity epoxy is employed. Furthermore, the tube is pressed against the copper tube while the epoxy is liquid, to achieve direct thermal contact. This copper tube is then soldered onto the copper probehead. This is done very carefully, so as to just exceed the melting point of the solder, but avoid damage on the epoxy, which can be operated at up to 300 °C. This method can be applied in reverse to remove the insert and thus to reuse the probehead. Note that the air gap between the tube and the copperhead ensures that no lateral heat loss occurs between the hot ZrB_2 and the water cooled copper. The gap is kept small to minimise freestream flow ingress. The lateral surfaces of the porous ZrB_2 are sealed by a 3D printed sleeve of dense ZrB_2 in order to ensure exclusive outflow through the front surface. The porous sample is sintered to the dense tube and therefore bonded on an atomic level.

The model was successfully manufactured and assembled as depicted in Fig. D.2. It was then connected to a cover plate to fit it onto a pressure testing rig. For safety reasons, the pressure tests were conducted with water. No visible damage was detected after 10 minutes at 8 bar, including a transient peak pressure of 11 bar. Therefore, the bond between the porous sample and the dense tube is sufficiently strong. Steady state thermal analysis was conducted in Ansys. This analysis assumed a convective heat flux of 2.5 MW/m^2 at the stagnation point, which would

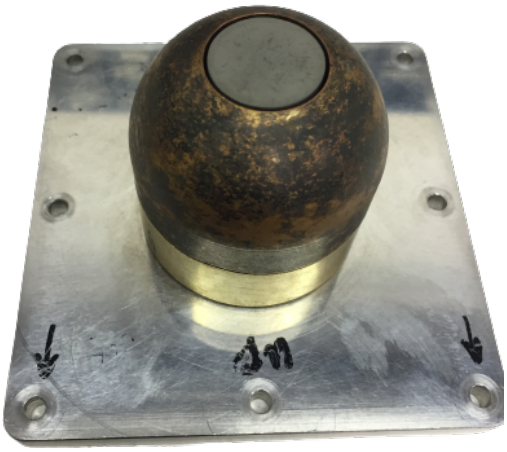

Figure D.2: Photo of revised probehead.

reduce to 1.5 MW/m^2 on the rest of the hemisphere. This is a conservative estimate, as the heat flux would reduce even further away from the stagnation point. Due to the high thermal conductivity of copper, most of the heat flux is absorbed by the coolant water and does not lead to an increase in probehead temperature. The water temperature was measured during the first test campaign and stayed relatively constant at 32 ° C. To complete the heat flux balance, radiative heat fluxes were simulated on all surfaces with the emissivities described in Table D.1, which also includes all other thermophysical parameters used in this calculation. Figure D.3 shows that the temperature at the epoxy interface is approximately 200 °C and thus well below its maximum operating temperature of 300 °C.

A further simulation was conducted in Ansys to model the steady state thermal stresses. As can be seen in Fig. D.4, they are much less than 0.1 MPa on the porous sample. At the intersection between the tube and the copper groove, the stress peaks at 50 MPa and is thus far below the 565 MPa strength of solid ZrB_2 [131].

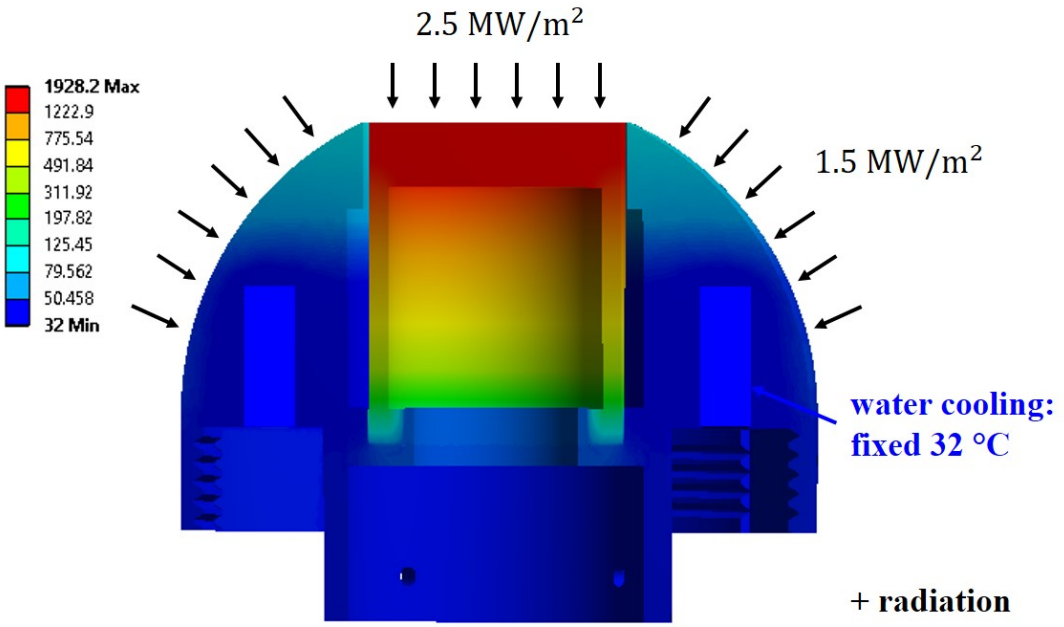

Figure D.3: Temperature distribution of a water cooled stagnation probe, exposed to a convective heat flux.

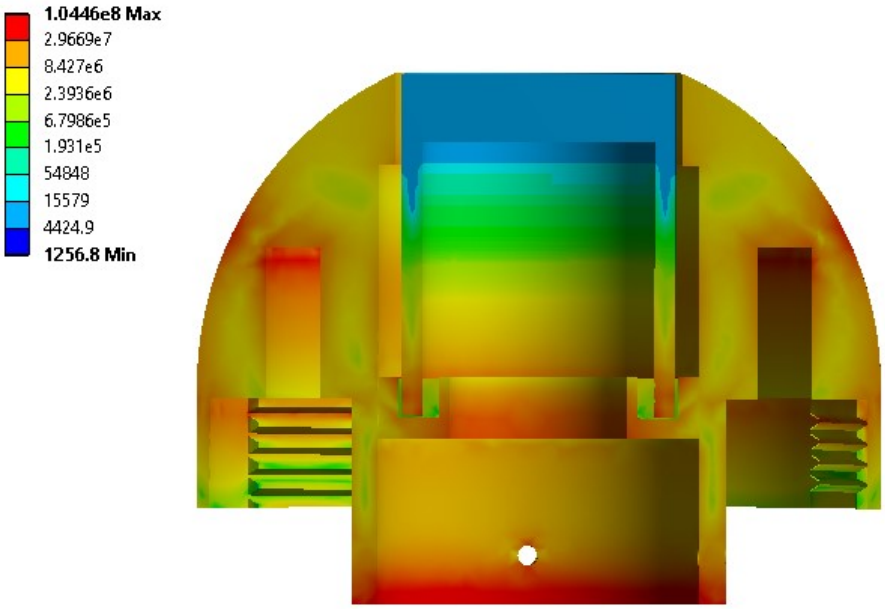

Figure D.4: Thermal stress distribution of a water cooled stagnation probe, exposed to a convective heat flux.

Table D.1: Thermophysical properties of materials used in the probehead.

Material	k	ε	CTE	Young's modulus	Poisson's ratio
Unit	[W/mK]	[-]	[-]	[GPa]	[-]
Copper	401	0.58	1.8×10^{-5}	110	0.34
42% porous ZrB_2	28	0.75	7.6×10^{-6}	98	0.3
Dense ZrB_2	48	0.75	7.6×10^{-6}	98	0.3
Epotek H77 epoxy	0.7	-	3.3×10^{-5}	3.5	0.33

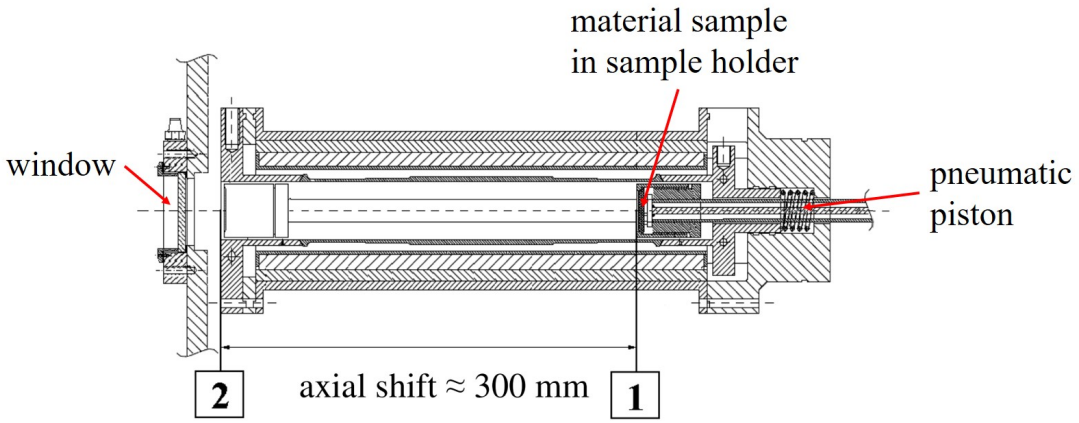

Figure D.5: Schematic of IRS emissivity measurement facility, taken from Ref. [132]

D.1 High temperature emissivity measurements

To improve the temperature readings it is critical to characterise the emissivity of the porous ZrB_2 for every temperature. This is particularly important, as the emissivity is strongly dependent on the surface microstructure and thus might differ from the emissivity taken from literature for the first experimental campaign. This will be achieved with the IRS emissivity measurement facility, schematically depicted in Fig. D.5

The material sample is mounted on a sample holder, which is initially recessed inside the cavity, creating a black body with an emissivity close to unity. The tube is sealed and evacuated to remove any oxygen and other gases that could react with the material surface at elevated temperatures. The testing temperature is reached through Joule heating and measured by a pyrometer just outside the window. The cavity is in thermal equilibrium through radiation exchange. When the sample reaches its steady state temperature in position 1, a pneumatic piston shifts it to

position 2. This shift is undertaken in less than 0.2 s and therefore assumed to be isothermal. As the sample is removed from the black body cavity, it displays grey body properties and thus the emissivity can be inferred from the ratio of thermal radiation in position 1 and 2, as detected by the same pyrometer.

D.2 Oxidation diagnostics

In the next experimental campaign, a pre-experiment SEM image of the surface microstructure will be taken. Through direct comparison with the post-experiment image, the impact of oxidation and high temperatures can be assessed better. Furthermore, the wavelength range of the Echelle spectrograph, which currently has a minimum of 249.33 nm, will be extended to include the 249 nm spectral line of Boron. As an atom, Boron has a particularly sharp emission signal. It is only produced as an intermediate product during oxidation and thus its emission line is considered a good indicator for oxidation activity. This method was validated by Ref. [67] and allows a time resolved quantification of oxidation.

References

[1] Kerry Millar and Kevin Brannon. *The rise of hypersonics*. `https://www2.deloitte.com/us/en/pages/energy-and-resources/articles/rise-of-hypersonics.html`. 2021. (accessed: 11.12.2021).

[2] BIS Research. *Hypersonic Technology Market - A Global and Country Analysis*. `https://bisresearch.com/industry-report/hypersonic-technology-market.html`. 2021. (accessed: 11.12.2021).

[3] NASA. *As Artemis Moves Forward, NASA Picks SpaceX to Land Next Americans on Moon*. `https://www.nasa.gov/press-release/as-artemis-moves-forward-nasa-picks-spacex-to-land-next-americans-on-moon`. 2021. (accessed: 11.12.2021).

[4] Thomas A Heppenheimer. *Facing the heat barrier: a history of hypersonics*. Vol. 4232. Government Printing Office, 2009.

[5] Roop N Gupta et al. "A review of reaction rates and thermodynamic and transport properties for an 11-species air model for chemical and thermal nonequilibrium calculations to 30000 K". In: *NASA STI/Recon Technical Report N* 90 (1990), p. 27064.

[6] James A Fay and Frederick R Riddell. "Theory of stagnation point heat transfer in dissociated air". In: *Journal of the Aerospace Sciences* 25.2 (1958), pp. 73–85.

[7] William Edward Nicolet. *Advanced methods for calculating radiation transport in ablation-product contaminated boundary layers*. Tech. rep. NASA, 1970.

[8] Michael E Tauber and Kenneth Sutton. "Stagnation-point radiative heating relations for Earth and Mars entries". In: *Journal of Spacecraft and Rockets* 28.1 (1991), pp. 40–42.

[9] R Byron Bird. "Transport phenomena". In: *Appl. Mech. Rev.* 55.1 (2002), R1–R4.

[10] TA Parthasarathy et al. "A model for the oxidation of ZrB2, HfB2 and TiB2". In: *Acta Materialia* 55.17 (2007), pp. 5999–6010.

[11] John Cleland and Francesco Iannetti. *Thermal Protection System of the Space Shutt1e*. Research Triangle Inst Research Triangle Park NC, 1989.

[12] Luke Uribarri and Edward H Allen. "Electron transpiration cooling for hot aerospace surfaces". In: *20th AIAA International Space Planes and Hypersonic Systems and Technologies Conference*. 2015, p. 3674.

[13] Hannah Böhrk, Henning Elsäßer, and Hendrik Weihs. "Flight Data from the Faceted TPS on SHEFEX II". In: *8th European Symposium on Aerothermodynamics for Space Vehicles*. ESA Conference Bureau Noordwijk, The Netherlands. 2015.

[14] Kenneth K Yoshikawa. *Linearized theory of stagnation point heat and mass transfer at hypersonic speeds*. Vol. 5246. National Aeronautics and Space Administration, 1969.

[15] Hassan Saad Ifti, Tobias Hermann, and Matthew McGilvray. "Flow characterisation of transpiring porous media for hypersonic vehicles". In: *22nd AIAA International Space Planes and Hypersonics Systems and Technologies Conference*. 2018, p. 5167.

[16] Marc Ewenz Rocher et al. "Pressure-sensitive paint diagnostic to measure species concentration on transpiration-cooled walls". In: *Experiments in Fluids* 63.1 (2022), pp. 1–11.

[17] Marc Ewenz Rocher et al. "Correlation for Species Concentration on a Hypersonic Stagnation Point with Mass Injection". In: *AIAA Journal* (2021), pp. 1–12.

[18] M Ewenz Rocher et al. *Measuring the concentration of freestream species on a hypersonic transpiration cooled stagnation point*. under review at AIAA Journal of Spacecraft and Rockets.

[19] Marc Ewenz Rocher et al. "Testing a transpiration cooled zirconium-di-boride sample in the plasma tunnel at IRS". In: *AIAA Scitech 2019 Forum*. 2019, p. 1552.

[20] M Ewenz Rocher, T Hermann, and McGilvray. *Oxidation response of transpiration cooled* ZrB_2 *on a hypersonic stagnation point*. under review at AIAA Journal of Spacecraft and Rockets.

[21] Charles Calvin Hoffman and Edmond Stephen Gillette. "A study of porous metal cooling". PhD thesis. California Institute of Technology, 1946.

[22] Pol Duwez and HL Wheeler Jr. "Experimental study of cooling by injection of a fluid through a porous material". In: *Journal of the Aeronautical Sciences* 15.9 (1948), pp. 509–521.

[23] M Hombsch and H Olivier. "Film cooling in laminar and turbulent supersonic flows". In: *Journal of Spacecraft and Rockets* 50.4 (2013), pp. 742–753.

[24] WD Rannie, Louis G Dunn, and Clark B Millikan. *A simplified theory of porous wall cooling*. Tech. rep. Pasadena, CA: Jet Propulsion Laboratory, National Aeronautics and Space ..., 1947.

[25] Ernst Rudolf Georg Eckert and John NB Livingood. *Comparison of effectiveness of convection-, transpiration-, and film-cooling methods with air as coolant*. Vol. 1182. National advisory committee for aeronautics, 1954.

[26] HS Mickley et al. "Heat, Mass, and Momentum Transfer for Flow over a Flat Plate with Blowing or Suction". In: 3208 (1954).

[27] DB Spalding. "A standard formulation of the steady convective mass transfer problem". In: *International Journal of Heat and Mass Transfer* 1.2-3 (1960), pp. 192–207.

[28] Robert J Moffat and William M Kays. "The turbulent boundary layer on a porous plate: experimental heat transfer with uniform blowing and suction". In: *International Journal of Heat and Mass Transfer* 11.10 (1968), pp. 1547–1566.

[29] W Mi Kays. "Heat transfer to the transpired turbulent boundary layer". In: *International Journal of Heat and Mass Transfer* 15.5 (1972), pp. 1023–1044.

[30] Robert T Swann. *Numerical Analysis of the Transient Responce of Advanced Thermal Protection Systems for Atmosphereic Entry: Robert T. Swann and Claud M. Pittman*. National Aeronautics and Space Administration, 1962.

[31] Leonard Roberts. *A theoretical study of stagnation-point ablation*. US Government Printing Office, 1959.

[32] William Morrow Kays. *Convective heat and mass transfer, 3rd ed.* Tata McGraw-Hill Education, 2012, p. 531.

[33] Joseph G Marvin and Ronald B Pope. "Laminar convective heating and ablation in the Mars atmosphere." In: *AIAA Journal* 5.2 (1967), pp. 240–248.

[34] Jens Meinert et al. "Investigations on the effect of foreign gas transpiration on a turbulent boundary layer". In: *36th AIAA/ASME/SAE/ASEE Joint Propulsion Conference and Exhibit*. 2000, p. 3386.

[35] Richard J Goldstein. "Film cooling". In: *Advances in heat transfer*. Vol. 7. Elsevier, 1971, pp. 321–379.

[36] John P Sellers Jr. "Gaseous film cooling with multiple injection stations". In: *AIAA Journal* 1.9 (1963), pp. 2154–2156.

[37] KA Heufer and H Olivier. "Experimental study of active cooling in 8 laminar hypersonic flows". In: *RESPACE–Key Technologies for Reusable Space Systems*. Springer, 2008, pp. 132–150.

[38] A. Gülhan and S. Braun. "An experimental study on the efficiency of transpiration cooling in laminar and turbulent hypersonic flows". In: *Experiments in Fluids* 50.3 (Mar. 2011), pp. 509–525. URL: https://doi.org/10.1007/s00348-010-0945-6.

[39] T Hermann et al. "Mixing characteristics in a hypersonic flow around a transpiration cooled flat plate model". In: *HISST 2018, International Conference on High-Speed Vehicle Science and Technology*. 2018.

[40] Je-Chin Han and Akhilesh P. Rallabandi. "TURBINE BLADE FILM COOLING USING PSP TECHNIQUE". In: *Frontiers in Heat and Mass Transfer* 1 (2010).

[41] Hirotaka Otsu, Kazuhisa Fujita, and Takeshi Ito. "Application of the transpiration cooling method for reentry vehicles". In: *45th AIAA Aerospace Sciences Meeting and Exhibit*. 2007, p. 1209.

[42] Tobias Langener, Jens Von Wolfersdorf, and Johan Steelant. "Experimental investigations on transpiration cooling for scramjet applications using different coolants". In: *AIAA journal* 49.7 (2011), pp. 1409–1419.

[43] Tobias Hermann and M McGilvray. "Analytical solution of flows in porous media for transpiration cooling applications". In: *Journal of Fluid Mechanics* 915 (2021).

[44] Arnold van Foreest et al. "Transpiration cooling using liquid water". In: *Journal of Thermophysics and Heat Transfer* 23.4 (2009), pp. 693–702.

[45] Leo T Chauvin and Howard S Carter. "Exploratory Tests of Transpiration Cooling on a Porous 8 Degree Cone at M= 2.05 Using Nitrogen Gas, Helium Gas, and Water as the Coolants". In: (1955).

[46] E. Ralph. *SpaceX CEO Elon Musk explains Starship's 'transpiring' steel heat shield in Q&A*. `https://www.teslarati.com/spacex-ceo-elon-musk-starship-transpiring-steel-heat-shield-interview/`. 2019. (accessed: 26.11.2021).

[47] Yuan-Qing Liu et al. "Transpiration cooling of a nose cone by various foreign gases". In: *International journal of heat and mass transfer* 53.23-24 (2010), pp. 5364–5372.

[48] Jens Meinert et al. "Turbulent boundary layers with foreign gas transpiration". In: *Journal of Spacecraft and Rockets* 38.2 (2001), pp. 191–198.

[49] Yuan-Qing Liu et al. "Experimental and numerical investigation of transpiration cooling for sintered porous flat plates". In: *Applied Thermal Engineering* 50.1 (2013), pp. 997–1007.

[50] M Arai and T Suidzu. "Porous ceramic coating for transpiration cooling of gas turbine blade". In: *Journal of Thermal Spray Technology* 22.5 (2013), pp. 690–698.

[51] Tobias Langener. "A contribution to transpiration cooling for aerospace applications using CMC walls". PhD thesis. University of Stuttgart, 2011.

[52] MP Bacos. "Carbon-carbon composites: oxidation behavior and coatings protection". In: *Le Journal de Physique IV* 3.C7 (1993), pp. C7–1895.

[53] Christian Dittert, Markus Selzer, and Hannah Böhrk. "Flowfield and pressure decay analysis of porous cones". In: *AIAA Journal* 55.3 (2017), pp. 874–882.

[54] William G Fahrenholtz and Greg E Hilmas. "Ultra-high temperature ceramics: materials for extreme environments". In: *Scripta materialia* 129 (2017), pp. 94–99.

[55] H Ifti, Tobias Hermann, and Matthew McGilvray. "Transpiration cooling at Mach 5 employing porous UHTC". In: *Conference on Flight vehicles, Aerothermodynamics and Re-entry Missions and Engineering (FAR)*. European Space Agency.

[56] Mark M Opeka, Inna G Talmy, and JA Zaykoski. "Oxidation-based materials selection for 2000 C+ hypersonic aerosurfaces: theoretical considerations and historical experience". In: *Journal of materials science* 39.19 (2004), pp. 5887–5904.

[57] Jochen Marschall et al. "Oxidation of ZrB2-SiC ultrahigh-temperature ceramic composites in dissociated air". In: *Journal of Thermophysics and Heat Transfer* 23.2 (2009), pp. 267–278.

[58] FH Brown. "Progress Report No. 20-252". In: *Jet Propulsion Laboratory, Pasadena, CA* 25 (1955).

[59] Mark M Opeka et al. "Mechanical, thermal, and oxidation properties of refractory hafnium and zirconium compounds". In: *Journal of the European Ceramic Society* 19.13-14 (1999), pp. 2405–2414.

[60] TA Parthasarathy et al. "A model for transitions in oxidation regimes of ZrB2". In: *Materials Science Forum*. Vol. 595. Trans Tech Publ. 2008, pp. 823–832.

[61] WC Tripp, HH Davis, and HC Graham. "Effect of an SiC addition on the oxidation of ZrB 2". In: *Amer. Ceram. Soc. Bull* 52.8 (1973), pp. 612–616.

[62] William G Fahrenholtz. "Thermodynamic analysis of ZrB2–SiC oxidation: formation of a SiC-depleted region". In: *Journal of the American Ceramic Society* 90.1 (2007), pp. 143–148.

[63] Elizabeth J Opila and Michael C Halbig. "Oxidation of ZrB2-SiC". In: (2001).

[64] JW Gregory et al. "A review of pressure-sensitive paint for high-speed and unsteady aerodynamics". In: *Proceedings of the Institution of Mechanical Engineers, Part G: Journal of Aerospace Engineering* 222.2 (2008), pp. 249–290.

[65] P Schreivogel, G Paniagua, and H Bottini. "Pressure sensitive paint techniques for surface pressure measurements in supersonic flows". In: *Experimental thermal and fluid science* 39 (2012), pp. 189–197.

[66] Tianshu Liu et al. "Temperature-and pressure-sensitive luminescent paints in aerodynamics". In: *Applied Mechanics Reviews* 50 (1997), pp. 227–246.

[67] Mickaël Playez et al. "Optical emission spectroscopy during plasmatron testing of ZrB2-SiC ultrahigh-temperature ceramic composites". In: *Journal of thermophysics and heat transfer* 23.2 (2009), pp. 279–285.

[68] Christopher Palmer and Erwin G Loewen. *Diffraction grating handbook*. Newport Corporation New York, 2005.

[69] KD Vernon-Parry. "Scanning electron microscopy: an introduction". In: *III-Vs Review* 13.4 (2000), pp. 40–44.

[70] Jürgen H Gross. *Mass spectrometry: a textbook*. Springer Science & Business Media, 2006.

[71] Jaeyong Ahn, Shantanu Mhetras, and Je-Chin Han. "Film-cooling effectiveness on a gas turbine blade tip using pressure-sensitive paint". In: *J. Heat Transfer* 127.5 (2005), pp. 521–530.

[72] Muhammad Hassan Bashir, Chao-Cheng Shiau, and Je-Chin Han. "Film cooling effectiveness for three-row compound angle hole design on flat plate using PSP technique". In: *International Journal of Heat and Mass Transfer* 115 (2017), pp. 918–929.

[73] Masaharu Kameda et al. "Adsorptive pressure-sensitive coatings on porous anodized aluminium". In: *Measurement Science and Technology* 15.3 (2004), p. 489.

[74] M Ewenz Rocher et al. "Studying the Film Effectiveness of Transpiration Cooled Walls Using Pressure Sensitive Paint". In: *FAR Conference*. Monopoli, Italy, 2019.

[75] Matthew McGilvray et al. "The Oxford High Density Tunnel". In: *20th AIAA International Space Planes and Hypersonic Systems and Technologies Conference*. 2015, p. 3548.

[76] Mark Kenneth Quinn, Leichao Yang, and Konstantinos Kontis. "Pressure-sensitive paint: effect of substrate". In: *Sensors* 11.12 (2011), pp. 11649–11663.

[77] RJ Anthony et al. "Development of high-density arrays of thin film heat transfer gauges". In: *Proceedings of the 5th ASME/JSME Thermal Engineering Joint Conference*. San Diego. 1999.

[78] MLG Oldfield. "Impulse response processing of transient heat transfer gauge signals". In: *Journal of turbomachinery* 130.2 (2008).

[79] Tobias Hermann, Imran Naved, and Matthew McGilvray. "Tool for Rapid Transient Transpiration-Cooled Reentry Simulation". In: *AIAA Journal* 58.2 (2020), pp. 842–853.

[80] Max E Rife and Luca di Mare. "Numerical flux function for flow through porous media with discontinuous properties". In: *Journal of Computational Physics* 397 (2019), p. 108833.

[81] ERG Eckert. "Engineering relations for heat transfer and friction in high-velocity laminar and turbulent boundary-layer flow over surfaces with constant pressure and temperature". In: *Transactions of the ASME* 78.6 (1956), pp. 1273–1283.

[82] Carl B Moyer and Roald A Rindal. *An analysis of the coupled chemically reacting boundary layer and charring ablator. part 2-finite difference solution for the in-depth response of charring materials considering surface chemical and energy balances*. Tech. rep. NASA, 1968.

[83] MS Holden and SJ Sweet. "Experimental Studies of Transpiration Cooling With Shock Interaction in Hypersonic Flow". In: *Final Report Part B, Grant Number NAG* (1994), pp. 1–790.

[84] Michael E Tauber. *A review of high-speed, convective, heat-transfer computation methods*. National Aeronautics and Space Administration, 1989.

[85] Kenneth Sutton and Randolph A Graves Jr. "A general stagnation-point convective heating equation for arbitrary gas mixtures". In: *No. NASA-TR-R-376* (1971).

[86] William D Henline. "Transpiration cooling of hypersonic blunt bodies with finite rate surface reactions". In: *No. A-89018* (1989).

[87] Tobias Hermann, Matthew McGilvray, and Imran Naved. "Performance of Transpiration-Cooled Heat Shields for Reentry Vehicles". In: *AIAA Journal* 58.2 (2020), pp. 830–841.

[88] RE Loehman et al. "Ultrahigh-Temperature Ceramics For Hypersonic Vehicle Applications." In: *Industrial Heating* 71.1 (2004), pp. 36–38.

[89] Arturo Francese. "Numerical and experimental study of UHTC materials for atmospheric re-entry". In: *Dottorato di ricerca in ingegneria aerospaziale* (2007).

[90] Thomas Reimer et al. "Transpiration cooling tests of porous CMC in hypersonic flow". In: *17th AIAA International Space Planes and Hypersonic Systems and Technologies Conference*. 2011, p. 2251.

[91] Ikhyun Kim, Gisu Park, and Jae Jeong Na. "Experimental study of surface roughness effect on oxygen catalytic recombination". In: *International Journal of Heat and Mass Transfer* 138 (2019), pp. 916–922.

[92] Yosheph Yang, Ikhyun Kim, and Gisu Park. "Experimental and numerical study of oxygen catalytic recombination of SiC-coated material". In: *International Journal of Heat and Mass Transfer* 143 (2019), p. 118510.

[93] Johannes Steinheuer. "Berechnung der laminaren Zweistoff-Grenzschicht in der hypersonischen Staupunktströmung mit temperaturabhängigen Stoffbeiwerten". In: *ZAMM-Journal of Applied Mathematics and Mechanics/Zeitschrift für Angewandte Mathematik und Mechanik* 51.3 (1971), pp. 209–223.

[94] AF Mills and A Wortman. "Two-dimensional stagnation point flows of binary mixtures". In: *International Journal of Heat and Mass Transfer* 15.5 (1972), pp. 969–987.

[95] John D Anderson Jr. *Hypersonic and high-temperature gas dynamics*. American Institute of Aeronautics and Astronautics, 2006.

[96] A Dorodnitsyn. "Laminar boundary layer in compressible fluid". In: *Dokl. Akad. Nauk SSSR*. Vol. 34. 8. 1942, pp. 213–219.

[97] Lester Lees. "Laminar heat transfer over blunt-nosed bodies at hypersonic flight speeds". In: *Journal of Jet Propulsion* 26.4 (1956), pp. 259–269.

[98] Hermann Schlichting and Klaus Gersten. *Boundary-layer theory*. Springer, 2016.

[99] ASTM E637-05(2016), Standard Test Method for Calculation of Stagnation Enthalpy from Heat Transfer Theory and Experimental Measurements of Stagnation-Point Heat Transfer and Pressure, ASTM International, West Conshohocken, PA, 2016, www.astm.org.

[100] C Snyder. *CEARUN*. `https://cearun.grc.nasa.gov`. 2012. (accessed: 22.08.2018).

[101] R Jacobs Gollan and PA Jacobs. "About the formulation, verification and validation of the hypersonic flow solver Eilmer". In: *International Journal for Numerical Methods in Fluids* 73.1 (2013), pp. 19–57.

[102] Peter Jacobs and Rowan Gollan. "Implementation of a compressible-flow simulation code in the D programming language". In: *Applied Mechanics and Materials*. Vol. 846. Trans Tech Publ. 2016, pp. 54–60.

[103] William Morrow Kays. "Heat transfer to the transpired turbulent boundary layer". In: *International Journal of Heat and Mass Transfer* 15.5 (1972), pp. 1023–1044. URL: `http://www.sciencedirect.com/science/article/pii/0017931072902372`.

[104] E Reginald Van Driest. *The problem of aerodynamic heating*. Institute of the Aeronautical Sciences, 1956.

[105] AF Kolesnikov. "The aerothermodynamic simulation in-and supersonic high-enthalpy jets: experiment and theory". In: *Aerothermodynamics for space vehicles*. Vol. 367. 1995, p. 583.

[106] Obinna Uyanna and Hamidreza Najafi. "Thermal protection systems for space vehicles: A review on technology development, current challenges and future prospects". In: *Acta Astronautica* 176 (2020), pp. 341–356.

[107] Jean Lachaud et al. "Detailed chemical equilibrium model for porous ablative materials". In: *International Journal of Heat and Mass Transfer* 90 (2015), pp. 1034–1045.

[108] Triplicane Parthasarathy et al. "A model for the oxidation of ZrB2, HfB2 and TiB2". In: *Acta Materialia* 55 (Mar. 2007), pp. 5999–6010.

[109] RB Evans III, GM Watson, and EA Mason. "Gaseous diffusion in porous media. II. Effect of pressure gradients". In: *The Journal of Chemical Physics* 36.7 (1962), pp. 1894–1902.

[110] Triplicane A Parthasarathy et al. "Thermal and oxidation response of UHTC leading edge samples exposed to simulated hypersonic flight conditions". In: *Journal of the American Ceramic Society* 96.3 (2013), pp. 907–915.

[111] Imran Naved, Tobias Hermann, and Matthew McGilvray. "Numerical Simulation of Transpiration Cooling for a High-Speed Vehicle with Substructure". In: *AIAA Journal* (2021), pp. 1–12.

[112] Sven Schweikert et al. "Characterization of actively cooled porous C/C wall segments according to pressure loss and internal temperature distribution". In: *7th European Workshop on Thermal Protection Systems & Hot Structures*. ESA Conference Bureau Noordwijk, The Netherlands. 2013.

[113] Hassan Saad Ifti et al. "Flow Characterization of Porous Ultra-High-Temperature Ceramics for Transpiration Cooling". In: *AIAA Journal* (2022), pp. 1–12.

[114] John David Anderson Jr. *Fundamentals of aerodynamics*. Tata McGraw-Hill Education, 2007.

[115] Manabu Iguchi and Olusegun J. Ilegbusi. "Diffusion and Mass Transfer". In: *Basic Transport Phenomena in Materials Engineering*. Tokyo: Springer Japan, 2014, pp. 135–147. URL: https://doi.org/10.1007/978-4-431-54020-5_8.

[116] G. Milgrom. *Space Shuttle Thermal Protection System*. English. Gary Milgrom, 2013.

[117] BV Coplan and RW King. "Applying the Ablative Heat Shield to the Apollo Spacecraft". In: *(4th) Space Congress Proceedings*. 1967.

[118] John J Bertin. *Hypersonic aerothermodynamics*. AIAA, 1994.

[119] Narottam P Bansal. *Handbook of ceramic composites*. Vol. 165. Springer, 2005.

[120] William G Fahrenholtz. "The ZrB2 volatility diagram". In: *Journal of the American Ceramic Society* 88.12 (2005), pp. 3509–3512.

[121] Fabian Hufgard et al. "Surface Heat Flux Measurement in Transpiration-Cooled Porous Materials Using Plenum Pressure Data". In: *AIAA Scitech 2019 Forum*. 2019, p. 2062.

[122] Monika Auweter-Kurtz and Thomas Wegmann. *Overview of IRS plasma wind tunnel facilities*. Tech. rep. STUTTGART UNIV (GERMANY FR) INST FUERRAUMFAHRTSYSTEME, 2000.

[123] Stefan Loehle et al. "Comparison of Heat Flux Gages for High Enthalpy Flows-NASA Ames and IRS". In: *46th AIAA Thermophysics Conference*. 2016, p. 4422.

[124] Ernest V Zoby. *Empirical stagnation-point heat-transfer relation in several gas mixtures at high enthalpy levels*. Vol. 4799. National Aeronautics and Space Administration, 1968.

[125] Matweb. [Online] Zirconium Oxide, Zirconia, ZrO2. Available at: http://www.matweb.com/search/datasheet.aspx?MatGUID=0742ddaddf80467fb6532e025c694e89. [Accessed 6 Jun. 2018].

[126] M Balat-Pichelin et al. "Emissivity, catalycity and microstructural characterization of ZrB2–SiCfiber based UHTC at high temperature in a non-equilibrium air plasma flow". In: *Ceramics International* 40.7 (2014), pp. 9731–9742.

[127] Stefan Löhle, Sven Schweikert, and Jens von Wolfersdorf. "Method for Heat Flux Determination of a Transpiration-Cooled Wall from Pressure Data". In: *Journal of Thermophysics and Heat Transfer* 30.3 (2016), pp. 567–572.

[128] James W. Zimmermann et al. "Thermophysical Properties of ZrB2 and ZrB2–SiC Ceramics". In: *Journal of the American Ceramic Society* 91 (Feb. 2008), pp. 1405–1411.

[129] BS EN ISO. *4022:2006*. 2006.

[130] Malcolm W Chase Jr. "NIST-JANAF thermochemical tables". In: *J. Phys. Chem. Ref. Data, Monograph* 9 (1998).

[131] Adam L Chamberlain et al. "High-strength zirconium diboride-based ceramics". In: *Journal of the American Ceramic Society* 87.6 (2004), pp. 1170–1172.

[132] M Schüßler et al. "Characterization of candidate Materials for the Catalytic Re-entry Experiment PHLUX on EXPERT". In: *Thermal Protection Systems and Hot Structures*. Vol. 631. 2006.